Pontifícia Universidade Católica
do Rio de Janeiro

Antonio Capanema Guerra Galvão

Multi-Messenger Perspectives on the High-Energy Universe through Neutrinos, Gamma Rays and Cosmic Rays

Tese de Doutorado

Thesis presented to the Programa de Pós–graduação em Física of PUC-Rio in partial fulfillment of the requirements for the degree of Doutor em Ciências – Física .

Advisor: Prof. Arman Esmaili Taklimi

Rio de Janeiro
June 2024

Pontifícia Universidade Católica
do Rio de Janeiro

Antonio Capanema Guerra Galvão

Multi-Messenger Perspectives on the High-Energy Universe through Neutrinos, Gamma Rays and Cosmic Rays

Thesis presented to the Programa de Pós–graduação em Física of PUC-Rio in partial fulfillment of the requirements for the degree of Doutor em Ciências – Física . Approved by the Examination Committee:

Prof. Arman Esmaili Taklimi
Advisor
Departamento de Física – PUC-Rio

Prof. Hiroshi Nunokawa
Departamento de Física – PUC-Rio

Prof. Pedro Cunha de Holanda
Unicamp

Prof. Aion da Escóssia Melo Viana
USP

Prof. João Ramos Torres de Mello Neto
UFRJ

Rio de Janeiro, June 21st, 2024

Antonio Capanema Guerra Galvão

Bachelor of Science and Master of Science degrees in Physics at the Pontifical Catholic University of Rio de Janeiro.

Bibliographic data

Galvão, Antonio Capanema Guerra

Multi-messenger perspectives on the high-energy universe through neutrinos, gamma rays and cosmic rays / Antonio Capanema Guerra Galvão; advisor: Arman Esmaili Taklimi. – 2024.

211 f: il. color. ; 30 cm

Tese (doutorado) – Pontifícia Universidade Católica do Rio de Janeiro, Departamento de Física, 2024.

Inclui bibliografia

1. Física – Teses. 2. Astrofísica Multimensageira. 3. Cascatas Eletromagnéticas. 4. Neutrinos Astrofísicos. 5. Raios Cósmicos Ultra-Energéticos. I. Taklimi, Arman Esmaili. II. Pontifícia Universidade Católica do Rio de Janeiro. Departamento de Física. III. Título.

CDD: 530

To my professors, friends and family,
for their unrelenting support and encouragement.

Acknowledgments

The joy in living an academic life comes not only from the science itself, but also from the opportunities it gives us to meet the most remarkable human beings from all around the world. It is thanks to them that my enthusiasm, willpower, and curiosity are still alive and strong to this day. Over the years, I have been fortunate enough to cross paths with many such people; it is now my pleasure to dedicate this moment to acknowledge all that you have done for me.

First and foremost, I would like to thank Professor Arman Esmaili, my advisor, mentor, inspiration, and friend. After knocking on your office all the way back in 2017, my naive undergraduate self could never have predicted such a fruitful partnership to develop. Thank you for your guidance (and patience) throughout these 7 years, especially during the most critical periods of my Master's and Ph.D. degrees. It will take another Hubble time for anyone to find a supervisor as great as you. I can only hope to make you proud, now that our academic journeys are about to diverge, and look forward to our future encounters.

The Pontifical Catholic University has been my home for just over a decade. It would be an impossible task to name all professors and students who made this experience all that more unique. However, it would be unfair to proceed without offering a special thanks to Professors Gero Gersdorff, Hiroshi Nunokawa and Thiago Guerreiro, for your lectures, physics discussions and life advice, whenever needed. I am also truly grateful to my dear friends, Marcelo, Anna Letícia, João Pedro, Brunna, Henrique, Lucas, Caio, Adriel, Pedro, Amir, Emilse, Fernanda, Lucianno, and Cíntia, who accompanied me through the ups and downs of my trajectory as a student at PUC.

I owe my deepest thanks to Prof. Markus Ahlers, for hosting me for a year within his research group at the University of Copenhagen. I appreciate all the time you took with me for meetings, discussions and feedback on presentations. Moreover, this exchange program has led to countless unforgettable moments alongside an amazing group of physicists. They took me in like I was family, kept me smiling the the cold Danish winters, and contributed to making 2023 the best year of my life thus far. Once again, a distinctive thanks to my beloved friends Tania, Kevin, Victor, Ersilia, Pedro, Marie, Marina, Kathrine, Damiano, Enrico (*l'importante*), Janni, Yago, Annika, Bernie, Manuel, Evelyn, Antonio, Arnau, Valentin and Pablo. Our paths are certainly bound to cross again, soon, somewhere in this tiny, tiny world. Tak for kaffe.

I am thankful to the government agencies responsible for funding my Ph.D. research projects. This study was financed in part by the Coordenação de Aperfeiçoamento de Pessoal de Nível Superior - Brasil (CAPES) - Finance Code 001, through the CAPES/PROEX No. 88887.511843/2020-00 and CAPES-PrInt No. 88887.717489/2022-00 scholarships. I would also like to thank the CNPq No. 140316/2021-3 and FAPERJ No. E-26/204.138/2022 scholarships contemplated during this period.

One final thank you must be given to my life-long friends (you all know who you are), my girlfriend, and my family, especially my parents, who have raised me with so much care.

This thesis is dedicated to all of you.

Abstract

Galvão, Antonio Capanema Guerra; Taklimi, Arman Esmaili (Advisor). **Multi-Messenger Perspectives on the High-Energy Universe through Neutrinos, Gamma Rays and Cosmic Rays**. Rio de Janeiro, 2024. 211p. Tese de Doutorado – Departamento de Física, Pontifícia Universidade Católica do Rio de Janeiro.

As we enter the precision era of multi-messenger astronomy, new windows are opened for us to better understand the Universe, from quantum to cosmic scales. In particular, the study of high-energy astrophysical phenomena has allowed us to probe the most extreme environments known to mankind, as well as obtain unprecedented breakthroughs within the realm of particle physics. This thesis summarizes the important findings of multi-messenger astrophysics over the years, before focusing its attention to three relevant topics currently being investigated in the field. Firstly, we tackle the problem of γ-ray propagation in space. High center-of-momenta interactions during this process leads to the formation of electromagnetic cascades that develop over cosmological distances. We describe a semi-analytical code called “γ-Cascade”, which calculates the fluxes at the Earth resulting from such cascades. We also explore the possibility of producing neutrinos in ultra-high-energy cascades. Secondly, we establish a new, original multi-messenger connection between the measured fluxes of TeV–PeV astrophysical neutrinos and ultra-high-energy cosmic rays. This is done by taking advantage of our precise γ-ray observations at sub-TeV energies, demonstrating the power of multi-messenger analyses. Finally, we study the evolution of the flavor composition of supernova neutrinos in a model-independent way. Our novel method allows for predictions of the neutrino flavor content measured at the Earth from supernovae, accounting for matter effects within its dense environment, while remaining completely agnostic about the outcome of self-induced flavor conversions in its core.

Keywords

Multi-Messenger Astrophysics; Electromagnetic Cascades; Astrophysical Neutrinos; Ultra-High-Energy Cosmic Rays.

Resumo

Galvão, Antonio Capanema Guerra; Taklimi, Arman Esmaili. **O Universo de Altas Energias sob a Perspectiva Multimensageira de Neutrinos, Raios Gama e Raios Cósmicos**. Rio de Janeiro, 2024. 211p. Tese de Doutorado – Departamento de Física, Pontifícia Universidade Católica do Rio de Janeiro.

Conforme entramos na era de precisão da astronomia multimensageira, novas janelas se abrem para compreendermos melhor o Universo, desde a escala quântica até a escala cósmica. Em particular, o estudo de fenômenos astrofísicos de altas energias tem nos permitido acessar os ambientes mais extremos conhecidos pela humanidade, bem como obter avanços sem precedentes no domínio da física de partículas. Esta tese resume as descobertas importantes da astrofísica multi-mensageira ao longo dos anos, e, em seguida, foca a sua atenção em três tópicos relevantes que estão atualmente sendo investigados neste campo. Primeiramente, abordamos o problema da propagação de raios gama no espaço. Interações durante este processo levam à formação de cascatas eletromagnéticas que se desenvolvem ao longo de distâncias cosmológicas. Apresentaremos um código semi-analítico chamado "γ-Cascade", que calcula os fluxos na Terra resultantes de tais cascatas. Também exploramos a possibilidade de se produzir neutrinos em cascatas ocorrendo a energias ultra-altas. Em segundo lugar, estabeleceremos uma relação multimensageira nova e original entre os fluxos medidos de neutrinos astrofísicos entre TeV–PeV e raios cósmicos ultra-energéticos. Para isso, utilizaremos nossas observações precisas de raios gama em energias abaixo de TeV, demonstrando o poder de uma análise multimensageira. Finalmente, estudaremos a evolução da composição de sabor de neutrinos produzidos em supernovas. Nosso novo método permite previsões genéricas sobre os possíveis sabores de neutrinos medidos na Terra. São levados em consideração os efeitos de matéria dentro dos ambientes densos de supernovas, enquanto permanecemos completamente agnósticos em relação ao resultado das conversões auto-induzidas de sabor em seus núcleos.

Palavras-chave

Astrofísica Multimensageira; Cascatas Eletromagnéticas; Neutrinos Astrofísicos; Raios Cósmicos Ultra-Energéticos.

Table of contents

List of figures

List of tables

List of codes

List of Abreviations

AGN – Active Galactic Nucleus

BH – Black Hole

CC – Charged Current

CIB – Cosmic Infrared Background

CMB – Cosmic Microwave Background

COB – Cosmic Optical Background

COM – Center-Of-Momentum

CRB – Cosmic Radio Background

CνB – Cosmic Neutrino Background

DOM – Digital Optical Module

DPP – Double Pair Production

EAS – Extensive Air Shower

EBL – Extragalactic Background Light

EGB – Extragalactic Gamma-ray Background

EM – Electromagnetic

EPP – Electron-positron Pair Production

ESTES – Enhanced Starting Track Event Selection

ETP – Electron Triplet Production

Fermi-LAT – Fermi Large Area Telescope

FSRQ – Flat Spectrum Radio Quasar

GRB – Gamma-Ray Burst

GW – Gravitational Wave

GZK – Greisen–Zatsepin–Kuzmin

HESE – High Energy Starting Events

ICS – Inverse Compton Scattering

IGM – Intergalactic Medium

IGMF – Intergalactic Magnetic Field

IGRB – Isotropic diffuse Gamma-ray Background

IMFP – Inverse Mean Free Path

IO – Inverted Ordering

ISM – Interstellar Medium

IR – Infrared

LHAASO – Large High Altitude Air Shower Observatory

MPP – Muon Pair Production

MSW – Mikheyev–Smirnov–Wolfenstein

NC – Neutral Current

NO – Normal Ordering

NS – Neutron Star

PAO – Pierre Auger Observatory

PBH – Primordial Black Hole

PMNS – Pontecorvo–Maki–Nakagawa–Sakata

RG – Radio Galaxy

SBG – Starburst Galaxy

SFG – Star-Forming Galaxy

SFR – Star Formation Rate

SM – Standard Model

SMBH – Supermassive Black Hole

SNR – Supernova Remnant

SN – Supernova

TA – Telescope Array

TDE – Tidal Disruption Event

(UHE)CR – (Ultra-high-Energy) Cosmic Ray

UV – Ultraviolet

If there is no point in the universe that we discover by the methods of science, there is a point that we can give the universe by the way we live, by loving each other, by discovering things about nature, by creating works of art.
- Steven Weinberg

Frankenberry, *The Faith of Scientists: In Their Own Words.*

Thesis Outline

This thesis is divided into 4 chapters,

1. Introduction,
2. The Physics of Electromagnetic Cascades,
3. A γ-Ray Connection between Neutrinos and UHECRs,
4. The Flavor Composition of Supernova Neutrinos

and 5 appendices,

A Neutrino Spectra from Muon Decay,

B Energy Conservation on a Grid,

C On-The-Spot Approximation on a Grid,

D γ-Cascade Functions,

E Neutrinos from Evaporating Primordial Black Holes.

The first four appendices pertain to the projects presented in the main text, while the last appendix contains a summary of a side project which has led to a publication (1) during my Ph.D. studies. We have separated it from the main text because its subject is somewhat unrelated to the focus of this thesis.

In the Introduction, we set the stage for the subsequent chapters by providing a broad overview of multi-messenger astrophysics, with a primary focus on γ rays, neutrinos, ultra-high-energy cosmic rays, and connections between these cosmic messengers. The following three chapters contain selected projects carried out during my Ph.D. program. Chapter 2 pertains to my research on electromagnetic cascades, a phenomenon occurring during high-energy γ-ray propagation through intergalactic space, which culminated in 1 publication (2) so far, with another one expected soon. Chapter 3 pertains to a multi-messenger analysis based on our current measurements of γ rays, neutrinos and ultra-high-energy cosmic rays. As of the writing of this thesis, this project is still ongoing, meaning we will only display partial results. Finally, Chapter 4 contains a reprint of (3), adapted to fit the model of this thesis. In this work, we introduce a model-independent way of predicting the observed flavor content of supernova neutrinos. These three chapters also include the necessary background context for each work, besides what was presented in the Introduction.

Planck natural units in which $c = \hbar = k_B = G = 1$ shall be used throughout this thesis, unless otherwise specified.

1
Introduction

Astronomy stands as one of the ancient disciplines within the realm of natural sciences, with a rich history spanning millennia. From ancient civilizations gazing at the night sky with wonder to the modern-day observatories peering deep into the cosmos, humanity's quest to unravel the mysteries of the Universe has been relentless. What began as a study of celestial motions and patterns has now developed beyond a purely observational science, and into a broad field of study that integrates principles of most branches of physics. This gradual paradigm shift marks the birth of astrophysics.

Astrophysicists are, as the name suggests, interested in investigating the physics behind the wide range of astronomical phenomena we see when we look out into the Universe. Our *modus operandi* consists in extracting information from these observations in order to better understand what happens inside, around and in between celestial bodies. By construction, however, this procedure entails a very distinct way of doing science. Unlike experiments conducted in controlled terrestrial environments, astrophysicists depend on signals coming from far away sources which we have absolutely no control over. Moreover, these signals may get distorted in all kinds of ways as they traverse vast regions of space on their way to us. In other words, we are but humble spectators of the external world, hinging upon the cosmic messengers that grace our instruments with whispers from the far reaches of the cosmos.

It is commonplace to use the aforementioned word "messengers" to refer to the various types of signal-carriers we detect at the Earth. Astrophysical messengers can come in the form of particles or waves. The study of particle messengers has developed significantly over the years and has naturally given rise to a rich subfield known as astroparticle physics.[1] Incidentally, as detection techniques have evolved, becoming more sophisticated and precise, we have transcended the traditional goal of only extracting information about the inner workings of astrophysical phenomena. Now, we are capable of making unprecedented measurements on the behaviour of the messengers themselves, contributing significantly to the body of knowledge of particle physics.

---

[1] "Astroparticle physics" is often used interchangeably with "particle astrophysics". However, some members of the community point out there is a slight conceptual distinction between the two: the former is more closely related to particle physics, studying the properties of fundamental particles in astrophysical contexts, while the latter aims to tackle astrophysical questions using particles as a tool. Since both approaches will be explored throughout this thesis, we will neglect this distinction.

Individually, each messenger tells us their own versions of events which took place at distant, mysterious, and potentially extreme, astrophysical environments. Yet, it is by combining the information from multiple different messengers that we unlock the true power of astroparticle physics. The unique characteristics of distinct astroparticle species allow us to probe their sources (and the medium they traverse en route to the Earth) in a complementary way. As a consequence, our understanding of stars, galaxies, black holes, cosmic voids, supernovae and countless other astronomical systems has been progressing faster than ever. The success of a *multi-messenger* approach to astrophysics is undeniable, as we hope to convey throughout this thesis with concrete examples. Before we begin, however, let us provide a comprehensive overview of the different types of cosmic messengers at our disposal.

1.1
Multi-Messenger Astronomy: An Overview

It is about time that we introduce the main characters of multi-messenger astrophysics: the messengers themselves. They are classified into four groups: *photons*, *cosmic rays*, *neutrinos* and *gravitational waves*. The first three are either fundamental particles in the Standard Model of particle physics, or composite particles made up of elementary constituents. Gravitational waves, on the other hand, are well understood within the framework of general relativity as ripples in the fabric of spacetime which propagate at the speed of light. In the following subsections, we will summarize the main characteristics of each of these cosmic messengers, emphasising what makes each of them unique. We will also present a brief historical review of how they were discovered, and report on the status of our current observational data.

1.1.1
Photons

Since the dawn of mankind, we know that the sky has always been lit. During the day, we looked up and saw the sun; during the night, we saw the moon and the stars. For millennia, visible light was the only cosmic signal we were aware of, long before it was perceived as an electromagnetic (EM) wave, and longer yet before the concept of a “photon” was even proposed. Nevertheless, this was enough for early astronomers, led by Nicolaus Copernicus, to revolutionize our understanding of our place in the Solar System. As telescopes improved, we eventually figured out our place in the Milky Way, and later still, its place in the Universe.

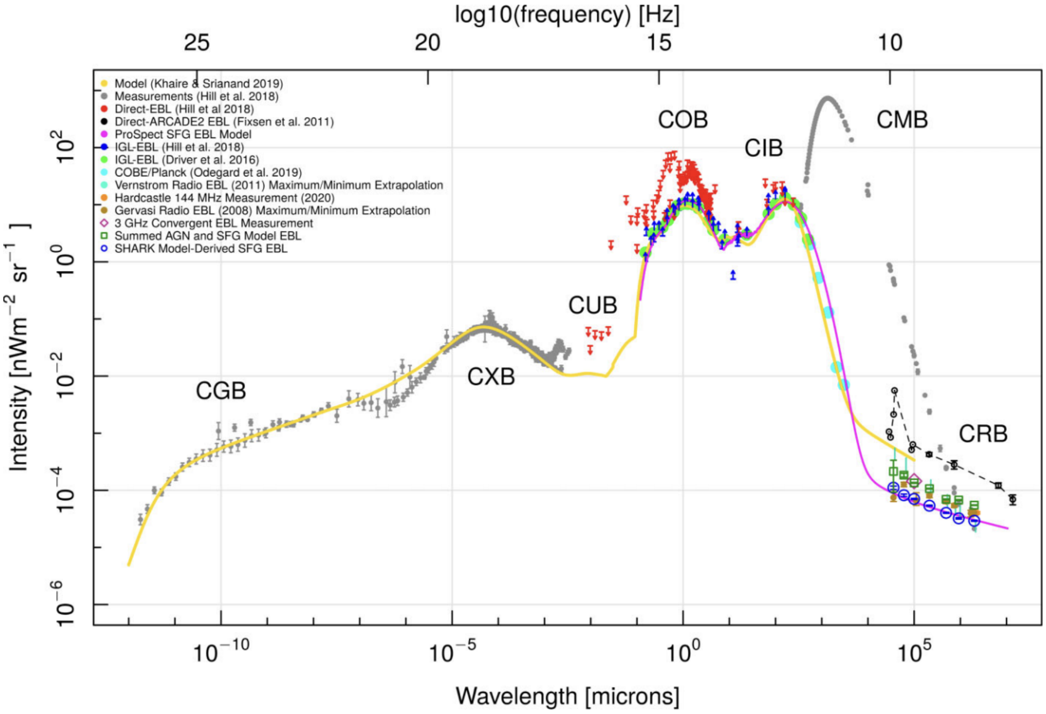

Figure 1.1: Compilation of measurements of the extragalactic photon spectrum. Figure from (4). The reader is referred to the original article for references on the datasets displayed.

Nowadays, we have populated the Earth (and its immediate surroundings) with instruments specifically optimized to collect photons from the skies. Their sensitivities lie far beyond what our eyes are capable of detecting in terms of frequency range and faintness of the signal. With the full EM spectrum at our disposal, multiwavelength astronomy became the prevalent technique to analyze astrophysical objects. As a result, we have identified and classified a plethora of them based on their spectroscopic emissions, from low-energy radio waves all the way up to high-energy γ rays. Not only that, we have discovered photon fluxes that cannot be resolved as individual point sources, but instead span over an extended region in the sky as a *diffuse* flux.

In this thesis, we will be dealing primarily with fluxes of particles coming from outside our galaxy. Figure 1.1 shows our current local measurements of the extragalactic photon flux (4). A lot can be said about this plot. Let us focus for now on the horizontal axis, encompassing an extremely wide range of wavelengths λ (or equivalently energies E, frequencies ν or angular frequencies ω, related by $E = \omega = 2\pi\nu = 2\pi/\lambda$) reflecting the vastly distinct EM phenomena taking place ubiquitously. These processes can be divided into two categories: *thermal* and *non-thermal*. Thermal processes are characterized by their output spectra following that of a *blackbody* with a well-defined temperature T given by (5),

$$n_E(T)\,\mathrm{d}E = \frac{8\pi}{(2\pi)^3}\frac{E^2}{e^{E/T}-1}\,\mathrm{d}E\ . \tag{1-1}$$

For clarity, $n_E(T)\,\mathrm{d}E$ is the number density of photons with energy between E and $E + \mathrm{d}E$ in equilibrium at temperature T. In astrophysics, $n_E(T)$ is often reported in units of [$\mathrm{cm}^{-3}\ \mathrm{eV}^{-1}$] and is sometimes (more intuitively) represented by $\mathrm{d}n(E)/\mathrm{d}E$, since integrating $n_E(T)$ over energy gives us the average number density of blackbody photons. Perhaps the most famous example of a blackbody realized in nature is that of the *cosmic microwave background* (CMB), shown in Figure 1.1. Non-thermal processes, on the other hand, are all of those in which the spectra of outgoing radiation is not that of a blackbody, meaning the energy of the emitted photons do not correspond to the temperatures of their sources. This is typical of processes such as synchrotron radiation, inverse Compton scattering and *bremsstrahlung*, which do not rely on thermal equilibrium to occur. Charged particles can also become non-thermal by being accelerated in astrophysical plasmas. This is believed to be the dominant production channel of high-energy particles in extreme environments throughout the Universe, being responsible for our γ-ray observations in Figure 1.1.

The vertical axis in Figure 1.1 labeled “Intensity”[2] represents a radiometric quantity λI_λ, where I_λ is called *spectral radiance* or *spectral intensity*, the power received per unit solid angle per unit wavelength crossing a unit projected area. Although spectral radiance is a directional quantity, the extragalactic flux of photons is approximately homogeneous and isotropic, such that the integration over solid angle essentially yields a factor of 4π. Much like n_E in Eq. (1-1), the subscript denotes a derivative with respect to that variable: $I_\lambda \equiv \partial I/\partial\lambda$, where I is simply called the *radiance*. It is also common to find νI_ν reported as intensity (see *e.g.*), where $I_\nu = \partial I/\partial\nu$, instead of λI_λ. This is because both quantities are actually the same:

$$I = \int_{\nu_1}^{\nu_2} I_\nu(\nu)\,\mathrm{d}\nu = \int_{\lambda(\nu_2)}^{\lambda(\nu_1)} I_\lambda(\lambda)\,\mathrm{d}\lambda = \int_{\nu_2}^{\nu_1} I_\lambda(\lambda)\,\frac{\mathrm{d}\lambda}{\mathrm{d}\nu}\,\mathrm{d}\nu\ , \tag{1-2}$$

where the change of variables in the last equality allows us to claim (note the inverted limits of integration since λ and ν are inversely proportional),

$$I_\nu = -I_\lambda\,\frac{\mathrm{d}\lambda}{\mathrm{d}\nu} = I_\lambda\,\frac{\lambda}{\nu} \quad\Rightarrow\quad \nu I_\nu = \lambda I_\lambda\ . \tag{1-3}$$

This means that we can plot either quantity and their curves will be the same.

---

[2] It is common in high-energy astrophysics to use the words “intensity” and “flux” loosely to represent different quantities. We will mention technical radiometric terminology for pedagogical clarity whenever it is necessary, but will employ the commonly used terms in most cases. When in doubt, paying attention to the units can be very helpful!

We could play a similar game with energy-differential quantities and we would equally find $EI_E = \nu I_\nu = \lambda I_\lambda$.

The radiance (*i.e.* the area under the curve in Figure 1.1) gives us a qualitative sense of the energy density of each component in the overall spectrum. The CMB constitutes the dominant contribution to the radiation energy budget of the Universe. It is followed by roughly equal contributions from the cosmic infrared (IR) and optical backgrounds (CIB and COB, respectively), collectively known as the *extragalactic background light* (EBL)[3]. Since the EBL will play a central role in this thesis, we shall dedicate Section 2.1.2 to talk about it more thoroughly. Next in the energy budget hierarchy is the cosmic X-ray background ("CXB"), followed by similar ultraviolet (UV) and γ-ray contributions, indicated by "CUB" and "CGB" respectively. Finally, we have the cosmic radio background (CRB), spanning all frequencies $\lesssim 10^{10}$ Hz. For condensed reviews on each of these components, see (6, 7).

This thesis will be particularly focused on the γ-ray band, where we detect the highest energy photons coming from powerful astrophysical accelerators. We can see from Figure 1.1 that there is a drop in the γ-ray flux beyond $10^{26.5}$ Hz $\approx$ 1 TeV. This does not reflect the energetic limitations of their sources, but instead the absorption of energetic γ rays during their propagation through the intergalactic medium (IGM). This absorption is caused by the ubiquitous presence of lower energy background photons, mainly from the CMB and the EBL, serving as obstacles – targets for electron(-positron) *pair production* (EPP; $\gamma + \gamma \rightarrow e^+ + e^-$) – along the path of $\gtrsim$ TeV γ rays. Although it may seem like most energetic γ rays are lost in this process, this is not quite the end of the story. The resulting particles from EPP (electrons and positrons) can later undergo *inverse Compton scattering* (ICS; $e^\pm + \gamma \rightarrow e^\pm + \gamma$), once again with low-energy background photons. This produces new high-energy γ rays, albeit at lower energies than the original ones, since the electron/positron itself also carries away part of the energy from ICS. This EPP–ICS loop can repeat multiple times, giving rise to a chain reaction called an *electromagnetic cascade*, schematically illustrated in Figure 1.2.

Historically, EM cascades were known to happen since the 1960s (as mentioned in (8)). In (9), the first calculations were performed on the absorption of γ rays by the CMB, predicting an opaque universe to > 100 TeV photons. Yet, it was in 1970 that significant progress was made by Berezinsky towards our understanding of this cascading process (10), including EBL effects and magnetic field losses. Magnetic fields can also provoke considerable deflections of electrons during the cascade (11).

[3] Some references refer to the entire photon spectrum in Figure 1.1 as the EBL.

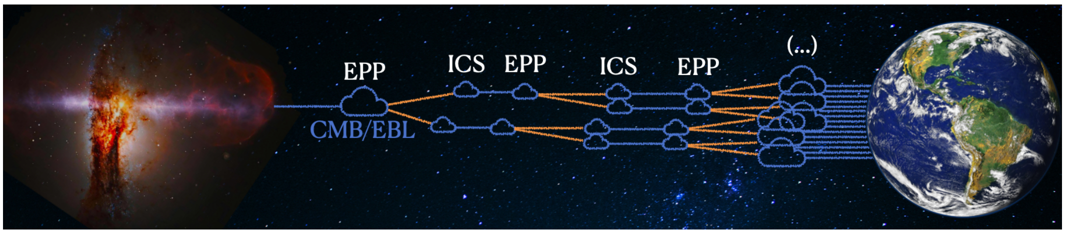

Figure 1.2: Schematic illustration of a cosmological EM cascade initiated by a high-energy γ ray emitted from an astrophysical source. Blue lines represent photons, orange lines represent electrons/positrons, and clouds represent CMB/EBL targets. The alternating and repeating EPP/ICS interactions result in a sub-TeV flux of cascaded γ rays at the Earth.

Evidently, γ-ray propagation in the IGM is not a straightforward problem to tackle. Especially now that γ-ray detection instruments have become quite precise, we require equally precise evaluations of cascaded spectra. We reserve a detailed discussion about EM cascades to Chapter 2 of this thesis, where we describe the elaboration of semi-analytical code for cascade calculations.

Nowadays, it is well established that any high-energy emission of γ rays cascades down into a flux at sub-TeV energies at the Earth. Of course, this is assuming the EM cascade is allowed to fully develop, which may not be the case for nearby sources due to the long distances required for EPP and ICS to take place. A natural consequence of this is the existence of an effective horizon, beyond which we cannot see γ rays at high energies. This can be visualized in Figure 1.3, showing the mean free path (*i.e.* the average distance a particle can travel before interacting) for photons at different energies (12). At $\gtrsim$ TeV energies, γ rays cannot travel further than $\sim$ 1 Mpc, which is roughly the average distance between galaxies. In other words, observing γ rays above TeV energies from extragalactic sources is difficult, requiring dedicated observational techniques (based on Cherenkov radiation or scintillation light), as well as highly sensitive telescopes capable of distinguishing the faint γ-ray signals from cosmic-ray background noise. The first TeV detection was made by the Whipple observatory in 1992 (13). Since then, we have identified several extragalactic sources of such γ rays with the aid of modern ground-based imaging atmospheric Cherenkov telescopes such as H.E.S.S., MAGIC and VERITAS (14). Figure 1.3 also tells us that photons with $\sim$ PeV are even more strongly constrained in their trajectory, having a mean free path of the same order as the size of the Milky Way. PeV observations are therefore a strong indication of Galactic γ-ray production. This has been achieved quite recently by the Large High Altitude Air Shower Observatory (LHAASO) (15), shortly after the notable detection of several > 100 TeV events by the Tibet ASγ experiment (16), nearly breaking the PeV barrier.

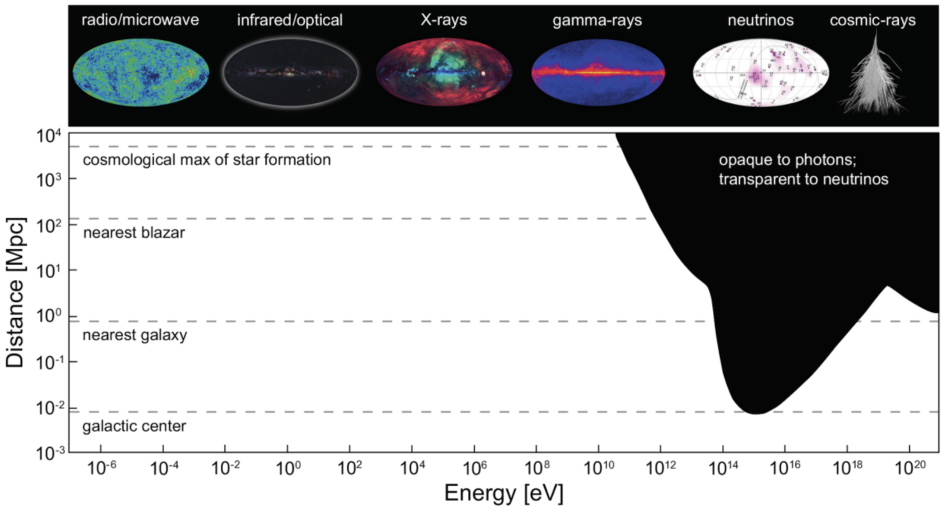

Figure 1.3: Horizon distance for photons as a function of their energy. Black regions indicate distances where γ rays at those energies cannot reach us before pair-producing with other background photons. Figure from (12).

At sub-TeV energies, the state-of-the-art γ-ray data comes from the Large Area Telescope on board the *Fermi* Gamma-ray Space Telescope (*Fermi*-LAT) (17). Their total measured astrophysical flux from 100 MeV to 820 GeV, after subtracting all of the known Galactic foregrounds, is called the *extragalactic gamma-ray background* (EGB), which is comprised of both resolved sources (point-like or extended) and a diffuse component. The latter is usually referred to as the *isotropic*[4] *diffuse gamma-ray background* (IGRB). Recall that, at these energies, we do not only receive "original" photons directly from their sources, but also γ rays reprocessed from higher energies, due to the aforementioned EM cascade phenomenon. This means that the EGB can contain indirect messages from the most powerful particle accelerators in the Universe, although their signal might be difficult to disentangle from the direct/uncascaded component. With that said, the origin of the EGB is mostly well understood, with well-established resolved and diffuse contributions from a few different classes of sources. In Chapter 3, we will assess rigorously whether any additional contribution can fit within our current interpretation of the EGB data. It is well known that there is little room left for any extra γ-ray flux; in the past, this has been exploited to obtain robust quantitative multi-messenger constraints on the sources of $\sim$ TeV neutrinos (19, 20). In this thesis, our aim is to include not only astrophysical neutrino sources into consideration, but also γ-ray byproducts from the most energetic cosmic rays ever observed. Let us then introduce these particles in the following section.

---

[4] The IGRB is not truly isotropic (18). Some more appropriate names found in the literature are the "unresolved" or "diffuse gamma-ray background". We will stick to the more common "IGRB" since we will not be concerned with its anisotropies in this thesis.

1.1.2
Cosmic Rays

Cosmic rays (CRs) constitute the second class of particles ever discovered to come from space. The first signal of their existence came as early as 1785, when Coulomb noticed the spontaneous discharge of electrometers due to what seemed to be ionized particles present in the air. Yet, nobody knew what these particles were or where they were coming from, and it took over 100 years for scientists to propose a cause for this phenomenon. Following the discovery of radioactivity in 1896, it became clear that the discharge rate of electrometers increased dramatically when exposed to radioactive materials. The natural explanation for Coulomb's spontaneous discharge phenomenon was then a flux of gamma radiation coming from radioactivity within the Earth. It was not until 1912 that Victor Hess concluded, after a series of measurements taken in high-altitude balloon flights, that the ionization was indeed coming from above, and proposed it had an extra-terrestrial origin (21). These observations later earned him the 1936 Nobel Prize in Physics "for his discovery of cosmic radiation".

The name "cosmic ray", although misleading, stuck with the community due to the original interpretation of Nobel laureate Robert Millikan that these particles were γ rays of $\sim$ MeV energies associated to the birth of abundant elements throughout the cosmos (22). This interpretation was short-lived; in the subsequent years, Bruno Rossi and others showed that these were in fact charged particles - mostly positively charged (23, 24, 25) - with energies above 1 GeV (26), putting an end to the γ-ray theory.

By the middle of the 20th century, it became well established that CRs are predominantly protons, but also include heavier nuclei[5], as well as electrons and positrons in smaller quantities. Their energies were found to be $\gtrsim$ a few GeV, while being seemingly unbounded from above, with events being detected at up to ultra-high energies (UHEs; $\geq 10^{18}$ eV $= 1$ EeV) (29, 30). The low-energy absence was found to be due to the solar activity: once CRs become trans- or non-relativistic, they can get easily pushed away by the magnetized solar wind and cannot penetrate into the inner heliosphere (31). A consequence of this hypothesis can be seen as a temporal correlation between the intensity of $\sim$ GeV CRs arriving at the Earth and the 11-year solar activity cycle, a phenomenon known as solar modulation (32) (*e.g.* see Fig. 4 in (33)). On the other extreme of the spectrum, a cutoff at UHEs was predicted soon after the discovery of the CMB. Above around 5×10^{19} eV, the proton flux should be

---

[5] We have observed CR nuclei from helium to uranium and beyond, as well as antiprotons; for a useful review, see (27, 28) and references therein.

strongly suppressed due to *photopion production* with CMB photons,

$$p + \gamma_{\rm cmb} \rightarrow \pi + N \ , \tag{1-4}$$

where N is some nucleon, leading to a cutoff in the spectrum known as the *Greisen–Zatsepin–Kuzmin* (GZK) *limit* (34, 35). Our current observations do indeed indicate the presence of a cutoff at UHEs, although its exact position and cause is still somewhat debated, as we will soon discuss.

Trying to identify the nature of the sources of CRs has not been an easy task. This is largely due to their non-zero electric charge, which produces a deflection in the presence of Galactic and extragalactic magnetic fields, scrambling their directions such that we cannot point back and identify where they are coming from. Still, we can divide their sources into Galactic and extragalactic populations. The standard picture for Galactic CRs is that they are accelerated by shock waves in astrophysical plasmas (see Section 1.3.1) to $\gtrsim$ GeV energies. They then get released into and magnetically confined within the Galactic halo, before reaching the Earth as a diffuse flux. Evidence for this confinement can be seen in the ratio of CR boron to carbon nuclei[6] (36).

However, a Galactic model alone cannot account for the presence of UHE CRs (usually abbreviated together as UHECRs), which are too energetic to stay magnetically confined inside the Milky Way. This can be understood through a simple argument: the Larmor radius for a relativistic particle of mass m and charge q in a uniform magnetic field $B \equiv |\mathbf{B}|$ is given by

$$r_L = \frac{p_\perp}{qB} = \frac{\gamma m v_\perp}{qB} \ , \tag{1-5}$$

where $p_\perp = \gamma m v_\perp$ is the momentum component perpendicular to the vector $\mathbf{B}$. This is also commonly written in terms of the cosine of the *pitch angle* (*i.e.* the angle between the momentum $\mathbf{p}$ and $\mathbf{B}$),

$$\mu \equiv p_\parallel / p \quad \Rightarrow \quad p_\perp = p\sqrt{1-\mu^2} \ , \tag{1-6}$$

and the rigidity $\mathcal{R} \equiv p/q$ (usually measured in GV) as

$$r_L = \frac{\mathcal{R}}{B}\sqrt{1-\mu^2} \ . \tag{1-7}$$

For $\mathbf{B} \perp \mathbf{p}$ and at high energies ($p \approx E$), a useful approximation to have in mind is

$$r_L \approx 1.08 \left(\frac{e}{q}\right) \left(\frac{E}{\rm PeV}\right) \left(\frac{B}{\mu{\rm G}}\right)^{-1} \ {\rm pc} \ . \tag{1-8}$$

---

[6] While carbon is mostly a primary CR species, produced directly in CR accelerators, boron is a predominantly secondary nucleus, coming from the spallation/fragmentation of carbon, nitrogen, and oxygen as they propagate diffusively in the Galaxy and interact with interstellar gas. Other secondary-to-primary ratios can also be used as probes of Galactic CR diffusion.

Equating r_L to the radius R of a certain astrophysical acceleration site gives us an estimate of the maximum energy these charges can have to remain magnetically confined in such an environment. In this same limit, we obtain

$$E_{\text{max}} \approx qRB \quad \Rightarrow \quad \mathcal{R}_{\text{max}} \approx RB \; . \tag{1-9}$$

This is known as the *"Hillas criterion"* (37). To confine particles with higher energies, a source requires either a stronger magnetic field or a larger size. For a mean Galactic magnetic field strength of $B_{\text{gal}} \sim \mu$G, the Milky Way ($R_{\text{gal}} \sim 10$ kpc) can only confine protons up to $\sim 10^{19}$ eV. Of course, this is a rather conservative upper limit, and the maximum energy could be instead limited by the acceleration capability of the Galactic sources themselves. There is indirect evidence for Galactic CRs present in the GeV–TeV range coming from diffuse γ-ray observations (38), but not much beyond that. As for the extragalactic CR sources, little is known as of yet, although there are quite a few candidate classes of astrophysical objects, to be discussed in Section 1.2. Evidence for the presence of accelerators outside the Milky Way has been seen as a dipole at UHEs (39, 40, 41), pointing $\sim 125°$ away from the Galactic center with a significance $> 5\sigma$ above 8 EeV.

Let us now take a look at the full CR spectrum (also commonly referred to as "flux" or "intensity" as in the plot, which we denote by ϕ), depicted in Figure 1.4, from a compilation of numerous experimental results (42). It usually appears multiplied by some power of energy – E^2 in this case – to emphasize its shape and spectral features. Its all-particle flux is given by the top curves (from the AMS-02 and CREAM experiments) and data points (from AUGER, HAWC, IceCube, IceTop, KASCADE, KASCADE-Grande, NUCLEON, Telescope Array, Tibet-III and TUNKA), revealing a near-perfect *power-law*

$$\phi(E) \propto E^{-\alpha} \tag{1-10}$$

across more than 10 orders of magnitude in energy. But by careful inspection, we can note the appearance of some interesting breaks where the *spectral index* α in Eq. (1-10) changes:

- A *softening* (*i.e.* the spectrum falls off more steeply) from $\alpha \approx 2.7$ to $\alpha \approx 3.1$ occurring at a break energy around 4 PeV, known as the *"knee"* of the CR spectrum. Since its discovery in (43), it has been confirmed and accurately measured by several experiments. Its characteristic energy is usually interpreted as the maximum energy that protons can get accelerated to inside the Galaxy, with a transition towards elements with higher atomic numbers Z giving the knee its shape (44). This can be achieved by assuming what is often referred to as the *Peters cycle*,

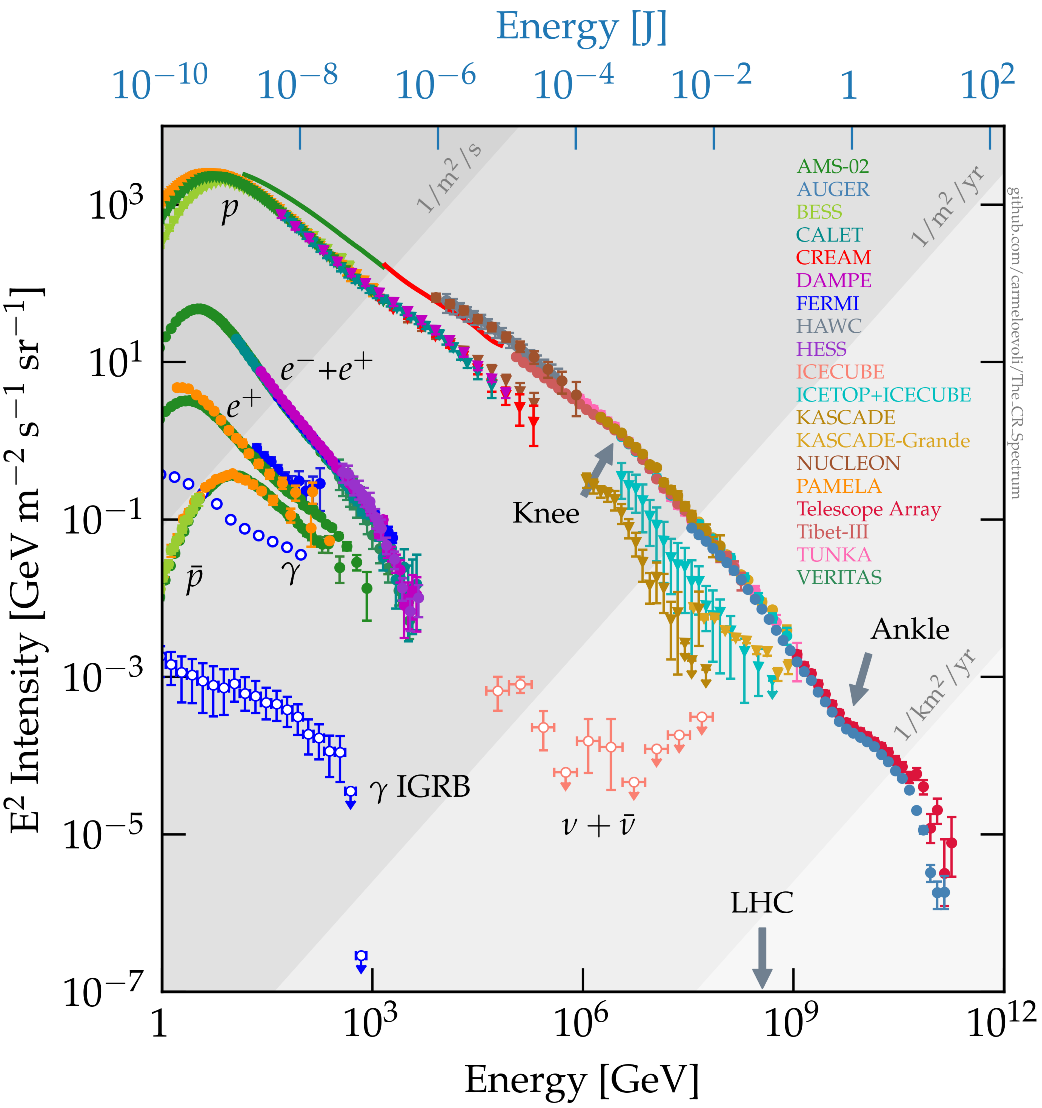

Figure 1.4: Cosmic ray spectrum from 1 GeV up to 1 ZeV (10^{21} eV $\approx$ 160 J), including protons and heavier nuclei, electrons and positrons, as well as antiprotons. Blue circles show the EGB ("γ") and its diffuse component ("γ IRGB"). Pink points show the diffuse neutrino flux measured by IceCube, to be discussed in the next section. This is a compilation of data from several experiments; for more information, see (42) and references therein.

in which the acceleration mechanism in question has a characteristic maximum rigidity $\mathcal{R}_{\text{max}}$ (given by Eq. (1-9), for example). This occurs naturally in processes which depend on magnetic fields confining charged particles inside their acceleration regions (37). Effectively, this introduces a Z-dependent cutoff to the Galactic CR fluxes, such that heavier nuclei (present in smaller abundances) can get accelerated to higher energies, producing a softening feature in the spectrum.

- A subtle *hardening* (as opposed to softening) of the spectrum from $\alpha \approx 3.1$ to $\alpha \approx 2.9$ at around 20 PeV known as the "low-energy ankle".

Its existence is likely due to a varying *mass composition* (*i.e.* nuclei of different atomic mass numbers) of Galactic CRs, although there is no consensus in the literature since this feature is relatively new.

- A second softening from $\alpha \approx 2.9$ to $\alpha \approx 3.3$ known as the "second knee", in the 10^{17} eV decade. In the same spirit as the original knee, the common interpretation is that this feature corresponds to the end of the Galactic iron flux, or perhaps that of stable nuclides – potentially up to uranium ($Z = 92$) (45). This is justified by the second knee occurring at an energy Z times larger than the original knee, as one would expect in the Peters cycle, which predicts $E_{\max}(Z) = Z \times E_{\max}(Z = 1)$.
- A strong hardening from $\alpha \approx 3.3$ to $\alpha \approx 2.5$ at a break energy ~ 5 EeV called the *"ankle"*. This feature was first discussed as early as 1963 (46), and its interpretation has been the subject of debate to this day. The traditional picture was that the ankle is a transition between a soft Galactic component and a hard extragalactic one, such that the latter would dominate the flux at UHEs. This has recently been disfavored by mass composition and anisotropy considerations (47, 48, 49, 50), which indicate that this transition actually occurs at $\lesssim$ EeV energies. Solutions have been proposed relying on CR interactions taking place inside their sources (51, 52, 53). An alternative idea, known as the "dip model", suggests that the ankle is a dip caused by *Bethe-Heitler pair production*,

$$p + \gamma_{\mathrm{cmb}} \to p + e^{+} + e^{-} \ , \tag{1-11}$$

in a proton-dominated spectrum (54, 55). Although quite popular, this model requires a high proton content which is also disfavored by the data (56). It also does not explain the next feature we list in the spectrum.
- A softening from $\alpha \approx 2.5$ to $\alpha \approx 3$ at around 14 EeV known as the "instep" of the CR spectrum. Such a softening can be modeled through an interplay between the emissions of different CR nuclei, after accounting for *photodisintegration* – the loss of nucleons in interactions with the CMB,

$$N + \gamma_{\mathrm{cmb}} \to N' + X \ , \tag{1-12}$$

where N' is the new nucleus after N has lost one or more nucleons X – during their propagation through the IGM (57).
- A cutoff near 50 EeV where the spectrum is suppressed ($\alpha \sim 5$). This is expected and usually interpreted as the aforementioned GZK limit, since the photopion production of protons in Eq. (1-4) becomes kinematically accessible around these energies. The exact position of the cutoff depends on the distances of UHECR sources to us, fluctuating precisely around

> 50 − 60 EeV. However, recent data challenges the GZK explanation (57, 56), revealing a heavier composition and a smaller characteristic energy[7] than that predicted by the GZK scenario. It is always possible to interpret the cutoff as being due to the limited acceleration capabilities of UHECR sources, or caused by a mixed-composition softening similar to what happens in the Peters cycle, or both.

Although the presence of these features is a general consensus, the exact values of the spectral indices and break energies reported above are still subject to debate among different experiments. We have also observed CRs considerably above the GZK threshold (58, 59, 60, 61), with incredible energies reaching up to $\sim$ 50 J. These rare events must originate from sources located at $\lesssim 50 - 100$ Mpc from us, such that they arrive before degrading their energy to photopion production or photodisintegration.

Just below the all-particle spectrum in Figure 1.4 is its proton-only contribution, labeled by "p", spanning from from $1 - 10^5$ GeV (data from AMS-02, BESS, CALET, CREAM, DAMPE, NUCLEON and PAMELA) and from $10^6 - 10^9$ GeV (data from IceCube, IceTop, KASCADE and KASCADE-Grande). Incidentally, we can spot the aforementioned solar modulation effect in the splitting of the proton fluxes below a kinetic energy of $\sim$ 10 GeV. This is because the three datasets shown were taken in different stages of the solar cycle. The smallest hadronic component of the CR flux is that of antiprotons, labeled by "$\bar{p}$" in Figure 1.4 (data from AMS-02, BESS and PAMELA). These are thought to be produced in proton and helium interactions with nuclei in the Galactic interstellar medium (ISM). No heavier antinuclei were ever found (27), although they are expected to be present in tiny amounts, also from CR collisions in the ISM (62).

Figure 1.4 also shows our measured spectra of CR electrons and positrons up to $\sim$ 5 TeV. The main contribution to this lepton flux comes from primary electrons, originating from the same Galactic sources as those producing CR nuclei. These sources, however, cannot accelerate and emit positrons. These antiparticles were believed to come from interactions of CR nuclei with the ISM. However, this natural picture has been recently challenged by the observation of an unexpected feature in the data. By comparing in Figure 1.4 the total "e^-+e^+" flux (data from AMS-02, CALET, CALET, DAMPE, *Fermi*, HESS and VERITAS) to the positron-only flux (data from AMS-02, *Fermi* and PAMELA), labeled by "e^+", one can notice that the positron fraction increases

---

[7] This characteristic energy, denoted by $E_{1/2}$, indicates the energy at which the integral spectrum (*i.e.* the cumulatively integrated spectrum; well approximated by a power-law) reaches half of the value expected from the extrapolation of its power-law to higher energies, neglecting energy losses from interactions. For quantitative details, see (57).

with energy above $\sim$ 10 GeV, peaking at around 100 GeV. This anomalous behaviour led the community to propose the existence of primary positron sources, in addition to the conventional secondary positron flux produced in the ISM (63, 64). Speculative solutions to this so-called “positron excess” also include new physics proposals such as dark matter annihilation inside the Milky Way (see (65) and references therein).

Historically, CRs have always been a beacon of new physics, revealing very early on the existence of new particles such as the muon, the pion, the kaon, and even the positron itself. However, with the exception of the positron (which is stable), these particles cannot have come from outer space due to their short lifetimes. They are in fact created when a CR reaches the atmosphere and interacts with its air molecules, producing unstable hadrons and leptons as a byproduct. While some of these particles are able to reach the surface and get detected, a significant fraction of them actually decay or interact further in the atmosphere, igniting a cascade reaction that results in a shower of energetic secondary particles. This is known as an *extensive air shower* (EAS). The EAS grows in width until the energy of its constituent particles cannot produce any new ones, at which point the shower shrinks. However, it can still hit a large surface area (several kilometers) as it reaches the ground, which is why our current CR detector arrays are so sparse. The physics of EAS is extremely rich and crucial for extracting information about the incoming CRs. The reader is directed to Section 3.2.1 for a more thorough discussion about them.

Let us finally focus specifically on UHECRs, which are central characters in this thesis. Currently, the largest and most influential UHECR detectors are the Pierre Auger Observatory (PAO) and the Telescope Array (TA), whose spectral measurements are displayed in Figure 1.5, multiplied by E^3 to accentuate the ankle, instep and cutoff features (66). Although both datasets reveal similar spectral shapes, there are some discrepancies worth pointing out. The most notable one seems to be a systematic difference in the overall flux normalization. This can be easily resolved by shifting the overall spectra by a constant factor of $\sim 9\%$, which is allowed since PAO and TA estimate that their systematic uncertainties on the energy scale are approximately 14% and 20% respectively (67, 68). However, above 30 EeV, we again encounter discrepancies, this time due to different shapes of the measured spectra. In order to fix this, one can introduce an energy-dependent shifting of the fluxes, in addition to the overall normalization rescaling (69). Finally, discrepancies arising from data at different declination[8] bands seem to have an astrophysical explanation, rather than an experimental one (66).

---

[8] Angular directions on the spherical sky are usually reported in equatorial coordinates:

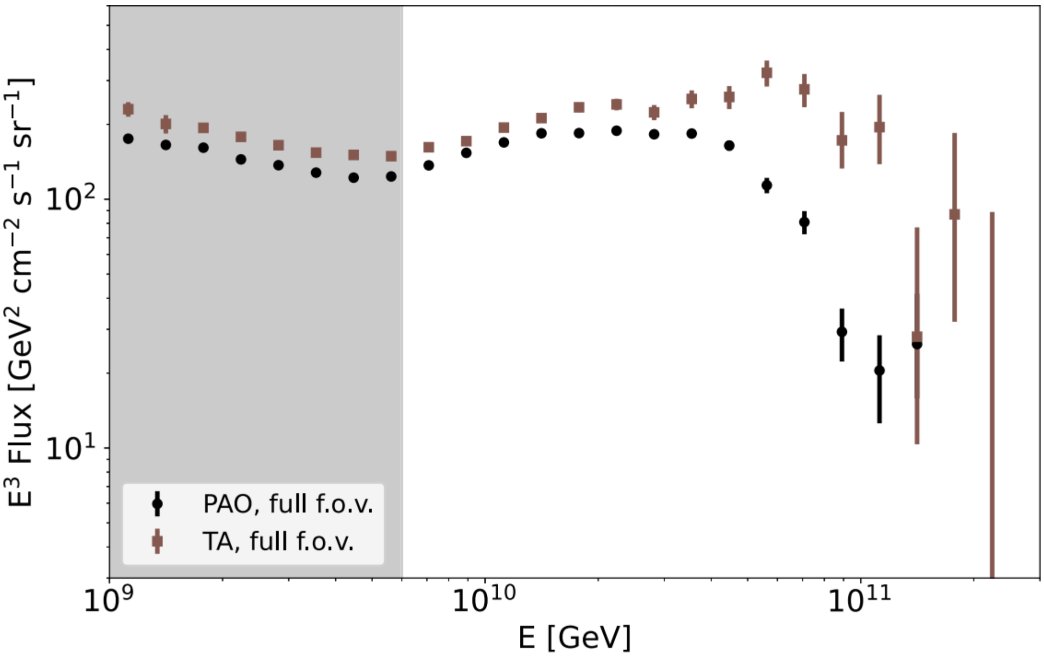

Figure 1.5: The ultra-high-energy cosmic-ray energy flux measured by the Pierre Auger Observatory (black circles) and Telescope Array (brown squares) collaborations. Figure from (66).

We shall reserve the discussion on the composition of UHECRs to Section 3.2.1. For now, it suffices to say that our observations indicate *(i)* a gradual transition from protons and intermediate-mass nuclei at the second knee to a lighter composition at the ankle (49), *(ii)* a mixed composition at the ankle, with a pure $p+\mathrm{He}$ scenario excluded at $> 6\sigma$ (70, 71), and *(iii)* a progressively heavier composition above the ankle (typical of the Peters cycle), with some disagreements between PAO and TA on the spread around the mean atomic mass of CRs above $10^{18.5}$ eV (72).

- *Right Ascension* ($\alpha \in [0, 2\pi)$: measured eastward along the longitudinal direction of the celestial equator, starting from the position of the Sun at March Equinox;
- *Declination* ($\delta \in [-\pi/2, \pi/2]$): following the lines of latitude from the South Pole ($\delta = -\pi/2$), across the equator ($\delta = 0$), all the way to the North Pole ($\delta = \pi/2$).

1.1.3
Neutrinos

Neutrinos as cosmic messengers are radically different from γ rays and CRs. This is mainly because they only experience weak interactions[9], which have very small cross sections $\sigma_{\text{weak}} \propto G_F^2 s$, where $G_F \simeq 11.7$ TeV^{-2} is the Fermi constant and s is the total center-of-momentum (COM) energy squared. For example, typical values for neutrinos of energy E_ν interacting with a nucleus N are $\sigma_{\nu N} \sim 10^{-38}$ cm^2 (E_ν/GeV). As a consequence, the Universe is essentially transparent to neutrinos; they can travel vast distances completely undisturbed, making them reliable for directional searches. They can also easily escape from the dense interiors of most astrophysical environments, allowing us to probe deep inside their sources and study their production mechanisms, with powerful multi-messenger implications. Unfortunately, this elusiveness also makes them quite difficult to catch. To detect an astrophysical neutrino typically requires instrumenting a large volume of dense material with photomultipliers to amplify the signal from secondary particles produced in these rare neutrino interactions.

After they were first proposed in 1930 by Wolfgang Pauli in a famous letter addressed to the participants of a conference in Tübingen, Germany, it took another 26 years for the existence of electron (anti)neutrinos from inverse beta decay,

$$\bar{\nu}_e + p \to e^+ + n \ , \tag{1-13}$$

to be experimentally confirmed (75). This established nuclear reactors as powerful neutrino emitters. By then, the muon neutrino had already been hypothesised (following the discovery of the muon in CRs), and soon after the violation of parity in weak interactions was verified (76). This established a general consensus that there were two types of neutrinos, both massless and left-handed (while antineutrinos were right handed).

Nowadays, it is well established that neutrinos, as well as their antiparticles, come in three kinds, or *flavors*,

$$\nu_e \ , \qquad \nu_\mu \ , \qquad \nu_\tau \ ,$$

which can be produced in interactions involving their respectively associated charged leptons from the three generations of the Standard Model (SM), the electron (e), the muon (μ) and the tau (τ). We also know that neutrinos

---

[9] This is true only within the context of the Standard Model of particle physics. Of course, neutrinos are susceptible to the effects of gravity, as are all particles. They also have tiny masses, which play an important role in cosmology (73, 74) and are crucial for the phenomenon of flavor oscillations (see Section 1.4.1).

can change between different flavors simply by propagating through space. This phenomenon is known as *neutrino oscillations*, to be treated in more detail in Section 1.4.1. The electroweak (EW) Lagrangian predicts two types of interactions involving neutrinos: charged current (CC) and neutral current (NC). The former occurs via the exchange of the $W^{\pm}$ bosons, while the latter involves exchanging Z bosons. Crucially, the distinctions between CC and NC interactions can produce different signals at high-energy neutrino detectors, as described in Section 3.3.1.1. This thesis is only concerned with phenomenological aspects of astrophysical neutrinos. As such, we refrain from delving into more technical aspects regarding the quantum field theory of EW interactions. For a comprehensive review on the EW sector of the SM, with particular focus on neutrinos, the reader is referred to (74).

Following their discovery in 1956, it was only a matter of time until scientists began the search for extraterrestrial neutrino sources. The Sun was a prime candidate, expected to produce them in copious amounts from its internal fusion reactions. In the 1960s, John Bachall estimated the flux of solar neutrinos at the Earth and predicted the event rate in $\nu_e + {}^{37}\mathrm{Cl} \to e^- + {}^{37}\mathrm{Ar}$ experiments[10] (78). However, once these experiments were conducted later that decade, the measured flux was found to be considerably less than anticipated by Bachall's calculations (79), giving rise to what became known as the solar neutrino problem. Not even accounting for neutrino oscillations in vacuum, as had just been developed by Pontecorvo, Maki, Nakagawa, and Sakata (80, 81), could explain this deficit. It was only in the early 2000s, when the all-flavor solar neutrino flux was measured by the Sudbury Neutrino Observatory (82, 83), that consistency with the solar models was obtained. This was not only evidence for vacuum neutrino oscillations, but also for the Mikheyev–Smirnov–Wolfenstein (MSW) effect describing neutrino flavor evolution in the presence of matter (84, 85).

Solar neutrinos represent only a small fraction of the neutrinos we receive from outer space, dominating in the eV to a few MeV range. The astrophysical neutrino spectrum across all energies is displayed in Figure 1.6 (86), adapted from (87). It also includes the local flux of the aforementioned reactor neutrinos, as well as geoneutrinos from the decay of radioactive nuclides inside the Earth. The focus of this thesis (with the exception of Chapter 4) shall be on ≥ TeV astrophysical neutrinos, marked by the shaded green region in Figure 1.6. As such, let us first quickly overview the other components across the spectrum.

---

[10] This reaction had already been proposed by Bruno Pontecorvo as a means to detect neutrinos (77).

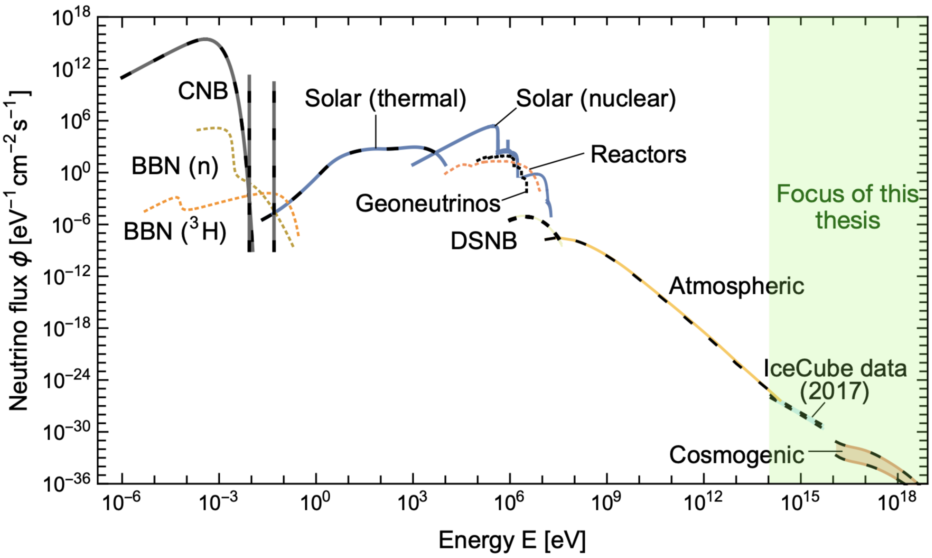

Figure 1.6: The grand unified neutrino spectrum, reproduced from (86) and adapted from (87), including the dominant sources of the neutrino flux at the Earth. The green shaded region indicates the energy range of interest to this thesis (except for Chapter 4), namely, $\geq$ TeV.

Starting at the lowest energies, we have the cosmic neutrino background (CνB; labelled as "CNB" in Figure 1.6). These are hot relics coming from the decoupling of neutrinos from the primordial plasma at a temperature of $\sim$ 1 MeV (88). Before that, they were kept in thermal equilibrium by weak interactions such as $\nu + \bar{\nu} \rightleftharpoons e^+ + e^-$ and $\overset{(-)}{\nu} + e^\pm \rightleftharpoons \overset{(-)}{\nu} + e^\pm$. Although they have never been detected, their blackbody spectrum is predicted to have a temperature (in the limit of massless neutrinos) of (74)

$$T_{\mathrm{c}\nu\mathrm{b},0} = \left(\frac{4}{11}\right)^{1/3} T_{\mathrm{cmb},0} = 1.945 \pm 0.001 \text{ K} = (1.676 \pm 0.001) \times 10^{-4} \text{ eV} ,$$

where the subscripts "0" denote values at present time (*i.e.* at redshift[11] zero) and T_{cmb} is the CMB temperature (see Section 2.1.1). In reality, we expect three blackbody CνB spectra, corresponding to each of the neutrino mass eigenstates. The blackbody-looking "CNB"-labelled curve corresponds to the lightest neutrino, which is assumed to have zero mass in the plot. Meanwhile, the nearly monochromatic lines that follow are copies of that curve for the two heavier mass eigenstates, that become horizontally compressed; for details, see (87). The last contributions at the lowest energies come from Big Bang nucleosynthesis, which is the epoch when the Universe began forming nuclei

---

[11] We assume the reader is familiar with the aspects of cosmology relevant to astroparticle physics in general. This includes the ΛCDM model, cosmological redshift and different distance concepts. For a brief and straightforward review of the useful concepts employed here, we recommend reading Appendix A in (89).

heavier than hydrogen (protons). Specifically, the contributions from the decay of the newly formed neutrons

$$n \to p + e^- + \bar{\nu}_e \tag{1-14}$$

and tritium nuclei ($^3\mathrm{H} \to {}^3\mathrm{He} + e^- + \bar{\nu}_e$) are shown in Figure 1.6, dominating the flux around the 10-100 meV energy range.

Besides nuclear fusion, the Sun produces thermal neutrinos via plasmon decay ($\gamma \to \nu + \bar{\nu}$), photoneutrino production ($\gamma + e \to e + \nu + \bar{\nu}$) and other processes, treated in detail in (90). Their fluxes dominate in the eV–keV range, yet little attention is given to them in the literature due to the lack of detection prospects at the moment. Above solar neutrino energies, the dominant astrophysical sources of neutrinos are supernovae (SNe). Only one SN has been observed in neutrinos so far: SN 1987A (91, 92, 93). Nevertheless, it is estimated that the collection of all SNe in the Universe across all times in its history produces a detectable diffuse flux of neutrinos around the 10 MeV band. This is known as the diffuse supernova neutrino background, labelled as "DSNB" in Figure 1.6, which is yet to be found in experiments.

The flux of atmospheric neutrinos spans across several orders of magnitude in energy has an indirect extraterrestrial origin: they are produced in EASs as byproducts of CR interactions. Most of them arise from the decay of secondary charged pions,

$$\pi^\pm \to \mu^\pm + \overset{(-)}{\nu}_\mu \ , \tag{1-15}$$

muons (although most high-energy muons reach the ground before decaying),

$$\mu^\pm \to e^\pm + \overset{(-)}{\nu}_e + \overset{(-)}{\nu}_\mu \ , \tag{1-16}$$

and kaons, producing what is known as the *conventional* atmospheric neutrino flux (94). This is what appears in Figure 1.6, with its typical $E^{-3.7}$ power-law behaviour[12]. As it happens, these were the first non-man-made neutrinos to ever be observed, as early as 1965 (95, 96), and they have also been historically important for the experimental confirmation of neutrino oscillations at the Super-Kamiokande detector (97). An additional contribution showing up at ∼ TeV energies (and likely dominating the atmospheric component at ∼ PeV and above) comes from the decay of heavier hadrons, containing charm or bottom quarks (98). Unlike pions and kaons, these hadrons are extremely short lived and therefore decay promptly before losing energy, producing the appropriately named *prompt* atmospheric neutrino flux. This flux, however, is always subdominant with respect to (i) the conventional atmospheric one at

---

[12] This is softer than the CR spectrum, $E^{-2.7}$, since these light mesons lose energy before decaying (94).

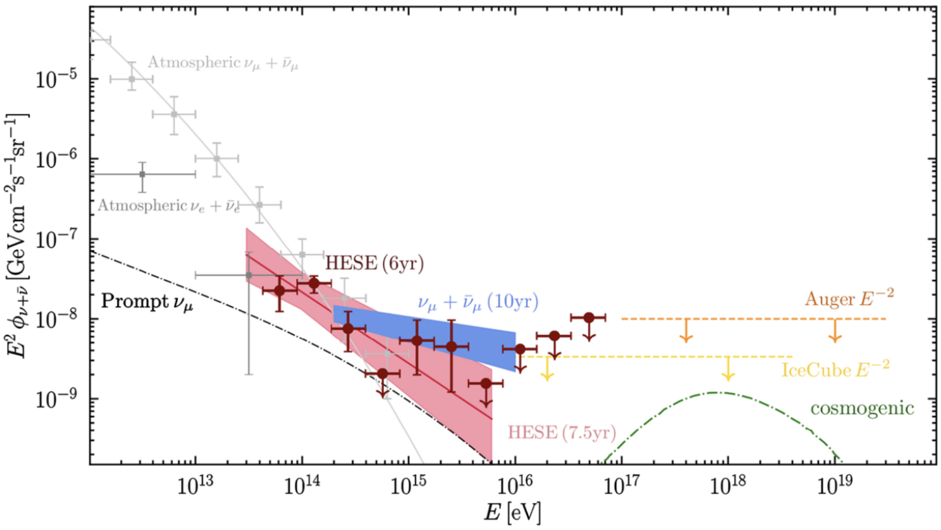

Figure 1.7: Neutrino flux (per flavor) above 1 TeV, containing atmospheric (gray) and astrophysical (maroon) data from IceCube. Two IceCube fits for astrophysical data are also shown as colored bands. At the highest energies, upper limits on the UHE neutrino flux are shown as horizontal dashed lines. The green dot-dashed curve depicts a specific model for the flux of cosmogenic neutrinos. Figure from (99), where the reader can find references to the original literature.

lower energies and (*ii*) the astrophysical one at higher energies. As such, it has never been detected.

We finally arrive at the energy range of interest to this thesis: $E_\nu \geq$ TeV, displayed more closely in Figure 1.7 (99). It shows the different neutrino fluxes reaching the surface of the Earth with different flavors. We can see that the high-energy part of the atmospheric fluxes, shown in grey, are indeed an important background to consider when trying to detect the so-called *astrophysical neutrinos* in the TeV–PeV range. For more on that, see Section 3.3.1.2. Measurements of this diffuse astrophysical neutrino flux have been carried out mainly by one single experiment: the IceCube Neutrino Observatory, or simply *IceCube*, located deep within the ice at the South Pole. The red and blue shaded bands in Figure 1.7 represent fluxes and their uncertainties corresponding to different datasets analyzed by IceCube. We reserve a detailed discussion on IceCube's observations and specific datasets to Sections 3.3.1 and 3.3.1.3, respectively. For now, it suffices to say that we have confidently detected hundreds of neutrinos from a few TeV up to a few PeV (*e.g.* see (100) for a subset of all events) which are not produced in the Earth's atmosphere, but instead in astrophysical sources of unknown identity. Candidate source classes shall be presented shortly in Section 1.2.

Lastly let us consider the realm of UHE neutrinos (usually defined to be $E_\nu \geq 100$ PeV). In this energy range, we expect to find a guaranteed neutrino flux coming from the interactions of UHECRs with the CMB and EBL backgrounds, producing neutrino secondaries. These are known as *cosmogenic* neutrinos. The GZK process, for example, produces charged pions which decay into neutrinos via Eq. (1-4), followed by (1-15) and (1-16), yielding a cosmogenic flux at UHEs whose existence has been proposed over half a century ago (101, 102). Photopion interactions can also produce neutrons (*e.g.* if $\pi = \pi^+$ and $N = n$ in Eq. (1-4)) which in turn decay, yielding a $\bar{\nu}_e$ component at $\gtrsim 2$ orders of magnitude lower energies than the neutrinos from pion decay. Cosmogenic neutrinos also arise as byproducts of UHECR photodisintegration via the decay of unstable secondary nuclei (*i.e.* unstable N' or X in Eq. (1-12)), as well as from photopion production off heavy nuclei (as opposed to protons). So far, cosmogenic neutrinos have never been observed; experiments such as PAO and IceCube have only been able to set upper limits on their fluxes, as shown in Figure 1.7 as orange and yellow horizontal dashed lines, respectively. There are several models for the expected cosmogenic neutrino flux, exhibiting a large variability between each other. This is mainly due to uncertainties in the spectrum, composition and distribution of UHECR sources across the Universe (*e.g.* see (103)).

Besides IceCube, there are other experiments aiming to detect neutrinos in the $\geq$ TeV range. Some already exist, some are currently under construction, some have already finished their operations and some are still planned for the future. We list the most important ones (in the context of this thesis) below:

- ANTARES (104), a detector located in the depths of the Mediterranean Sea, has been collecting data since 2007 and has ended its operations in 2022. In its 15 years of existence, it has shown the viability of undersea neutrino detectors, opening the path for more modern experiments in that area such as KM3NeT to flourish. ANTARES has been able to measure the atmospheric neutrino flux and confirm their flavor oscillations. However, it has not able to claim with statistical significance the presence of any astrophysical flux (105).
- KM3NeT (106), a cubic-kilometer-scale (hence the “KM3”) detector also in the Mediterranean Sea is currently under construction, with its partial assembly already yielding some physics results (107). Its infrastructure will house two separate telescopes, ARCA and ORCA. Both are collections of detection units arranged in different geometric configurations to optimize different goals. While the former aims to perform astrophysical neutrino searches in the TeV–PeV range, the latter is ideal for measuring the oscillation of $\sim$ GeV atmospheric neutrinos. As

such, ORCA works mainly as a neutrino particle physics detector, not so much as a telescope. ARCA, on the other hand, is expected to detect the diffuse astrophysical neutrino flux within 6 months of operation at a 5σ level (108). KM3NeT has received a lot of attention not only for its promising sensitivity thanks to design and technological advancements, but also because its observations will be complementary to IceCube, since they are located in opposite hemispheres of the globe. In other words, IceCube and KM3NeT together will have a clear view of the full sky.

- AMANDA (109), IceCube's precursor, took data between 1996 and 2005. After this period, it was integrated into IceCube during its construction, before being officially shut down in 2009. Like ANTARES for KM3NeT, AMANDA served as a proof-of-concept for IceCube, but was never able to measure the astrophysical neutrino flux (110).
- Baikal-GVD (111), under construction since 2016, is another underwater neutrino detector in the Northern hemisphere (at Lake Baikal, Russia), supplementing KM3NeT/ARCA's view of the sky. Its collaboration has recently claimed a detection of the astrophysical neutrino flux with a significance of $\sim 3\sigma$ (112). Alas, there is still room to grow for Baikal-GVD as the experiment gets closer to full instrumentation.
- ANITA (113), a balloon experiment flying high above Antarctica, was designed to detect UHE neutrinos by looking for their Askaryan radio signals (114, 115). This has led to the strongest current limits on the $\gtrsim 10^{19.5}$ eV neutrino flux (116). Incidentally, ANITA is also sensitive to geomagnetic radiation emitted by UHECR-induced EASs. This radiation either come directly from the shower or be reflected off the surface of the ice and show as an upgoing event with phase-inverted polarity. This has brought a lot of attention to ANITA after it observed anomalous upgoing events with noninverted polarity that could not have come from an EASs or neutrinos (117, 118). More recently, four more such events were found, this time consistent with Earth-skimming $\sim$ EeV tau neutrinos (119, 120). This would make them the most energetic neutrinos ever observed, but tensions with the PAO and IceCube non-observations still leave the problem lingering (120, 121). As of the writing of this thesis, all of these events have yet to be fully explained.
- Numerous other detectors under construction, planned or proposed for the future, including P-ONE (122) in the TeV–PeV range, IceCube-Gen2 (12), TAMBO (123), TRIDENT (124), and Trinity (125) filling the energy gap between IceCube and UHE detectors, and ANDIAMO (126),

ARA (127), BEACON (128), GRAND (129), POEMMA (130), PUEO (131), RET (132), RNO-G (133) and TAROGE (134) in the UHE range. This is likely a non-exhaustive list.

We have thus concluded an extensive overview of the relevant cosmic messengers for this thesis. The next step will be to discuss about their sources. Before that, however, let us comment briefly on the last class of cosmic messengers currently studied: gravitational waves.

1.1.4
Gravitational Waves

Gravitational waves (GWs) are beyond the scope of this thesis, yet their importance for multi-messenger astronomy is indisputable (135, 136, 137). In Einstein's theory of General Relativity, GWs arise from small perturbations around the Minkowski metric (138),

$$g_{\mu\nu}(x) = \eta_{\mu\nu} + h_{\mu\nu}(x) \ , \qquad |h_{\mu\nu}| \ll 1 \ , \tag{1-17}$$

where the spacetime indices (always shown as Greek letters) vary from 0 to 3, with $x^0 = t$ and x^i representing the 3 spatial dimensions. We adopt the convention $\eta_{\mu\nu} = \mathrm{diag}(1, -1, -1, -1)$, popular among particle physicists. The Einstein field equations,

$$G_{\mu\nu} = 8\pi T_{\mu\nu} \ , \tag{1-18}$$

where $G_{\mu\nu}$ is the Einstein tensor and $T_{\mu\nu}$ is the stress-energy tensor in general relativity, then tell us that these perturbations satisfy the wave equation

$$\Box \bar{h}_{\mu\nu} = -16\pi \, T_{\mu\nu} \ , \tag{1-19}$$

under the Lorentz gauge $\partial_\mu h^\mu{}_\nu - (1/2)\partial_\nu h = 0$, where $\Box = \partial^\mu \partial_\mu$ is the flat-space d'Alembertian operator and $\bar{h}_{\mu\nu} = h_{\mu\nu} - (1/2)\eta_{\mu\nu} h$ is the trace-reversed perturbation ($h = \mathrm{tr}\, h_{\mu\nu} = h^\mu{}_\mu$). Eq. (1-19) corresponds to a wave equation with a source term, whose solutions are GWs propagating at the speed of light.

Although gravitational radiation has been well understood since the early 20th century (139, 140), it took around 100 years for GWs to finally be observed: a spectacular experimental achievement. In 2015, the first GW signal, GW150914, was detected by the LIGO and Virgo collaborations coming from a merger of two $\sim 30\ M_\odot$ black holes (BHs) into a $\sim 60\ M_\odot$ one (141), where $M_\odot \approx 2 \times 10^{30}$ kg is the solar mass. Since then, the LIGO, Virgo and KAGRA collaborations have reported almost 100 GW events from binary merger systems during their first three operational periods, with the fourth run currently ongoing.

It can be shown (142) that these waves are radiated by objects with an accelerating quadrupole moment, $\ddot{I}_{ij} \neq 0$, with an emission power proportional to its time derivative squared, $\mathrm{d}E/\mathrm{d}t \propto (\dddot{I}_{ij})^2$. This means that astrophysical systems with enough asymmetry to produce time-varying quadrupole moments can be powerful sources of GWs. This is the case for compact object[13] binaries such as the aforementioned BH-BH binary from 2015, as well as for other potential astrophysical (*e.g.* core-collapse SNe, pulsars) and cosmological sources (*e.g.* inflation, phase transitions in the early universe).

Until very recently, our detectors were only sensitive to the GW frequencies between $\sim$ 1–10^4 Hz, typical for binaries containing around 1–100 $M_\odot$. However, in 2023, several pulsar timing array experiments reported evidence for an isotropic, low-frequency ($\sim$ yr^{-1}), stochastic GW background (143, 144, 145, 146), whose origin is still under debate, although a likely astrophysical interpretation is that of supermassive BH binaries. Future detectors will also be able to probe massive and supermassive BH binaries with more precision; for an interesting interactive reference, see (147).

An honorable mention must be given to the GW event GW170817, which occurred at a near-simultaneous temporal and spatial correlation with a NS merger that also produced EM counterparts in the form of the gamma-ray burst (see Section 1.2) GRB 170817A, and the kilonova AT 2017gfo (148, 149). As we shall see throughout this thesis, this is one of the very few multi-messenger success stories, associating different types of cosmic messengers with high significance to a single astronomical source.

1.2
Revealing the Sources of High-Energy Astroparticles

High-energy astroparticle sources are separated into two classes: their signals can be either *steady* or *transient*. As the name suggests, steady sources produce a constant or a regular periodic flux of particles, while transient sources generate an irregular time-varying signal lasting for a finite duration[14]. Steady sources that are known or expected to emit particles at the highest energies include active galactic nuclei, star-forming galaxies, supernova remnants, among many others. High-energy transients include gamma-ray bursts, flaring blazars, tidal disruption events, etc.

---

[13] The term "compact object" is commonly used in the literature to refer to either a BH or neutron star (NS).

[14] Of course, astrophysical objects have not existed and will not exist forever, in the same state they are observed today. What we mean by "constant" and "transient" signals usually refers to time scales accessible to humans and our detectors, with transient events ranging from milliseconds to a few years. This is in great contrast to the evolution time scales of steady sources, which can last millions of years.

All of these objects were discovered via their EM emissions, which is why they are generally classified based on their distinct photon spectra. Nevertheless, the extreme environments expected inside these sources have a strong potential for multi-messenger emission, making them interesting within our context. Although the analyses and results presented in this thesis are independent of the exact nature of astrophysical sources, we briefly review below those which have received more attention in the past years, within the multi-messenger community. In Section 3.1.1, we will discuss in more depth about some of these source populations, focusing on their diffuse γ-ray and potential neutrino emissions.

1.2.1
Steady Sources

Here is a non-exhaustive list of popular high-energy, steady sources:

- *Active Galactic Nuclei* (AGNi): central regions ($\lesssim 10$ pc radius) of so-called "active" galaxies, where huge amounts of gas accumulate around a supermassive black hole (SMBH), forming an accretion disk surrounded by a torus of dust. The intense accretion of material onto the SMBH powers a strong energy release in the form of radiation and mechanical outflows into the ISM of its host galaxy.

  Historically, astronomers have observed a "zoo" of phenomena which are now associated to AGNi thanks to AGN unification models (150) (for a quick and straightforward guide, see (151)). These models classify AGN in several ways. One such classification pertains to the orientation of the dusty torus' plane with respect to us, separating them into 2 types[15]. In a "type I" AGN, the absence of dust along our line of sight means we have a clear view of its hot and fast-moving central engine, along with its broad and narrow emission lines in the optical/UV range. "Type II" AGN, on the other hand, have their nuclei obscured by the toroidal mass of dust, displaying only narrow lines in their optical spectra, as well as reprocessed IR radiation. Other classification categories involve their radio-wave luminosity ("radio-loud" vs. "radio-quiet"), their mass accretion rate, and the presence (or not) of *relativistic jets*. These jets are highly collimated beam-like emissions of radiation and relativistic ionized matter which can form in AGN with magnetized accretion disks and spinning SMBHs (153). The formation mechanisms and composition

---

[15] Interpretations solely based on torus orientation have recently been challenged (152) and are the subject of ongoing research.

of astrophysical jets are still not completely understood and beyond the scope of this thesis.

The majority of extragalactic γ-ray sources are a subclass of jetted AGNi called *blazars*, which have their jets pointed towards the Earth. Relativistic beaming amplifies their EM radiation luminosities from synchrotron (in the radio to X-ray range), inverse Compton ($\sim$ X-rays and above) and potential hadronic processes, making them powerful γ-ray emitters and likely multi-messenger sources (154). Blazars can be further subdivided into flat spectrum radio quasars[16] (FSRQs) and BL Lacertae objects (or BL Lacs), whose multi-messenger prospects will be discussed in Section 3.1.1. In the literature, BL Lacs are further classified based on the position of their synchrotron peak frequencies; here, we refrain from entering such details. FSRQs exhibit strong and broad emission lines in the optical/UV range, which are mostly weak or absent in BL Lacs (155). Both classes of AGN have comparable local density distributions, although the density of BL Lacs falls off more quickly with redshift than that of FSRQs (156, 157).

Another group of AGNi contributing significantly to the EGB is that of *radio galaxies* (RGs). They are also sometimes called “misaligned AGN”, since they are similar to blazars, but have jets pointing obliquely to our line of sight. Since they are not as bright, the population of RGs produces a diffuse γ-ray flux that contributes significantly more than blazars to the IGRB. On the other hand, blazars are much more easily resolved as γ-ray individual sources, with relatively few RGs present in state-of-the-art point-source catalogs (158). We reserve a more thorough discussion on the multi-messenger aspects of RGs to Section 3.1.1.

- *Star-Forming Galaxies* (SFGs): galaxies where star formation processes are actively taking place and sustained over long periods of time (possibly billions of years). SFGs harbor molecular clouds, denser-than-average ISM regions containing gas molecules, ions and dust, which collapse under their own gravity, leading to the formation of new stars. The Milky Way itself can be considered a modest SFG, with current estimates on its star formation rate (SFR) of $\sim 2\ M_\odot/\mathrm{yr}$ (159). However, especially at high redshifts, galaxy SFRs can reach extremely high values – up to thousands of solar masses per year.

  Observationally and theoretically, SFGs are well-established γ-ray emitters (160, 161) and potential multi-messenger sources, as we will discuss

---

[16] The term “quasar” simply refers to an extremely luminous AGN.

in Section 3.1.1. Their production can occur in stellar winds from young massive star clusters or around SN remnants (both shall be discussed soon) within star-forming clusters (162). Indeed, IR observations have shown us that a higher SFR leads to a higher SN rate (163).

- *Starburst Galaxies* (SBGs): galaxies undergoing a period of exceptionally high SFR, often triggered by mergers or tidal interactions between gas-rich galaxies. They are quite similar to SFGs (in fact, sometimes considered a subset of SFGs) in that their intense star-formation makes them prime candidates for high-energy particle production. Both SBGs and SFGs have low γ-ray luminosities when compared to blazars and RGs, with only a few point-sources active at high energies being catalogued so far (164).
- *Supernova Remnants* (SNRs): a structure leftover from a SN explosion, surrounded by shock waves that sweep up the SN ejecta along with the circumstellar gas. These shock waves are capable of accelerating charged particles, promoting them to CRs and producing non-thermal multimessenger spectra, as we shall later discuss. Indeed, it has been believed for a long time that SNRs are a major source of CRs (165), likely contributing to the bulk of the Galactic flux observed below the knee. Fermi-LAT has indeed observed direct γ-ray signals from pion decay in SNRs (166), solidifying their status as Galactic CR acceleration sites.

  On rare occasions, exceptionally massive progenitor stars can collapse and produce explosions which are significantly more energetic than regular SNe. These are known as hypernovae, whose post-collapse remnants provide even more favorable environments for particle acceleration and high-energy emission (167, 168).
- *Pulsar Wind Nebulae*: magnetized winds of relativistic charged particles powered by a central pulsar (a rapidly rotating, strongly magnetized NS), typically found inside SNRs whenever the SN explosion results in the formation a pulsar. These structures have been found to produce very energetic γ rays, with a recent surprising detection of PeV photons from the famous Crab Nebula (169), located inside the Milky Way. When pulsar winds stream into the ISM, shock waves can form at their interfaces. These so-called "wind termination shocks" can accelerate electrons and positrons (170) and perhaps even nuclei extracted from the pulsar itself (171), possibly up to UHEs.

1.2.2
Transient Sources

Transient events typically considered in the literature as sources of high-energy astroparticles include:

- *Supernovae*[17] (SNe): catastrophic explosions marking the end of the life of stars above the Chandrasekhar limit of around 1.4 $M_\odot$ (172). SNe can be triggered by several different mechanisms and give rise to distinct EM features which give rise to a rich taxonomy of classifications. Let us mention a few of them. Type Ia SNe are caused by runaway nuclear fusion in white dwarf stars and are commonly used as standard candles for our measurements of cosmic distances. All other SNe occur via core collapse, when the inward pull of gravity exceeds the outward pressure holding the star together. For massive enough stars, core collapse can lead to especially energetic explosions called hypernovae, or especially luminous ones called superluminous SNe.

  Regular SNe tend to last anywhere from days to a few months and produce γ rays and neutrinos mostly up to the MeV range (173). However, TeV and above multi-messenger production may be achieved in SNR shock waves, as we have already discussed, as well as in hypernovae or superluminous SNe, associated to another kind of transient event which shall be discussed next. Incidentally, core collapse SNe are also expected to source GWs between its core bounce and explosion stages (see (174) for a recent review), although these have yet to be detected.

- *Gamma-Ray Bursts* (GRBs): extremely luminous bursts of energetic γ rays, likely produced in relativistic jets, typically followed by a long afterglow from TeV energies all the way down the EM spectrum (175). It is believed that these jets are produced in hypernovae/superluminous SNe, producing what are known as "long-duration GRBs" (> 2 s, see *e.g.* (176)) or from the merger of compact object binary systems, giving rise to "short-duration GRBs" (usually < 2 s, although this is not always the case (177)). If these short GRBs originate from NS-NS or NS-BH mergers, thermal SN-like transients known as "kilonovae" emerge, lasting from days to weeks. More importantly for us, the environment created by GRB jets may be capable of performing efficient particle acceleration, making them prime source candidates of CRs and astrophysical neutrinos during its prompt and afterglow phases (see (178) Vol. II, Chap. 9).

---

[17] We have already mentioned them in the context of SNRs and as neutrino sources in the MeV band, so it is perhaps a good time to explain exactly what they are.

- *Tidal Disruption Events* (TDEs): spaghettification of stars that get tidally disrupted after approaching a SMBH. The stellar debris from such an event can get caught in the BH's accretion disk and produce bright multiwavelength flares, primarily in the radio to X-ray range (see (179) Chap. 5). Jetted TDEs have also been found (180), providing interesting multi-messenger prospects as high and ultra-high energies (181, 182). On top of that, certain models for non-jetted TDEs have also been able to predict GeV-PeV neutrino fluxes (183).

1.2.3
Current Status of Multi-Messenger Source Searches

Now that we have listed several classes of astrophysical objects known to emit EM waves with distinct spatial, temporal and energetic features, it is important to comment on our current knowledge regarding their high-energy multi-messenger emissions. The only way this can be done is by searching for directional, temporal and/or energetic coincidences between our EM, CR and neutrino observations (we will no longer mention GWs in this thesis). This usually means looking for point-like or extended regions in the sky from which we receive one or more cosmic messengers. For example, comparing the direction of neutrino events at IceCube and catalogs of known blazar directions might lead us to identify potential astrophysical neutrino sources (or source classes). If coincidences are found, the astrophysical neutrino flux would be "promoted" from completely diffuse to partially resolved, clearing the way for an improved multi-messenger modeling of sources.

There is good reason to believe that the same sources that comprise the IGRB also produce our observed astrophysical neutrino and UHECR fluxes. From a theoretical perspective, multi-messenger production models typically predict comparable energy budgets emitted in CRs, neutrinos and γ rays, as we shall soon discuss in Section 1.3. Despite their disparate energy regimes, we find that the diffuse fluxes of these messengers possess similar energy contents. This can be visually seen in Figure 1.8, where the comparable energy fluxes ($E^2\Phi$) become clear. Needless to say, this is only a naïve expectation, which seems to become less and less likely as time goes by. We will discuss about this further in Chapter 3.

Although CRs get deflected by ubiquitous magnetic fields (see Section 2.1.4), we may still be capable of spotting nearby UHECR sources directly. This is because the Larmor radius given by Eq. (1-5) increases with energy, such that EeV protons are only expected to deflect significantly after ~ 1 Mpc for a coherent nanoGauss magnetic field. Motivated by this possibility, angular

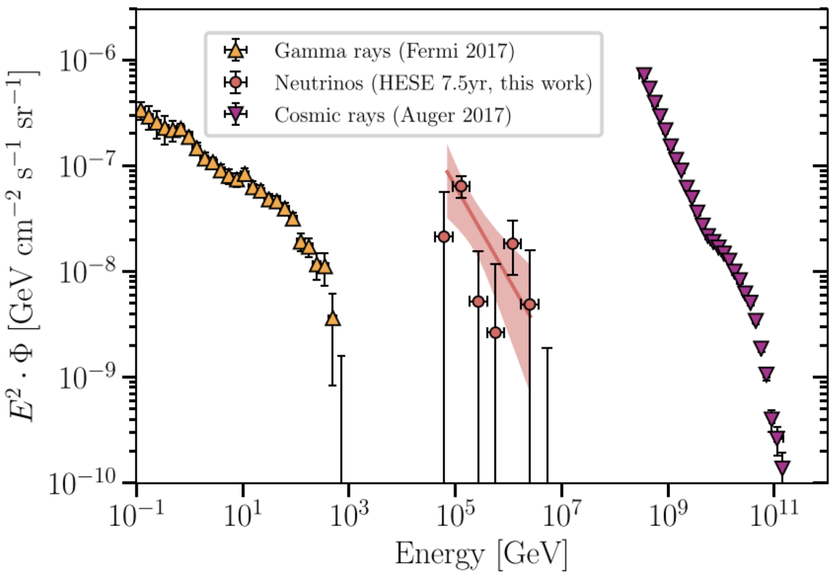

Figure 1.8: Compilation of high-energy fluxes of γ rays (IGRB), astrophysical neutrinos, and UHECRs. Figure from (184).

correlation searches were performed between UHECR directions and *Fermi*-LAT sources (185, 186, 187), as well as neutrino events (188), none yielding 5σ-level coincidences as of yet. At this point, we have good reason to believe that UHECR sources either lack γ-ray emission outright, or are currently unresolved by our telescopes. In fact, it has been recently shown that the UHECR dipole should be significantly stronger if catalogued γ-ray sources were responsible for the observed UHECR flux (189).

Regarding the origin of astrophysical neutrinos, many attempts have been made to correlate IceCube events to γ-ray sources, making use of different strategies depending on the type of source being considered. Steady sources benefit from time-integrated searches, looking for both directional and energy correlations between neutrino events and known γ-ray emitters, throughout IceCube's entire operating lifetime. Time-integrated searches for point-like and extended sources have mostly yielded null results so far (*e.g.* see (190, 191, 192, 193, 194, 195, 196, 197) for recent analyses by the IceCube collaboration), with a few mild-to-high-significance exceptions. The most notable finding was that of the Seyfert galaxy[18] NGC 1068 (193), detected at 4.2σ from an excess of 70^{+22}_{-20} events above the background expectation. Curiously, the neutrino flux observed from this object is at least an order of magnitude higher than its γ-ray flux at TeV energies, indicating that we could be dealing with a source opaque to the escape of γ rays. This is expected to be a prevailing property of astrophysical neutrino sources (20, 19), to be discussed

---

[18] A common type of AGN-harboring galaxy with a nucleus obscured by its torus.

further in Chapter 3.

Time-dependent searches take into consideration temporal information from the signals, making them ideal for transient sources. Numerous such analyses have also been conducted by IceCube (195, 196, 198, 199), resulting in very few successful correlations. In particular, the neutrino event IceCube-170922A triggered an alert that was subsequently followed up by several other experiments in an extensive multiwavelength campaign, revealing a 3σ coincidence with the flaring[19] blazar TXS 0506+056 (200). This news was received with a lot of appraise by the multi-messenger community, as it was the first strong indication of a potential astrophysical neutrino source. Complementary searches later displayed evidence for multiple neutrino events in the same direction prior to the flaring episode (201), raising its significance to 3.5σ. More recently, a few TDEs have also appeared in possible association with neutrino counterparts, AT2019dsg being the most prominent one (202).

Another analysis technique commonly used involves summing over ("stacking") the emission from an entire population of sources to enhance its signal (203, 204). This may reveal classes of γ-ray emitters whose individual luminosities are too faint to produce any significant multi-messenger correlation, but when considered collectively, become neutrino-bright. As of the writing of this thesis, IceCube stacking searches have not uncovered any steady-state (190, 191, 192, 194, 195, 197, 205, 206, 207, 208) or transient (198, 209) neutrino source classes.

Null results are not useless. They provide us with upper limits on the neutrino fluxes of individual sources (in the case of point-like searches) or entire populations (in the case of stacking analyses). Since these limits depend of several assumptions specific to each search method, we refer to the original publications for quantitative constraints. For the reader's convenience, here are some latest results constraining a few commonly considered source classes: AGNi (196, 197, 205, 207, 208, 210), SNRs/PWNe (192, 211), galaxy clusters (194), galaxy mergers (212), radio pulsars (213), GRBs (214), TDEs (215), and SNe (198). These also include searches for low-energy EM counterparts, which are clearly important if we are really dealing with γ-ray-opaque objects that reprocess internal γ rays to X-rays and beyond.

Finally, it is worthwhile mentioning that IceCube has recently established the existence of a diffuse neutrino emission from the Galactic plane between around 1–100 TeV at a 4.5σ level (216). This flux is ~ 1 order of magnitude lower than the total astrophysical flux, and can arise either as secondary

---

[19] Blazars can go from their quiescent/regular state to a flaring state, increasing by many orders of magnitude their jet emission of optical/γ rays. The cause and frequency of these flares is still not well understood.

byproducts of CR interactions in the Milky Way's ISM, or come directly from unresolved Galactic sources, which could be revealed by next-generation neutrino telescopes (217).

1.3
Multi-Messenger Production

Let us take a step back from trying to identify potential multi-messenger sources and instead study the general requirements and mechanisms behind the production of high-energy astroparticles. The first requirement is that these sources must somehow be capable of accelerating charged particles (electrons, ions or nuclei), producing energetic, non-thermal spectra. This can be done in a few different ways, which we describe in Section 1.3.1. Next, these accelerated particles can either be released into space, becoming CRs, or interact within the source to produce secondary byproducts, including γ rays and neutrinos.

Secondary production channels can be divided into two categories: *leptonic* or *hadronic*. Leptonic processes include ICS, bremsstrahlung, photon-photon annihilation into leptons, synchrotron radiation and, in general, any process involving only leptons and bosons. For example, the EM cascades described in Section 1.1.1, which shall also be the main topic of Chapter 2, are purely leptonic.

Inside radiation- and gas-filled astrophysical environments, ICS[20] and bremsstrahlung of accelerated electrons in particular are responsible for $>$ TeV γ-ray emission in most leptonic source models. In order to obtain its spectrum, one must know in advance the distribution of relativistic electrons inside the source, which can usually be inferred from low energy observations of their synchrotron emission (typically from radio to X-rays). However, a severe consequence of such models is that no UHECRs can be produced. It has also been a consensus within the multi-messenger community that neutrinos too cannot arise by leptonic means, and that the observation of astrophysical neutrinos at IceCube provides indirect evidence for the existence of hadronic accelerators. We will see in Section 2.4 that this is not necessarily true: at high COM energies, *muon pair production* (MPP; $\gamma + \gamma \to \mu^+ + \mu^-$), can lead to neutrinos following from the decay of the muons.

Hadronic processes, as the name suggests, necessarily involve hadrons. These are typically mesons, such as pions and kaons, baryons, such as protons and neutrons, as well as nuclei. The main interaction channels for multi-messenger production will be discussed shortly in Section 1.3.2. In a nutshell,

---

[20] This includes synchrotron self-Compton, when the up-scattered photon comes from the electron's own synchrotron radiation field. To distinguish different ICS contributions, the ICS of external/ambient target photons is usually called "external Compton".

hadronic sources accelerate protons/nuclei, potentially up to UHEs, which eventually escape or interact with ambient targets, yielding secondary γ rays and neutrinos. Secondary high-energy electrons can also be produced, giving rise to leptonic activity as well. In the most general case, sources can be lepto-hadronic.

Observationally, it can be very hard to distinguish between hadronic and leptonic signals from astrophysical sources just by their γ-ray fluxes. Not only can each of them vary significantly by changing model parameters, but also they can reproduce the same high-energy spectra, requiring multi-wavelength or polarization data to break their degeneracy (see (218, 219) for examples). On top of that, γ-ray escape can be partially blocked by dense material/radiation fields surrounding the source.

For the analyses we will perform in Chapter 3, we will consider a population of sources emitting the observed astrophysical neutrino flux, which conventionally requires that they are hadronic by nature. We will then assume their corresponding γ-ray emission is minimal (without invoking γ-ray opacity of the source). In other words, we will neglect any possible leptonic emission such that their γ-ray flux at the Earth is the smallest possible. Let us then understand the steps necessary for this scenario to realize itself.

1.3.1
Acceleration Mechanisms

Hadronic multi-messenger production starts with the acceleration of nuclei to high energies. Since they are charged particles, we would like to take advantage of the EM force to perform this acceleration quickly and efficiently. This can be done in a few different ways.

Since magnetic fields always apply forces perpendicular to the motion of charges, the magnetic force does no work. Thus, one would naively expect that the only way of accelerating nuclei in astrophysical environments is if they contain strong, coherent electric fields. While this indeed can happen in some astrophysical systems (*e.g.* at pulsar magnetospheres (220)), most acceleration sites are composed of plasmas that prevent such fields to exist. Positive and negative charges in plasmas can freely move to guarantee charge neutrality at short distances. This is known as Debye screening, and the characteristic distance beyond which electrostatic effects are no longer felt is called the Debye length,

$$\lambda_D = \sqrt{\frac{\varepsilon_0 k_B T}{e^2(n_e + Z^2 n_I)}}\ , \tag{1-20}$$

written in SI units, where T is the temperature of the plasma, $n_{e/I}$ are the number densities of electrons/ions, and ε_0 is the permittivity of free space.

In the middle of the 20th century, Enrico Fermi came up with a solution that involved solely the use of magnetic fields (221). The key insight was to notice that magnetic fields are simply Lorentz boosted electric fields. Thus, by assuming a magnetized plasma region moving with respect to the test particle, work can in fact be done to accelerate it. Consider a magnetized cloud (bulk of particles) moving with velocity $\boldsymbol{\beta}$ and a charged particle entering it with energy $E_1 \approx p_1$ in at an angle θ_1 and exiting it with E_2 and θ_2, as depicted in the left panel of Figure 1.9. In the rest frame of the cloud (indicated by primed quantities), its initial energy is $E_1' = \Gamma E_1(1 - \beta \cos\theta_1)$, where $\Gamma = (1 - \beta^2)^{-1/2}$ is the cloud's Lorentz factor. After entering the cloud, the test particle undergoes collisionless diffusion[21] through elastic scatterings off magnetic field perturbations, scrambling its exit orientation in the cloud rest frame, $\langle \cos\theta_2' \rangle = 0$, while energy remains conserved, $E_1' = E_2'$. After all, there are only magnetic fields in this frame, and these do zero work. Once it leaves the cloud with an angle θ_2', its energy in the original frame is $E_2 = \Gamma E_2'(1+\beta\cos\theta_2')$, leading to an overall fractional energy change of (223)

$$\frac{\Delta E}{E_1} = \frac{1 - \beta\cos\theta_1 + \beta\cos\theta_2' - \beta^2\cos\theta_1\cos\theta_2'}{1-\beta^2} - 1 \ . \tag{1-21}$$

This quantity will be positive or negative depending on the orientations of entrance/exit of the test particle. A useful picture to have in mind is: if $\cos\theta_1 < 0$ (head-on collision), then energy increases in most cases, whereas if $\cos\theta_1 > 0$ (tail-on collision), then energy tends to decrease. On average, after scattering off many such clouds, we obtain (for $\beta \ll 1$) a net energy gain

$$\frac{\langle \Delta E \rangle}{E_1} \simeq \frac{4}{3}\beta^2 \ . \tag{1-22}$$

In short, the energy increases on average because head-on collisions with the cloud are more likely than tail-on collisions.

This process is known as stochastic or *second-order Fermi acceleration*, since the energy gain is proportional to β^2. This is quite small, resulting in a relatively inefficient acceleration. It can also be shown that the resulting CR spectrum would be a power law with model dependent spectral indices, unlike the (mostly) universal index observed in Figure 1.4 (224).

This idea can be further exploited if we consider a shock wave instead of a cloud (225, 226, 227, 228). Shock waves are sharp, near-discontinuities in the density of a fluid, moving faster than the speed of sound in that medium. They are expected (and seen) to form in extreme astrophysical environments such as SNRs, stellar winds, relativistic jets and accretion regions, occurring whenever

---

[21] In the presence of small magnetic field perturbations, it can be shown that a charged particle undergoes collisionless pitch angle diffusion (222).

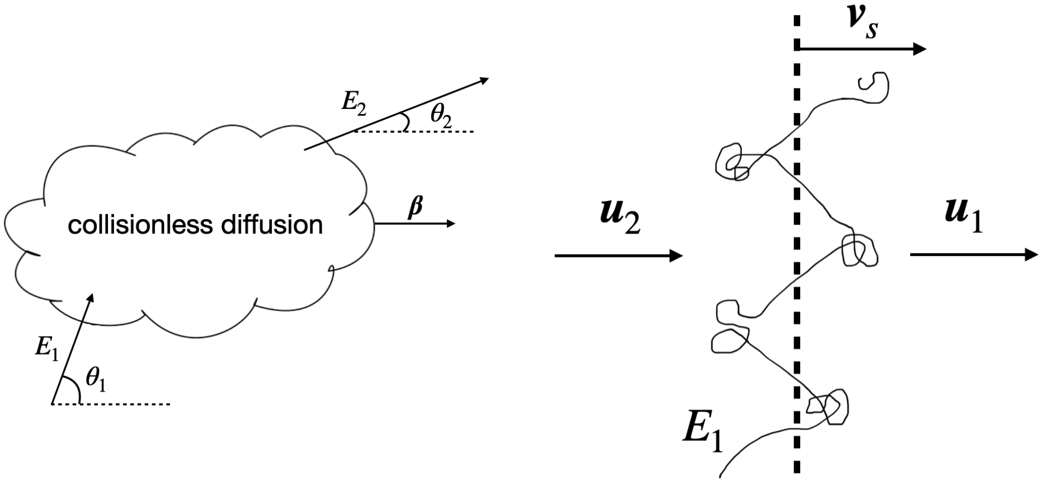

Figure 1.9: Pictorial representation of Fermi acceleration mechanisms. Left: second-order Fermi acceleration in magnetized clouds. A particle enters it with energy E_1, diffuses elastically due to magnetic field inhomogeneities, and leaves with energy E_2. Right: first-order Fermi acceleration in shock waves. A particle crosses back and forth across the wave front, diffusing elastically each time before crossing back with a high energy.

there are objects moving or gas flowing at supersonic speeds (229). It is believed that particles can get accelerated by crossing back and forth across the shock wave, oscillating between the shocked/downstream and unshocked/upstream regions around the wave front, depicted in the right panel of Figure 1.9. The supersonic shock velocity is represented by $\boldsymbol{v}_s$ while the upstream and downstream velocities are $\boldsymbol{u}_1$ and $\boldsymbol{u}_2$, respectively.

Same as before, each time the particle crosses the shock wave, it diffuses elastically due to magnetic fields. However, once the particle diffuses into either side's rest frame, it always sees the other side coming towards it because of the movement of the shock. For example, for strong shocks (v_s much greater than the sound speed) surrounded by an ideal monoatomic gas, we find $\boldsymbol{u}_1 = -\boldsymbol{v}_s = 4\boldsymbol{u}_2$ in the rest frame of the shock (223). Hence, the upstream region sees the downstream region approaching with $3v_s/4$, and the downstream region also sees the upstream region approaching with $3v_s/4$. This means that head-on collisions always occur, in contrast to second order Fermi acceleration (also, only half of the exit directions are available). A similar calculation to the previous one yields

$$\frac{\langle \Delta E \rangle}{E_1} \simeq \frac{4}{3}\beta \ , \tag{1-23}$$

with $\beta = |\boldsymbol{u}_1 - \boldsymbol{u}_2|/c \ll 1$ being the relative speed between the upstream and downstream regions.

This more efficient, and more popular, acceleration mechanism is called *first-order Fermi acceleration* or *diffusive shock acceleration*. Its popularity is not only due to $\Delta E/E_1 \propto \beta$ – a great improvement with regards to stochastic acceleration, allowing particles to reach much higher energies[22] – but also because it predicts a universal E^{-2} power law spectrum for the resulting CRs (230). Although this does not match the $E^{-2.7}$ spectrum observed for CRs below the knee, the injection spectrum can be steepened by considering the nonlinear effects of CRs themselves in the shock structure (231, 232), the presence of neutral particles in the gas swept up by the shock (233), and the escape of CRs from our Galaxy (234).

Alternative particle acceleration mechanisms include magnetic reconnection (235) and shear acceleration (236), topics which are beyond the scope of this thesis. While these models also succeed in reproducing the high-energy non-thermal power-law spectra observed in astrophysical systems, there is no conclusive evidence distinguishing them, or favoring one over the others. Our analyses from here onwards will be independent on the specific acceleration mechanism considered.

1.3.2
Hadronic Processes in Astrophysical Sources

Simultaneous neutrino and γ-ray production in hadronic interactions can occur via two main channels: the pp/hadronuclear and $p\gamma$/photohadronic channels. In both cases, accelerated protons encounter a target – either a proton from ambient gas (pp) or a photon from ambient radiation ($p\gamma$) – and produce charged and neutral pions. These pions then decay via

$$\pi^+ \to \mu^+ + \nu_\mu \ , \qquad \pi^- \to \mu^- + \bar{\nu}_\mu \ , \qquad \pi^0 \to 2\gamma \ , \tag{1-24}$$

followed by

$$\mu^+ \to e^+ + \nu_e + \bar{\nu}_\mu \ , \qquad \mu^- \to e^- + \bar{\nu}_e + \nu_\mu \ , \tag{1-25}$$

producing photons and neutrinos in the end. We therefore reach a very important conclusion for multi-messenger astrophysics: conventional routes leading to the emission of astrophysical neutrinos also predict an accompanying γ-ray flux. In what follows, we shall more closely examine each of these channels separately and discuss their implications within the context of this thesis.

---

[22] CRs cannot be accelerated up to arbitrary energies. The primary reason for this in diffusive shock acceleration is that the time it takes for a particle to diffuse back to the shock increases with energy, making each energy gain cycle longer. Eventually, this time becomes comparable to the shock dissipation timescale, and acceleration stops. The size of the source may also not be able to magnetically confine particles above certain energies, causing CRs to escape before they can accelerate further.

1.3.2.1
pp Channel

Hadronuclear interactions between accelerated and non-relativistic ambient protons is expected to occur mainly in CR reservoirs with high gas densities (*e.g.* SBGs, galaxy clusters), where CRs that have escaped from their accelerators can stay confined by magnetic fields for a long time and eventually encounter target protons (and possibly nuclei). Secondary pions are produced in inelastic[23] collisions,

$$p + p_{\rm bkg} \rightarrow \pi^{\pm,0} + X \ , \tag{1-26}$$

along with other hadrons X. We denote the energy of the incoming proton by E_p in the lab frame (*i.e.* $p_{\rm bkg}$ initially at rest).

Denoting the proton and neutral pion masses, respectively, by m_p and m_{π^0}, we find that process (1-26) has a proton kinetic energy threshold of $T_{p,th} = E_{p,th} - m_p = (m_{\pi^0}^2/2m_p) + 2m_{\pi^0} \simeq 280$ MeV, corresponding to the first kinematically accessible process $pp \rightarrow pp\pi^0$. Together with $pp \rightarrow pn\pi^+$ and $pp \rightarrow d\pi^+$, these are the only accessible channels near threshold, partially contributed by the presence of the $\Delta(1232)$ resonance (238, 239, 240). The cross sections and secondary distributions can be well described in this regime using so-called "isobar models" (241), which have isospin symmetry as one of its pillars.

As the energy increases to around $T_p \gtrsim 600$ MeV, isospin symmetry breaks down and multi-pion production kicks in (242),

$$p + p_{\rm bkg} \rightarrow X + N_{\pi^+}\pi^+ + N_{\pi^-}\pi^- + N_{\pi^0}\pi^0 \ , \tag{1-27}$$

where $N_{\pi^{\pm,0}}$ are the pion multiplicities. See Table 1 in (242) for a list of low-energy pp interactions and their lab-frame thresholds. Just above the two-pion production threshold, the pion multiplicities follow a ratio $(N_{\pi^+} : N_{\pi^0} : N_{\pi^-}) \approx (4 : 3 : 1)$ (243).

At intermediate energies (T_p between $\sim$ 10–100 GeV), hadron collisions approximately obey an important property known as Feynman scaling (244). It postulates that the outgoing spectra from hadronic interactions only depend on the Feynman-x variable $x \equiv 2p_{\parallel}/\sqrt{s}$, defined as the ratio between the longitudinal momentum of the outgoing particle in the COM frame, $p_{\parallel}$, and

---

[23] The term "inelastic" refers to collisions in which at least one new secondary hadron is produced. This is in contrast with "elastic" collisions, in which there is only momentum transfer between the protons without changing their identity. In the case of nuclei, collisions can also be "quasi-elastic", when the nucleus disintegrates, but no new secondary hadrons are produced. In the literature, "inelastic" is sometimes used to indicate any process which is not elastic. To remove ambiguities with quasi-elastic interactions, one should use the alternative term "particle production" collisions to refer to processes forming new secondaries (237).

the half of the COM energy of the system[24], $\sqrt{s}/2$, as well as on the transversal momentum of the outgoing particle $p_\perp$. Ignoring the $p_\perp$ dependence, this scaling property for secondary particle A can be expressed as

$$E_A \frac{\mathrm{d}\sigma_{pp\to A}}{\mathrm{d}p_\parallel}(p_\parallel, s) = f_{pp\to A}(x) \ , \qquad \text{for } s \to \infty \ , \tag{1-28}$$

where $\mathrm{d}\sigma_{pp\to A}/\mathrm{d}p_\parallel$ is the inclusive[25] differential cross section for the process $pp \to A$ and $f_{pp\to A}$ is a function that does not depend explicitly on s, only on x. Note that this unchanged in the lab frame, as $\mathrm{d}p_\parallel/E_A$ is invariant under boosts along the longitudinal direction. Two interesting consequences follow from the Feynman scaling assumption :

1. The spectra of secondaries should replicate the shape of the initial proton spectrum (245). In particular, if the distribution of protons follows a power-law, $\mathrm{d}N_p/\mathrm{d}E_p \propto E_p^{-\alpha}$, as predicted for CRs by diffusive shock acceleration, then all of the outgoing γ rays and neutrinos should also be produced in power-law spectra with the same index α.
2. The multiplicity distributions of secondary particles at different energies are just rescaled versions of each other. This property is known as KNO scaling (246, 247).

Historically, Feynman scaling was very relevant for pp interactions in extrapolating the high-energy behaviour of pion and γ-ray spectra from low energy data. Nowadays, it is known that the running of the strong coupling and multiple parton scatterings lead to Feynman scaling violation (248, 249), which has been observed through KNO scaling violation (*e.g.* (250)). Modern calculations of pp secondary spectra must, and do, take this into account (251), although the effect of scaling violation in the resulting spectra is mostly seen as a change in the multiplicity, with only mild changes to their shapes.

At the > TeV energies expected in astrophysical neutrino sources, proton-proton collisions lead to the hadronization of its byproducts, producing electrically-neutral jets of hadrons (also called “minijets”). These jets contain large amounts of pions and heavier mesons (η, $K^\pm$, etc.) which all decay to produce outgoing γ rays, electrons and neutrinos. Precise evaluation of their spectra requires the use of modern Monte Carlo event generators such as Sibyll (252), QGSJet (253) and EPOS-LHC (254). Interestingly, if we assume a power-law proton spectrum $\mathrm{d}N_p/\mathrm{d}E_p \propto E_p^{-\alpha}$, we also find approximate power-laws for the final γ-ray and neutrino spectra, with a spectral index close

---

[24] $s = (p_1 + p_2)^2 = E_{\mathrm{CM}}^2$ is the usual Maldelstam variable defined in terms of the initial four-momenta p_1 and p_2, corresponding to the squared COM energy of an interacting system.

[25] This means any process producing particle A, regardless of the other byproducts.

to (slightly harder than) α (255, 256). Additionally, the *inelasticity* (*i.e.* fraction of initial proton energy lost to pions in the final state) is found to be $\kappa_p = \Delta E_p/E_p \sim 50\%$, with a smaller portion of this energy being distributed to low energy pions with a high multiplicity and a larger portion given to a few high-energy pions. The peak of the pion energy distribution is found to be around $E_\pi/E_p \sim 0.1$–0.2.

After summing up the contributions from all neutrino flavors, we find that

$$\frac{\mathrm{d}N_\gamma}{\mathrm{d}E_\gamma}(E_\gamma) \simeq \frac{1}{6}\,\frac{\mathrm{d}N_\nu}{\mathrm{d}E_\nu}(E_\nu)\bigg|_{E_\nu = E_\gamma/2} . \tag{1-29}$$

This relation can be understood through some simple arguments which are commonly found in the multi-messenger literature under the so-called δ-functional approximation (257). In this description, each pion species receives on average 1/5 (the typically quoted value is 17% for π^0 at GeV–TeV energies) of the parent proton's energy. The name "δ-functional" then comes from assuming that pions are produced with fixed energy, such that the differential cross section for pion production is

$$\frac{\mathrm{d}\sigma_{pp\to\pi}}{\mathrm{d}E_\pi}(E_p, E_\pi) = \sigma_{pp,inel}(E_p)\,\delta(E_\pi - E_p/5) \ , \tag{1-30}$$

where $\sigma_{pp,inel}(E_p)$ is the total inelastic cross-section of pp collisions. These pions are produced with approximately equal multiplicities, $(N_{\pi^+} : N_{\pi^0} : N_{\pi^-}) \approx (1 : 1 : 1)$, such that the ratio of neutrinos of all flavors to photons generated is $(N_\nu : N_\gamma) \approx (3 : 1)$. Additionally, Eq. (1-30) implies that the spectral shape of pions and incoming protons are identical. Assuming Feynman scaling, we would also expect the spectral shapes of photons and neutrinos to be the same.

Regarding energetics, the muons from (1-24) leave with approximately 3/4 of the pions' energies, and distribute it almost evenly among their decay byproducts in (1-25) (see Table 1 in (94) for $\alpha = 2$). This means that the each of the three neutrinos carries around 1/4 of the original charged pion's energy. Meanwhile, The photons produced via the neutral pion decay (1-24) share its energy equally by simple kinematic considerations. So, in summary, we have

$$E_\nu \approx \frac{E_\pi}{4} \approx \frac{E_p}{20} \ , \qquad E_\gamma \approx \frac{E_\pi}{2} \approx \frac{E_p}{10} \ . \tag{1-31}$$

Gathering all of these conclusions, we find $E_\nu \approx E_\gamma/2$, arriving at Eq. (1-29). One can check by integrating over energy that the factor of 1/6 properly accounts for $(N_\nu : N_\gamma) \approx (3 : 1)$.

1.3.2.2
$p\gamma$ Channel

The photohadronic path for the production of astrophysical neutrinos and γ rays can occur inside the accelerating regions themselves, provided there are target photons available for

$$p + \gamma_{\rm bkg} \rightarrow \pi^{\pm,0} + X \tag{1-32}$$

to take place. High luminosity objects like GRBs, TDEs and AGNi are good candidates for hosting such processes; as we have seen in Section 1.2, they are also known to be powerful γ-ray emitters and likely origins of UHECRs. The threshold for (1-32) comes from $p\gamma \rightarrow p\pi^0$ and evaluates, in the relativistic limit ($E_p \gg m_p$), to[26]

$$E_{p,th} = \frac{2m_p m_{\pi^0} + m_{\pi^0}^2}{4\epsilon} \ , \tag{1-33}$$

where ϵ is the energy of the target photon in the lab frame.

In particular, if this photon comes from the CMB, it has a typical energy of $\langle\epsilon_{\rm cmb}\rangle \approx 2.7\,T_{\rm cmb} \approx 0.63$ meV , which would lead to a GZK threshold of $E_{p,\rm GZK} \approx 10^{20}$ eV. A more accurate calculation taking into account the blackbody shape of the CMB spectrum yields a slightly lower threshold, corresponding to those quoted in Section 1.1.2. Note that, although you get the proton back from this interaction, a significant fraction κ_p ($\sim 14\%$ at threshold, rising to a relatively constant $\sim 50\%$ at high COM energies) of the initial energy is in fact transferred to the outgoing pion (258, 259). With this, one can estimate the minimum energy of cosmogenic neutrinos: $E_\nu \approx (\kappa_p/4)E_{p,\rm GZK} \approx E_{p,\rm GZK}/20 \sim 5\times10^{18}$ eV. Recall the κ_p accounts for the proton-to-pion energy transfer (near threshold, single pion processes dominate, meaning all of the inelasticity fraction goes into a single pion) and the 1/4 accounts for the pion's energy going into neutrinos.

Near threshold, the $p\gamma$ cross section is dominated by the $\Delta(1232)$ resonance,

$$p + \gamma_{\rm bkg} \rightarrow \Delta^+ \rightarrow \begin{cases} p + \pi^0 & 2/3 \text{ of the cases} \\ n + \pi^+ & 1/3 \text{ of the cases} \end{cases} . \tag{1-34}$$

The Δ^+ decay branching fractions can be deduced from the SU(2) isospin

---

[26] The exact threshold can be easily derived by shifting our perspective to the required photon energy in the rest frame of the initial proton: $\tilde{\epsilon}_{th} = m_\pi + (m_\pi^2/2m_p)$, where the tilde indicates the quantity is in the proton rest frame. This makes sense: once the photon acquires an energy comparable to the pion mass, a pion can be created.

symmetry, by simply reading Clebsch–Gordan coefficients:

$$\begin{aligned}|\Delta^+\rangle &= |J=3/2, M=1/2\rangle \\ &= \sqrt{\frac{2}{3}}\,|j_1=1/2, m_1=1/2\rangle|j_2=1, m_2=0\rangle \\ &\quad + \sqrt{\frac{1}{3}}\,|j_1=1/2, m_1=-1/2\rangle|j_2=1, m_2=1\rangle \\ &= \sqrt{\frac{2}{3}}\,|p\rangle|\pi^0\rangle + \sqrt{\frac{1}{3}}\,|n\rangle|\pi^+\rangle\ .\end{aligned}$$

It has always been very common within the astrophysical community to only mention this resonance channel when displaying neutrino-to-γ-ray yields such as the one in Eq. (1-29) (260). By itself, this leads to $(N_{\pi^+} : N_{\pi^0} : N_{\pi^-}) = (1 : 2 : 0)$, which turns out to be inaccurate even at low energies. The direct $p\gamma \to n\pi^+$ (through the t-channel) plays an important role in increasing the π^+ multiplicity, such that $(N_{\pi^+} : N_{\pi^0})$ actually lies closer to $(1 : 1)$ (261).

As it happens, this turns out to reflect quite well the reality of most cases, since the $p\gamma$ inelastic cross section peaks around the $\Delta(1232)$ resonance (262), such that high-energy protons tend to interact more often with low energy background photons, and vice-versa. Neglecting the π^- contribution and taking pion energy as $E_\pi \approx E_p/5$ (258, 263), we end up with

$$\frac{\mathrm{d}N_\gamma}{\mathrm{d}E_\gamma}(E_\gamma) \simeq \frac{2}{6}\frac{\mathrm{d}N_\nu}{\mathrm{d}E_\nu}(E_\nu)\bigg|_{E_\nu=E_\gamma/2}\ , \tag{1-35}$$

through a very similar deduction to the one in the last section. This ratio of secondary fluxes is often quoted in the multi-messenger astrophysics literature.

Of course, at higher energies these approximations lose some precision due to higher resonances, multi-pion and heavy hadron production (255). In particular, multi-pion processes which dominate at high COM energies (where the cross section is relatively small) yield $(N_{\pi^+} : N_{\pi^0} : N_{\pi^-}) \approx (1 : 1 : 1)$, affecting the overall pion multiplicities and increasing the neutrino spectra relative to the γ rays. For the best accuracy, one should rather use Monte Carlo simulators such as SOPHIA (262).

One last distinction worth pointing out from the pp scenario is the difference in the spectral shape of secondaries. Consider the case of a power law proton injection $\mathrm{d}N_p/\mathrm{d}E_p \propto E_p^{-\alpha}$. The (approximate) Feynman scaling in hadronuclear interactions, together with their low pion production threshold, predicts outgoing neutrino and γ-ray spectra following (approximately) the same unbroken power law as the primaries. Meanwhile, the threshold for photomeson production can be potentially quite high, depending on the available background photon energies. If an astrophysical source is permeated by keV photons (*e.g.* X-rays from synchrotron radiation of electrons in a strong magnetic field), then the $p\gamma$ threshold given in Eq. (1-33) evaluates to $E_{p,th} \approx 70$ TeV. This leads to a steep suppression of the secondary fluxes below threshold, which results in a near broken power law spectrum

$$\frac{\mathrm{d}N_i}{\mathrm{d}E_i}(E_i) = \begin{cases} \text{const} \ , & E_i < E_{b,i} \\ E^{-\alpha} \ , & E_i > E_{b,i} \end{cases} \ , \tag{1-36}$$

where $E_{b,i}$ is the spectral break energy for secondary particle type i. Realistically, shapes of $p\gamma$ spectra depend on the source's target photon spectrum, which is typically thermal. This turns the sharp break in the power law into a continuous bump (264, 265).

1.3.2.3
Neutrino-γ-ray Connection

The main takeaway message from the previous two sections is that hadronic neutrino production in astrophysical sources automatically predicts a comparable γ-ray yield. We have quantified this relation in Eqs. (1-29) and (1-35), which are usually summarized as

$$\varepsilon_\gamma^2 \frac{\mathrm{d}N_\gamma}{\mathrm{d}\varepsilon_\gamma}(\varepsilon_\gamma) \simeq \frac{4}{3K_\pi} \left[\varepsilon_\nu^2 \frac{\mathrm{d}N_\nu}{\mathrm{d}\varepsilon_\nu}(\varepsilon_\nu) \right] \Bigg|_{\varepsilon_\nu = \varepsilon_\gamma/2} \ , \tag{1-37}$$

where K_π is the ratio of charged to neutral pions in each process: $K_\pi = 2$ (pp) or $K_\pi = 1$ ($p\gamma$). We have changed the notation from $E \to \varepsilon$ to indicate that these energies are to be measured in the comoving frame of the source. For the remaining of this thesis, ε will be used for energies in this frame, while E will be reserved for energies measured at the Earth. Even in the absence of interactions during the propagation of these particles to us, cosmological redshift still makes $\varepsilon \neq E$. More precisely, they are related by

$$\varepsilon = (1+z)E \ , \tag{1-38}$$

where z is the source's redshift.

The idealized relation (1-37) can sometimes be found in the literature in terms of the (differential) energy density generation rates[27]

$$\varepsilon_i Q_{\varepsilon_i}(\varepsilon_i, z) = \mathcal{F}(z)\, \varepsilon_i \frac{\mathrm{d}L_i}{\mathrm{d}\varepsilon_i}(\varepsilon_i, z) = \mathcal{F}(z)\, \varepsilon_i^2 \frac{\mathrm{d}N_i}{\mathrm{d}\varepsilon_i}(\varepsilon_i, z) \ , \tag{1-39}$$

where $\mathcal{F}(z)$ is the comoving number density of sources at redshift z and $L_i(z)$ is a single source's bolometric luminosity of particle type i ($= \gamma, \nu$),

---

[27] Q_{ε_i} is sometimes (perhaps more conveniently) written as $\mathrm{d}Q_i/\mathrm{d}\varepsilon_i$.

$$L_i(z) = \int_0^\infty \mathrm{d}\varepsilon_i \, \frac{\mathrm{d}L_i}{\mathrm{d}\varepsilon_i}(\varepsilon_i, z) = \int_0^\infty \mathrm{d}\varepsilon_i \, \varepsilon_i \, \frac{\mathrm{d}N_i}{\mathrm{d}\varepsilon_i}(\varepsilon_i, z) \ . \tag{1-40}$$

Note that the emission spectrum of an isotropic population of sources can evolve along cosmic timescales, and thus depend on redshift.

We can connect the energy generation rates of neutrinos and photons at their sources to the energy generation rate of CRs. For that, we need to introduce the interaction efficiencies for each scenario f_{pp} and $f_{p\gamma}$, defined by

$$f_{pp/p\gamma} = \frac{t_{\mathrm{dyn}}}{t_{pp/p\gamma}} \ , \tag{1-41}$$

where $t_{\mathrm{dyn}} \approx L/c$ is called the dynamical time, representing the characteristic time over which the accelerated particles cross through the region of length L where they can interact, and $t_{pp/p\gamma}^{-1} \approx c\kappa_p \sigma_{pp/p\gamma} n_{p/\gamma}$ is the energy loss rate[28] of these particles due to pp interactions with target protons of density n_p or $p\gamma$ interactions with target photons of density n_γ. The cross sections for these inelastic scatterings is represented by σ_{pp} and $\sigma_{p\gamma}$, respectively. The interaction efficiencies can also be interpreted as "effective optical depths", $f_{pp/p\gamma} = \kappa_p \tau_{pp/p\gamma}$, where the optical depth is given by $\tau_{pp/p\gamma} \approx L\sigma_{pp/p\gamma} n_{p/\gamma}$, and clearly depends on the source modeling details. For neutrinos, we can write

$$\varepsilon_\nu Q_{\varepsilon_\nu} \approx \frac{3K_\pi}{4(1+K_\pi)} \, \min[1, f_{pp/p\gamma}] \, (\varepsilon_p Q_{\varepsilon_p})|_{\varepsilon_p = 20\varepsilon_\nu} \ . \tag{1-42}$$

The factor 3/4 is the fraction of the total charged pion energy that is converted into neutrinos, the factor $K_\pi/(1+K_\pi)$ represents the fraction of the total pion energy present in charged pions (2/3 for pp and 1/2 for $p\gamma$) and $\min[1, f_{pp/p\gamma}]$ is the fraction of the total proton energy going into pions. We make use of the "min" function since $f_{pp/p\gamma}$ can be > 1, in which case essentially all the proton energy is converted into pions due to a large number of scatterings during the dynamical time. For γ rays, we have instead

$$\varepsilon_\gamma Q_{\varepsilon_\gamma} \approx \frac{1}{1+K_\pi} \, \min[1, f_{pp/p\gamma}] \, (\varepsilon_p Q_{\varepsilon_p})|_{\varepsilon_p = 10\varepsilon_\gamma} \ , \tag{1-43}$$

where $(1+K_\pi)^{-1}$ is the fraction of total pion energy contained in neutral pions (1/3 for pp and 1/2 for $p\gamma$). Recall that neutral pions convert all their energy into photons after decaying.

These emission spectra $\varepsilon_i^2 \frac{\mathrm{d}N_i}{\mathrm{d}\varepsilon_i}$ [$\mathrm{eV\,s^{-1}}$] and energy generation rates $\varepsilon_i Q_{\varepsilon_i}$ [$\mathrm{eV\,Mpc^{-3}\ s^{-1}}$] can be related to the fluxes $E_i^2 \Phi_i$ [$\mathrm{eV\,cm^{-2}\,s^{-1}\,sr^{-1}}$] ob-

---

[28] Recall the mean free path of a particle crossing a region of targets with uniform density n and interaction cross section σ is given by $\ell = (\sigma n)^{-1}$. The interaction rate during this crossing is then given by $t_{\mathrm{int}}^{-1} = \beta/\ell = \beta\sigma n$, where β is the particle's velocity, while the energy loss rate $t_{\mathrm{loss}}^{-1} = \kappa t_{\mathrm{int}}^{-1}$ accounts for the inelasticity κ of the process in question. If the entire interacting region has length L, then its optical depth is $\tau = L/\ell = L\sigma n$.

served at the Earth. Consider a single source at redshift z emitting a neutrino spectrum $\varepsilon_\nu^2 \frac{\mathrm{d}N_\nu}{\mathrm{d}\varepsilon_\nu}$. Since neutrinos don't interact during their journey, we just need to account for cosmological redshift effects in order to obtain the corresponding neutrino flux at the Earth,

$$E_\nu^2 \Phi_\nu^{\mathrm{pt-source}}(E_\nu, z) = \frac{\left[\varepsilon_\nu^2 \frac{\mathrm{d}N_\nu}{\mathrm{d}\varepsilon_\nu}(\varepsilon_\nu)\right]\Big|_{\varepsilon_\nu=(1+z)E_\nu}}{(1+z)^2\, 4\pi d_c^2} \; . \tag{1-44}$$

The factor of $(1+z)^{-2}$ can be obtained by dimensional considerations: one factor of $(1+z)^{-1}$ comes from the redshifting of the energies in [eV] and another comes from the cosmological time dilation of [s^{-1}]. The comoving distance d_c is usually appended with a $(1+z)$ factor to define the luminosity distance $d_L = (1+z)\, d_c$, such that Eq. (1-44) resembles the inverse square law for fluxes in flat spacetime. This can be generalized to the case of a population of sources evolving with redshift according to a comoving density distribution $\mathcal{F}(z)$ [Mpc^{-3}]. By multiplying the point-source flux by this density of sources and integrating over all space, we obtain the diffuse flux at the Earth due to all sources. This integration is usually done by changing the integration variable from the comoving volume[29] $\mathcal{V}_c$ to redshift (and dividing by 4π to get the desired [sr^{-1}] units, assuming the flux is isotropic):

$$\begin{aligned} E_\nu^2 \Phi_\nu^{\mathrm{diff}}(E_\nu) &= \frac{1}{4\pi}\int_0^\infty \mathrm{d}z \left|\frac{\mathrm{d}\mathcal{V}_c}{\mathrm{d}z}\right| \mathcal{F}(z)\, E_\nu^2 \Phi_\nu^{\mathrm{pt-source}}(E_\nu, z) \\ &= \frac{1}{4\pi}\int_0^\infty \mathrm{d}z\, \frac{\mathcal{F}(z)}{(1+z)^2\, H(z)} \left[\varepsilon_\nu^2 \frac{\mathrm{d}N_\nu}{\mathrm{d}\varepsilon_\nu}(\varepsilon_\nu, z)\right]\Bigg|_{\varepsilon_\nu=(1+z)E_\nu} \; , \end{aligned} \tag{1-45}$$

where $H(z) = H_0\sqrt{\Omega_m(1+z)^3 + \Omega_\Lambda}$ is the Hubble parameter, written in terms of the Hubble constant $H_0 \simeq 67.7\ \mathrm{km\,s^{-1}\,Mpc^{-1}}$ and the dimensionless density parameters $\Omega_m \simeq 0.308$ and $\Omega_\Lambda \simeq 0.691$. Note that we have also generalized to allow for redshift dependent emission spectra. By using the definition of the energy generation rate (1-39), we can also write

$$\begin{aligned} E_\nu^2 \Phi_\nu^{\mathrm{diff}}(E_\nu) &= \frac{1}{4\pi}\int_0^\infty \frac{\mathrm{d}z}{(1+z)^2\, H(z)} \left[\varepsilon_\nu Q_{\varepsilon_\nu}(\varepsilon_\nu, z)\right]\Big|_{\varepsilon_\nu=(1+z)E_\nu} \\ &= \frac{\xi_z(E_\nu)}{4\pi H_0}\, E_\nu Q_{E_\nu}(E_\nu, z=0) \\ &\approx \frac{\xi_z(E_\nu)}{4\pi H_0}\, \frac{3K_\pi}{4(1+K_\pi)}\, \min[1, f_{pp/p\gamma}]\, E_p Q_{E_p}(E_p, z=0) \; , \end{aligned} \tag{1-46}$$

[29] The comoving volume is $\mathcal{V}_c = 4\pi d_c^3/3$, with a Jacobian conversion to redshift given by

$$\left|\frac{\mathrm{d}\mathcal{V}_c}{\mathrm{d}z}\right| = 4\pi d_c^2 \left|\frac{\mathrm{d}\,d_c}{\mathrm{d}z}\right| = \frac{4\pi d_c^2}{H(z)} \; .$$

where in the last step we made use of Eq. (1-42) at redshift zero, and encoded the redshift evolution of the neutrino energy density generation in the factor

$$\xi_z(E_\nu) = \int_0^\infty \frac{\mathrm{d}z}{(1+z)^2} \frac{H_0}{H(z)} \frac{\left[\varepsilon_\nu Q_{\varepsilon_\nu}(\varepsilon_\nu, z)\right]\Big|_{\varepsilon_\nu=(1+z)E_\nu}}{E_\nu Q_{E_\nu}(E_\nu, z=0)} \ , \tag{1-47}$$

typically of order unity. In the case of γ rays, the situation is more subtle. As we mentioned earlier, high-energy γ rays degrade their energy through EM cascades as they travel across space. We refer the reader to (266) for the details of how to address this case.

One final, yet important, note: Eq. (1-37) is a conservative estimate of the γ-ray yield given a neutrino emission spectrum. It neglects γ rays coming from any leptonic interaction that might be taking place within the source. This includes the electrons/positrons from muon decay, which could be converted into photons via ICS. Therefore, Eq. (1-37) predicts the smallest possible γ-ray flux at the Earth associated to our observation of astrophysical neutrinos, assuming their sources are transparent (allow γ rays to escape). In Chapter 3, we will adopt this *minimal assumption* in order to obtain conservative constraints on the nature of the astrophysical neutrino sources.

1.3.3
The Waxman-Bahcall Bound

One of the landmark connections between UHECRs and neutrinos was established when Waxman and Bahcall inferred a model-independent, calorimetric, upper limit on the astrophysical neutrino flux from the observed UHECR flux (267). This bound was established through the following argument: assuming a pure proton composition of UHECRs, the measured UHECR flux can be interpreted by a local ($z \ll 1$) population of sources with injection spectrum $\mathrm{d}N_p/\mathrm{d}E_p \propto E_p^{-2}$, as expected by diffusive shock acceleration, and energy density generation rate (268)

$$E_p Q_{E_p}(E_p, z=0) \sim 10^{44}\,\mathrm{erg\,Mpc^{-3}\,yr^{-1}} \ . \tag{1-48}$$

High redshift UHECR sources would not impact significantly our observations since photopion production (1-4) makes the energy loss time of protons much smaller than the Hubble time $t_H = H_0^{-1}$. In the most optimistic scenario for neutrino production, Eq. (1-46) must be evaluated with maximum efficiency $f_{pp/p\gamma} \geq 1$. Taking $\xi_z \approx 1$ and $K_\pi = 1$ ($p\gamma$ scenario), we obtain as an upper bound for the all-flavor measured neutrino flux at

$$E_\nu^2 \Phi_\nu(E_\nu)^{\mathrm{WB}} \lesssim 10^{-8}\ [\mathrm{GeV\,cm^{-2}\,s^{-1}\,sr^{-1}}] \ . \tag{1-49}$$

Changing $K_\pi \to 2$ (pp), assuming a strong redshift evolution ($\xi \approx 3$), accounting for CR absorption inside their sources and invoking magnetic fields may increase the bound slightly, but Eq. (1-49) is mostly robust when taken as an order-of-magnitude estimate (269). It should also acquire an energy dependence in more careful calculations taking into account the precise inelasticities, pion multiplicity ratios and spectral shapes. Furthermore, accounting for the heavier composition measured by PAO and TA could result in a lowering of this bound by an order of magnitude (270).

At is so happens, the flux measured by IceCube is just about saturating the Waxman-Bahcall bound (see Figure 1.7). If this UHECR-neutrino multi-messenger picture is true, this would indicate high pion production efficiencies $f_{pp/p\gamma}$ at their sources.

1.4

The Flavor Content of Astrophysical Neutrinos

It is of tremendous phenomenological importance to consider the flavor composition of astrophysical neutrinos. Both pp and $p\gamma$ scenarios predict a $(\nu_e : \nu_\mu : \nu_\tau) \approx (1 : 2 : 0)$ flavor ratio at creation, if we consider both neutrinos and antineutrinos together. Since IceCube is mostly insensitive to their distinction, as we shall see in Section 3.3.1, this is a useful estimation to keep in mind. The exception to this is the Glashow resonance (271) signature at around $E_\nu \approx 6.3$ PeV, corresponding to resonant $\bar{\nu}_e$ scattering with atomic electrons at the W^- pole, $\bar{\nu}_e + e^- \to W^- \to$ hadrons. So far, IceCube has only claimed the detection of a single Glashow resonance event (272).

Electron antineutrinos come from μ^- decays, which themselves come from π^- decays. Negative pions are produced in both pp from $p\gamma$ scenarios at the multi-pion-dominated regime. However, due to the muon's relatively long lifetime (2.2 μs, compared to 26 ns for $\pi^\pm$ and the 81 as (attoseconds) for π^0 (273)), they can lose their energy before decaying by synchrotron radiation or multiple scattering in the strongly magnetized and/or dense astrophysical medium. If this *muon damping* process is dominant, the neutrino flavor ratio changes to $(0 : 1 : 0)$, and no electron (anti)neutrinos are produced. A pronounced signal around the Glashow resonance would rule out this scenario.

It is important to note that these reported flavor ratios are only valid at their sources. As neutrinos propagate, their flavor content changes. Specifically, when traversing cosmological distances en route to the Earth, their mass eigenstate wave packets lose coherence, and they interact with out detectors as incoherent superpositions of mass eigenstates. This effect is described in the following section, where we briefly introduce neutrino oscillations in vacuum.

1.4.1
Neutrino Oscillations in Vacuum

We can understand the phenomenon of neutrino oscillations using a quantum mechanical approach in which neutrinos interact as flavor eigenstates $|\nu_\alpha\rangle$, $\alpha = e, \mu, \tau$ (within the Standard Model framework, these are the fields appearing in the electroweak Lagrangian), and propagate as mass eigenstates $|\nu_i\rangle$, $i = 1, 2, 3$, with masses m_i. These bases are related by the Pontecorvo–Maki–Nakagawa–Sakata (PMNS) unitary transformation matrix,

$$|\nu_\alpha\rangle = U^*_{\alpha i}\,|\nu_i\rangle\ , \qquad U_{\text{PMNS}} = \begin{pmatrix} U_{e1} & U_{e2} & U_{e3} \\ U_{\mu 1} & U_{\mu 2} & U_{\mu 3} \\ U_{\tau 1} & U_{\tau 2} & U_{\tau 3} \end{pmatrix}\ . \tag{1-50}$$

For antineutrinos, one should exchange $U^*_{\alpha i} \to U_{\alpha i}$.

As a 3×3 unitary matrix, U_{PMNS} should in principle have 9 real degrees of freedom. However, we can reduce this number to 4 (if neutrinos have Dirac mass) or 6 (if neutrinos have Majorana mass) by rephasings of the neutrino eigenstates. Since neutrino oscillations are insensitive to the additional two Majorana parameters (274), we neglect them in our discussion. The most common parametrization of U_{PMNS} is in terms of 3 mixing angles θ_{ij} and 1 CP-violating phase δ as

$$U_{\text{PMNS}} = \begin{pmatrix} c_{12}c_{13} & s_{12}c_{13} & s_{13}e^{-i\delta} \\ -s_{12}c_{23} - c_{12}s_{13}s_{23}e^{i\delta} & c_{12}c_{23} - s_{12}s_{13}s_{23}e^{i\delta} & c_{13}s_{23} \\ s_{12}s_{23} - c_{12}s_{13}c_{23}e^{i\delta} & -c_{12}s_{23} - s_{12}s_{13}c_{23}e^{i\delta} & c_{13}c_{23} \end{pmatrix}\ . \tag{1-51}$$

where $c_{ij}(s_{ij})$ is short-hand for $\cos\theta_{ij}(\sin\theta_{ij})$. Because neutrinos are difficult to detect, the PMNS entries $U_{\alpha i}$ are much harder to determine than those from its quark equivalent, the CKM matrix. State-of-the-art global fit results at the time of writing this thesis are displayed in Table 1.1 (275).

Different mass eigenstates propagate with different velocities, causing their superposition to be potentially different at the points of creation and detection of a neutrino, separated by a distance L. This leads to an oscillating probability of observing the neutrino as a specific flavor eigenstate as a function of L. Namely, the probability of measuring flavor $|\nu_\beta\rangle$ after a neutrino of initial flavor $|\nu_\alpha\rangle$ and energy E has travelled a distance L is given by

$$\begin{aligned} P_{\nu_\alpha \to \nu_\beta}(L, E) &= |\langle \nu_\beta | \nu_\alpha(L) \rangle|^2 \\ &= \delta_{\alpha\beta} - 4\sum_{i>j} \text{Re}(U^*_{\alpha i}U_{\beta i}U_{\alpha j}U^*_{\beta j})\ \sin^2\left(\frac{\Delta m^2_{ij}L}{4E}\right) \\ &\quad + 2\sum_{i>j} \text{Im}(U^*_{\alpha i}U_{\beta i}U_{\alpha j}U^*_{\beta j})\ \sin\left(\frac{\Delta m^2_{ij}L}{2E}\right)\ . \end{aligned} \tag{1-52}$$

Table 1.1: Best-fit parameter values for the PMNS matrix following the parametrization in Eq. (1-51). The fit assumes either normal ordering (NO; $m_3 > m_1$) or inverted ordering (IO; $m_3 < m_1$) for the neutrino masses and includes data from solar, reactor, accelerator and atmospheric (including Super-Kamiokande and IceCube DeepCore) neutrino experiments (275).

	NO (best-fit $\pm 1\sigma$)	**IO (best-fit $\pm 1\sigma$)**
$\theta_{12}/°$	34.3 ± 1.0	34.3 ± 1.0
$\theta_{13}/°$	$8.53^{+0.13}_{-0.12}$	$8.58^{+0.12}_{-0.14}$
$\theta_{23}/°$	49.26 ± 0.79	$49.46^{+0.60}_{-0.97}$
$\delta/°$	194^{+24}_{-22}	284^{+26}_{-28}
$\Delta m^2_{21}/10^{-5}$ [eV^2]	$7.50^{+0.22}_{-0.20}$	$7.50^{+0.22}_{-0.20}$
$\Delta m^2_{31}/10^{-3}$ [eV^2]	$2.55^{+0.02}_{-0.03}$	$-2.45^{+0.02}_{-0.03}$

The derivation of Eq. (1-52) can be obtained in many different ways, and can be found extensively in the literature through all sorts of approximate schemes or detailed wave packet formulations (276, 74). For convenience, we will not derive it here.

Notice how the oscillation probabilities depend on the ratio L/E and the mass-squared differences $\Delta m^2_{ij} = m^2_i - m^2_j$. Since there are 3 masses, there are only 2 independent mass-squared differences, chosen by convention to be Δm^2_{21} and Δm^2_{31}. They are dubbed the "solar" and "atmospheric" mass splitting, respectively, reflecting the origins of the observational evidence for these mass differences. Experimentally, it is quite difficult to determine the sign of these quantities, since only the second term in Eq. (1-52) is sensitive to its absolute value, and it is quite small[30]. So far, we have been able to determine the solar mass splitting sign $\Delta m^2_{21} > 0$ with the help of matter-induced flavor conversions inside the Sun, but the sign of Δm^2_{31} remains unknown. This gives rise to two possible *mass orderings* (sometimes called mass hierarchies): normal ordering (NO; $m_3 > m_2 > m_1$) and inverted ordering (IO; $m_2 > m_1 > m_3$). Table 1.1 displays global fits for both cases, including the mass-squared differences.

Neutrino oscillations are produced by the interference of different mass eigenstates during propagation. Therefore, this phenomenon relies entirely on the assumption that the wave packets corresponding to different mass eigenstates maintain coherence throughout their trajectories. However, these wave packets have slightly different group velocities from each other, causing them

---

[30] For example, for atmospheric $P_{\nu_\mu \to \nu_e}$ conversion, we have $\mathrm{Im}(U^*_{\mu 3} U_{e3} U_{\mu 1} U^*_{e1}) \propto s_{13}$, which is very small (see Table 1.1).

Table 1.2: Expected flavor ratios at astrophysical neutrino sources from different production mechanisms, and their corresponding compositions at the Earth after decoherence. Both neutrinos and antineutrinos are included. Ratios at the Earth are normalized such that they add up to 1.

Production Mechanism	$(\nu_e : \nu_\mu : \nu_\tau)_S$	$(\nu_e : \nu_\mu : \nu_\tau)_\oplus$
$pp/p\gamma$	$(1:2:0)$	$(0.30:0.36:0.34)$
Muon damped $pp/p\gamma$	$(0:1:0)$	$(0.18:0.45:0.37)$
Neutron decay	$(1:0:0)$	$(0.54:0.18:0.28)$
Muon pair production	$(1:1:0)$	$(0.36:0.31:0.33)$

to eventually separate as neutrinos travel along cosmological distances (74). In case of decoherence, flavor conversions can still occur (without oscillations) simply because the PMNS matrix is not diagonal. This transition probability can be easily calculated via the incoherent sum

$$P^{\text{incoherent}}_{\nu_\alpha \to \nu_\beta} = \sum_i \left| \langle \nu_\beta | \nu_i \rangle \, e^{iE_i t} \, \langle \nu_i | \nu_\alpha \rangle \right| = \sum_i |U_{\alpha i}|^2 \, |U_{\beta i}|^2 \; . \tag{1-53}$$

Note that this remains the same under $U_{\text{PMNS}} \to U^*_{\text{PMNS}}$, and thus works for both neutrinos and antineutrinos.

This is precisely what happens to astrophysical neutrinos. If we know their initial flavor content at the source, $(\nu_e : \nu_\mu : \nu_\tau)_S$, Eq. (1-53) straightforwardly gives us the corresponding flavor ratios at the Earth $(\nu_e : \nu_\mu : \nu_\tau)_\oplus$. For the conventional $pp/p\gamma$ scenarios without muon damping, we find that

$$(1:2:0)_S \xrightarrow{\approx} (1:1:1)_\oplus \; . \tag{1-54}$$

Table 1.2 shows the flavor ratios at the source and their corresponding ratios at the Earth for some notable neutrino production scenarios. Besides the already discussed $pp/p\gamma$ with and without muon damping, we include the cases in which neutrinos come from neutron decay (which produces only $\bar{\nu}_e$) and only from muon decay. This last case may be relevant if astrophysical neutrino sources are purely leptonic, with MPP responsible for their production, which shall be considered in Section 2.4. At the moment of writing this thesis, IceCube data strongly disfavors the neutron decay scenario, but is incapable of distinguishing between the other scenarios (277).

1.4.2
Matter Effects and the MSW Resonance

In the presence of dense matter, neutrinos can interact with their medium via CC and NC interactions. While NC interactions are the same for all flavors, the presence of copious electrons (and no muons or taus) in regular matter leads to an asymmetry with respect to ν_e and ν_x ($x = \mu, \tau$) due to CC interactions. This leads to a phase difference acquired by $|\nu_e\rangle$ with respect to $|\nu_x\rangle$ that cannot be removed by field rephasings, ultimately resulting in the Hamiltonian (74)

$$\mathcal{H}_\nu = \frac{1}{2E} U \begin{pmatrix} 0 & 0 & 0 \\ 0 & \Delta m^2_{21} & 0 \\ 0 & 0 & \Delta m^2_{31} \end{pmatrix} U^\dagger + \begin{pmatrix} V_e & 0 & 0 \\ 0 & 0 & 0 \\ 0 & 0 & 0 \end{pmatrix} . \tag{1-55}$$

in the flavor basis, where U is the PMNS matrix and $V_e = \sqrt{2}\, G_F n_e$ is the matter potential due to the coherent forward scattering of neutrinos on electrons. It depends on the electron number density $n_e \approx \rho_m Y_e / m_N$, where ρ_m is local matter density, dominated by the contribution of nucleons of mass m_N, and Y_e is the electron number fraction in the medium.

In the Schrodinger picture, the neutrino oscillation amplitudes $\psi_{\alpha\beta}(x) = \langle \nu_\beta | \nu_\alpha(x) \rangle$, with $\alpha, \beta = e, \mu, \tau$, evolve in flavor space along the propagation distance x according to

$$i \frac{\mathrm{d}}{\mathrm{d}x} \Psi_\alpha = \mathcal{H}_\nu \Psi_\alpha \ , \tag{1-56}$$

where $\Psi_\alpha = (\psi_{\alpha e}, \psi_{\alpha\mu}, \psi_{\alpha\tau})$. In the literature, it is more common to find this written in the Heisenberg picture, where the density matrix[31] $\rho_\nu = |\nu\rangle\langle\nu|$, describing the neutrino flavor state $|\nu\rangle = \sum_\alpha c_\alpha |\nu_\alpha\rangle$, evolves according to the von Neumann equation

$$i \frac{\mathrm{d}\rho_\nu}{\mathrm{d}t} = [\mathcal{H}_\nu, \rho_\nu] \ , \tag{1-57}$$

In the case of antineutrinos, the only modification is a negative sign on the matter potential, $V_e \to -V_e$.

The diagonalization of $\mathcal{H}_\nu$ can no longer be achieved with the PMNS matrix. Instead, it requires a new unitary matrix U_M, with new mixing angles. To solve this problem, we can first consider a simpler two-flavor scenario[32] in which we have the following relation between our flavor and (vacuum) mass eigenstates:

---

[31] Recall that, for pure states $\rho = |\psi\rangle\langle\psi|$, the diagonal elements of the density matrix ρ correspond to the probabilities of measuring each of the basis eigenstates that make up $|\psi\rangle$. Meanwhile, the off-diagonal terms, also called "coherences", correspond to the superposition of these basis states in $|\psi\rangle$.

[32] Δm^2_{21} and Δm^2_{31} differ by a factor of ~ 30. To a good approximation, we can consider a 2×2 problem if the oscillation frequency of the system is close to one of these natural frequencies determined by Δm^2_{21} or Δm^2_{31}.

$$|\nu_\alpha\rangle = U_{\alpha i}\,|\nu_i\rangle \ , \qquad U = \begin{pmatrix} U_{e1} & U_{e2} \\ U_{\mu 1} & U_{\mu 2} \end{pmatrix} = \begin{pmatrix} \cos\theta & \sin\theta \\ -\sin\theta & \cos\theta \end{pmatrix} \ , \tag{1-58}$$

where U is now a 2×2 version of the PMNS matrix, with only one mixing angle θ. Oscillations now depend on a single mass-squared difference Δm^2.

Adding the matter potential, we have, up to a global phase (74),

$$\mathcal{H}_\nu = \frac{1}{4E} \begin{pmatrix} -\Delta m^2\,\cos 2\theta + 2EV_e & \Delta m^2\,\sin 2\theta \\ \Delta m^2\,\sin 2\theta & \Delta m^2\,\cos 2\theta - 2EV_e \end{pmatrix} \ , \tag{1-59}$$

which is diagonalized by the matrix

$$U_\mathrm{M} = \begin{pmatrix} \cos\theta_\mathrm{M} & \sin\theta_\mathrm{M} \\ -\sin\theta_\mathrm{M} & \cos\theta_\mathrm{M} \end{pmatrix} \ , \tag{1-60}$$

such that

$$\mathcal{H}_{\nu,\mathrm{diag}} = U_\mathrm{M}^\mathrm{T} \mathcal{H}_\nu U_\mathrm{M} = \frac{1}{4E} \begin{pmatrix} -\Delta m^2_\mathrm{M} & 0 \\ 0 & \Delta m^2_\mathrm{M} \end{pmatrix} \ , \tag{1-61}$$

with $\Delta m^2_\mathrm{M} = m^2_{M2} - m^2_{M1} = \sqrt{(\Delta m^2 \cos 2\theta - 2EV_e)^2 + (\Delta m^2 \sin 2\theta)^2}$ being the new effective mass-squared difference. The new basis in which this Hamiltonian is diagonal is normally referred to as the *matter eigenbasis*, which we label by $|\nu_{\mathrm{M},1}\rangle$ and $|\nu_{\mathrm{M},2}\rangle$. These are related to the flavor eigenbasis by

$$|\nu_e\rangle = \cos\theta_\mathrm{M}\,|\nu_{\mathrm{M},1}\rangle + \sin\theta_\mathrm{M}\,|\nu_{\mathrm{M},2}\rangle \ , \tag{1-62}$$

$$|\nu_\mu\rangle = -\sin\theta_\mathrm{M}\,|\nu_{\mathrm{M},1}\rangle + \cos\theta_\mathrm{M}\,|\nu_{\mathrm{M},2}\rangle \ . \tag{1-63}$$

The following useful relations can also be easily obtained:

$$\cos 2\theta_\mathrm{M} = \frac{\Delta m^2 \cos 2\theta - 2EV_e}{\Delta m^2_\mathrm{M}} \ , \qquad \sin 2\theta_\mathrm{M} = \frac{\Delta m^2 \sin 2\theta}{\Delta m^2_\mathrm{M}} \ . \tag{1-64}$$

Equipped with them, we can analyze what happens at high matter densities (large V_e) and at low matter densities (small V_e). At high matter densities,

$$\Delta m^2_\mathrm{M} \approx 2EV_e \ , \qquad \cos 2\theta_\mathrm{M} \approx -1 \ , \qquad \theta_\mathrm{M} \approx \frac{\pi}{2} \ , \tag{1-65}$$

$$|\nu_e\rangle \approx |\nu_{\mathrm{M},2}\rangle \ , \qquad |\nu_\mu\rangle \approx |\nu_{\mathrm{M},1}\rangle \ , \tag{1-66}$$

whereas at low matter densities we recover the expected vacuum solution,

$$\Delta m^2_\mathrm{M} \approx \Delta m^2 \ , \qquad \cos 2\theta_\mathrm{M} \approx \cos 2\theta \ , \qquad \theta_\mathrm{M} \approx \theta \ , \tag{1-67}$$

$$|\nu_1\rangle \approx |\nu_{\mathrm{M},1}\rangle \ , \qquad |\nu_2\rangle \approx |\nu_{\mathrm{M},2}\rangle \ . \tag{1-68}$$

However, something very interesting happens in the crossing between these two regimes.

When the density reaches the value

$$n_e^{\mathrm{res}} = \frac{\Delta m^2 \cos 2\theta}{2\sqrt{2} E G_F} \ , \tag{1-69}$$

a resonance occurs at

$$2EV_e = \Delta m^2 \cos 2\theta \quad \Rightarrow \quad \cos 2\theta_{\mathrm{M}} = 0 \quad \Rightarrow \quad \theta_{\mathrm{M}} = \frac{\pi}{4} \ , \tag{1-70}$$

where the matter mixing angle becomes very sensitive to density variations, *i.e.*

$$\frac{\mathrm{d}\theta_{\mathrm{M}}}{\mathrm{d}x} = \frac{\sqrt{2} G_F E \sin 2\theta_{\mathrm{M}}}{\Delta m_{\mathrm{M}}^2} \frac{\mathrm{d}n}{\mathrm{d}x} \quad \xrightarrow{\mathrm{res}} \quad \frac{\sqrt{2} G_F E}{\Delta m^2 \sin 2\theta} \frac{\mathrm{d}n}{\mathrm{d}x} \tag{1-71}$$

is maximized, and $\mathcal{H}_\nu$ in Eq. (1-59) becomes completely off-diagonal. We call this a resonance because the maximal mixing ($\theta_{\mathrm{M}} = \pi/4$) between the flavor and matter bases allows for a transition (not oscillation!) from $|\nu_{\mathrm{M},1}\rangle$ to $|\nu_{\mathrm{M},2}\rangle$ during propagation, leading to a conversion in the neutrino flavor. This is called the *MSW effect*, named after Mikheyev, Smirnov and Wolfenstein who contributed to our understanding of this phenomenon (84, 85, 278, 279).

The transition between matter eigenstates can be interpreted as a jump between the different m_{Mi}^2 eigenvalues, which has an enhanced probability at resonance where Δm_{M}^2 has a minimum. The occurrence or not of such a transition depends if the resonance region is wide or narrow. Carefully solving the two-flavor version of the Schrodinger Eq. (1-56) for a varying $n_e(x)$, we find that an efficient conversion from $|\nu_{\mathrm{M},1}\rangle$ to $|\nu_{\mathrm{M},2}\rangle$ happens when the adiabaticity parameter (74)

$$\gamma = \frac{\Delta m_{\mathrm{M}}^2}{4E|\mathrm{d}\theta_{\mathrm{M}}/\mathrm{d}x|} \quad \xrightarrow{\mathrm{res}} \quad \frac{\Delta m^2 \sin^2 2\theta}{2E \cos 2\theta |\mathrm{d} \ln n_e/\mathrm{d}x|_{\mathrm{res}}} \tag{1-72}$$

is large (> 1) at resonance. This is the so-called non-adiabatic regime, in which $\nu_{\mathrm{M},1} \longleftrightarrow \nu_{\mathrm{M},2}$ can take place. If $\gamma < 1$, we have the adiabatic regime where no switching happens.

The adiabatic regime can still lead to flavor changes after the resonance. Take for example an neutrino initially produced as a ν_e in a high-density region inside an astrophysical source. At such high densities, we can consider $\nu_e \approx \nu_{\mathrm{M},2}$, which stays as a $\nu_{\mathrm{M},2}$ while crossing the resonance region adiabatically. After the electron density becomes small, this outgoing $\nu_{\mathrm{M},2}$ becomes a ν_2 (in vacuum). In the case of a small vacuum mixing angle θ, this ν_2 would coincide with a ν_μ, completely changing the flavor of the initial neutrino! This is indeed what happens at the Sun, leading to the correct ν_e disappearance necessary to resolve the famous solar neutrino problem.

The three-flavor scenario, which we will explore in more detail in Chapter 4, is analogous. This time, there are two possible resonances, corresponding to the two different effective mass-squared differences in matter, which produce $\nu_e \leftrightarrow \nu_x$, $x = \mu, \tau$ transitions. Meanwhile, the ν_μ and ν_τ interact equally with matter[33] (only via NC), and their evolution within the ν_x sector can be regarded as analogous to the vacuum case.

---

[33] Differences arise at loop level and are negligible at densities below 10^7 g/cm^3 (280).

2
The Physics of Electromagnetic Cascades

In this chapter, we shall study the propagation of high-energy γ rays through intergalactic space. In particular, we will focus on the physical processes affecting $\gtrsim$ TeV γ rays as they travel cosmological distances towards us. As mentioned in Section 1.1.1, the presence of ubiquitous photon fields makes the Universe opaque to these messengers, leading to the formation of EM cascades. These cascades are responsible for degrading the energy of the initial γ rays down to sub-TeV energies.

Our first goal will be to describe these photon backgrounds, which are key to understanding the different cascade regimes. Then, we will outline the formalism for calculating the fluxes resulting from EM cascades. Employing this formalism will require a previous comprehension of the main physical processes involved in EM cascades: EPP and ICS. Once that is done, we shall present one of the main results of this thesis: a complete rework of the semi-analytical code "*γ-Cascade*", designed to calculate cascaded fluxes from point-like and diffuse distributions of γ-ray sources. Along with a description of the code's inner workings, a summary of improvements with regards to the previous version of γ-Cascade will be given. Finally, we will discuss another important outcome of this thesis regarding the relevance of MPP in EM cascades at high energies and redshifts. This process would result in a flux of UHE neutrinos at the Earth, which we estimate through a Monte Carlo method.

2.1
Cosmic Voids are not Empty

This section is dedicated to introducing the main photon backgrounds permeating our Universe that affect the evolution of cosmological EM cascades. These include the CMB, the EBL, and the CRB, shown in Figure 2.1, as well as weak, yet important, magnetic fields. Traditionally, only the CMB and the EBL have been considered as important target fields for EPP and ICS, although the CRB does become important at UHEs, we shall see in Section 2.2.4. Meanwhile, magnetic fields could play an important role in deflecting cascade electrons and positrons, although very little is currently known about them.

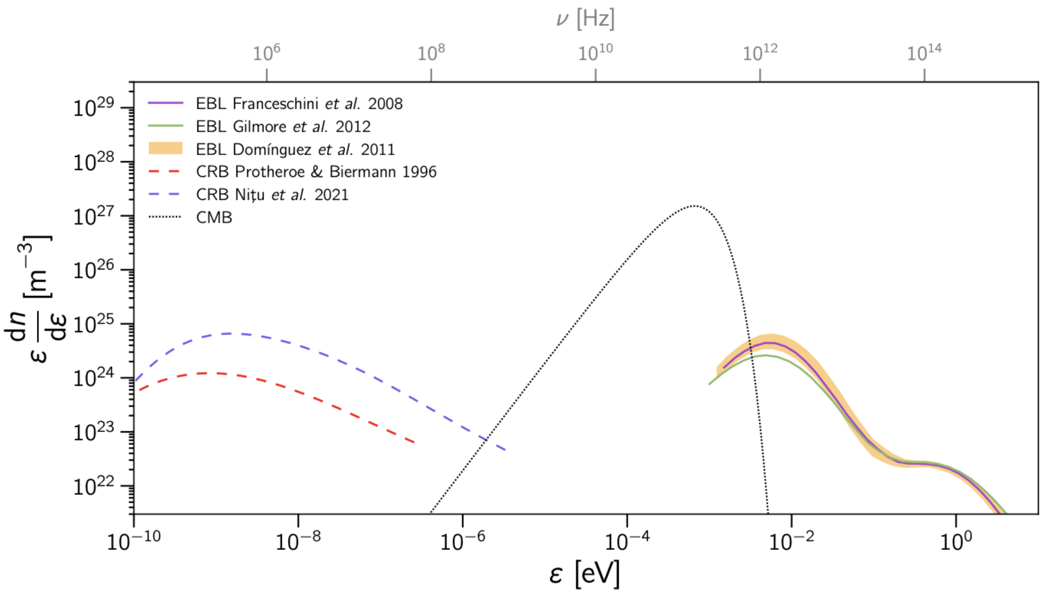

Figure 2.1: Differential density of the relevant photon backgrounds for EM cascades. Figure reproduced from (281). For references to the specific EBL and CRB models shown, see original reference.

2.1.1
Cosmic Microwave Background

The CMB consists of a nearly isotropic[1], blackbody-like background of relic photons from the epoch of recombination. Approximately 370,000 years after the Big Bang ($z \approx 1100$), the Universe became cool enough (~ 3000 K) for electrons to pair with protons, forming the first Hydrogen atoms. Suddenly, photons who used to scatter off of free electrons became decoupled from matter and free to travel through space as they did not interact with neutral atoms. These are the photons which are currently observed as the CMB with a (monopole) temperature of (283)

$$T_{\mathrm{cmb},0} = 2.72548 \pm 0.00057 \text{ K} \simeq 0.235 \text{ meV} . \tag{2-1}$$

After its accidental discovery by A. Penzias and R. Wilson (284), the CMB has been studied in great detail, with the latest data acquisition and analysis having been done by the Planck Collaboration (285). It is not pertinent for this thesis to delve into CMB details (we will certainly not be concerned with temperature or polarization anisotropies); it suffices for us to know the energy and number density distributions of CMB photons. Its local energy spectrum is that of a blackbody, given by the energy-differential density $n_E(T_{\mathrm{cmb},0}) \equiv \frac{\mathrm{d}n_{\mathrm{cmb}}}{\mathrm{d}\epsilon}(\epsilon, z = 0)$ in Eq. (1-1). From it, we can obtain the total CMB number and energy densities,

---

[1] Temperature variations are roughly of the order $\Delta T/T \sim 10^{-5}$ (282).

$$n_{\mathrm{cmb},0} = \int_0^\infty \mathrm{d}\epsilon \, \frac{\mathrm{d}n_{\mathrm{cmb}}}{\mathrm{d}\epsilon}(\epsilon, z=0) \simeq 410 \ \mathrm{cm}^{-3} \ , \tag{2-2}$$

$$u_{\mathrm{cmb},0} = \int_0^\infty \mathrm{d}\epsilon \, \epsilon \, \frac{\mathrm{d}n_{\mathrm{cmb}}}{\mathrm{d}\epsilon}(\epsilon, z=0) \simeq 0.26 \ \mathrm{eV\,cm}^{-3} \ , \tag{2-3}$$

respectively, as well as the mean and peak CMB photon energies,

$$\langle \epsilon \rangle_{\mathrm{cmb},0} \simeq 2.7\, T_{\mathrm{cmb},0} \simeq 0.634 \ \mathrm{meV} \ , \tag{2-4}$$

$$\epsilon^{\mathrm{peak}}_{\mathrm{cmb},0} \simeq 2.82\, T_{\mathrm{cmb},0} \simeq 0.663 \ \mathrm{meV} \ . \tag{2-5}$$

The redshift evolution of these quantities can also be easily obtained from dimensional considerations. In the CMB proper frame, we have

$$\frac{\mathrm{d}n_{\mathrm{cmb}}}{\mathrm{d}\epsilon}(\epsilon, z) = (1+z)^2 \, \frac{\mathrm{d}n_{\mathrm{cmb}}}{\mathrm{d}\epsilon}\Big(\epsilon/(1+z), z=0\Big) \ , \tag{2-6}$$

which correctly accounts for its temperature scaling,

$$T_{\mathrm{cmb}}(z) = (1+z)\, T_{\mathrm{cmb},0} \ , \tag{2-7}$$

and reproduces the expected energy $(1+z)$ and density $(1+z)^3$ scalings.

2.1.2
Extragalactic Background Light

Following the CMB, the EBL is the next most energy-dense photon background in the Universe, defined roughly between 0.1–1000 μm wavelengths. It consists of direct and reprocessed radiation from billions of years of stellar and galaxy evolution processes, which means that it is only present at low to moderate redshifts ($z \lesssim 5$), after galaxy formation took place. What we detect as the EBL today is the result of the accumulated production, redshifting and dilution of this radiation along cosmic history (286).

Figure 2.2 displays the EBL energy distribution at $z = 0$ in terms of the intensity λI_λ [nW m^{-2} sr^{-1}] described in Section 1.1.1. Unlike relic photons, the EBL does not possess a simple blackbody spectrum. In fact, its local energy distribution is closely approximated by three blackbody curves: two large peaks around $\lambda \sim 1$ μm and $\lambda \sim 100$ μm (representing the COB and CIB, respectively), and a smaller peak around $\lambda \sim 10$ μm. Direct emission from thermonuclear fusion reactions in stars is the main contributor to the EBL from UV to near-IR wavelengths, with more massive and younger stars dominating the UV band, while older and cooler stars emit predominantly in the IR. A second (and sometimes neglected) direct contribution to the EBL comes from the accretion of matter around and into AGNi (287), which is expected to contribute no more than 10% of the total intensity across all

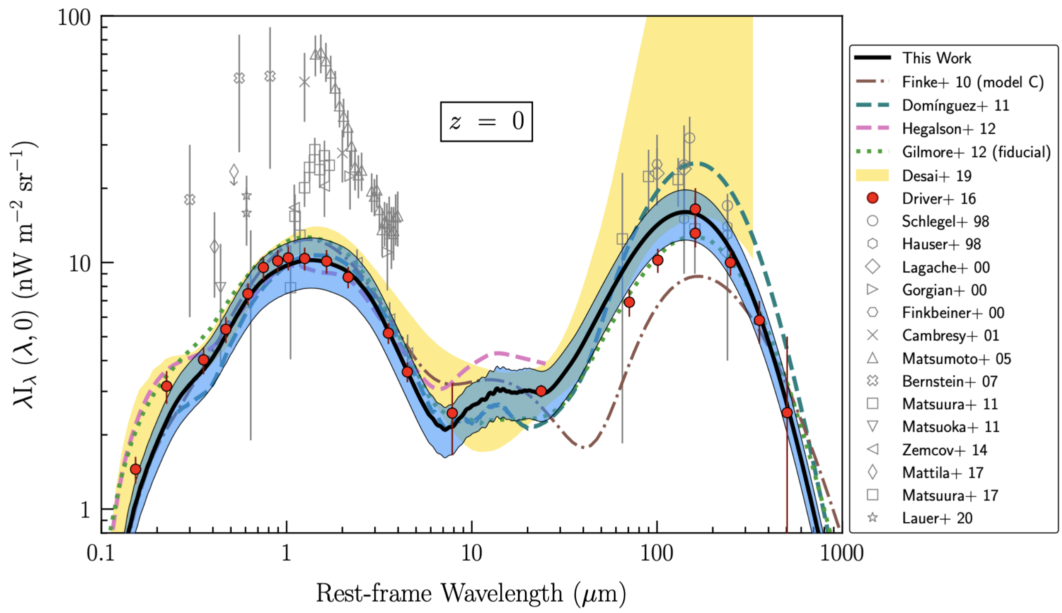

Figure 2.2: Local ($z = 0$) EBL spectral energy distribution, including popular semi-analytical models from the literature (all curves), indirect measurements (yellow shaded region), and direct measurements (points). Figure from (289), where the reader is referred to the original references of the models and data displayed.

wavelengths (288). In both cases, around half of the photons are expected to be reprocessed by dust in their host galaxies, leading to a significant secondary contribution to the EBL at lower energies. This reprocessing occurs through the excitation of vibrational and rotational modes of molecules and ions in the ISM which, once heated, radiate in the far-IR region.

Due to its continuous emission, the redshift evolution of the EBL spectrum is not trivial, as can be seen in Figure 2.3. Its comoving intensity, $\lambda I_\lambda(\lambda, z)$, is shown as a function of the rest-frame[2] wavelength λ at a given redshift z. Admittedly, this is a rather confusing way of reporting results, since λI_λ is in the comoving frame while λ itself is not. In order to calculate relevant quantities for EM cascades, we would like to have the EBL expressed in its proper frame at each redshift, rather than its comoving counterpart. From dimensional analysis, we transform the "power per unit area" in λI_λ from the comoving to the proper frame by multiplying it by $(1+z)^4$. However, we should take into account that λ (or, equivalently, the energy) is already in the correct frame, so we must drop one of the $(1 + z)$ factors and we are left with

$$\lambda I_\lambda|_{\text{proper}} = (1+z)^3 \lambda I_\lambda|_{\text{comoving}} \ . \tag{2-8}$$

---

[2] This is the frame of an observer at rest with respect to the source of radiation. A more careful definition of the spectral radiance I_λ than the one given in Section 1.1.1 is required: I_λ is the *comoving* power received per unit solid angle per unit *rest-frame* wavelength crossing a unit *comoving* projected area.

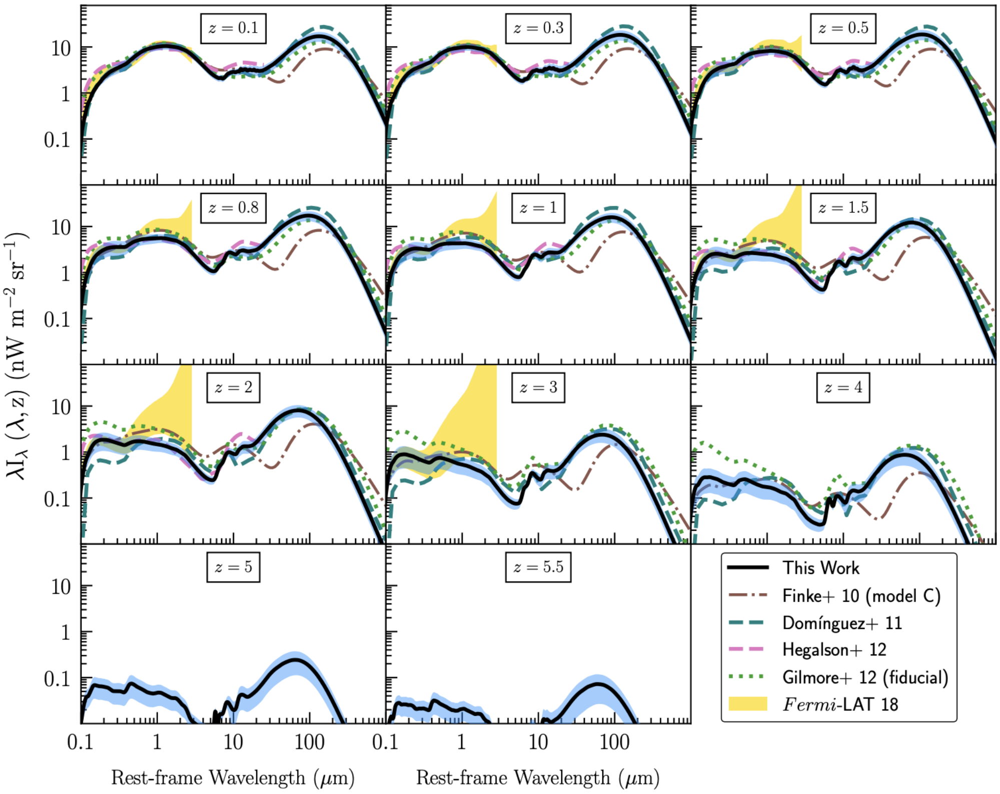

Figure 2.3: EBL redshift evolution according to several models (all curves) and indirect measurements (yellow shaded region). Figure from (289).

To go from λI_λ to the EBL's proper-frame differential energy density $\epsilon^2 \frac{\mathrm{d}n_{\mathrm{ebl}}}{\mathrm{d}\epsilon}$, we simply multiply by $4\pi/c$,

$$\epsilon^2 \frac{\mathrm{d}n_{\mathrm{ebl}}}{\mathrm{d}\epsilon}(\epsilon, z) = \frac{4\pi}{c}\, \lambda I_\lambda(hc/\epsilon, z)|_{\mathrm{proper}}\ . \tag{2-9}$$

There are numerous ways to obtain the EBL, both directly and indirectly. The most common methods found in the literature are outlined below:

- Direct measurement, capturing all the photon flux in the relevant energy range averaged over the sky. These types of measurements have strong contamination from atmospheric emission, zodiacal light (sunlight scattered by interplanetary dust), diffuse galactic light, and scattered starlight from other nearby bright stars, making them quite challenging (290). This is the reason for the large error bars and inconsistencies among data points in Figure 2.2. Another downside of this method is that it can only ever give us the EBL at $z = 0$. For EM cascade simulations starting at high redshfits, we need to account for the EBL evolution, and thus we must rely on extrapolations based on alternative methods.
- Indirect modeling using multiwavelength data from deep galaxy surveys. This requires stacking the luminosities of all galaxies at different redshifts

to obtain a total comoving luminosity density as a function of redshift, $j_\nu(\lambda', z')$ [erg s^{-1} Mpc^{-3} Hz^{-1}], *i.e.* the comoving power emitted per unit comoving volume per unit rest-frame frequency, as a function of the rest-frame wavelength λ'. From there, one can obtain the comoving intensity $\lambda I_\lambda(\lambda, z)$ as a function of the new rest-frame wavelength λ at redshift z by integrating over the redshifted contributions from all earlier emissions along the light travel path (that is, coming from shorter rest-frame wavelengths $\lambda' = \lambda\frac{1+z}{1+z'})$[3],

$$\lambda I_\lambda(\lambda, z)|_{\text{comoving}} = \frac{c}{4\pi}\int_z^\infty \lambda j_\lambda(\lambda', z')\,\frac{\mathrm{d}z'}{(1+z')H(z')} \tag{2-10}$$

$$= \frac{c^2}{4\pi\lambda}\int_z^\infty j_\nu\Big(\lambda\,\frac{1+z}{1+z'}, z'\Big)\left|\frac{\mathrm{d}t}{\mathrm{d}z'}\right|\mathrm{d}z'\ , \tag{2-11}$$

where we recall that $\lambda j_\lambda = \nu j_\nu = c j_\nu/\lambda$. The more convenient proper-frame intensity requires some additional factors of $(1+z)$ to account for (i) the redshifting of λ from the different rest-frames at z and z', (ii) the unit frequency interval in the definition of j_ν from the rest-frame to the comoving frame at each z' and (iii) the integrated comoving luminosity density itself from the comoving to the proper frame at z,

$$\lambda I_\lambda(\lambda, z)|_{\text{proper}} = (1+z)^4\,\frac{c}{4\pi}\int_z^\infty \frac{c}{\lambda\frac{1+z}{1+z'}}\,\frac{j_\nu\Big(\lambda\,\frac{1+z}{1+z'}, z'\Big)}{1+z'}\left|\frac{\mathrm{d}t}{\mathrm{d}z'}\right|\mathrm{d}z'\ . \tag{2-12}$$

Note that we recover Eq. (2-8), as expected from our previous heuristic argument.

- Indirect estimation from the absorption imprint the EBL leaves in the spectra of γ-ray sources. As we shall see in Section 2.2.1, γ rays with $E_\gamma \lesssim (1+z)\,100$ TeV undergo EPP predominantly with EBL photons, causing an attenuation of the spectra observed in many astrophysical sources (mostly blazars, but also GRBs and other types of AGNi),

$$\frac{\mathrm{d}N_\gamma}{\mathrm{d}E_\gamma}(E_\gamma)\bigg|_{\text{attenuated}} = e^{-\tau_{\text{EPP}}(E_\gamma, z_i)}\,\frac{\mathrm{d}N_\gamma}{\mathrm{d}\varepsilon_\gamma}(\varepsilon_\gamma)\bigg|_{\text{intrinsic},\,\varepsilon_\gamma=(1+z_i)E_\gamma}\ , \tag{2-13}$$

where τ_{EPP} is the EPP optical depth given by

$$\tau_{\text{EPP}}(E_\gamma, z_i) = c\int_0^{z_i}\mathrm{d}z\left|\frac{\mathrm{d}t}{\mathrm{d}z}\right|\int_{m_e^2/E_\gamma(1+z)}^\infty \mathrm{d}\epsilon\,\frac{\mathrm{d}n(\epsilon, z)}{\mathrm{d}\epsilon}\,\langle\sigma_{\text{EPP}}\rangle(E_\gamma(1+z), \epsilon)\ , \tag{2-14}$$

---

[3] We have introduced the Jacobian $\mathrm{d}t/\mathrm{d}z = -[H(z)(1+z)]^{-1}$, which can be obtained from the definition of the Hubble parameter $H(z) = \dot{a}/a$ in terms of the FLRW scale factor $a(t)$, and the definition of cosmological redshift, $1+z = a^{-1}$.

> (see Section 2.2.1 for definitions) which is sensitive to the EBL energy-differential density $\mathrm{d}n_{\mathrm{ebl}}/\mathrm{d}\epsilon$ and the redshift z_i of the source. A clear drawback of this method is that, in order to extract the EBL, one should first model the inaccessible intrinsic spectra of the γ-ray source by extrapolating their GeV spectra to the multi-TeV range (*e.g.* see Figure 5 in (291)). These are typically taken to be simple smooth functions which fall off at higher energies. Finally, the redshift evolution of the EBL can be reconstructed by considering sources located at different redshifts.

At last, let us comment briefly on an intriguing and ongoing discussion that currently exists within the "EBL community". In Figure 2.2, it is clear that direct measurements usually find a COB at least twice as bright as that obtained via indirect methods, which in turn all agree with each other. This agreement has led to a preference towards indirectly-obtained EBL models, with the usual explanation being that direct measurements are underestimating their foregrounds. However, recent measurements (292, 293) taken by the New Horizons spacecraft, now over 50 AU away from the Sun and free from any atmospheric and zodiacal light contamination, challenges this interpretation. These papers also offer explanations in favor of their direct results as opposed to the indirect estimations. Still, we will only use EBL models coming from indirect methods simply because they are self-consistent and available at all relevant wavelengths and redshifts.

2.1.3
Cosmic Radio Background

At frequencies below the CMB, we find the CRB, a universal background of radio waves at $\lesssim$ 100 GHz frequencies. It is produced mainly by the free-free emission of thermal electrons in the ISM of SFGs and from the synchrotron radiation of high-energy electrons in SFGs and RGs (294).

Much like the EBL, the local CRB intensity can be either obtained directly or indirectly. Direct measurements are once again quite difficult, suffering from distortions/attenuation in the Earth's ionosphere, as well as the subtraction of Galactic radio foregrounds and the Raleigh-Jeans CMB tail. Meanwhile, indirect estimations are usually obtained by modeling the cumulative SFG and RG radio emissions along cosmic history, much like the EBL, also giving us some insight into the CRB's redshift evolution. However, the source counts are scarce since a large fraction of the SFG/RG populations lies below our detection thresholds. Thus, one must rely on some sort of extrapolation to reconstruct their total radio emission. Currently, our knowledge of the CRB is still quite poor, with a large discrepancy seen between direct (295) and indirect (4) methods.

The CRB is sometimes disregarded within the context of EM cascades since it only participates in EPP at UHEs ($\gtrsim 10^{19}$ eV) (296). However, in Section 2.4 we will be considering exactly this scenario, which is why we must be reminded of its existence. Fortunately, we will not require precise CRB models in our analyses. It suffices to know that EPP with the CRB becomes the dominant interaction channel for UHE γ rays propagating through the Universe.

2.1.4
Magnetic Fields

Besides the photon fields described in the previous sections, the Universe is also permeated with magnetic fields that affect the propagation of high-energy charged particles. In Section 1.1.2, we mentioned how a uniform coherent magnetic field $B = |\mathbf{B}|$ can set charges into helical motion with a projected radius given by Eq. (1-5). The acceleration induced by this curved motion on a charge q with mass m and pitch angle cosine μ produces synchrotron radiation, causing the particle to lose energy at a rate (in SI units) (224)

$$\frac{\mathrm{d}E}{\mathrm{d}t} = -\frac{q^4\gamma^2 B_\perp v^2}{6\pi\varepsilon_0 m^2 c^3} , \tag{2-15}$$

where $\gamma = E/mc^2$ is the particle's Lorentz factor, $B_\perp = B\sqrt{1-\mu^2}$ is the magnetic field perpendicular to the charge's momentum and ε_0 is the vacuum permittivity.

It is common in astrophysical contexts for magnetic fields to be coherent only up to some distance scale λ_B known as its coherence length. That is, magnetic fields at large scales are scrambled, pointing into random directions. In this case, an average over pitch angle yields (in SI units)

$$\left\langle \frac{\mathrm{d}E}{\mathrm{d}t} \right\rangle = -\frac{4}{3}\sigma_\mathrm{T} u_B c \left(\frac{q m_e}{e m}\right)^4 \left(\frac{p}{m_e c}\right)^2 , \tag{2-16}$$

where $p = \gamma m v$ is the particle's 3-momentum, $\sigma_\mathrm{T} = e^4\mu_0/6\pi\varepsilon_0 m_e^2 c^2$ is the Thomson cross section, and $u_B = B^2/2\mu_0$ is the magnetic field energy density, written in terms of the vacuum permeability μ_0. Angular deflection in the case of random field orientations is also different from the coherent field case, as illustrated in Figure 2.4. Using the values defined in the figure, one can easily find a total deflection of $\sin\theta = qcB_\perp D/2E$ in the coherent case. If a charged particle propagates a distance $D \gg \lambda_B$, it will deflect in a random direction at each "coherence cell". Its total deflection can be modeled as a random walk

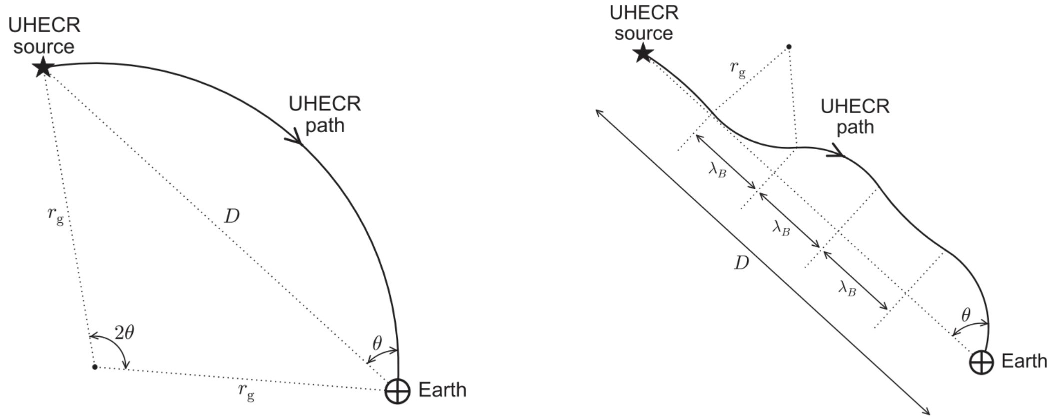

Figure 2.4: Illustration of charged particle deflection in the presence of coherent ($D < \lambda_B$, left) and incoherent ($D \gg \lambda_B$, right) magnetic fields. The latter case can be modeled as a random walk in the deflection angle θ. Figures from (297).

in θ with mean $\langle\theta\rangle = 0$ and root mean square value $\theta_{\rm rms} \approx qcB_\perp\sqrt{D\lambda_B}/2E$ (297). If there are several UHECRs coming from a single astrophysical source, their signal would appear smeared by an angle $\theta_{\rm rms}$ in the sky. Both of these cases can also lead to a significant time delay with respect to a straight-line trajectory[4].

The spectral emissivity (power radiated per differential energy band) of photons produced by synchrotron radiation of an ultra-relativistic charge is given by (224)

$$\frac{\mathrm{d}P}{\mathrm{d}E_\gamma}(E_\gamma, E) = \frac{\sqrt{3}\,q^3B_\perp}{2\pi mc^2}\frac{E_\gamma}{E_c}\int_{E_\gamma/E_c}^{\infty} \mathrm{d}x\, K_{5/3}(x)\ , \tag{2-17}$$

where $K_{5/3}$ is the modified Bessel function of second kind and the critical energy is defined as

$$E_c = \frac{3hqE^2B_\perp}{2m^3c^4}\ , \tag{2-18}$$

where h is Planck's constant. The spectrum in Eq. (2-17) peaks at around $E_\gamma \approx 0.29E_c$; this can be used as a good estimate for the energy of synchrotron radiated photons. Notably, this spectrum is linearly polarized and strongly forward-beamed in the direction of the charge's movement.

Now that we have made the importance of magnetic fields clear by their effects on astroparticle propagation and production, we should mention where do we expect to find them. The short answer is quite straightforward: magnetic fields are truly ubiquitous. They exist in the interiors of galaxies, galaxy clusters, superclusters, filaments and even in cosmic voids (299). The latter is usually what is referred in the literature as the *intergalactic magnetic field* (IGMF). They are also mysterious: there is still no consensus on how these

---

[4] In some scenarios, this delay can be so large that even steady sources could have evolved/disappeared before the signal arrives (298).

magnetic fields came to be, despite the plentiful observational evidence for their existence. An excellent review on this topic can be found in (300).

The strength and structure of magnetic fields can be inferred from their imprints on the intensity and polarization of synchrotron radiation. One of the most widely used methods exploits the Faraday rotation phenomenon. It can be shown (301) that opposite circularly polarized waves travel at different speeds in a magnetized medium. This causes a rotation in the polarization of linearly polarized waves, such as those from synchrotron emission. This change in polarization angle $\Delta\chi$ is related to the so-called "rotation measure" (RM), which depends on the magnetic field intensity along the line of sight direction $B_{\parallel} = \mathbf{B} \cdot \hat{\mathbf{n}}$ crossed by the wave:

$$\Delta\chi = \lambda^2 \times \mathrm{RM}(\hat{\mathbf{n}}) \ , \quad \mathrm{RM}(\hat{\mathbf{n}}) = \frac{e^3}{8\pi^2 \varepsilon_0 m^2 c^3} \int_{\mathrm{l.o.s.}} \mathrm{d}\ell \, n_e(\ell) \, B_{\parallel}(\ell) \ , \tag{2-19}$$

where λ is its wavelength, $n_e(\ell)$ is medium's free the electron density along the line of sight and we have neglected redshift effects for simplicity. For details on this and more observational methods besides Faraday rotation, see (300).

Let us now specifically direct our focus on perhaps the most important magnetic field for high-energy multi-messenger astrophysics: that from our very own Milky Way. Its coherent global structure can be obtained from Faraday rotation of extragalactic radio waves as they cross the Galaxy and from the polarization intensity of synchrotron emission from Galactic CR electrons (302). In order to capture its essential features, the Galactic magnetic field is modeled by the superposition of a halo field (including toroidal and poloidal components) and a spiral disk field component in the form of a logarithmic spiral. Nominal values for its strength can vary between tenths to a few μG, depending on the location being considered. The Galactic spiral arms have strongest fields, increasing towards the Galactic center (302, 303). Besides this coherent component, it is also expected that there are small-scale random fields, also of the order of μG, with short ($\lesssim$ 100 pc) coherence lengths generated by astrophysical phenomena (*e.g.* supernova outflows) and potentially amplified by hydrodynamic instabilities (304), as well as "striated" fields (large-scale "bubbles" with a random fixed orientation, with small-scale variations in strength/sign). Such random turbulences are crucial for the diffusion of CRs in the Galaxy.

In the context of cosmological EM cascades, the most relevant magnetic field to consider is the IGMF. Its characteristics are mostly unknown: there is no clear picture of its origin, no meaningful knowledge of its strength, structure or redshift evolution, and, for the skeptics among us, no guarantee of its existence. Constraints on the IGMF are usually displayed in a B versus λ_B plot

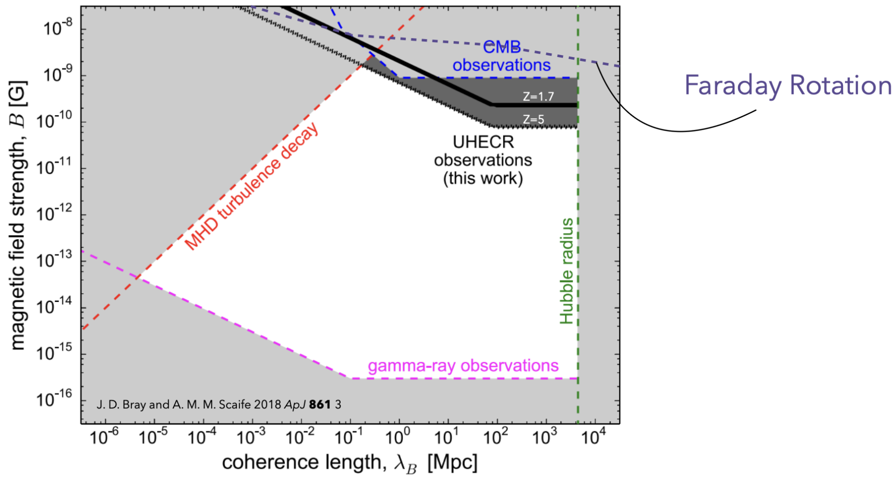

Figure 2.5: Constrains on the strength and coherence length of the IGMF, obtained from several different methods. Figure adapted from (297) to include Faraday rotation limits, available in (305). Other constraints from (306, 307).

such at the one in Figure 2.5. These constraints were all derived in (297, 305) and references therein. We can see that, besides Faraday rotation, the CMB also gives us powerful upper limits on the IGMF, down to the nanoGauss level. This is typically assumed as a safe upper limit of its field strength. At short coherence lengths, the IGMF power would have dissipated into heat by magnetohydrodynamical turbulences, also making this scenario unfeasible. Lack of deflection in UHECRs can also be used to constrain IGMFs if we assume to know the direction of their sources in the sky. This is also shown in Figure 2.5, but should be taken with a grain of salt. Finally, there have been recent claims on lower limits to the IGMF from the non-observation of γ-ray pair halos and pair echoes coming from distant blazars, γ-ray bursts, etc (308, 306, 309, 310). However, there are several assumptions and uncertainties going into these analyses (*e.g.* (311)) such as the extrapolation of intrinsic source spectra, making these results quite debatable. If one takes them to be true, then the IGMF must exist.

2.2

Particle Interactions in Electromagnetic Cascades

Now that we have a better notion of the obstacles that high-energy γ rays and electrons[5] must traverse through as they travel across the IGM, we shall study the possible interactions between them. Traditionally, EPP and ICS have been considered on the development of cascades. These will be discussed the first, followed by rares processes that are subdominant and/or only relevant at UHEs.

---

[5] Hereby, “electrons” refers to both electrons and positrons.

2.2.1
Electron Pair Production

An EM cascade initiates when a γ ray with energy E_γ interacts with a background photon with energy ϵ, producing an electron-positron pair,

$$\gamma + \gamma_{\rm bkg} \to e^+ + e^- \ . \tag{2-20}$$

Let $p_1 = (E_\gamma, 0, 0, E_\gamma)$ and $p_2 = (\epsilon, \epsilon \sin\theta, 0, \epsilon\cos\theta)$ be the 4-momenta of the incoming particles and $s = (p_1 + p_2)^2$ be the squared COM energy of the system. For EPP to occur, it is kinematically required that

$$s = 2E_\gamma\epsilon(1-\mu) \geq (2m_e)^2 \equiv s_{\rm th} \ , \tag{2-21}$$

where $\mu = \cos\theta$ is the cosine of the angle between the incoming photons in the lab frame. The total EPP cross section given by (312, 313)

$$\sigma_{\rm EPP}(s) = \sigma_{\rm T}\,\frac{3}{16}\,(1-\beta^2)\left[(3-\beta^4)\ln\frac{1+\beta}{1-\beta} - 2\beta(2-\beta^2)\right] \ , \tag{2-22}$$

where $\sigma_{\rm T}$ is the Thomson cross section and $\beta = (1-4m_e^2/s)^{1/2}$ is the velocity of the outgoing electron in the COM frame. Given an isotropic background photon field with energy-differential number density $\mathrm{d}n/\mathrm{d}\epsilon$, one can obtain the average interaction rate $\Gamma_{\rm EPP}$ by[6]

$$\Gamma_{\rm EPP}(E_\gamma, z) = c\int_0^\infty \mathrm{d}\epsilon \int_{-1}^{1-\frac{2m_e^2}{E_\gamma\epsilon}} \mathrm{d}\mu\,\frac{1-\mu}{2}\,\sigma_{\rm EPP}(E_\gamma,\epsilon,\mu)\,\frac{\mathrm{d}n(\epsilon,z)}{\mathrm{d}\epsilon} \ . \tag{2-23}$$

A few comments regarding Eq. (2-23) are in order.

1. The mean free path of γ rays is related to the interaction rate by $\lambda_{\rm EPP} = c/\Gamma_{\rm EPP}$.

2. The upper limit on the μ-integration comes from the threshold condition $s \geq s_{\rm th}$. It is implied for all such integrals in this section.

3. Although analytical expressions exist for the angle-averaged cross section[7] $\langle\sigma_{\rm EPP}\rangle \equiv \int \mathrm{d}\mu\,\sigma_{\rm EPP}\,(1-\mu)/2$, they are either too cumbersome (*e.g* the exact formula obtained in (315)) or approximations that fail near threshold (*e.g* (316)). We find it more convenient to use numerical integration instead.

4. Since the CMB evolves predictably with redshift via Eq. (2-6), we have as a consequence that, for the CMB,

---

[6] The so-called "flux factor" $(1-\beta_1\beta_2\mu)/2 = (1-\boldsymbol{\beta}_1\cdot\boldsymbol{\beta}_2)$, where $\boldsymbol{\beta}_1$ and $\boldsymbol{\beta}_2$ are the velocities of the incoming particles, is required for a Lorentz invariant angle averaging (314).

[7] Here, angle brackets "$\langle\rangle$" always indicate averages over the incoming particles' directions.

$$\Gamma^{\rm cmb}_{\rm EPP}(E_\gamma, z) = (1+z)^3\, \Gamma^{\rm cmb}_{\rm EPP}(E_\gamma(1+z), 0)\ . \tag{2-24}$$

5. Interaction rates are additive in the presence of multiple background photon fields. For example, when considering both the CMB and the EBL: $\Gamma^{\rm tot}_{\rm EPP} = \Gamma^{\rm cmb}_{\rm EPP} + \Gamma^{\rm ebl}_{\rm EPP}$.

For cascade simulations, one needs to calculate the spectrum of electrons (+ positrons) $\mathrm{d}N_e/\mathrm{d}E'_e$ (primed energies always refer to outgoing particles in interactions) generated from the EPP of a spectrum of γ rays $\mathrm{d}N_\gamma/\mathrm{d}E_\gamma$. In order to do that, one must have the (angle-averaged) differential interaction rate

$$\gamma^{\rm EPP}_{\gamma\to e}(E_\gamma, E'_e, z) = c \int \mathrm{d}\epsilon \int \mathrm{d}\mu\, \frac{1-\mu}{2}\, \frac{\mathrm{d}\sigma_{\rm EPP}}{\mathrm{d}E'_e}(E_\gamma, E'_e, \epsilon, \mu)\, \frac{\mathrm{d}n(\epsilon, z)}{\mathrm{d}\epsilon}\ . \tag{2-25}$$

The EPP differential cross section has been calculated exactly in (317). To avoid their cumbersome expressions, we use the following approximate formula (318), valid for $E_\gamma \gg m_e \gg \epsilon$:

$$\begin{aligned}\frac{\mathrm{d}\sigma_{\rm EPP}}{\mathrm{d}E'_e}(E_\gamma, E'_e, \epsilon, \mu) = \sigma_{\rm T}\, \frac{3}{4}\, \frac{m_e^2}{s}\, \frac{1}{E_\gamma} \Bigg[&\frac{E'_e}{E_\gamma - E'_e} + \frac{E_\gamma - E'_e}{E'_e} \\ &+ E_\gamma \left(1-\beta^2\right) \left(\frac{1}{E'_e} + \frac{1}{E_\gamma - E'_e} \right) \\ &- \frac{E_\gamma^2 \left(1-\beta^2\right)^2}{4} \left(\frac{1}{E'_e} + \frac{1}{E_\gamma - E'_e} \right)^2 \Bigg]\ ,\end{aligned} \tag{2-26}$$

restricted to the range

$$\frac{1-\beta}{2} \le \frac{E'_e}{E_\gamma} \le \frac{1+\beta}{2}\ . \tag{2-27}$$

For the computation of (2-25) it is more convenient to use directly the angle-averaged differential cross section (316, 319), valid for $E_\gamma \gg m_e$:

$$\begin{aligned}\left\langle \frac{\mathrm{d}\sigma_{\rm EPP}}{\mathrm{d}E'_e} \right\rangle &\equiv \int \mathrm{d}\mu\, \frac{1-\mu}{2}\, \frac{\mathrm{d}\sigma_{\rm EPP}}{\mathrm{d}E'_e} \\ &= \frac{3\sigma_{\rm T}}{32}\, \frac{m_e^4}{E_\gamma^3 \epsilon^2} \Bigg[\frac{4E_\gamma^2}{\left(E_\gamma - E'_e\right) E'_e} \ln\left(\frac{4\epsilon E'_e \left(E_\gamma - E'_e\right)}{m_e^2 E_\gamma} \right) - \frac{8E_\gamma \epsilon}{m_e^2} \\ &\quad + \frac{2E_\gamma^2 \left(2E_\gamma\epsilon - m_e^2\right)}{\left(E_\gamma - E'_e\right) E'_e m_e^2} - \left(1 - \frac{m_e^2}{E_\gamma \epsilon}\right) \frac{E_\gamma^4}{\left(E_\gamma - E'_e\right)^2 E'^2_e} \Bigg]\ .\end{aligned} \tag{2-28}$$

The energy of the outgoing electrons is restricted to

$$E'_{e,\rm min} \equiv \frac{E_\gamma}{2}\left(1 - \sqrt{1 - \frac{m_e^2}{E_\gamma \epsilon}}\right) \le E'_e \le \frac{E_\gamma}{2}\left(1 + \sqrt{1 - \frac{m_e^2}{E_\gamma \epsilon}}\right) \equiv E'_{e,\rm max}\ . \tag{2-29}$$

Note that the differential interaction rate satisfies the following properties:

1. $\int_{E'_{e,\min}}^{E'_{e,\max}} \mathrm{d}E'_e\, \gamma^{\mathrm{EPP}}_{\gamma\to e} = \Gamma_{\mathrm{EPP}}$,
2. $\int_{E'_{e,\min}}^{E'_{e,\max}} \mathrm{d}E'_e\, E'_e\, \gamma^{\mathrm{EPP}}_{\gamma\to e}/\Gamma_{\mathrm{EPP}} = \langle E'_e \rangle = E_\gamma/2$,
3. $\gamma^{\mathrm{EPP}}_{\gamma\to e}(E_\gamma, E'_e, z) = (1+z)^4\, \gamma^{\mathrm{EPP}}_{\gamma\to e}(E_\gamma(1+z), E'_e(1+z), 0)$, for the CMB,
4. $\gamma^{\mathrm{EPP,tot}}_{\gamma\to e} = \gamma^{\mathrm{EPP,cmb}}_{\gamma\to e} + \gamma^{\mathrm{EPP,ebl}}_{\gamma\to e}$, just like the additive property of Γ_{EPP}.

We suppress the integration limits of all future integrals over the outgoing particles' energies, which are implied from the allowed kinematic ranges such as the one in Eq. (2-29). With these quantities, one can obtain the properly normalized spectrum of pair-produced electrons from monoenergetic γ rays of energy E_γ,

$$\frac{\mathrm{d}N_{\gamma\to e}}{\mathrm{d}E'_e}(E'_e, E_\gamma, z) = 2\,\frac{\gamma^{\mathrm{EPP}}_{\gamma\to e}(E_\gamma, E'_e, z)}{\Gamma_{\mathrm{EPP}}(E_\gamma, z)} \ . \tag{2-30}$$

The factor of 2 accounts for both electrons and positrons being produced with symmetric probability distributions. Property 1 above ensures particle number is fixed,

$$\int \mathrm{d}E'_e\, \frac{\mathrm{d}N_{\gamma\to e}}{\mathrm{d}E'_e}(E'_e, E_\gamma, z) = 2 \ , \tag{2-31}$$

while property 2 guarantees energy conservation,

$$\int \mathrm{d}E'_e\, E'_e\, \frac{\mathrm{d}N_{\gamma\to e}}{\mathrm{d}E'_e}(E'_e, E_\gamma, z) = E_\gamma \ . \tag{2-32}$$

It can be useful to think of Eq. (2-31) as a normalization condition for the spectrum, while Eq. (2-32) can be seen as the expectation value for the energy of outgoing electrons,

$$\langle E'_e \rangle = \frac{\int \mathrm{d}E'_e\, E'_e\, \frac{\mathrm{d}N_{\gamma\to e}}{\mathrm{d}E'_e}}{\int \mathrm{d}E'_e\, \frac{\mathrm{d}N_{\gamma\to e}}{\mathrm{d}E'_e}} = \frac{E_\gamma}{2} \ . \tag{2-33}$$

From an arbitrary spectrum of photons $\mathrm{d}N_\gamma/\mathrm{d}E_\gamma$, the resulting $e^\pm$ spectrum is then straightforwardly given by

$$\frac{\mathrm{d}N_e}{\mathrm{d}E'_e}(E'_e, z) = \int \mathrm{d}E_\gamma\, \frac{\mathrm{d}N_{\gamma\to e}}{\mathrm{d}E'_e}(E'_e, E_\gamma, z)\, \frac{\mathrm{d}N_\gamma}{\mathrm{d}E_\gamma}(E_\gamma, z) \ . \tag{2-34}$$

These expressions guarantee energy and particle number conservation, which are essential requirements for the proper development of EM cascades. We naturally recover (2-30) by setting the $\mathrm{d}N_\gamma/\mathrm{d}E_\gamma$ to a Dirac delta centered at a given E_γ. Energy conservation can be easily verified.

2.2.2
Inverse Compton Scattering

After EPP, the resulting electrons of energy E_e can undergo ICS off of target background photons,

$$e^{\pm} + \gamma_{\text{bkg}} \to e^{\pm} + \gamma \ , \tag{2-35}$$

generating new high-energy γ rays. The cross section for this process is given by (301)

$$\sigma_{\text{ICS}} = \frac{3\sigma_{\text{T}}}{8}\frac{m_e^2}{s\beta}\left[\frac{2}{\beta(1+\beta)}(2+2\beta-\beta^2-2\beta^3) - \frac{1}{\beta^2}(2-3\beta-\beta^3)\ln\frac{s}{m_e^2}\right] \ , \tag{2-36}$$

where $s = m_e^2 + 2E_e\epsilon(1-\beta_e\mu)$ is the squared COM energy, written in terms of the incoming electron's velocity $\beta_e = (1-m_e^2/E_e^2)^{1/2} \approx 1$ and the cosine of the angle between the incoming particles μ, and $\beta = (s-m_e^2)/(s+m_e^2)$ is the velocity of the outgoing electron in the COM frame. With Eq. (2-36), we can calculate interaction rates Γ_{ICS} (or mean free paths λ_{ICS}) in a similar fashion to Eq. (2-23), with only two subtle changes when taking angular averages: *(i)* the flux factor becomes $(1-\mu)/2 \to (1-\beta_e\mu)/2$, although it leads to negligible corrections, and *(ii)* the upper limit of μ-integrations is now 1, since there is no kinematic threshold. Once again, we prefer numerical integration for $\langle\sigma_{\text{ICS}}\rangle$, rather than complicated analytical expressions (*e.g.* (320)).

Unlike in EPP, where the outgoing particles have symmetric distributions, we have two distinct differential interaction rates for ICS with respect to the energy of each outgoing particle E'_γ and E'_e:

$$\gamma^{\text{ICS}}_{e\to\gamma}(E_e, E'_\gamma, z) = c\int \mathrm{d}\epsilon \int_{-1}^{1} \mathrm{d}\mu\, \frac{1-\beta_e\mu}{2}\, \frac{\mathrm{d}\sigma_{\text{ICS}}}{\mathrm{d}E'_\gamma}(E_e, E'_\gamma, \epsilon, \mu)\, \frac{\mathrm{d}n(\epsilon, z)}{\mathrm{d}\epsilon} \ , \tag{2-37}$$

$$\gamma^{\text{ICS}}_{e\to e}(E_e, E'_e, z) = c\int \mathrm{d}\epsilon \int_{-1}^{1} \mathrm{d}\mu\, \frac{1-\beta_e\mu}{2}\, \frac{\mathrm{d}\sigma_{\text{ICS}}}{\mathrm{d}E'_e}(E_e, E'_e, \epsilon, \mu)\, \frac{\mathrm{d}n(\epsilon, z)}{\mathrm{d}\epsilon} \ . \tag{2-38}$$

The exact differential cross sections above have been obtained by (321), containing extremely cumbersome expressions which are numerically unstable and contain some misprints (later corrected and improved in subsequent works (322, 323)). In the useful limits for ICS in cascades ($E_e \gg m_e$ and $E_e \gg \epsilon$), one may use (318)

$$\frac{\mathrm{d}\sigma_{\mathrm{ICS}}}{\mathrm{d}E'_e}(E_e, E'_e, \epsilon, \mu) = \frac{3\sigma_{\mathrm{T}}}{8}\frac{m_e^2(1+\beta)}{sE_e\beta}\left[\frac{E'_e}{E_e} + \frac{E_e}{E'_e} + \frac{2(1-\beta)}{\beta}\left(1 - \frac{E_e}{E'_e}\right)\right.$$
$$\left. + \frac{(1-\beta)^2}{\beta^2}\left(1 - \frac{E_e}{E'_e}\right)^2\right] , \quad (2\text{-}39)$$

with the kinematic range restricted to

$$\frac{1-\beta}{1+\beta} \leq \frac{E'_e}{E_e} \leq 1 \; . \quad (2\text{-}40)$$

To obtain the differential cross-section with respect to the outgoing photon's energy E'_γ, one can substitute $E'_e \to E_e - E'_\gamma$ in (2-39). Alas, for the calculation of the differential interaction rates (2-37) and (2-38), we can use directly the angle averaged differential cross sections. The first of them is given by (324, 325)

$$\left\langle \frac{\mathrm{d}\sigma_{\mathrm{ICS}}}{\mathrm{d}E'_\gamma} \right\rangle \equiv \int \mathrm{d}\mu \, \frac{1-\beta_e\mu}{2} \frac{\mathrm{d}\sigma_{\mathrm{ICS}}}{\mathrm{d}E'_\gamma}$$
$$= \frac{3\sigma_{\mathrm{T}} m_e^2}{4\epsilon E_e^2}\left[1 + \frac{z^2}{2\,(1-z)} + \frac{z}{b\,(1-z)} - \frac{2z^2}{b^2\,(1-z)^2}\right.$$
$$\left. - \frac{z^3}{2b\,(1-z)^2} - \frac{2z}{b\,(1-z)}\ln\frac{b\,(1-z)}{z}\right] , \quad (2\text{-}41)$$

in the limit $E'_\gamma \gg \epsilon$ and $E_e \gg m_e$, where $b \equiv 4\epsilon E_e/m_e^2$, $z \equiv E'_\gamma/E_e$ and the kinematically allowed range is constrained to $\epsilon/(E_e+\epsilon) \leq z \leq b/(1+b)$. By substituting $E'_\gamma \to E_e - E'_e$ in Eq. (2-41), we obtain the second differential cross section $\langle \mathrm{d}\sigma_{\mathrm{ICS}}/\mathrm{d}E'_e \rangle$. We can then define normalized spectra of inverse-Compton-scattered photons and electrons from incoming electrons with a fixed energy E_e as

$$\frac{\mathrm{d}N_{e\to\gamma}}{\mathrm{d}E'_\gamma}(E'_\gamma, E_e, z) = \frac{\gamma^{\mathrm{ICS}}_{e\to\gamma}(E_e, E'_\gamma, z)}{\Gamma_{\mathrm{ICS}}(E_e, z)} \; , \quad \frac{\mathrm{d}N_{e\to e}}{\mathrm{d}E'_e}(E'_e, E_e, z) = \frac{\gamma^{\mathrm{ICS}}_{e\to e}(E_e, E'_e, z)}{\Gamma_{\mathrm{ICS}}(E_e, z)} \; , \quad (2\text{-}42)$$

satisfying the particle number and energy conservations conditions

$$\int \mathrm{d}E'_\gamma \, \frac{\mathrm{d}N_{e\to\gamma}}{\mathrm{d}E'_\gamma}(E'_\gamma, E_e, z) = \int \mathrm{d}E'_e \, \frac{\mathrm{d}N_{e\to e}}{\mathrm{d}E'_e}(E'_e, E_e, z) = 1 \; , \quad (2\text{-}43)$$

$$\int \mathrm{d}E'_\gamma \, E'_\gamma \, \frac{\mathrm{d}N_{e\to\gamma}}{\mathrm{d}E'_\gamma}(E'_\gamma, E_e, z) + \int \mathrm{d}E'_e \, E'_e \, \frac{\mathrm{d}N_{e\to e}}{\mathrm{d}E'_e}(E'_e, E_e, z) = E_e \; , \quad (2\text{-}44)$$

in analogy to Eqs. (2-31) and (2-32), respectively. We can obtain outgoing γ-ray and electron spectra from an arbitrary incoming spectrum of electrons in a similar fashion to Eq. (2-34).

Because ICS has no threshold, both the CMB and the EBL are accessible photon fields for this interaction at all energies. However, recall that $\mathrm{d}n_{\mathrm{cmb}}/\mathrm{d}\epsilon \gg \mathrm{d}n_{\mathrm{ebl}}/\mathrm{d}\epsilon$ at peak. Since the (differential) interaction rates depend linearly on the differential energy density of the background field, it is common to neglect the subdominant EBL contribution for ICS: $\Gamma_{\mathrm{ICS}}^{\mathrm{tot}} \approx \Gamma_{\mathrm{ICS}}^{\mathrm{cmb}}$ and the same for $\gamma_{e\to\gamma}^{\mathrm{ICS}}$ and $\gamma_{e\to e}^{\mathrm{ICS}}$.

2.2.3
Energy-Space Evolution of Cascades

Besides the cross sections and rates presented in the previous sections, another crucial quantity to understand how cascades develop is the inelasticity of interactions. This concept, introduced in Section 1.3.2 within a different context, will allow us to study cascade evolution in energy space. For EPP, we define the inelasticity η_{EPP} as the fraction of the incoming γ ray's energy transferred to the outgoing non-leading particle (*i.e.* the outgoing electron carrying the least amount of energy). Thus, by definition, $\eta_{\mathrm{EPP}} \leq 50\%$. Since the differential cross section $\mathrm{d}\sigma_{\mathrm{EPP}}/\mathrm{d}\epsilon' = E_\gamma\, \mathrm{d}\sigma_{\mathrm{EPP}}/\mathrm{d}E'_e$ can be interpreted as a relative probability distribution function for producing electrons with fractional energy $\epsilon' = E'_e/E_\gamma$, then we can obtain the inelasticity by

$$\eta_{\mathrm{EPP}}(s) = 1 - \frac{2}{\sigma_{\mathrm{EPP}}(s)} \int_{0.5}^{(1+\beta)/2} \mathrm{d}\epsilon'\, \epsilon'\, \frac{\mathrm{d}\sigma_{\mathrm{EPP}}}{\mathrm{d}\epsilon'}(s, \epsilon') \; . \tag{2-45}$$

The factor of 2 once again ensures that the differential cross section accounts for both electrons and positrons. One can check that $\mathrm{d}\sigma_{\mathrm{EPP}}/\mathrm{d}\epsilon'$ is a function of s and ϵ' only, without explicit dependences on the energies or μ. For ICS, the inelasticity is defined as the energy fraction going into the outgoing γ ray,

$$\eta_{\mathrm{ICS}}(s) = 1 - \frac{1}{\sigma_{\mathrm{ICS}}(s)} \int_{(1-\beta)/(1+\beta)}^{1} \mathrm{d}\epsilon'\, \epsilon'\, \frac{\mathrm{d}\sigma_{\mathrm{ICS}}}{\mathrm{d}\epsilon'}(s, \epsilon') \; , \tag{2-46}$$

where now we have $\epsilon' = E'_e/E_e$.

We can analyse the behavior of these inelasticities by looking at Figure 2.6. For EPP (left panel), we find that the inelasticity starts from 50% at threshold (as expected) and falls off significantly at high s. This means that, at high COM energies, one of the outgoing electrons carries out most of the incoming γ ray's energy, while the other leaves with only a few percent of that. Similarly, the high-s behavior of ICS makes the outgoing γ ray take most of the incoming electron's energy. This means cascade evolution in E-space is slow at the highest energies, requiring many EPP-ICS cycles before the leading particles' energies are significantly degraded. At around $s \approx 8m_e^2$, we have η_{ICS} falling below 0.5, meaning that the outgoing electron from that interaction

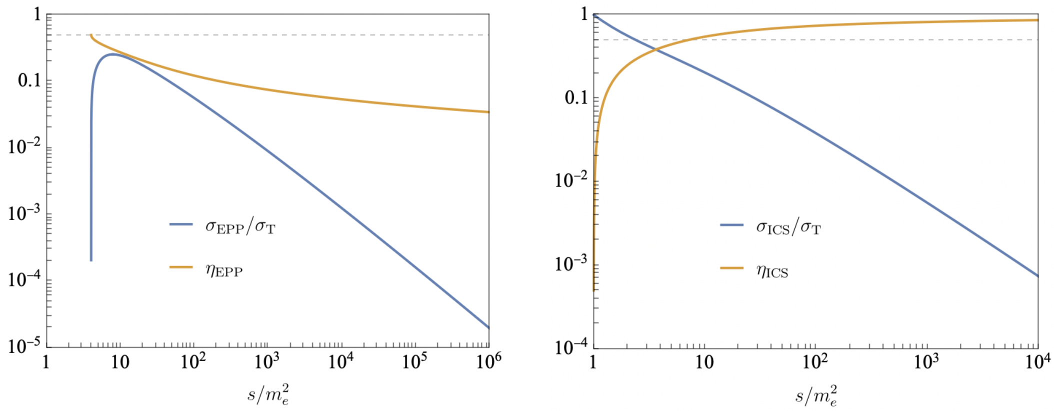

Figure 2.6: Cross sections, in units of the Thomson cross section $\sigma_{\rm T}$, and inelasticities for EPP (left) and ICS (right) as a function of the COM energy squared s for each interaction. Gray dashed lines mark the 50% line, a useful reference point for inelasticities.

carries away most of the incoming energy instead. In fact, $\eta_{\rm ICS} \approx 0$ at low COM energies causes a significant stalling of electron energy loss, which will come up again in Appendix C.

It may also be helpful to visualize these inelasticities in a different way, within the context of EM cascades with the CMB and EBL backgrounds. Figure 2.7 shows the average energy fraction going to the outgoing leading electron from EPP (left panel) and to the outgoing photon from ICS (right panel), for interactions with cosmic background photons at $z = 0$. These are obtained by using the monoenergetic spectra defined in Eqs. (2-30) and (2-42),

$$\langle E'_{e,\text{leading}}\rangle(E_\gamma) = \int_{E_\gamma/2}^{E_\gamma} \mathrm{d}E'_e\, E'_e\, \frac{\mathrm{d}N_{\gamma\to e}}{\mathrm{d}E'_e}(E'_e, E_\gamma, z=0)\ , \tag{2-47}$$

$$\langle E'_\gamma\rangle(E_e) = \int_0^{E_e} \mathrm{d}E'_\gamma\, E'_\gamma\, \frac{\mathrm{d}N_{e\to\gamma}}{\mathrm{d}E'_\gamma}(E'_\gamma, E_e, z=0)\ . \tag{2-48}$$

At $E_\gamma \gtrsim 0.2$ PeV, EPP in the cascade is dominated by interactions with the CMB. As the energy decreases, we approach threshold with EPP photons and the inelasticity falls, bringing $\langle E'_{e,\text{leading}}\rangle/E_\gamma$ closer to 50%. Then, the EBL takes over EPP, giving rise to two bumps corresponding to the optical and IR peaks in Figure 2.2. Eventually ($E_\gamma \lesssim 2.5\times10^{10}$ eV), EPP is no longer possible even with the EBL, but we still see the ratio approaching 0.5 at threshold. The ICS curve on the right panel does not show the EBL-features since this interaction has no threshold and is always dominated by the CMB. We once again see the outgoing photon carrying away most the incoming energy at high E_e, while at low E_e this is done by the outgoing electron.

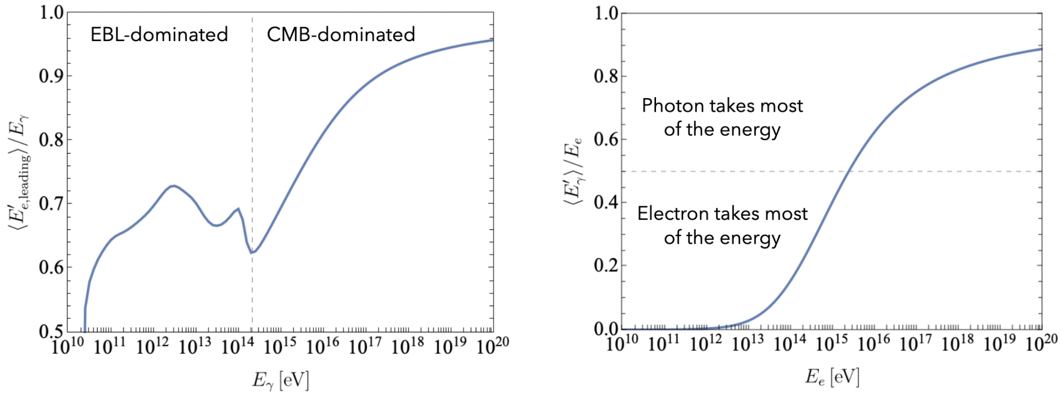

Figure 2.7: *Left*: Average energy of the outgoing leading electron from EPP, in units of the incoming γ-ray energy. The gray dashed line represents the transition between a preference in the cascade for EPP with different photon backgrounds. *Right*: Average energy of the outgoing photon from ICS, in units of the incoming electron energy. The gray dashed line marks the 50% point.

2.2.4
Cascade Processes at Ultra-High Energies

Other interactions between high-energy γ rays/electrons and target photons become possible at UHEs, requiring that we move beyond the standard EPP-ICS cascade picture. Of particular interest to us will be muon-producing processes taking place at large COM energies, since muons decay into neutrinos, allowing for multi-messenger cascade studies. In this section, we will review the main processes responsible for the production of such muons, as well as the relevant competing interactions at UHEs.

Starting with γ-γ interactions, first and foremost, we have MPP,

$$\gamma + \gamma_{\mathrm{bkg}} \to \mu^+ + \mu^- \ , \tag{2-49}$$

which becoming possible above the threshold squared COM of $s = 2E_\gamma\epsilon(1-\mu) \geq (2m_\mu)^2$. This threshold is $(m_\mu/m_e)^2 \approx 4.3\times10^4$ times greater than the equivalent condition for EPP, making it an UHE process in EM cascades. All cross sections, interaction rates, kinematic energy ranges and spectra can be obtained from identical expressions as those written in Section 2.2.1 for EPP, with the substitution $m_e \to m_\mu$. This means that the cross sections are related by

$$\sigma_{\mathrm{MPP}}(s) = \left(\frac{m_e}{m_\mu}\right)^2 \sigma_{\mathrm{EPP}}(s m_e^2/m_\mu^2) \ , \tag{2-50}$$

and are actually quite close to each other at high-s due to their suppression far from threshold.

The importance of (2-49) in EM cascades has been mostly neglected over the years, despite its early mention in (10). It was remarked in (326) that MPP could produce high-energy neutrinos in cascades at high redshifts ($z \sim 5-10$), although no follow-up study was performed. Later, this process was studied at low redshifts ($z \leq 5$) under some approximations (327), where it was found that only a minor energy budget from cascades could be converted into UHE neutrinos. Also, the resulting neutrino flux would be considerably subdominant with respect to the expected cosmogenic neutrino flux. Soon, we shall see that the absence of the CRB at high redshifts makes MPP quite important for cascades happening at such early times.

Competing with MPP, we can also have double pair production (DPP),

$$\gamma + \gamma_{\rm bkg} \to e^+ + e^- + e^+ + e^- \ , \tag{2-51}$$

with a threshold of $s_{\rm th} = (4m_e)^2$. A fully analytic expression for its cross section is quite involved, although a decent approximation for it is (328)

$$\sigma_{\rm DPP}(s) \simeq 6.45\,\mu{\rm b} \left(1 - \frac{16m_e^2}{s}\right) \ . \tag{2-52}$$

Instead of using the full expression for the DPP differential cross section, we simply approximate the process in assuming that one of the outgoing pairs carries the quasi-totality of the projectile photon energy, sharing it equally among the pair. This captures the main qualitative effect of DPP on the cascade development (329).

Moving over to e-γ interactions besides ICS, we can have electron triplet production (ETP; also usually called triplet pair production),

$$e^\pm + \gamma_{\rm bkg} \to e^\pm + e^+ + e^- \tag{2-53}$$

kicking in at $s \geq (3m_e)^2$. Its differential cross sections have been calculated in many works (330, 331, 332); the total cross section requires numerical integration of their complicated expressions, and can be well approximated at $s \gg m_e$ by[8] (333)

$$\sigma_{\rm ETP}(s) \simeq \frac{3\alpha\sigma_{\rm T}}{8\pi}\left(\frac{28}{9}\ln\frac{s}{m_e} - \frac{218}{27}\right) \ . \tag{2-54}$$

This process was studied within the context of EM cascades in (334). Although it dominates over ICS beyond $E_e(1{+}z) \gtrsim 10^{17}$ eV (because of the Klein-Nishina suppression of $\sigma_{\rm ICS}$), the newly created electron-positron pair carries away a negligible fraction ($\lesssim 10^{-2}$) of the total energy in the interaction (318). Thus, ETP mainly serves to increase the multiplicity of electrons below UHEs in the cascade. Additionally, if the IGMF is above 10^{-12} G, synchrotron cooling would dominate above ETP, rendering its effect unimportant for cascades.

---

[8] Its exact behaviour near threshold is unimportant since ICS dominates over ETP in this energy regime.

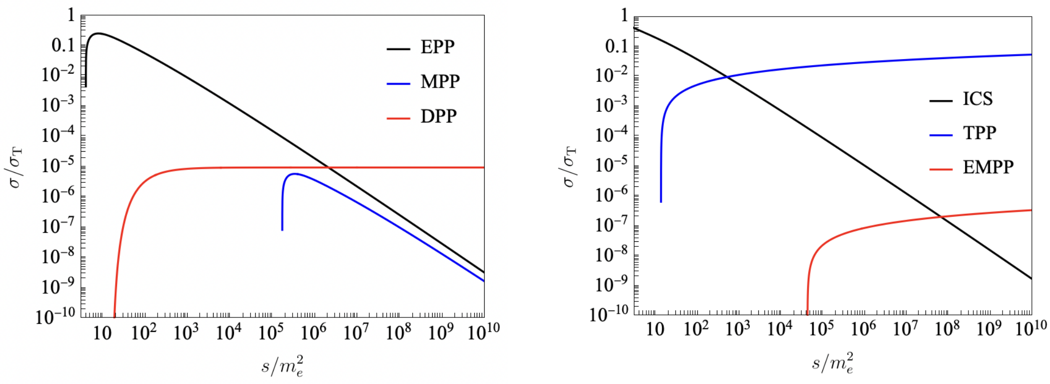

Figure 2.8: Cross sections for the processes mentioned in the previous sections. *Left*: γ-ray interactions. *Right*: Electron interactions ("EMPP" represents electron muon-pair production).

In principle, it is also possible to produce muons via electron muon-pair production,

$$e^\pm + \gamma_{\rm bkg} \rightarrow e^\pm + \mu^+ + \mu^- \ , \tag{2-55}$$

beyond $s \geq (m_e + 2m_\mu)^2$. Although its cross section at $s \gg m_e^2$ (326),

$$\sigma_{\rm EMPP} \simeq \frac{2\alpha^3}{m_\mu^2} \ln(2) \ln \frac{s}{m_e^2} \ , \tag{2-56}$$

is always $\sim$ 5 orders of magnitude below that of ETP, (2-55) is still a viable interaction because the ETP inelasticity[9] is even smaller. Nevertheless, neutrino production via (2-55) is subleading with respect to MPP.

2.3
γ-Cascade V4: Updating an EM Cascade Simulation Program

One of the main results in this thesis is the release of an updated version of the EM cascade simulation program γ-Cascade (335). The code takes into account EPP and ICS in cascade evolution, as well as synchrotron losses from the IGMF. In this section, we describe how γ-Cascade works and what improvements have been made from the previous version (γ-Cascade V3) to the new one (V4).

As an important side note, γ-Cascade V4 has not yet been released to the public. There are still some final calculations and checks to be made before the code is fully functional. With that said, we expect it to be released quite soon. Here, we only show preliminary results comparing V4 to V3 and other works in the literature.

---

[9] Recall that "inelasticity" refers to the energy of the incoming leading particle, $E_{\gamma/e}$, lost to the outgoing non-leading particle(s).

2.3.1
The γ-Cascade Library

The γ-Cascade code is written entirely in Wolfram language, intended for use in Mathematica. All of its variables and functions are contained inside one package file: `GCascadeV4.wl`. However, γ-Cascade also contains a library with several pre-computed tables necessary for the code's functionality which contain the numerical results of some key integrals from Sections 2.2.1 and 2.2.2, *e.g.* the normalized EPP and ICS spectra. These tables are evaluated at discrete energy and redshift values, listed in the arrays "`energies`" and "`zReg`". The former contains a list of 300 energies between 10^{-1}–10^{12} GeV, evenly spaced in a logarithmic scale, and is available to the user in order to generate injection spectra that is readable to the code. Meanwhile, the latter is internal to the code and contains a list of 1001 redshifts from 0 to 10, equally spaced in intervals of 0.01. Here is a list of the tables available in the γ-Cascade library:

- Inverse mean free paths (IMFPs), $\lambda^{-1}_{\mathrm{EPP/ICS}} = \Gamma_{\mathrm{EPP/ICS}}/c$, in units of $[\mathrm{m}^{-1}]$, for both EPP and ICS with the CMB and each of the EBL models available in the code. Recall that IMFPs for different photon backgrounds are additive. These tables have dimensions 1001×300 corresponding to the entries in the `zReg` and `energies` arrays, respectively. In other words, the entry i, j of each IMFP array contains $\lambda^{-1}_{\mathrm{EPP/ICS}}(E_j, z_i)$.
- Differential IMFPs, $\gamma^{\mathrm{EPP/ICS}}/c$, in units of $[\mathrm{m}^{-1}\ \mathrm{eV}^{-1}]$, for both EPP and ICS with bot the CMB and EBL. Recall that they are also additive. These tables have dimensions $1001 \times 300 \times 300$ corresponding to the entries in `zReg` and `energies` (twice). Two energy dimensions are necessary for the incoming particle (unprimed) and the outgoing particle (primed): $\gamma^{\mathrm{EPP/ICS}}(E_j, E'_k, z_i)/c$.
- Normalized spectra of outgoing particles from EPP and ICS, in units of $[\mathrm{eV}^{-1}]$. These tables contain $dN_{\gamma/e\to\gamma/e}/dE'_{\gamma/e}(E'_k, E_j, z_i)$ values in a $1001 \times 300 \times 300$ grid analogous to the differential IMFP tables. They contain important numerical post-processing to ensure energy conservation on the γ-Cascade grid, as described in Appendix B.
- γ-ray spectral tables containing the sum of all ICS contributions in our on-the-spot approximation, described in Appendix C. These tables contain $dN_{e\to\gamma,\mathrm{OTS}}/dE'_{\gamma}(E'_k, E_j, z_i)$, defined by Eq. (2-69), organized in a $1001 \times 300 \times 300$ grid and in units of $[\mathrm{eV}^{-1}]$, same as before.
- Normalized γ-ray spectra $dN_{\gamma\to e\to\gamma,\mathrm{OTS}}/dE'_{\gamma}(E'_k, E_j, z_i)$, from Eq. (2-68), in $[\mathrm{eV}^{-1}]$ and over the same $1001 \times 300 \times 300$ grid. These are the core

cumulative result of our numerical treatment and are imported by the γ-Cascade code to evaluate cascaded spectra after each EPP/ICS cycle, using Eqs. (2-63) and (2-67).

- Auxiliary arrays `stepSizeArray.mat` and `zRegIndexArray.mat`. The former contains light-travel distances in [kpc] in redshift steps of 10^{-6} arranged in a particular structure for internal use in γ-Cascade. The latter contains indexing conversions between different redshift tables inside the code.

The fact that all of the physical quantities and operations within γ-Cascade are evaluated on a grid invites an intuitive tensor-like interpretation. Interaction rates/IMFPs on a grid are denoted by $\Gamma_{ij} \equiv \Gamma(E_j, z_i) = \lambda^{-1}(E_j, z_i) \equiv \lambda_{ij}^{-1}$, differential interaction rates are denoted by $\gamma_{ijk} \equiv \gamma(E_j, E'_k, z_i)$, and so on. The order of the indices follow the order they appear in the array dimensions, with i always representing the i'th redshift entry in the `zReg` array. This allows us to recast equations from the previous two sections into index notation. For example, Eq. (2-30) on a grid looks like

$$\left(\frac{dN_{\gamma\to e}}{dE'_e}\right)_{ijk} = 2\frac{(\gamma^{\text{EPP}}_{\gamma\to e})_{ijk}}{(\Gamma_{\text{EPP}})_{ij}} \ , \tag{2-57}$$

and integrals such as Eq. (2-31) can be done by trapezoidal integration, which reduces to computationally-efficient matrix multiplication and addition,

$$\sum_{k=1}^{299}\left[\left(\frac{dN_{\gamma\to e}}{dE'_e}\right)_{i,j,k+1} + \left(\frac{dN_{\gamma\to e}}{dE'_e}\right)_{i,j,k}\right]\frac{E_{k+1}-E_k}{2} = 2 \ , \quad \forall\ i,j \ . \tag{2-58}$$

In particular, the discrete version of spectral integrals such as Eq. (2-34) is evaluated in γ-Cascade by trapezoidal integration rather than adaptive sampling of the continuous integral, thereby saving a significant amount of computational time:

$$\begin{aligned}\left(\frac{dN_e}{dE'_e}\right)_{i,k} = \sum_{j=1}^{299}\Bigg[&\left(\frac{dN_{\gamma\to e}}{dE'_e}\right)_{i,j+1,k}\left(\frac{dN_\gamma}{dE_\gamma}\right)_{i,j+1} \\ &+ \left(\frac{dN_{\gamma\to e}}{dE'_e}\right)_{i,j,k}\left(\frac{dN_\gamma}{dE_\gamma}\right)_{i,j}\Bigg]\frac{E_{j+1}-E_j}{2} \ . \end{aligned}\tag{2-59}$$

This proves to be extremely useful when evaluating spectra after multiple EPP/ICS steps, which would normally require nested numerical integration in the continuous realm.

2.3.2
Structure of the Main Code

The main code `GCascadeV4.wl` contains several functions that perform cascades, modify magnetic fields and switch between EBL models. They are described in Appendix D, as well as in a tutorial notebook that comes with the γ-Cascade package. All of the cascade modules have a similar structure, which we shall describe in this section.

Distances in γ-Cascade are divided into redshift steps of Δz determined by an array called `diffuseDistances`, which contains redshift values from 10^{-6} – 10^{1} in non-uniform spacings, varying between $10^{-6} \leq \Delta z \leq 10^{-2}$. Each of these intervals is further subdivided into fine redshift steps of $\delta z = 10^{-6}$. During the propagation of γ rays, their spectrum will get attenuated by EPP and regenerated by ICS at every δz step, which we call a "cycle"[10].

The attenuated flux after each cycle is given by

$$\left.\frac{\mathrm{d}N_\gamma}{\mathrm{d}E_\gamma}\right|_{\mathrm{att}} (E_\gamma) = e^{-\tau_{\mathrm{EPP}}} \frac{\mathrm{d}N_\gamma}{\mathrm{d}E_\gamma}(E_\gamma) \ , \tag{2-60}$$

where the optical depth upon traversing the region of light-travel length ℓ corresponding to the redshift interval δz is

$$\tau_{\mathrm{EPP}}(E_\gamma, z^*) \approx \frac{\ell}{\lambda_{\mathrm{EPP}}(E_\gamma, z^*)} \ , \tag{2-61}$$

and λ_{EPP} is the mean free path as a function of the energy E_γ in the lab (not comoving) frame. Since λ_{EPP} is only evaluated on a grid, we use its value at the closest `zReg` array entry, z^*. The remaining part of the spectrum, $(1 - e^{-\tau_{\mathrm{EPP}}})\mathrm{d}N_\gamma/\mathrm{d}E_\gamma$ undergoes EPP and will be added back into the spectrum at lower energies after ICS. In γ-Cascade, electrons are assumed to lose their entire energy through successive ICSs within a single cycle. We call this an *on-the-spot approximation*, which we describe in detail on the next section.

These cycles repeat until we reach the end of a Δz window, where we apply cosmological redshifting corrections to the spectrum. More specifically, if a spectrum of γ rays entered a redshift window at z_i and left it at z_f, their energies get shifted down by

$$E \to E \times \frac{1 + z_f}{1 + z_i} \ . \tag{2-62}$$

We do not apply a global $(1 + z_f)^2/(1 + z_i)^2$ factor to the spectrum $\mathrm{d}N_\gamma/\mathrm{d}E_\gamma$, which does occur in reality, due to time dilation and energy redshifting (which also can be deduced by dimensional considerations). This is because these

---

[10] The function `GCascadeAttenuate` skips this ICS regeneration step, producing only the attenuated flux at the Earth without any cascade contributions.

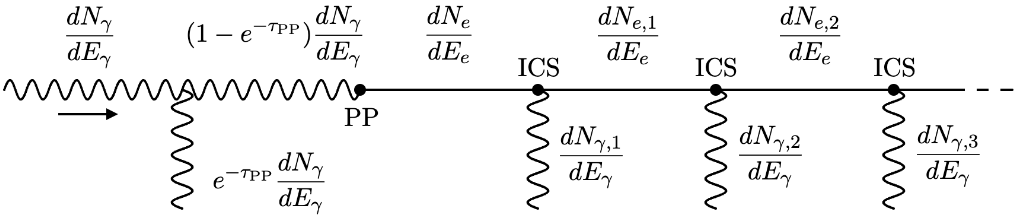

Figure 2.9: Schematic representation of an interaction cycle in γ-Cascade. Besides the γ rays that do not undergo EPP, $e^{-\tau_{PP}}(\mathrm{d}N_\gamma/\mathrm{d}E_\gamma)$, the next cycle receives photons from successive ICSs of electron spectra, $\sum_n \mathrm{d}N_{\gamma,n}/\mathrm{d}E_\gamma$, according to our on-the-spot approximation.

factors eventually cancel after all Δz windows, and the only factor left over is a $(1+z_s)^2$, where z_s is the redshift of the source. At the end of the cascade, we multiply the resulting spectrum by this factor, as well as by $(4\pi d_L^2)^{-1}$ to turn it into a flux, where d_L is the luminosity distance of the source to us. In the case of a distribution of sources, we also add the spectrum coming from sources inside each Δz window once the cascade crosses it.

2.3.2.1
On-The-Spot Approximation for Inverse Compton Scattering

γ-Cascade adopts an on-the-spot approximation in which all electrons produced at a given redshift undergo infinitely many ICS interactions, losing all their energy in the form of photons, at that same redshift. As a consequence, the γ-ray spectrum exiting each interaction cycle is the sum of the attenuated spectrum (*i.e.* the surviving photons which did not undergo EPP in that cycle), the γ rays from the ICS of the pair-produced electrons, the γ rays from the ICS of the electrons produced after the first ICS, and so on. This is represented schematically in Figure 2.9, showing what happens inside each interaction cycle within γ-Cascade. Following its notation, the γ-ray spectrum leaving the interaction cycle after EPP and infinitely many ICSs is

$$\frac{\mathrm{d}N_{\gamma,tot}}{\mathrm{d}E'_\gamma}(E'_\gamma, z) = \left[e^{-\tau_{\mathrm{EPP}}(E_\gamma,z)}\frac{\mathrm{d}N_\gamma}{\mathrm{d}E_\gamma}(E_\gamma, z)\right]\Bigg|_{E_\gamma=E'_\gamma} + \frac{\mathrm{d}N_{\gamma,\mathrm{OTS}}}{\mathrm{d}E'_\gamma}(E'_\gamma, z)\ , \quad (2\text{-}63)$$

where the first term represents the surviving γ rays that do not undergo EPP, and the second term represent the sum of all ICS contributions on-the-spot, given by

$$\frac{\mathrm{d}N_{\gamma,\mathrm{OTS}}}{\mathrm{d}E'_\gamma}(E'_\gamma, z) = \sum_{n=1}^{\infty}\frac{\mathrm{d}N_{\gamma,n}}{\mathrm{d}E'_\gamma}(E'_\gamma, z)\ . \quad (2\text{-}64)$$

The electron spectrum $\mathrm{d}N_e/\mathrm{d}E'_e$ arising from the partial EPP of a generic initial γ-ray flux $\mathrm{d}N_\gamma/\mathrm{d}E_\gamma$, as in in Figure 2.9, is obtained analogously to Eq.

(2-34):

$$\frac{\mathrm{d}N_e}{\mathrm{d}E'_e}(E'_e, z) = \int \mathrm{d}E_\gamma \left\{ \frac{\mathrm{d}N_{\gamma\to e}}{\mathrm{d}E'_e}(E'_e, E_\gamma, z) \right. \\ \left. \left[\left(1 - e^{-\tau_{\mathrm{EPP}}(E_\gamma, z)}\right) \frac{\mathrm{d}N_\gamma}{\mathrm{d}E_\gamma}(E_\gamma, z) \right] \right\} . \quad (2\text{-}65)$$

In the same spirit, we would like to find $\mathrm{d}N_{\gamma,\mathrm{OTS}}/\mathrm{d}E'_\gamma$ given a generic electron spectrum from Eq. (2-65), by considering the corresponding photon spectra for a monoenergetic electrons, $\mathrm{d}N_{e\to\gamma,\mathrm{OTS}}/\mathrm{d}E'_\gamma$. This would allow us to write

$$\frac{\mathrm{d}N_{\gamma,\mathrm{OTS}}}{\mathrm{d}E'_\gamma}(E'_\gamma, z) = \int \mathrm{d}E'_e \, \frac{\mathrm{d}N_{e\to\gamma,\mathrm{OTS}}}{\mathrm{d}E'_\gamma}(E'_\gamma, E'_e, z) \, \frac{\mathrm{d}N_e}{\mathrm{d}E'_e} \, . \quad (2\text{-}66)$$

To simplify, we can skip the intermediate electrons altogether, relating $\mathrm{d}N_{\gamma,\mathrm{OTS}}/\mathrm{d}E'_\gamma$ directly to the incoming γ-ray spectrum by using Eq. (2-65),

$$\frac{\mathrm{d}N_{\gamma,\mathrm{OTS}}}{\mathrm{d}E'_\gamma}(E'_\gamma, z) = \int \mathrm{d}E_\gamma \left\{ \frac{\mathrm{d}N_{\gamma\to e\to\gamma,\mathrm{OTS}}}{\mathrm{d}E'_\gamma}(E'_\gamma, E_\gamma, z) \right. \\ \left. \left[\left(1 - e^{-\tau_{\mathrm{EPP}}(E_\gamma, z)}\right) \frac{\mathrm{d}N_\gamma}{\mathrm{d}E_\gamma}(E_\gamma, z) \right] \right\} , \quad (2\text{-}67)$$

where

$$\frac{\mathrm{d}N_{\gamma\to e\to\gamma,\mathrm{OTS}}}{\mathrm{d}E'_\gamma}(E'_\gamma, E_\gamma, z) = \int \mathrm{d}E'_e \, \frac{\mathrm{d}N_{\gamma\to e}}{\mathrm{d}E'_e}(E'_e, E_\gamma, z) \, \frac{\mathrm{d}N_{e\to\gamma,\mathrm{OTS}}}{\mathrm{d}E'_\gamma}(E'_\gamma, E'_e, z) \, . \quad (2\text{-}68)$$

Our problem then boils down to obtaining $\mathrm{d}N_{e\to\gamma,\mathrm{OTS}}/\mathrm{d}E'_\gamma$. Similarly to Figure 2.9, it is given by the contribution of all on-the-spot ICS generations $\mathrm{d}N_{e\to\gamma,n}/\mathrm{d}E'_\gamma$, this time coming from an initial monoenergetic electron of energy E_e (rather than from a generic spectrum as in $\mathrm{d}N_{\gamma,n}/\mathrm{d}E'_\gamma$ in Figure 2.9),

$$\frac{\mathrm{d}N_{e\to\gamma,\mathrm{OTS}}}{\mathrm{d}E'_\gamma}(E'_\gamma, E_e, z) = \sum_{n=1}^{\infty} \frac{\mathrm{d}N_{e\to\gamma,n}}{\mathrm{d}E'_\gamma}(E'_\gamma, E_e, z) \, . \quad (2\text{-}69)$$

This is essentially the Green's function version of Eq. (2-64). Note that we have dropped the prime in E'_e from Eq. (2-68), not only for convenience, but also because we now shift our perspective to consider the electrons as the incoming particles. The first generation of photons/electrons after ICS are given by Eqs. (2-42),

$$\begin{aligned} \frac{\mathrm{d}N_{e\to\gamma,1}}{\mathrm{d}E'_\gamma}(E'_\gamma, E_e, z) &= \frac{\mathrm{d}N_{e\to\gamma}}{\mathrm{d}E'_\gamma}(E'_\gamma, E_e, z) \, , \\ \frac{\mathrm{d}N_{e\to e,1}}{\mathrm{d}E'_e}(E'_e, E_e, z) &= \frac{\mathrm{d}N_{e\to e}}{\mathrm{d}E'_e}(E'_e, E_e, z) \, , \end{aligned} \quad (2\text{-}70)$$

and the subsequent generations have spectra given by

$$\frac{\mathrm{d}N_{e\to\gamma,n}}{\mathrm{d}E'_\gamma}(E'_\gamma, E_e, z) = \int \mathrm{d}E''_e \, \frac{\mathrm{d}N_{e\to\gamma}}{\mathrm{d}E'_\gamma}(E'_\gamma, E''_e, z) \, \frac{\mathrm{d}N_{e\to e,n-1}}{\mathrm{d}E'_e}(E''_e, E_e, z) \ , \quad (2\text{-}71)$$

$$\frac{\mathrm{d}N_{e\to e,n}}{\mathrm{d}E'_e}(E'_e, E_e, z) = \int \mathrm{d}E''_e \, \frac{\mathrm{d}N_{e\to e}}{\mathrm{d}E'_e}(E'_e, E''_e, z) \, \frac{\mathrm{d}N_{e\to e,n-1}}{\mathrm{d}E''_e}(E''_e, E_e, z) \ . \quad (2\text{-}72)$$

It is straightforward to prove, by induction, that the electron particle number stays constant,

$$\int \mathrm{d}E'_e \, \frac{\mathrm{d}N_{e\to e,n}}{\mathrm{d}E'_e}(E'_e, E_e, z) = 1 \ , \quad (2\text{-}73)$$

while the total photon particle number grows with each generation,

$$\int \mathrm{d}E'_\gamma \, \frac{\mathrm{d}N_{e\to\gamma,n}}{\mathrm{d}E'_\gamma}(E'_\gamma, E_e, z) = 1$$
$$\Rightarrow \qquad \int \mathrm{d}E'_\gamma \, \frac{\mathrm{d}N_{e\to\gamma,\mathrm{OTS}}}{\mathrm{d}E'_\gamma}(E'_\gamma, E_e, z) = N \ , \quad (2\text{-}74)$$

where N is the number of generations included in the summation (2-69), tending to infinity. Energy conservation can also be easily verified:

$$\int \mathrm{d}E'_\gamma \, E'_\gamma \, \frac{\mathrm{d}N_{e\to\gamma,n}}{\mathrm{d}E'_\gamma}(E'_\gamma, E_e, z) + \int \mathrm{d}E'_e \, E'_e \, \frac{\mathrm{d}N_{e\to e,n}}{\mathrm{d}E'_e}(E'_e, E_e, z)$$
$$= \int \mathrm{d}E''_e \, E''_e \, \frac{\mathrm{d}N_{e\to e,n-1}}{\mathrm{d}E''_e}(E''_e, E_e, z) \ . \quad (2\text{-}75)$$

There is an elegant way of writing the solution to this problem. Eq. (2-69) can be rewritten by using expressions (2-71) and (2-72), yielding

$$\frac{\mathrm{d}N_{e\to\gamma,\mathrm{OTS}}}{\mathrm{d}E'_\gamma}(E'_\gamma, E_e, z) = \int \mathrm{d}E'_e \, \frac{\mathrm{d}N_{e\to\gamma}}{\mathrm{d}E'_\gamma}(E'_\gamma, E'_e, z) \, F(E'_e, E_e, z) \ , \quad (2\text{-}76)$$

where the “kernel function” F satisfies the Fredholm equation of the second kind

$$F(E'_e, E_e, z) = \delta(E_e - E'_e) + \int \mathrm{d}E''_e \, \frac{\mathrm{d}N_{e\to e}}{\mathrm{d}E'_e}(E'_e, E''_e, z) \, F(E''_e, E_e, z) \ . \quad (2\text{-}77)$$

Solving Eq. (2-77) for F would avoid the difficult task of having to perform nested integrations increasing in depth with each generation. Unfortunately, Eq. (2-77) can only be solved recursively, which means there is no direct way of obtaining an analytical expression for F.

Fortunately, numerical integrations can be done quickly on the γ-Cascade grid via trapezoidal integration. In particular, Eqs. (2-71) and (2-72) can be rewritten in a similar fashion to Eq. (2-59) for fast evaluation, such that we can solve the problem iteratively up to whatever generation we desire in a reasonable amount of time. This approach, however, comes with its own complications on a discrete grid, requiring modifications of the normalized ICS spectra described in Appendix C.

With the $\mathrm{d}N_{e\to\gamma,\mathrm{OTS}}/\mathrm{d}E'_\gamma$ grid, we can use Eq. (2-68) to calculate the $\mathrm{d}N_{\gamma\to e\to\gamma,\mathrm{OTS}}/\mathrm{d}E'_\gamma$ grid, which is used in γ-Cascade to calculate the total on-the-spot spectrum $\mathrm{d}N_{\gamma,\mathrm{OTS}}/\mathrm{d}E'_\gamma$ via Eq. (2-67). This last spectrum is the one actually used in γ-Cascade to calculate the final photon output, Eq. (2-63), after each cycle illustrated in Figure 2.9.

Some comments regarding the limitations of γ-Cascade and the validity of this on-the-spot approximation are in order. Although it seems to be quite a drastic assumption, it actually yields reliable results in practically all scenarios. This can be understood by comparing the characteristic lengths of the relevant processes in EM cascades, shown in Figure 2.10. Besides the ICS mean free path at $z = 0$, we also show the Larmor radius $r_L = p/eB$ and the synchrotron energy-loss length $\ell_{\mathrm{sync}} = cE/|\mathrm{d}E/\mathrm{d}t|_{\mathrm{sync}}$, where $|\mathrm{d}E/\mathrm{d}t|_{\mathrm{sync}} = 4\sigma_{\mathrm{T}} u_B p^2/3m_e^2 c$ is the energy-loss rate and $u_B = B^2/2\mu_0$ is the magnetic field energy density (in SI units), for an intergalactic magnetic field of $B = 10^{-12}$ G. The important length scale intrinsic to γ-Cascade is marked as the green line and labeled as "γ-Cascade stepsize". As we have seen, the individual EPP-ICS cycles occur in redshift intervals of $\Delta z = 10^{-6}$, but γ-Cascade only applies redshift updates to the CMB/EBL backgrounds in steps of $\Delta z = 0.01$, corresponding to the entries on the `zReg` array. The green line in Figure 2.10 specifically marks the light-travel distance between $0 < z < 0.01$, which all particles must cross before ending the cascade. The following conclusions can be obtained from this plot:

- At $E_e \lesssim 1$ TeV and $B = 10^{-12}$ G, we have $r_L < \lambda_{\mathrm{ICS}}$, meaning that deflection starts becoming important and the cascade "isotropizes". This means that, for point sources, the flux calculated by γ-Cascade is the total isotropized flux coming from that source[11]. Increasing the magnetic field would increase the maximum energy at which this isotropization occurs. For diffuse source distributions, this is not an issue, since we should observe a diffuse flux anyways.
- At $E_e \lesssim 10^{20}$ eV, we have λ_{ICS} below the γ-Cascade stepsize. This indicates that many ICS interactions are expected to happen inside a single `zReg` bin in the code, just as assumed in our on-the-spot approximation.

---

[11] γ-Cascade is insensitive to time delay and angular spread effects due to magnetic fields of point sources. A more careful treatment can be obtained by Monte Carlo codes specifically designed to account for these effects (336, 337).

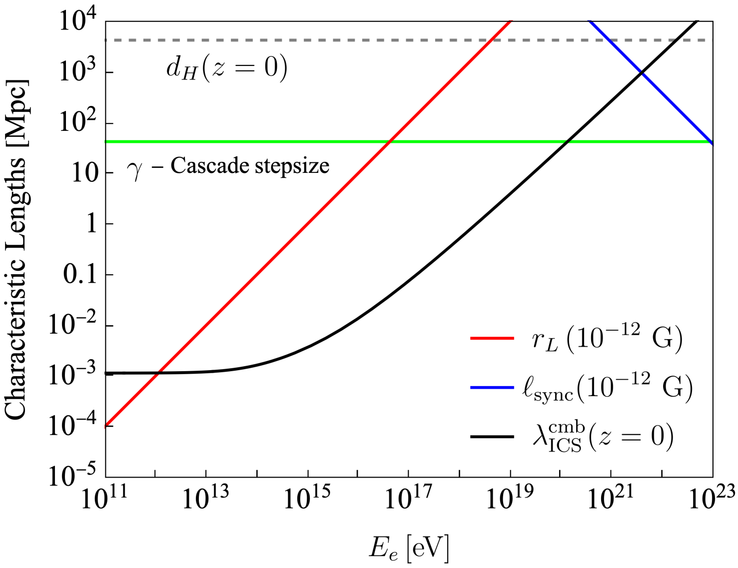

Figure 2.10: Characteristic lengths for electrons in the cascade.

- Above $\sim 10^{20}$ eV, the on-the-spot approximation is no longer valid, but also is the standard cascade picture of only PP and ICS. At such high center-of-momenta, new interactions kick in, changing how the cascade develops (338), as we have seen in Section 2.2.4. In particular, ETP with the CMB dominates over all other electron interactions above EeV energies (at $z = 0$).
- Energy-loss through synchrotron radiation is irrelevant in electromagnetic cascades below 10^{21} eV for $B = 10^{-12}$ G, since its energy-loss length $\ell_{\rm sync}$ is greater than the Hubble length $d_H = c/H_0$. Assuming magnetic fields at the conservative upper limit of $\sim$ nanoGauss (339), synchrotron loss becomes significant ($\ell_{\rm sync} < \lambda_{\rm ICS}$) above a few EeV.

Synchrotron loss in γ-Cascade is taken into account through the factor

$$f_{\rm ICS}(E_e, z) = \frac{|{\rm d}E/{\rm d}t|_{\rm ICS}}{|{\rm d}E/{\rm d}t|_{\rm sync} + |{\rm d}E/{\rm d}t|_{\rm ICS}} \,, \tag{2-78}$$

representing the energy fraction going into γ rays through ICS (while the remaining $1 - f_{\rm ICS}$ is lost to synchrotron radiation). The ICS energy-loss rate is given by

$$\left.\frac{{\rm d}E}{{\rm d}t}\right|_{\rm ICS}(E_e, z) = \int {\rm d}E'_\gamma\, E'_\gamma\, \gamma^{\rm ICS}_{e\to\gamma}(E_e, E'_\gamma, z) \,, \tag{2-79}$$

which is valid in the continuous-energy-loss regime, at low E_e. At high E_e, the stochastic nature of ICS becomes important (340), requiring a more careful treatment beyond the scope of γ-Cascade. Eqs. (2-70) – (2-72) are then modified by multiplying all ICS spectra by $f_{\rm ICS}$,

$$\frac{{\rm d}N_{e\to\gamma}}{{\rm d}E'_\gamma}(E'_\gamma, E_e, z) \quad\to\quad f_{\rm ICS}(E_e, z)\frac{{\rm d}N_{e\to\gamma}}{{\rm d}E'_\gamma}(E'_\gamma, E_e, z) \,. \tag{2-80}$$

Although this is technically not the most precise way of doing this, we remind the reader that synchrotron losses are only important at UHEs. For most purposes (*i.e.* injection spectra peaking below $\sim$ EeV energies), this does not affect the result of γ-Cascade.

2.3.3
Improvements in γ-Cascade V4 and Preliminary Results

Several improvements have been made to γ-Cascade and a few new features have also been added with respect to its predecessor version. We list them below:

1. The main change was fixing the EBL redshift evolution. In V3, the EBL was taken to be in the comoving frame rather than in the proper frame (see Section 2.1.2), and extended up to $z = 10$ for ICS spectra calculations. This led to unphysical behaviours of the cascade at high redshifts. This difference can be seen in the right panel of Figure 2.11, where we compare the V3 and V4 cascaded fluxes (for the same EBL model (288)). The V4 result matches more closely other cascaded flux calculations from the literature.
2. Adjustments to the grids for secondary spectra from EPP and ICS were made, as described in Appendix B.
3. The EBL models by Saldana-Lopez *et al.* (289), Finke *et al.* (341), and Franceschini and Rodighiero (342) were added into the code, which only had the Domínguez *et al.* EBL model (288). Now, the user can change between them using the newly implemented function `changeEBLModel`.
4. Fixed a bug which prevented γ-Cascade from working with injected monoenergetic fluxes.
5. The array `zRegIndexArray`, internal to the code, was fixed to translate correctly between `zReg` and `diffuseDistances`.
6. Recalculated the f_{ICS} arrays and re-implemented the `changeMagneticField` function, which was not working in V3.
7. Added a vast library of documentation, for the user to have access to all grids used in our calculations.
8. Several other minor tweaks and clean-ups in the code.

The importance of having different EBL models is to test their effect on the cascaded fluxes. By comparing their optical depths, shown in the left

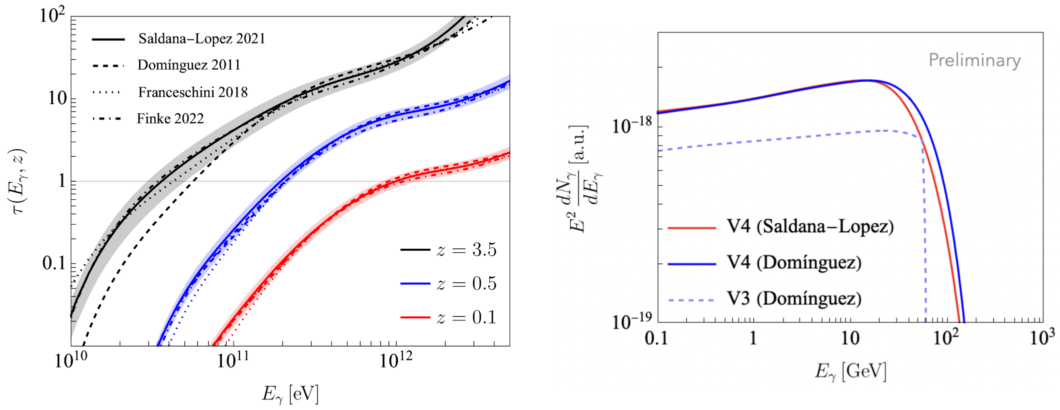

Figure 2.11: *Left*: EPP optical depths for different EBL models, represented by different line styles, calculated using Eq. (2-14). At high redshifts, we expect EBL attenuation to produce high-energy cutoffs in the cascaded spectra at slightly different energies (around where $\tau_{\mathrm{EPP}} = 1$) for each model. *Right*: Cascaded fluxes produced in γ-Cascade V4 from point sources at $z = 2$, assuming EBL models by Saldana-Lopez *et al.* (best-fit; (289)) and Domínguez *et al.* (288). Also shown in the cascaded flux from V3, which only has a faulty implementation of the Domínguez *et al.* EBL model at high redshifts.

panel of Figure 2.11, one can expect a difference in where the spectrum cutoff occurs due to EBL absorption at high redshifts. On the right panel, we have tested this hypothesis by injecting the same initial spectrum from a point-source at $z = 2$, and comparing the cascaded spectra for different EBL models (289, 288), showing their difference.

The next steps are making sure that the code is consistent with other state-of-the-art EM cascade simulators (336, 337). These are typically Monte Carlo based codes, specialized in calculating point-source cascades in the presence of magnetic fields, accounting for deflection. By construction, γ-Cascade does not account for magnetic deflection, but has a crucial advantage over the other codes: it is ideal for calculating cascades from isotropic distributions of sources. This will prove quite useful for the analysis we wish to perform in Chapter 3.

2.4
Cascade Neutrinos from Muon Pair Production

So far, we have only studied the traditional picture of EM cascades involving EPP and ICS (and synchrotron losses). This is a good approximation below EeV energies, but we have seen in Section 2.2.4 that other processes become kinematically accessible at UHEs. It is now time to consider this energy regime, where neutrino production from MPP (2-49) followed by muon decay (1-25) is possible.

2.4.1
Comparing Relevant Length Scales

Let us first assess the feasibility of MPP in UHE EM cascades. At first glance, we notice that EPP is always the preferred interaction of high-energy γ rays, based on a simple cross section comparison in Eq. (2-50) or Figure 2.8. Indeed, the EPP interaction rate (2-23) will always be greater than that of MPP. However, it can be shown that MPP is in fact a relevant process for UHE cascades, and neutrino production does actually occur.

The crucial observation is that, at UHEs, both EPP and ICS have high inelasticities,

$$\eta_{\mathrm{EPP/ICS}}(s) = 1 - \frac{1}{\sigma_{\mathrm{EPP/ICS}}(s)} \int \mathrm{d}\epsilon' \, \epsilon' \, \frac{\mathrm{d}\sigma_{\mathrm{EPP/ICS}}}{\mathrm{d}\epsilon'}(\epsilon', s) \; , \tag{2-81}$$

where ϵ' is the ratio of the outgoing non-leading particle's energy and the incoming leading particle's energy (γ rays in EPP, electrons in ICS). This means that they restore the UHE γ rays after each EPP-ICS cascade cycle. This gives γ rays another opportunity to produce muon pairs. In full cascades, there are many opportunities for MPP to take place over regular EPP, and it only takes a single MPP for some cascade energy to be permanently lost to neutrinos. A more appropriate comparison would be between the MPP mean free path, λ_{MPP}, and the EPP energy-loss length Λ_{EPP}, given by

$$\Lambda^{-1}_{\mathrm{EPP}}(E_\gamma, z) = \int \mathrm{d}\epsilon \int \mathrm{d}\mu \, \frac{1-\mu}{2} \, \sigma_{\mathrm{EPP}}(s) \, \eta_{\mathrm{EPP}}(s) \, \frac{\mathrm{d}n(\epsilon, z)}{\mathrm{d}\epsilon} \; , \tag{2-82}$$

because EPP-ICS cycles eventually degrade the cascade energy below the MPP threshold.

In Figure 2.12, we can see that $\lambda_{\mathrm{MPP}} > \Lambda_{\mathrm{EPP}}$ at energies $E_\gamma > 10^{20}$ eV. This means that MPP becomes more likely to happen than EPP at such UHEs. However, notice that DPP also plays an important role, dominating over MPP at all energies. There is only a narrow window around 10^{20} eV where λ_{MPP} is comparable to the other characteristic lengths, therefore becoming likely to occur. Alas, at low redshifts we have the presence of the CRB, which becomes the main target for EPP, completely washing out any chance for MPP to yield a significant flux of neutrinos.

The solution is to consider UHE EM cascades happening at high redshifts, $z \gtrsim 5$, where the CRB is practically absent (as well as the EBL, for that matter). Figure 2.13 shows the situation at high-z: MPP becomes viable in a small window around $E_\gamma(1+z) \sim 10^{20}$ eV. We use the well-known redshift scaling of the interaction/energy-loss lengths with the CMB, as in Eq. (2-24), such that these characteristic lengths scaled by $(1+z)^3$, as a function

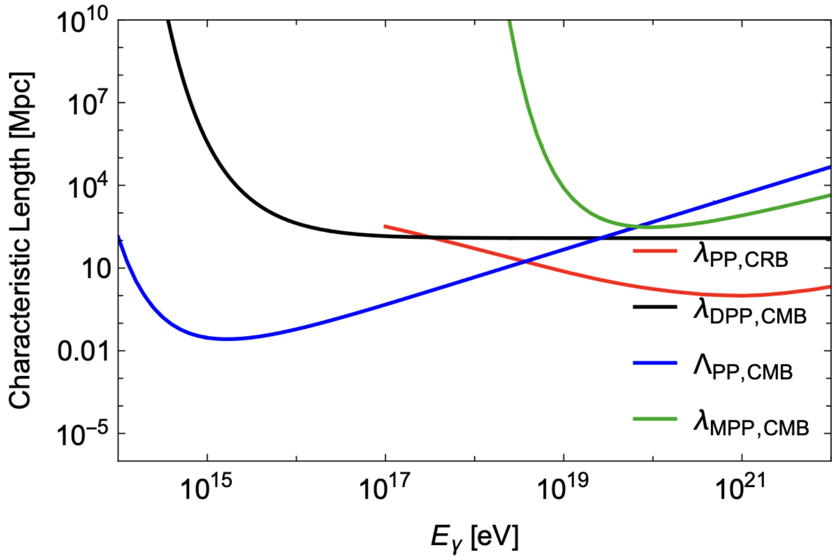

Figure 2.12: Energy-loss length for EPP (here, labelled as "PP") with the CMB, along with the mean free paths for MPP and DPP with the CMB, and EPP with the CRB, at $z = 0$. The lower the characteristic length, the more likely that process dominates the γ-ray cascade evolution.

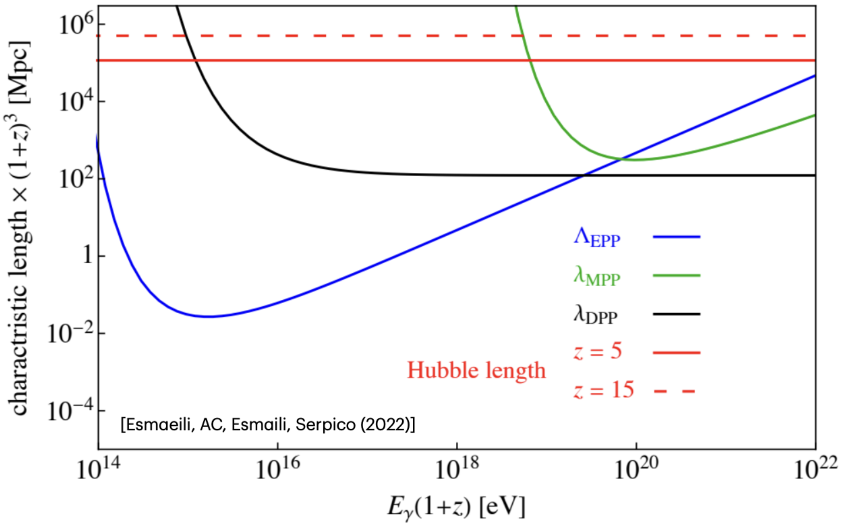

Figure 2.13: Same as Figure 2.12, but at high ($\gtrsim 5$) redshifts, where the CRB is absent. Axes scale with redshift such that the curves coincide for any redshift value. The Hubble lengths for $z = 5$ and $z = 15$ are also shown. Figure from (2).

of $E_\gamma(1 + z)$, become redshift-independent. Also note that, as shown in Fig. 2.13, these interaction lengths are well below the Hubble length $c/H(z)$ for the redshifts of interest. Hence, particle dynamics rather than cosmology rules the evolution in E-space, and the cascade development that can be considered almost instantaneous in z.

Let us summarize our findings. Qualitatively, starting from an UHE photon, we expect DPP to split the initial photon's energy into a pair $e^\pm$

almost equally. This is followed by ICS events, where the upscattered photons initiate a new multiplicative process via DPP and so on, until the photon energies end up close to the minimum of the MPP interaction length, around $E_\gamma(1+z) \simeq 10^{20}$eV. At that point, the particles are only a factor $2-3$ less likely to undergo muon generation via MPP than to degrade below the MPP threshold via a final DPP event, or to start a "conventional" cascade via EPP; this explains why MPP matters. In an MPP event, about 65% of the energy is carried by the neutrinos (see Appendix A), a rough expectation is that, away from threshold effects, on average slightly under $65\%/2 \sim 30\%$ of E_γ should be drained into the neutrino flux. We also expect that the higher the energy, the larger is the multiplicity of muons through which the drainage is happening, with this number scaling proportionally to $E_\gamma(1+z)/10^{20}$ eV. Finally, we can anticipate that a significant spread around the average should be present due to the stochastic nature of these events.

These qualitative arguments motivate a more quantitative study of the effects of MPP, which we embark on in the next section. Before moving on, however, let us mention our rationale for ignoring some additional processes (a synoptic description of which can be found in (318)). Charged pion production ($\gamma\gamma_{\rm bkg} \to \pi^+\pi^-$) becomes possible at $s \geq (2m_{\pi^\pm})^2$, but its cross section is only comparable to EPP and MPP in a small window of energies (corresponding to the $f_2(1270)$ resonance) (343, 344) and is otherwise sub-leading. Including this process would only mildly strengthen the conclusions of this chapter. The production of neutral pions, kaons and heavier hadrons in $\gamma\gamma_{\rm bkg}$ scattering is even more suppressed (345, 346), justifying that we neglect them. ETP has already been discussed, and leads to a negligible energy loss. Its inclusion is expected to change our conclusions at the few percent level at most, along with electron muon-pair production. Finally, we also neglect the synchrotron energy losses of UHE electrons on extragalactic magnetic fields. While these may be of importance at low redshift (see (327)), unless the fields are of primordial origin, their role with respect to losses on the CMB should vanish going to high-z, with an argument qualitatively similar to what we discussed for the CRB. Note that, despite limited information on extragalactic magnetogenesis, current evidence suggests indeed that extragalactic fields grow at low-z via an astrophysical dynamo mechanism, rather than being primordial (347) (or implying much smaller primordial seeds), consistent with the hypothesis done here.

2.4.2
Monte Carlo Simulations of UHE Cascades

To quantitatively assess the role of MPP at UHEs, we proceed with a Monte Carlo simulation. This is unavoidable if one is to take into account the discrete and stochastic nature of the processes involved. As previously discussed, it turns out that the mean free path between interactions is so short compared to the cosmological scales that the change in the redshift of two successive processes can be safely ignored. Thus, starting with a photon[12] with a specified energy E_γ and redshift z, only the evolution in $E-$space is relevant, described as a sequence of interactions where the leading electromagnetically interacting particle's energy degrades, until the MPP process is no longer kinematically open.

Following the Monte Carlo approach, at each photon interaction, we compare a random number in the interval $[0,1]$ with the probability

$$p_{\rm MPP} = \frac{\lambda_{\rm MPP}^{-1}}{\lambda_{\rm EPP}^{-1} + \lambda_{\rm MPP}^{-1} + \lambda_{\rm DPP}^{-1}} \, . \tag{2-83}$$

to yield an MPP. We can also define analogous probabilities for the other processes,

$$p_{\rm EPP} = \frac{\lambda_{\rm EPP}^{-1}}{\lambda_{\rm EPP}^{-1} + \lambda_{\rm MPP}^{-1} + \lambda_{\rm DPP}^{-1}} \, , \qquad p_{\rm DPP} = 1 - p_{\rm EPP} - p_{\rm MPP} \, . \tag{2-84}$$

These quantities depend on the incoming γ-ray energy E_γ and on the redshift z where this interaction takes place. For $z = 5$ and $z = 15$, they are shown in Figure 2.14, where we identify the small window around $E_\gamma \sim 10^{20}$ eV where MPP is non-negligible. For example, at $z = 15$ we estimate $p_{\rm MPP} \approx (0.07, 0.07, 0.02)$ and $p_{\rm DPP} \approx (0.18, 0.62, 0.93)$ for $E_\gamma = (10^{19}, 10^{20}, 10^{21})$ eV, respectively.

The cascade development depends on the selected interaction at each step. When MPP is chosen, the $e^\pm$ from the $\mu^\pm$ decays are injected again into the simulation by performing ICS on CMB photons, creating a new UHE γ ray which starts a new branch of cascade. If DPP is chosen, an e^+e^- pair will be tracked (the other pair is assumed to carry negligible energy). Each member of the pair will carry away $E_\gamma/2$ and initiate a new branch after a single ICS event. Finally, the EPP case will also be followed by ICS. The outgoing photon energy coming from ICS events, as well as the e^+/e^- energies from EPP events, are sampled from their corresponding differential cross sections.

The quantities of main interest for phenomenology are the fraction of the initial photon energy channeled into neutrinos, f_ν, and the neutrino spectra

---

[12] Starting with an electron would not lead to appreciable differences.

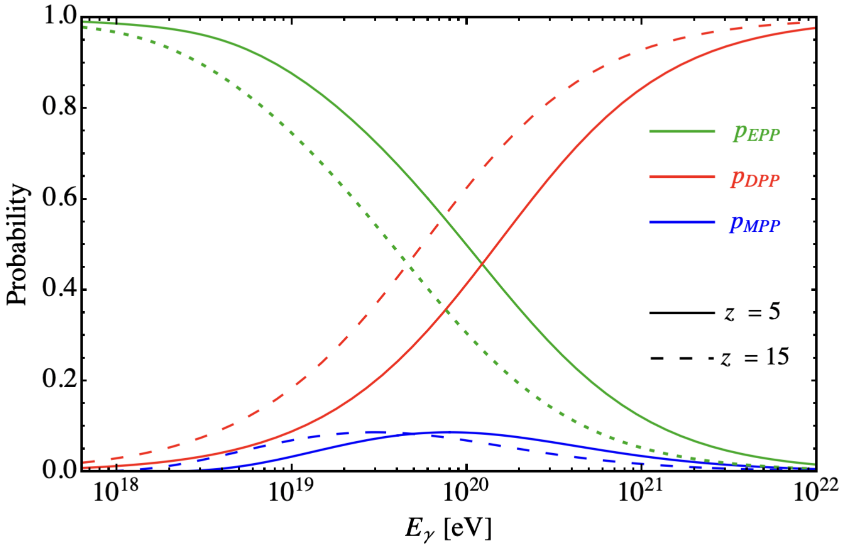

Figure 2.14: Probabilities of undergoing MPP, EPP and DPP at a single interaction step, at redshifts $z = 5$ and $z = 15$, as a function of the incoming γ-ray energy.

resulting from this process. Figure 2.15 shows the distribution of f_ν for 10^4 injected photons with energy $E_\gamma = 10^{19}$ eV, 10^{20} eV and 10^{21} eV in panels (a), (b) and (c), respectively, from top to bottom; the panels in the leftmost column report results at $z = 5$, in the middle ones at $z = 10$ and in the rightmost column at $z = 15$. The plots show that at 10^{19} eV and $z = 5$ only about 12% of the photons experience MPP. This fraction grows to about 25% at $z = 10$ and 35% at $z = 15$. At 10^{20} eV, well above 70% of photons experience MPP at $z \geq 5$, with this fraction exceeding 94% at $z = 15$. Eventually, for $E_\gamma = 10^{21}$ eV, basically every cascade involves one or more MPP events. This behaviour makes sense once realising that, at lower energy, threshold effects reducing the importance of MPP are important. At the highest energies, the multiplicity of energetic $e^\pm$ pairs due to DPP makes the probability that none of them undergo MPP vanishingly small. Note how the distributions of f_ν are broad (and skewed), reflecting the stochastic nature of the processes.

The mean value of f_ν is a strongly dependent function of energy near the threshold, while being almost constant with energy at high-E, as reported in Figure 2.16, for the initial photon energies $E_\gamma = 10^{19}$ eV (green), 10^{20} eV (red), and 10^{21} eV (blue). The bar around each curve shows the standard deviation, calculated from the distributions in Figure 2.15. It mildly shrinks with E_γ, since high multiplicities make the process “more deterministic”.

Figure 2.17 illustrates the point that, especially at high-E_γ and high-z, the multiplicity of muons via MPP events is considerable. For instance, at $E_\gamma = 10^{21}$ eV, on average $\sim$ 6, 11 and 15 MPPs will be realized for

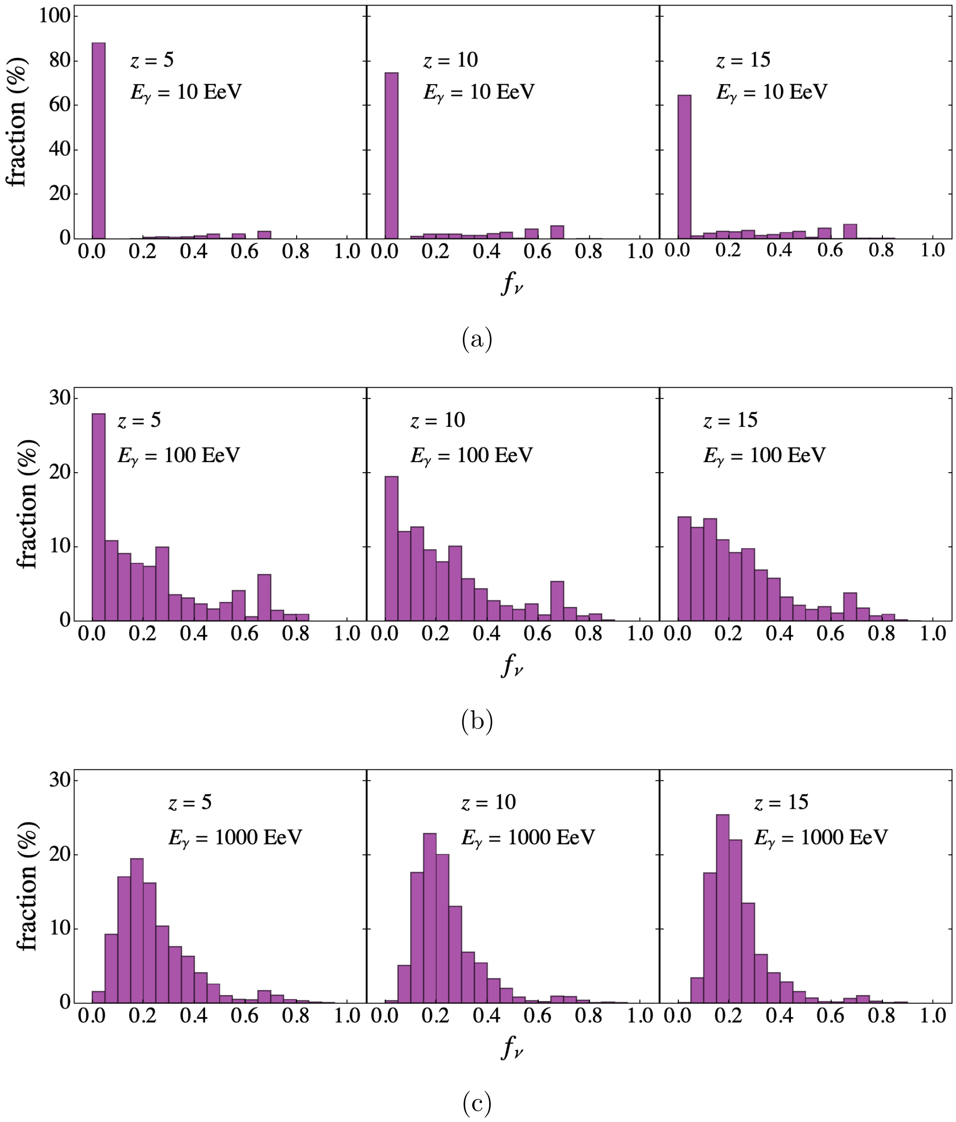

(a)

(b)

(c)

Figure 2.15: The fraction of energy channeling into neutrinos in the simulation of 10^4 photons with energies $E_\gamma = 10^{19}$ eV, 10^{20} eV and 10^{21} eV, respectively in panels (a), (b) and (c). The left, middle and right panels are respectively for injection at $z = 5$, 10 and 15. Figure from (2).

injections at $z = 5$, 10 and 15, respectively. Even in the cases in which MPP intervenes only when the particles have degraded to energies significantly lower than the injected ones, the DPP-induced multiplicity makes its impact on the energy budget not negligible. Note that in the early study (348) this aspect was completely missed "by construction", since no follow-up of the leptons produced via DPP was performed. Their estimate of only $\sim$ few percent of the EM energy drainage into neutrinos is thus not only due to the different conditions relevant at low-z, but also to the fact that they did not include this important effect.

The average all-flavor neutrino spectrum at the Earth from a photon injected at $z = 10$ with energy $E_\gamma = 10^{20}$ eV is depicted in Figure 2.18 by

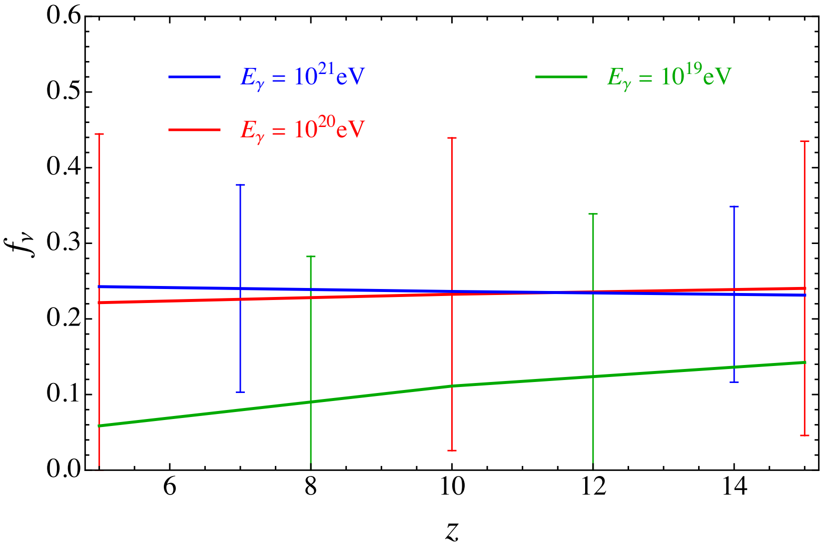

Figure 2.16: The mean fraction of the initial photon's energy ending up in neutrinos, f_ν, for three different energies of the initial cascade photon. The bars show the standard deviation around the mean value depicted by solid curves. Figure from (2).

the blue solid curve. This is based on the well-known analytical descriptions of neutrino spectra from muon decay (see the formulae in (94), also summarised in Appendix A) which have been averaged over the 10^4 injected photons in our simulation. The wiggles at the peak come from multiple MPPs in a single cascade, which for the case of Figure 2.18 can reach up to five MPPs, with $\sim 46\%$ of cases leading to two or three MPPs. In the conventional pp and $p\gamma$ scenarios described in Sections 1.3.2.1 and 1.3.2.2, UHE photons are the product of π^0 decays, that are unavoidably accompanied by $\pi^\pm$'s, whose decays produce neutrinos. In Figure 2.18 we also show, by the black dotted curve, the neutrino spectrum from the pion decay chain (see the formulae in Appendix A), with the energy of $\pi^\pm$ equal to 2×10^{20} eV, as expected by the pp and $p\gamma$ mechanisms. The little discontinuity in the dotted curve comes from the contribution of the neutrino emitted directly from the pion decay $\pi^\pm \to \mu^\pm \nu_\mu(\bar{\nu}_\mu)$. Note how the neutrinos from MPP emerge over those from $\pi^\pm$ in the low-energy part of the distribution, where they dominate the flux by one order of magnitude.

At higher E_γ and z, where the number of MPPs grows, yet more pronounced features are expected in the neutrino spectrum, as can be seen in Figure 2.19 which shows the case of $E_\gamma = 10^{21}$ eV injected at $z = 15$. The same features of Figure 2.18 are now present in a more exacerbated form. This clearly illustrates the relevance of the MPP process in shaping the UHE neutrino spectra from high-z/high-E sources.

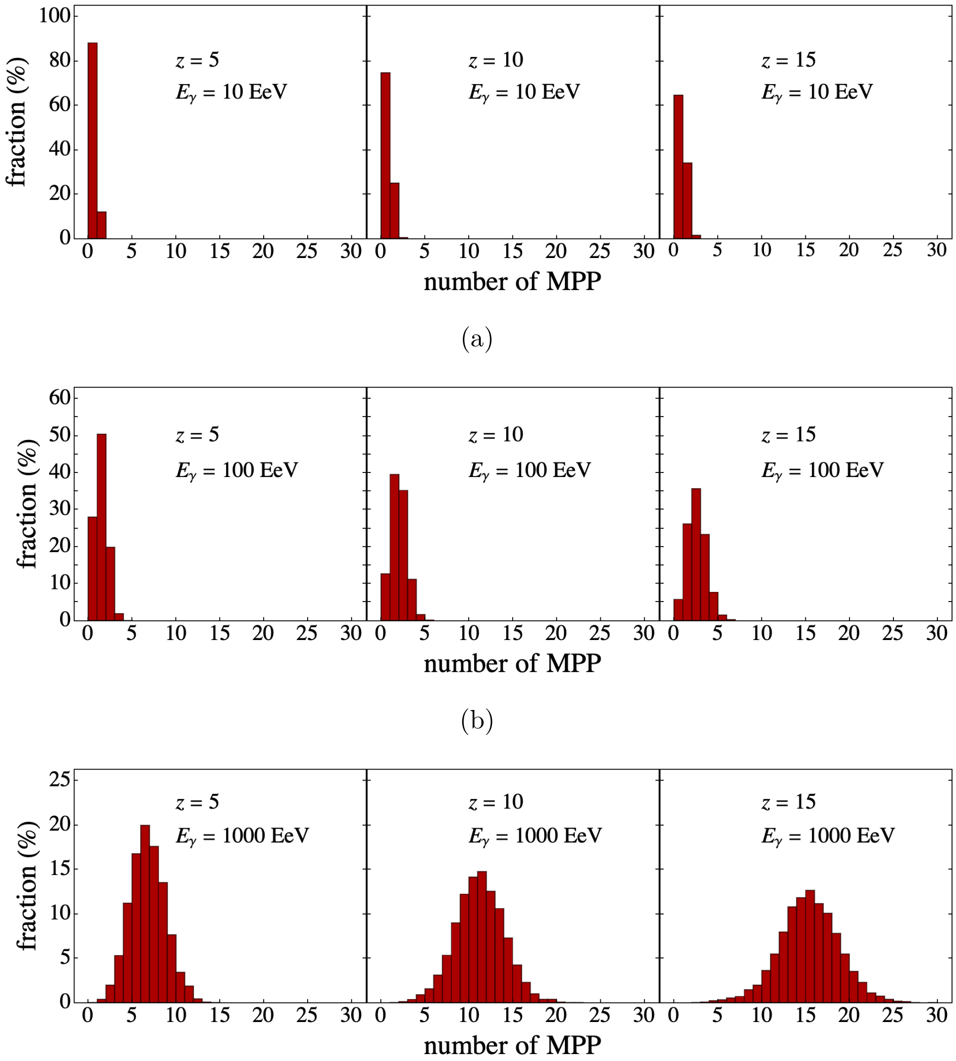

(a)

(b)

(c)

Figure 2.17: The distribution of the number of MPP occurrences, for the same energies and redshifts as in Figure 2.15. Figure from (2).

Another implication worth commenting upon is that the process discussed here alters the multimessenger γ-ν correlation. Conventional production scenarios arising from pp or $p\gamma$ interactions in an UHE astrophysical source predict that the neutrino and γ-ray emission spectra are related by Eq. (1-37). Integrating both sides of that equation over energy implies that, at the source, the ratio of total energies in γ's and ν's obeys

$$\mathcal{E}_\gamma \simeq 2/3\,(4/3)\,\mathcal{E}_\nu \ , \qquad \text{for } pp\,(p\gamma) \ . \tag{2-85}$$

The net effect of MPP is to alter this ratio towards the neutrino sector. For example, from Figure 2.16 we read that, for a source emitting 10^{21} eV γ rays/neutrinos at $z = 5$, approximately 24% of the initial photon energy is transferred to neutrinos during the cascade above MPP threshold. Naively,

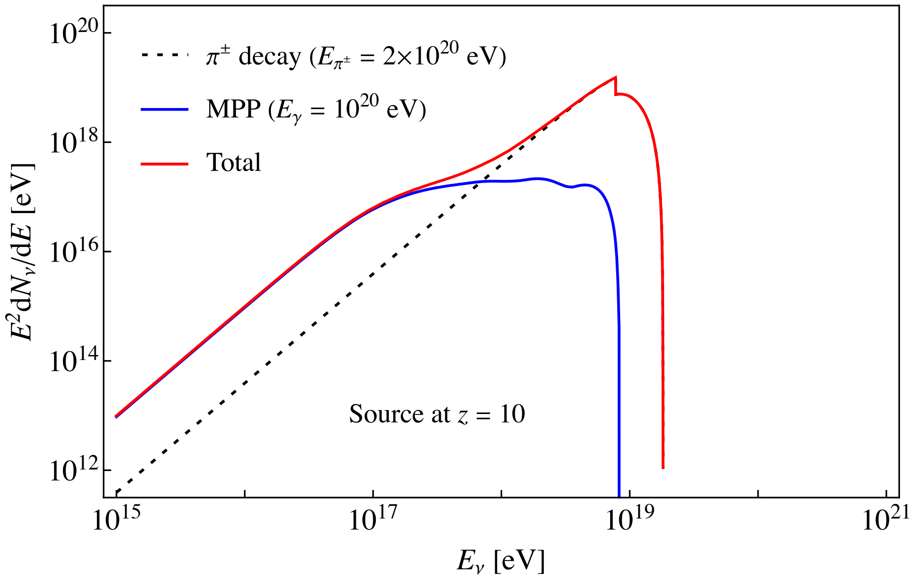

Figure 2.18: Neutrino spectrum at the Earth from MPP (solid blue curve) and charged pions decay chain (dotted black curve), from a source at redshift $z = 10$ injecting photons at $E_\gamma = 10^{20}$ eV. The solid red curve is their sum. Figure from (2).

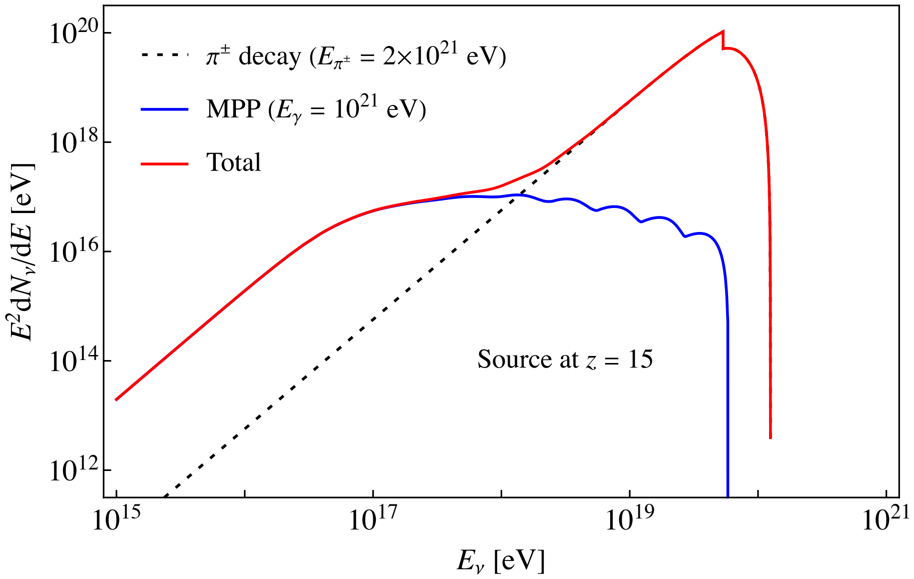

Figure 2.19: Same as Fig. 2.18, but for a source at redshift $z = 15$ injecting photons at $E_\gamma = 10^{21}$ eV. Figure from (2).

the new balance would be

$$\mathcal{E}'_\gamma \to 0.76\,\mathcal{E}_\gamma\ , \qquad \mathcal{E}'_\nu \to (1 + 0.24 \times 2/3\,(4/3))\,\mathcal{E}_\nu\ , \tag{2-86}$$

and hence

$$\mathcal{E}'_\gamma/\mathcal{E}'_\nu \simeq 0.44\,(0.77)\ , \qquad \text{for } pp\,(p\gamma) \tag{2-87}$$

That is, the ratio changed by about 40%. The actual energy budget ending up in the low energy diffuse photon flux is more complicated to compute, since one must account for the contribution seeded by $e^{\pm}$ from charged pion decays, as well as the fraction of the electromagnetic cascade channelled away by $e^{\pm}$. However, this simple calculation shows that the role of MPP is to make UHE sources at high redshift *γ-ray darker* than their low-z counterparts, while making them correspondingly *neutrino brighter* at UHEs.

2.4.3
Summary and Future Prospects

In this work, we studied some microphysics aspects associated to the UHE neutrino flux production which has been largely neglected: the role of MPP (and its interplay with DPP) in draining energy from EM messengers at UHEs, producing a non-negligible UHE neutrino flux. We argued that MPP is expected to be relevant above $E \gtrsim 10^{19}$ eV and at high redshifts, $z \gtrsim 5$. The resulting flux would fall at the Earth in the $E \gtrsim 10^{17}$ eV range, of interest for an instrument like GRAND (129). The physics of the process would somewhat loosen constraints from the diffuse γ-ray flux (20, 19), and induce characteristic spectral features in the neutrino flux, such as the transition between the muon and pion channels around 10^{18} eV, visible in Figures 2.18 and 2.19. These may be the least elusive of their signatures.

We have limited ourselves to generic considerations, in order to be as model-independent as possible, and we did not attempt to link the injected EM particles to primary UHECRs either. A few qualitative comments can however be made. Naive expectations from energetics would suggest that the UHE neutrino signal is dominated by relatively low-z sources, making it hard in this case to dig such a signal out of a larger flux. However, so little is known about UHECR sources at high-z, since energy losses make their flux subleading to the low-z one, that one cannot exclude that new classes of very energetic UHE emitters could be unveiled, for which our considerations are particularly relevant. One conceivable example is provided by the processes associated to the birth and growth of supermassive black holes (349), which are still unsolved astrophysical problems (350). Additionally, if an astrophysical flux of UHECRs is present, it is likely dominated by a light (proton-helium) composition, compared to the local observations indicating a nuclear enriched CR composition above ~ 10 EeV (49). This is due to the declining metallicity at high-z (see *e.g.* (351)). Also, reaching the highest energies considered here clearly relies on the acceleration mechanism not being limited by energy-losses on the CMB, which impose tighter constraints at high-z. Another flux that would have likely escaped detection at low-z

could be due to exotic supermassive relics produced in the early universe, if decaying within a lifetime shorter than the Hubble time. Similar scenarios were considered in the past as "top-down" models of UHECRs (352) and are still considered in relation to dark matter candidates (353). Related models would generally leave a major imprint in the UHE neutrino flux, although the complementary sensitivity of cosmological probes remains to be studied. For decays into hadronic final states, the prompt neutrinos and γ rays are expected to originate from comparable numbers of π^+, π^0 and π^-, so that the spectral considerations made in the previous section should roughly apply. A slightly more favourable situation (in the sense of energetically enhancing the relevance of the effects discussed here) could arise in models with preferentially leptonic final states, with comparable energy budgets of prompt neutrinos (now leading to a quasi-monoenergetic spectrum, modulo the z-dependence of the source and $Z, W-$strahlung corrections) and charged leptons. Once again, the modified electromagnetic cascades would be visible in the lower energy part of the spectrum. Of course, for definite scenarios which our results apply to, it would be interesting to perform specific calculations, perhaps including also sub-leading microphysics processes, and moving to full-fledged multimessenger studies. Such tasks are left for future investigations.

In conclusion, if the past is of any guidance, it is wise to be ready for possible surprises from the opening of any new astrophysical window. For the UHE sky at high-z, one should be aware that differences are present with respect to naive expectations valid at low-z, which is, without a doubt, the most important message of this work.

3

A γ-Ray Connection between Neutrinos and UHECRs

In this Chapter, we describe a multi-messenger correlation established between TeV – PeV astrophysical neutrinos and UHECRs, made possible through our observations of γ rays at sub-TeV energies. IceCube is the main experiment responsible for collecting the neutrino data. Although we have relatively good measurements of the total diffuse neutrino flux, the community is far from reaching a consensus about the exact nature of its sources. A particularly interesting property of their sources to consider is whether or not they are opaque to the escape of γ rays. These photons should be produced alongside neutrinos through the *pp* and $p\gamma$ scenarios, described in Sections 1.3.2.1 and 1.3.2.2. If they are able to escape their sources without getting absorbed, they should undergo EM cascades en route to the Earth, as studied extensively in the previous chapter, ending up at energies $\lesssim$ TeV.

This diffuse flux of γ rays accompanying the astrophysical neutrino flux should be end up as part of the EGB, which was presented in Section 1.1.1. We begin this chapter by describing the EGB in more detail in Section 3.1, pointing out its contributions coming from well-established classes of astrophysical objects. Another component of the EGB comes from cosmogenic γ rays, that is, those coming from the interactions of UHECRs with the CMB/EBL/CRB as they propagate across the Universe. These should also cascade down to the EGB energy range, although their precise flux shape can vary depending on the original spectra and composition of UHECR emitters. This will be the topic of Section 3.2, where we discuss our method for simulating UHECR propagation using the public code CRPropa 3.2 (354).

Finally, in Section 3.3 we will move on to calculating the diffuse γ-ray flux coming from the astrophysical neutrino sources. This will require the approximate formalism developed in Section 1.3.2.3 and the sections leading up to it. Together, these three contributions to the EGB should impose tight constraints on the opacity of the IceCube neutrino sources, as well as revealing an interplay between the TeV – PeV neutrino flux and the (quite uncertain) composition of UHECRs. Unfortunately, due to time constraints, this analysis has not yet been concluded. However, some preliminary results are presented in this thesis.

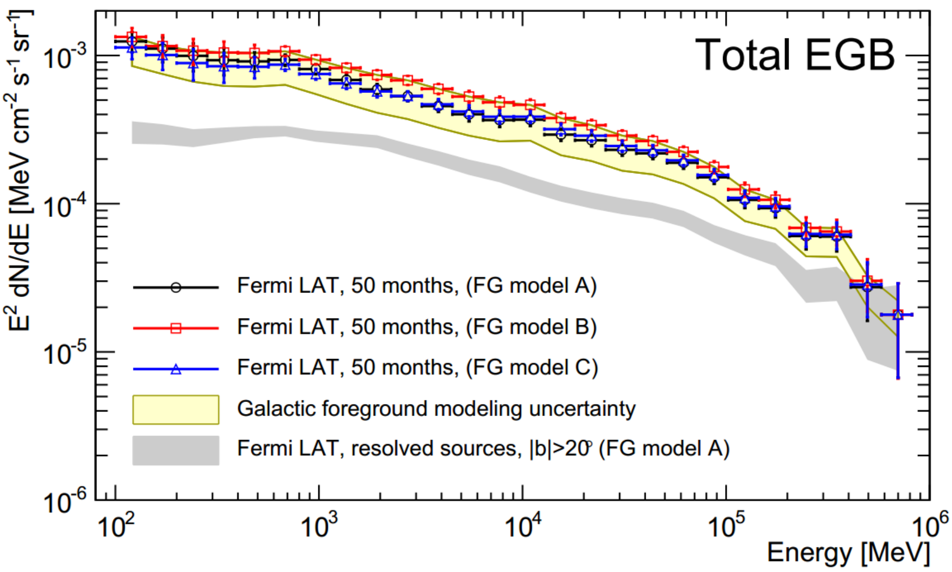

Figure 3.1: Total EGB flux, including point-source and diffuse contributions, measured by *Fermi*-LAT between 100 MeV and 820 GeV at $|b| > 20°$ (17). The data is presented for three different foreground models for the diffuse Galactic emission (see Table 2 in (17) for their differences). Error bars include statistical and systematic uncertainties. The yellow shaded region represents the systematic uncertainty coming specifically from the modeling of the diffuse Galactic emission. For foreground model A, the flux solely from resolved sources is shown as a gray band.

3.1
The Extragalactic γ-Ray Background

The EGB has been measured between 100 MeV and 820 GeV by *Fermi*-LAT (17) and is shown in Figure 3.1. The main challenge in measuring the extragalactic γ rays in this energy band involves subtracting the Galactic foregrounds. Notably, the Galactic center produces an intense flux of γ rays which is quite difficult to model. For this reason, the EGB intensities are only reported for high galactic latitudes ($|b| > 20°$; b is measured starting from the Galactic plane).

Besides the Galactic center, another background which is comparable to the EGB at $\gtrsim$ 1 GeV is the diffuse Galactic emission. This is a result from CR interactions with gas and radiation in the ISM. To model the diffuse Galactic emission, three assumptions regarding the CR injection and propagation were assumed, denoted as foreground models A, B and C in Figure 3.1. For a summary of their main differences, we refer the reader to Table 2 in (17). Naturally, subtracting each foreground model from the total observed flux results in different EGB intensities reported by *Fermi*-LAT, all displayed in Figure 3.1, along with error bars including statistical and systematic uncertainties in each case.

A last residual background contamination comes from CRs. Once they interact with the detector, some of them can be misclassified as γ rays. Additionally, CRs can induce atmospheric showers, containing γ rays that may be picked up by *Fermi*-LAT. To subtract these mis-reconstructed events, their expected distribution must be obtained from simulations based on our knowledge of detector-response and atmospheric models. Achieving the best compromise between a low CR background uncertainty and high statistics is actually the reason why *Fermi*-LAT restricts their analysis between 100 MeV and 820 GeV.

Fermi-LAT also makes available for download a detailed list of their measured EGB intensities[1] for each model as supplementary material in (17). For the convenience of the reader, we convert the EGB intensities into fluxes in each energy bin in *Fermi*-LAT's analysis and display them in Table 3.1, along with their uncertainties (including statistical and instrument-related systematics), for all three foreground models.

If we remove all resolved point-like and extended sources from the EGB[2], we are leftover with the purely unresolved IGRB, briefly mentioned in Section 1.1.1, and now displayed in Figure 3.2 for all three Galactic foreground models. A readable table containing IGRB intensities is also available in the supplemental material provided in (17).

3.1.1
Conventional EGB Contributions

We shall now point out what classes of astrophysical objects yield well-established and meaningful contributions to the EGB (and the IGRB). Crucially, we will also comment on their potential as source candidates of the observed IceCube neutrino flux. As a reminder to the reader, most of the classes of sources mentioned in this section have been introduced in Section 1.2. For a quick summary of what is about to be presented, one can go straight to Figure 3.4, showing the main components adding up to produce the EGB and IGRB, respectively.

---

[1] What *Fermi*-LAT reports in their tables as "intensity", F_i [$\mathrm{cm}^{-2}\,\mathrm{s}^{-1}\,\mathrm{sr}^{-1}$], in each energy bin i is actually the flux Φ [$\mathrm{MeV}^{-1}\ \mathrm{cm}^{-2}\,\mathrm{s}^{-1}\,\mathrm{sr}^{-1}$] integrated over that energy bin:

$$F_i = \int_{\Delta E_i} \Phi(E)\,\mathrm{d}E \approx \Phi(E_i)\Delta E_i \ , \tag{3-1}$$

where E_i is the central energy of bin i and ΔE_i is its bin width. To recover the flux in that bin, we simply calculate $\Phi(E_i) = F_i/\Delta E_i$. Figure 3.1 is displaying $E^2\Phi(E)$ in the y-axis, under a different notation.

[2] Technically, *Fermi*-LAT first obtains the IGRB through the isotropic component of a multi-component fit (355). Then, the EGB is calculated by adding the sky-averaged intensity of $|b| > 20°$ resolved sources.

Table 3.1: EGB fluxes and their uncertainties, in [GeV cm^{-2} s^{-1} sr^{-1}], for each FG model considered in (17).

Energy Bins [GeV]		**EGB Fluxes** $E^2\Phi(E)$ [GeV cm^{-2} s^{-1} sr^{-1}]		
Lower bound	Upper bound	FG Model A	FG Model B	FG Model C
0.1	0.1414	$(1.29 \pm 0.20) \times 10^{-6}$	$(1.39 \pm 0.20) \times 10^{-6}$	$(1.17 \pm 0.20) \times 10^{-6}$
0.1414	0.2	$(1.15 \pm 0.22) \times 10^{-6}$	$(1.20 \pm 0.22) \times 10^{-6}$	$(1.04 \pm 0.22) \times 10^{-6}$
0.2	0.2828	$(1.03 \pm 0.22) \times 10^{-6}$	$(1.12 \pm 0.22) \times 10^{-6}$	$(9.2 \pm 2.2) \times 10^{-7}$
0.2828	0.4	$(9.6 \pm 2.0) \times 10^{-7}$	$(1.08 \pm 0.20) \times 10^{-6}$	$(8.8 \pm 2.0) \times 10^{-7}$
0.4	0.5657	$(9.5 \pm 1.4) \times 10^{-7}$	$(1.08 \pm 0.15) \times 10^{-6}$	$(8.7 \pm 1.4) \times 10^{-7}$
0.5657	0.8	$(9.7 \pm 0.8) \times 10^{-7}$	$(1.11 \pm 0.09) \times 10^{-6}$	$(9.0 \pm 0.8) \times 10^{-7}$
0.8	1.1314	$(8.4 \pm 0.7) \times 10^{-7}$	$(9.7 \pm 0.7) \times 10^{-7}$	$(7.8 \pm 0.6) \times 10^{-7}$
1.1314	1.6	$(7.1 \pm 0.6) \times 10^{-7}$	$(8.6 \pm 0.6) \times 10^{-7}$	$(6.7 \pm 0.6) \times 10^{-7}$
1.6	2.2627	$(6.1 \pm 0.5) \times 10^{-7}$	$(7.7 \pm 0.6) \times 10^{-7}$	$(5.9 \pm 0.5) \times 10^{-7}$
2.2627	3.2	$(5.5 \pm 0.4) \times 10^{-7}$	$(7.1 \pm 0.5) \times 10^{-7}$	$(5.5 \pm 0.4) \times 10^{-7}$
3.2	4.5255	$(4.7 \pm 0.4) \times 10^{-7}$	$(6.2 \pm 0.5) \times 10^{-7}$	$(4.9 \pm 0.4) \times 10^{-7}$
4.5255	6.4	$(4.2 \pm 0.4) \times 10^{-7}$	$(5.5 \pm 0.5) \times 10^{-7}$	$(4.3 \pm 0.4) \times 10^{-7}$
6.4	9.051	$(3.8 \pm 0.4) \times 10^{-7}$	$(5.0 \pm 0.5) \times 10^{-7}$	$(4.0 \pm 0.4) \times 10^{-7}$
9.051	12.8	$(3.8 \pm 0.4) \times 10^{-7}$	$(4.8 \pm 0.4) \times 10^{-7}$	$(4.0 \pm 0.4) \times 10^{-7}$
12.8	18.1019	$(3.04 \pm 0.28) \times 10^{-7}$	$(3.93 \pm 0.35) \times 10^{-7}$	$(3.31 \pm 0.30) \times 10^{-7}$
18.1019	25.6	$(2.79 \pm 0.25) \times 10^{-7}$	$(3.52 \pm 0.30) \times 10^{-7}$	$(2.99 \pm 0.26) \times 10^{-7}$
25.6	36.2039	$(2.40 \pm 0.21) \times 10^{-7}$	$(3.00 \pm 0.25) \times 10^{-7}$	$(2.55 \pm 0.22) \times 10^{-7}$
36.2039	51.2	$(2.28 \pm 0.20) \times 10^{-7}$	$(2.76 \pm 0.23) \times 10^{-7}$	$(2.39 \pm 0.20) \times 10^{-7}$
51.2	72.4077	$(1.97 \pm 0.18) \times 10^{-7}$	$(2.33 \pm 0.20) \times 10^{-7}$	$(2.04 \pm 0.18) \times 10^{-7}$
72.4077	102.4	$(1.57^{+0.16}_{-0.15}) \times 10^{-7}$	$(1.85 \pm 0.17) \times 10^{-7}$	$(1.63 \pm 0.16) \times 10^{-7}$
102.4	144.8155	$(1.11 \pm 0.13) \times 10^{-7}$	$(1.31^{+0.15}_{-0.14}) \times 10^{-7}$	$(1.15 \pm 0.14) \times 10^{-7}$
144.8155	204.8	$(9.8 \pm 1.3) \times 10^{-8}$	$(1.12 \pm 0.14) \times 10^{-7}$	$(1.01^{+0.14}_{-0.13}) \times 10^{-7}$
204.8	289.6309	$(6.4 \pm 1.2) \times 10^{-8}$	$(7.3 \pm 1.3) \times 10^{-8}$	$(6.6 \pm 1.2) \times 10^{-8}$
289.6309	409.6	$(6.4^{+1.4}_{-1.3}) \times 10^{-8}$	$(7.0^{+1.4}_{-1.3}) \times 10^{-8}$	$(6.6^{+1.4}_{-1.3}) \times 10^{-8}$
409.6	579.2619	$(3.0^{+1.3}_{-1.2}) \times 10^{-8}$	$(3.3 \pm 1.3) \times 10^{-8}$	$(3.1^{+1.3}_{-1.2}) \times 10^{-8}$
579.2619	819.2	$(2.0 \pm 1.2) \times 10^{-8}$	$(2.0 \pm 1.3) \times 10^{-8}$	$(2.0^{+1.3}_{-1.2}) \times 10^{-8}$

Let us start with the point-like contributions to the EGB. Thousands of γ-ray sources have been catalogued in several data releases by the *Fermi*-LAT Collaboration, the latest one at the time of writing this thesis being (356). The vast majority of them are resolved AGNi, mostly blazars (catalogued separately in (357)), although there are also several other types of astrophysical sources. Only a subset of them are extragalactic objects active in the range 100 MeV – 820 GeV (and above), where we have EGB data. Figure 3.3 shows an estimation of the resolved BL Lacs and FSRQs to the EGB (358). Notice how they are subdominant with respect to the IGRB, implying that most of the EGB comes from unresolved sources. Indeed, it is estimated that blazars account for $50^{+12}_{-11}\%$ of the EGB photons, and only $\sim 70\%$ of them have been resolved (359). As mentioned in the Introduction, very few of these point-sources have shown statistically significant correlations with neutrino events at IceCube. Therefore,

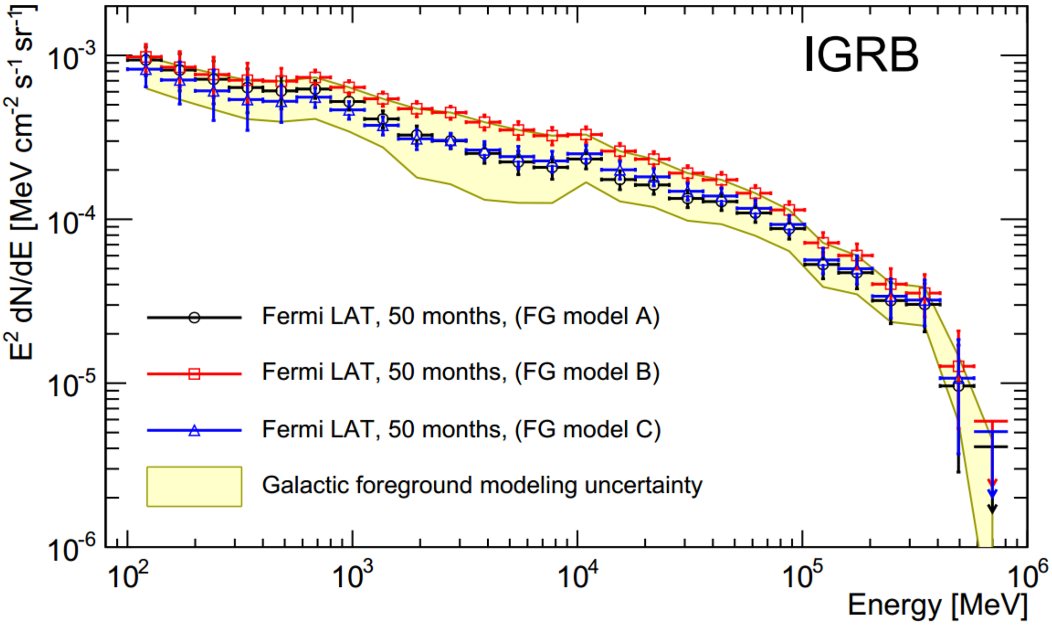

Figure 3.2: Same as Figure 3.1 but for the IGRB (17).

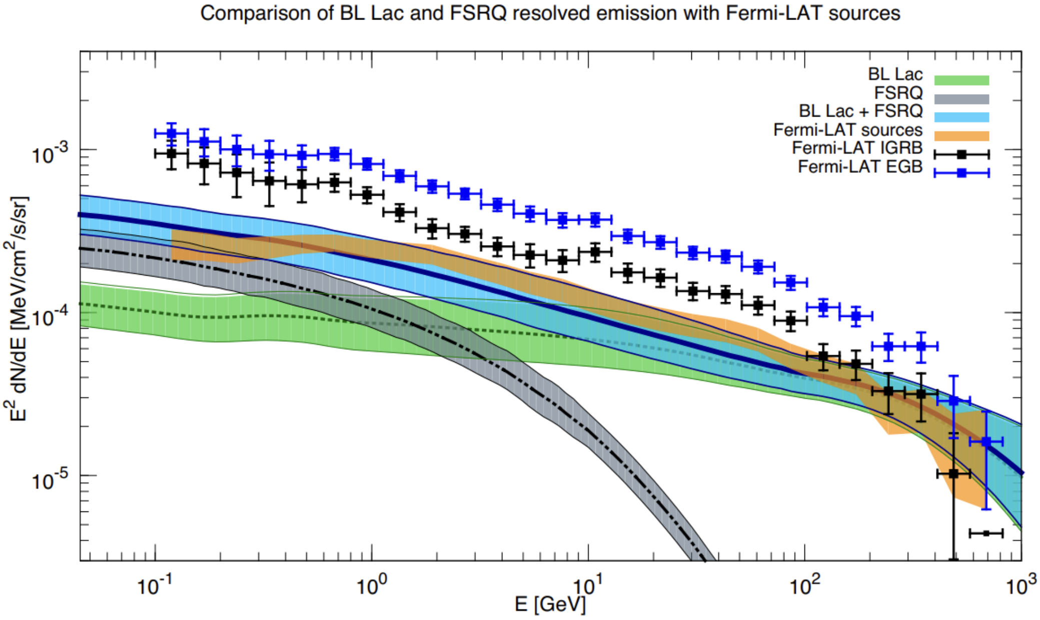

Figure 3.3: γ-ray flux from resolved *Fermi* sources (orange band; identical to the gray band in Figure 3.1, considering blazars from the 2FGL catalog within the Galactic foreground model A), along with estimated contributions from resolved BL Lacs (green band) and FSRQs (grey band). The total estimated blazar flux from point sources is shown as a blue band. Figure from (358).

these objects cannot account for any meaningful fraction of the astrophysical neutrino flux.

Broadening our discussion to include both the resolved and unresolved/diffuse parts of the EGB, relevant contributions come from blazars, RGs and SFGs[3]. In most models, BL Lacs dominate at $\gtrsim 100$ GeV energies, while FSRQs, RGs, and SFGs become more relevant at the low-energy part of the EGB. Because they are so γ-ray bright, the resolved and unresolved blazar fluxes are usually comparable. The RG and SFG components, on the other hand, tend to be, essentially, totally diffuse.

The general method to calculate the diffuse emission from a γ-ray source class is the following:

1. First, one must infer their intrinsic spectra $\mathrm{d}N/\mathrm{d}E_\gamma$ based on our observations of resolved objects in that class. For example, high-energy blazar spectra typically contain two broad bumps, one spreading across IR to X-ray energies coming from internal synchrotron emission of electrons, and another peaking in the MeV – TeV range[4], with a less clear origin (361). These curved shapes invite many kinds of intrinsic spectral functional forms, including broken power laws (362), double power laws (157, 359), power laws with exponential cutoffs, log-parabolas, single power laws (363, 364) and others (365).

   RG spectra are less well understood (since there are few resolved sources at our disposal (357)), being typically modeled by simple power laws (366, 367, 368). SFGs are also modeled with power laws, log-parabolas or more complicated spectra (160, 369, 161).

   A common theme among most of spectra is that they do not predict a significant emission above TeV energies. This means that, even if we believe the models presented to us, and consider their γ rays to have a purely hadronic origin, they should still not produce the neutrino flux observed by IceCube. The astrophysical neutrino flux should come from an additional population of sources, or from an additional > TeV component present in these sources.

2. Secondly, one must adopt a γ-ray *luminosity function* for the sources,

   $$\rho(z, L_\gamma) = \frac{\mathrm{d}^2 N}{\mathrm{d}L_\gamma\,\mathrm{d}\mathcal{V}_c}\ . \tag{3-2}$$

   This function describes the redshift evolution of the comoving number density of sources $\mathrm{d}N/\mathrm{d}\mathcal{V}_c$ per differential γ-ray luminosity interval

---

[3] A hidden population of Galactic millisecond pulsars, which has not been accounted for in *Fermi*-LAT's subtraction of Galactic foregrounds, is also estimated to contribute $\lesssim 0.9\%$ of the IGRB above $|b| > 10^\circ$ at around 2 GeV (360). See the bottom left panel in Figure 3.5.

[4] FSRQ spectra typically peak in the MeV band, while BL Lacs have a second peak at GeV energies and above.

> dL_γ. Several parametrizations exist for Eq. (3-2), the most popular ones being the pure luminosity, pure density, and luminosity-dependent density evolutions (370). These parametrizations are fit by comparing the number of expected objects from a given model to the actual observed number. Details of this procedure can be found in (363) and references therein, as well as many other works.
>
> Additionally, to account for the variability in the power-law spectral index Γ of sources, one has to assume a specific distribution for $\mathrm{d}N/\mathrm{d}\Gamma$. This is normally taken to be independent of redshift and follow a Gaussian distribution.

Once these assumptions are made, calculating the resulting EGB flux is relatively straightforward and requires no further modeling (except for the choice of EBL used in estimating γ-ray attenuation). We leave the details for the interested reader to find in (157, 363). Note that some calculations in the literature disregard the cascaded contribution from these source classes to the EGB, since their $>$ TeV emission is typically negligible.

We close off by showing the wide range of predictions for the conventional EGB and IGRB contributions in Figures 3.4 and 3.5, respectively. The first of these shows several models for the total (point-like + unresolved) blazar fluxes (as well as unresolved and cascaded BL Lac fluxes individually, on the top right) comprising the EGB. It also shows different estimations for the RG and SFG total fluxes, which are basically completely diffuse, found in the literature. In all of them we notice a common trend: BL Lacs dominating at high energies and an uncertain composition of source classes at low energies, with the total sum saturating our EGB observations, within their uncertainties.

Figure 3.5 is analogous to Figure 3.4, but for the IGRB. In the case of diffuse emissions, the variability between different models is quite large. In the top two panels, the behavior of blazar contributions is quite similar to each other (as well as to the bottom two panels of Figure 3.4). RGs also account for a large fraction of the IGRB across the entire energy range on the two left panels. Interestingly, there have been recent claims that SFGs individually dominate the IGRB (161). This is in conflict with most other models found in the literature (not just those estimating the SFG diffuse emission, but also those claiming that RGs dominate the IGRB instead), and still an ongoing subject of debate.

These figures reveal the main takeaway from this section: conventional EGB contributions nearly saturate the observed flux, leaving very little wiggle room for any additional contribution. In the past, this has already proven useful in establishing multi-messenger constraints on the γ-ray counterpart of the

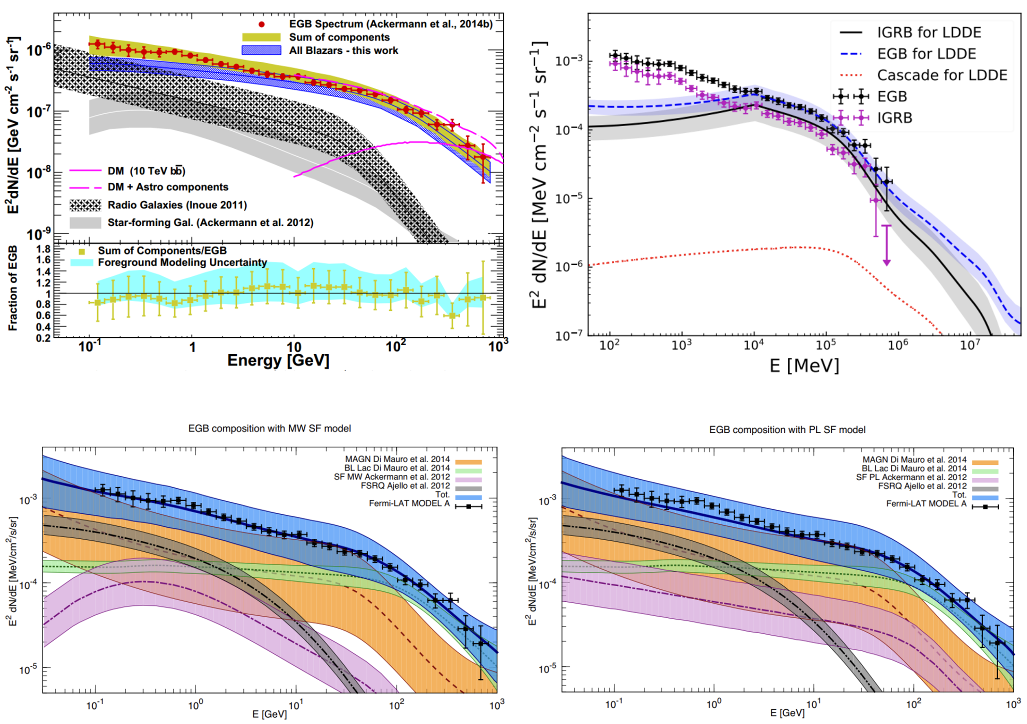

Figure 3.4: Several models for the different EGB contributions. All of them show EGB data points, unless specified. The reader is referred to the original references for details. *Top left*: Blazars from (359) (where the plot was taken from), RGs from (367), and SFGs from the "Milky Way model" in (371). The sum of all these components, along with its uncertainty, is shown as a yellowish-green band. *Top right*: BL Lac contribution from (362), where the plot was taken from, separated into resolved + unresolved ("EGB for LDDE"), unresolved only ("IGRB for LDDE"), and cascaded unresolved components. *Bottom left*: BL Lac contribution from (363), FSRQ contribution from (157), RG contribution from (366), and SFG contribution from the "Milky Way model" in (371). *Bottom right*: Same as bottom left, but for the "Power Law model" model for SFGs in (371). Both bottom plots were taken from (358), and have the sum of all their components represented by blue bands.

IceCube neutrino flux (20, 19), as well as new physics constraints (359). A study including both the astrophysical neutrino counterpart in photons, as well as the contribution of UHECRs have never been made. This is the goal of the work presented here, which should establish an interesting and novel connection between these cosmic messengers, involving their source distributions and emission spectra/composition. In the next section, we describe how we obtain the cosmogenic flux from UHECR propagation, which cascades down into the EGB energy range.

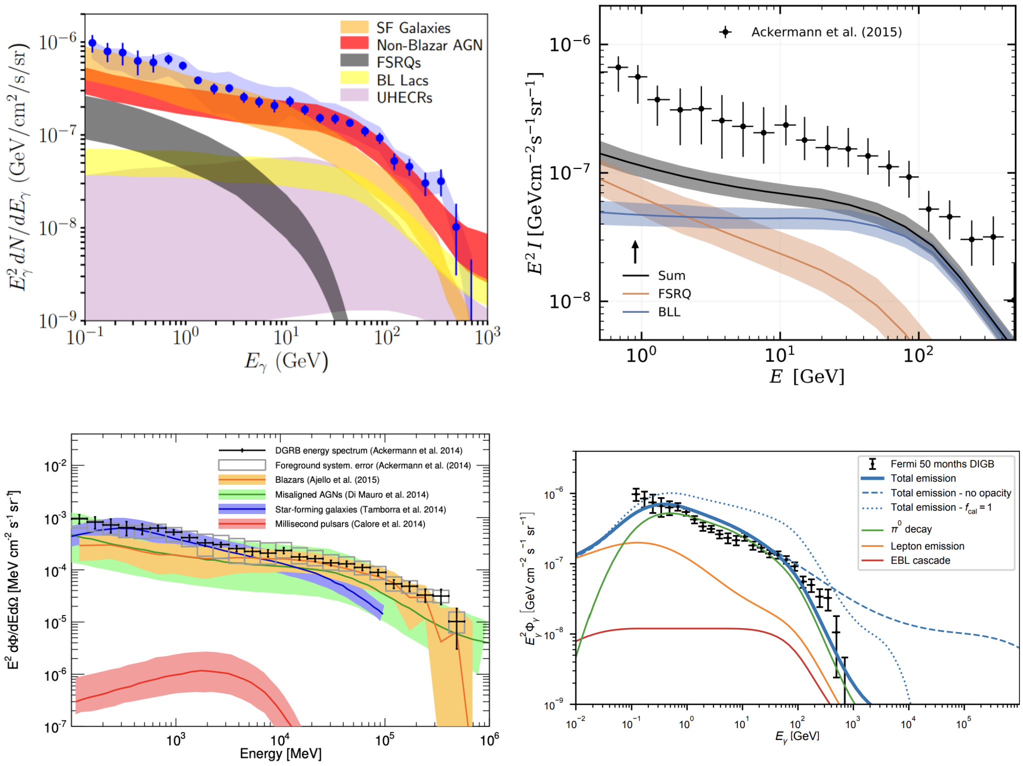

Figure 3.5: Similar to Figure 3.4, showing many models for the diffuse IGRB contributions. All of them show IGRB data points by *Fermi*-LAT. The reader is referred to the original references for details. *Top left*: RGs from (368), SFGs from (372), BL Lacs/FSRQs from (373), and UHECR cascaded contribution from cosmogenic γ rays from (374). Figure taken from (375). *Top right*: Blazar contributions from (364), where the plot was taken from. *Bottom left*: Blazars from (359), RGs from (366), SFGs from (369), and millisecond pulsar diffuse Galactic emission from (360). *Bottom right*: SFG contribution to the IGRB estimated by (161), with its different leptonic and hadronic components, as well as the additional flux resulting from EM cascades.

3.2
Cosmogenic γ rays from UHECRs

Besides the conventional contributions to the EGB presented in the last section, another guaranteed flux in this energy range comes from the interactions of UHECRs with the cosmic radiation fields as they propagate through the Universe. These interactions lead to the production of neutral pions, which decay to produce UHE cosmogenic γ rays. Together with electron-positron pairs, also produced during CR propagation, these particles initiate electromagnetic cascades that bring them down to sub-TeV energies, resulting in an additional component to the EGB observed at the Earth.

This flux depends not only on the cascade dynamics, as described in Chapter 2, but also on the characteristics of the sources responsible for UHECR production. Namely, their distribution with redshift and their CR emission spectra and composition are known to significantly affect the final cosmogenic γ-ray flux (374, 376, 377). Our best chance at reconstructing these source properties is by inferring them based on our UHECR observations at the Earth. The observed spectrum has already been presented in Figure 1.5, their redshift distribution is mostly unknown, and in the next section, we summarize the current status on their composition measurements. After that, we shall describe the processes taking place during UHECR propagation through intergalactic space, which will also lead us to understand how cosmogenic γ rays (and neutrinos) are produced. We then describe out methodology for simulating cosmological propagation of CRs and their secondary particles by using the publicly available Monte Carlo code CRPropa 3 (354). Finally, we show some estimates of cosmogenic γ-ray fluxes at the Earth for different scenarios.

3.2.1
The Observed Composition of UHECRs

As stated in the Section 1.1.2, the main UHECR detectors at present are PAO and TA. Both of them consist in a large surface array of detectors[5] along with fluorescence detector telescopes overseeing the ground array. These instruments capture the secondary particles produced in EASs that arise from CR interactions in the atmosphere. The arrival time differences at the ground detectors of particles in the EAS can be used to reconstruct the CR's arrival direction. The EAS also produces an UV fluorescence by exciting nitrogen molecules in the atmosphere, allowing the fluorescence detectors to observe the longitudinal development of the shower.

We can use the morphology of the shower and the energy of the detected particles to reconstruct other important information about the original CR, such as its energy and mass. While the energy can be determined via calorimetric measurements by the fluorescence detector, obtaining the mass of the initial CR is more complicated. We define the *slant depth* (X, typically expressed in [g/cm^2]) as the cumulative density of matter traversed by the EAS from its origin O down to a given point P on the shower's trajectory,

$$X = \int_O^P \rho_{\mathrm{atm}}(\ell)\, \mathrm{d}\ell \ , \tag{3-3}$$

where $\rho_{\mathrm{atm}}(\ell)$ is the atmospheric density as a function of the distance along the trajectory of the shower. The slant depth at the point where the shower has its maximum number of particles is known as the "depth of shower maximum", X_{max}, and can be measured by the fluorescence detectors even at UHEs (378).

---

[5] PAO uses an array of water Cherenkov detectors, while TA uses scintillation detectors that are sensitive to ionized particles passing through.

$X_{\rm max}$ is an important quantity because it can be used to infer the mass of the initial CRs. More precisely, one can measure many EASs and utilize the first two moments of their $X_{\rm max}$ distribution – its mean $\langle X_{\rm max}\rangle$ and dispersion $\sigma(X_{\rm max})$ – to extract the first two moments of the (natural log of the) mass composition A from that sample. The key relations are (379)

$$\langle \ln A\rangle = \frac{\langle X_{\rm max}\rangle - \langle X_{\rm max}\rangle_p}{f_E} \ , \qquad \sigma^2_{\ln A} = \frac{\sigma^2(X_{\rm max}) - \sigma^2_{\rm sh}(\langle \ln A\rangle)}{b\sigma_p^2 + f_E^2} \ , \tag{3-4}$$

where $\langle X_{\rm max}\rangle_p$ and σ_p^2 are the mean and variance of $X_{\rm max}$ for proton showers, f_E and b are parameters that depend on the specific hadronic interaction model used in EAS simulations, and $\sigma^2_{\rm sh}(\ln A) = \sigma^2_{\rm sh}(X_{\rm max}|\ln A)$ is the variance intrinsic to shower-to-shower fluctuations from primary CRs of mass A. In reality, there are variations on this method (380), as well as other methods altogether that enable mass discrimination using signals from the ground detector (381, 382, 383, 384). With all of these techniques combined, PAO and TA determine their observed composition of UHECRs. However, both experiments use different strategies when it comes to selecting the data sets used in $X_{\rm max}$ measurements, which leads to incompatibilities between their results. There has been an ongoing working group between the collaborations making progress towards analyzing both results in an equal footing (72), although no agreement has been reached yet regarding $\sigma(X_{\rm max})$ above $10^{18.5}$ eV.

PAO results are shown in Figure 3.6. The top panels display their energy-dependent $\langle X_{\rm max}\rangle$ and $\sigma(X_{\rm max})$ data from four different detector stations (labelled "HEAT", "FD", "SD", and "AERA"; see (56) and references therein). They can be compared with pure-proton or pure-iron composition expectations from three hadronic interaction models (QGSJet-II.04, EPOS-LHC, and Sibyll 2.3c). More important for us, the bottom panels show the corresponding energy dependence of the $\ln A$ moments for each detector station and hadronic model considered. The bottom left plot shows a decrease in the average mass number of CRs from ~ 0.2 EeV until the ankle region (~ 3 EeV), where the composition starts becoming progressively heavier.

Meanwhile, TA results can be found in Figure 3.7, where their own $\langle \ln A\rangle$ estimations under QGSJet-II.04 are shown for two different groupings of detectors (left panel) and compared with PAO data (right panel). Clearly, above $10^{18.5}$ eV, both measurements diverge, with TA claiming a relatively light and energy-independent average atomic number, in contrast to the increasingly heavier composition seen by PAO. The composition of UHECRs is definitely still an open problem and one worthwhile studying in this project. Our method to tackle this issue will be via their cascaded cosmogenic γ-ray fluxes, strongly constrained by the EGB.

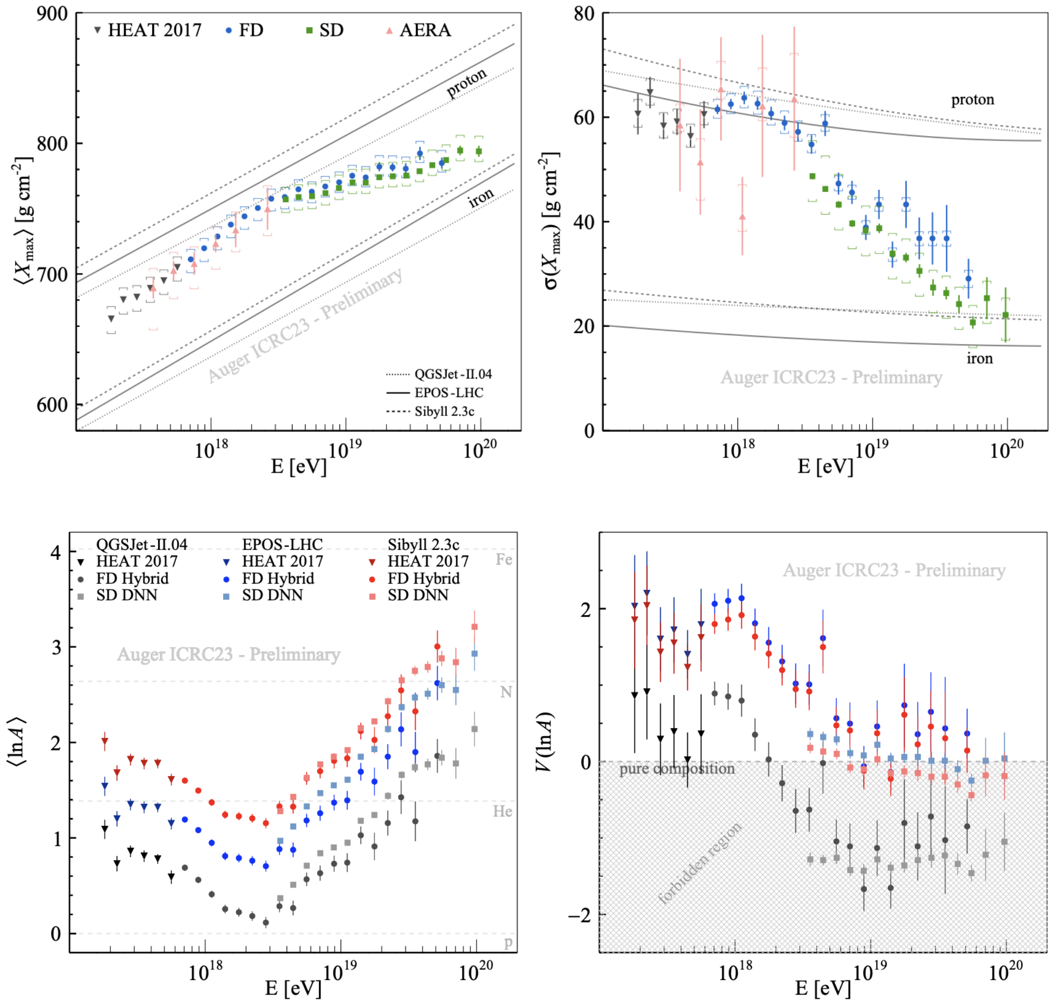

Figure 3.6: Composition measurements from PAO. *Top*: average depth of shower maxima (left) and their variance (right) between 0.2 – 100 EeV. Results are shown for different detector arrays (different colors and point shapes), and can be compared to pure-proton and pure-iron predictions from different hadronic interaction models (different line tracings). *Bottom*: corresponding values obtained for the mean (left) and variance (right) of the natural logarithm of the CR atomic mass numbers. Gray dashed lines in the background of the left panel mark the $\ln A$ values for a few reference elements. Figure from (56).

One should always keep in mind that the composition arriving at the Earth is not necessarily the same as the one emitted at the source. A CR nucleus can undergo several interactions with background photons as they propagate through intergalactic space. In particular, it can break apart into smaller nuclei, resulting in a lighter composition at the Earth than at its source. These propagation effects are the topic of the next section.

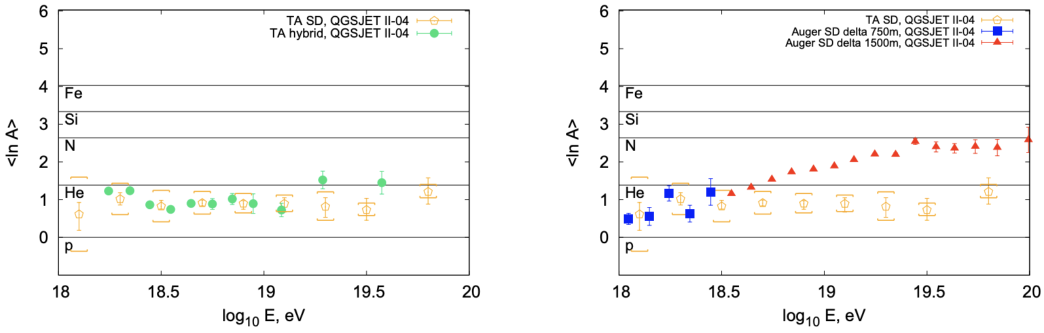

Figure 3.7: Composition measurements by the TA Collaboration, using different groups of detector arrays (left), and compared with PAO data (right). Figure from (385).

3.2.2
UHECR Propagation through Intergalactic Space

High-energy nuclei N are susceptible to various energy-loss and composition-changing processes during their propagation through the cosmos, due to cosmological redshift, magnetic fields, and interactions with the CMB and other ubiquitous background photons $\gamma_{\rm bkg}$. All of these have already been mentioned before, but we recap them below.

- Bethe-Heitler pair production,

$$N + \gamma_{\rm bkg} \to N + e^+ + e^- \ , \tag{3-5}$$

  producing secondary electrons and positrons. This interaction has a threshold at $s_{\rm th} = (Am_p + 2m_e)^2$, corresponding to

$$E_{N,{\rm th}} = \frac{m_e(Am_p + m_e)}{\epsilon} \tag{3-6}$$

  in the ultra-relativistic limit (lab frame). For a reference CMB photon energy of 10^{-3} eV, one finds $E_{N,{\rm th}} \approx A \times 4.8 \times 10^{17}$ eV. The differential and total cross sections are cumbersome and not necessary for our purposes, although they can be found in (386, 387, 313, 388, 389). More important is the qualitative behavior of CRs under this interaction: (3-5) has a very low inelasticity, meaning that the $e^\pm$ pair carries away a small fraction ($\lesssim 10^{-3}$) of the parent nucleus' energy (388, 390, 391, 392). As such, (3-5) can be treated approximately as a continuous energy loss process.

- Photomeson production (responsible for the GZK cutoff discussed earlier),

$$N + \gamma_{\rm bkg} \to \pi^{\pm,0} + X \ , \tag{3-7}$$

  with the main proton channels being $p + \gamma_{\rm bkg} \to n(p) + \pi^+(\pi^0)$. As mentioned in Section 1.3.2.2, multi-pion production is also possible at

UHEs. This process kicks in at a higher threshold energy than Bethe-Heitler pair production (see Eq. 1-33), but provokes a catastrophic energy loss for the incoming CR (258, 259).

- Photodisintegration of composite nuclei,

$$N + \gamma_{\rm bkg} \rightarrow N' + X \ , \tag{3-8}$$

  where N' is the new nucleus after N has lost one or more nucleons X (*e.g.* $X = n, p, n+p, \alpha, ...$). The cross sections for these process are dominated by the giant dipole resonance (393, 394, 395) (see Figure 1 in (396) as an example for Fe-γ collisions) at photon energies of $\sim 10 - 30$ MeV in the nucleus rest frame, which translates to an energy region between Bethe-Heitler pair production and photomeson production for UHECRs. Although there are models to parametrize these processes for astrophysical applications (397, 398), modern simulations use nuclear event generators (399, 400, 401) to extract interaction rates and branching ratios (354). In practice, the most glaring effect of photodisintegration is the change the composition of UHECRs as they propagate, maintaining the energy per nucleon approximately conserved.
- α-, $\beta^{\pm}$-, or γ-decay of unstable nuclei N' or X produced in photodisintegration reactions (3-8).
- Elastic scattering of CRs off of background photons, similar to the ICS process for electrons, where some energy from the nucleon is transferred to the photon. The energy loss induced by this process is negligible with respect to the other processes (397), and only relevant at low energies, below Bethe-Heitler pair production threshold.
- Adiabatic energy loss due to the expansion of the Universe, occurring at a rate

$$\frac{1}{E}\frac{\mathrm{d}E}{\mathrm{d}t} = -H(z) \ . \tag{3-9}$$

- Magnetic field deflection, which can lead to the diffusion of UHECRs and suppression of their flux at energies below $\sim$ EeV (402). This effect is quite model-dependent and only important outside of our considered energy range. As such, we neglect it. Synchrotron energy losses can also be safely neglected for nuclei, as opposed to electrons, since Eq. (2-16) scales with $(qm_e/me)^4 \sim 10^{-13}\,(Z/A)^4$.

In Figure 3.8, we show the mean free paths of the aforementioned processes different UHECR nuclei at EeV and above, at $z = 0$. Target fields included in these calculations include the CMB and the EBL, modeled by (403). The evolution of protons during propagation is dominated by photopion

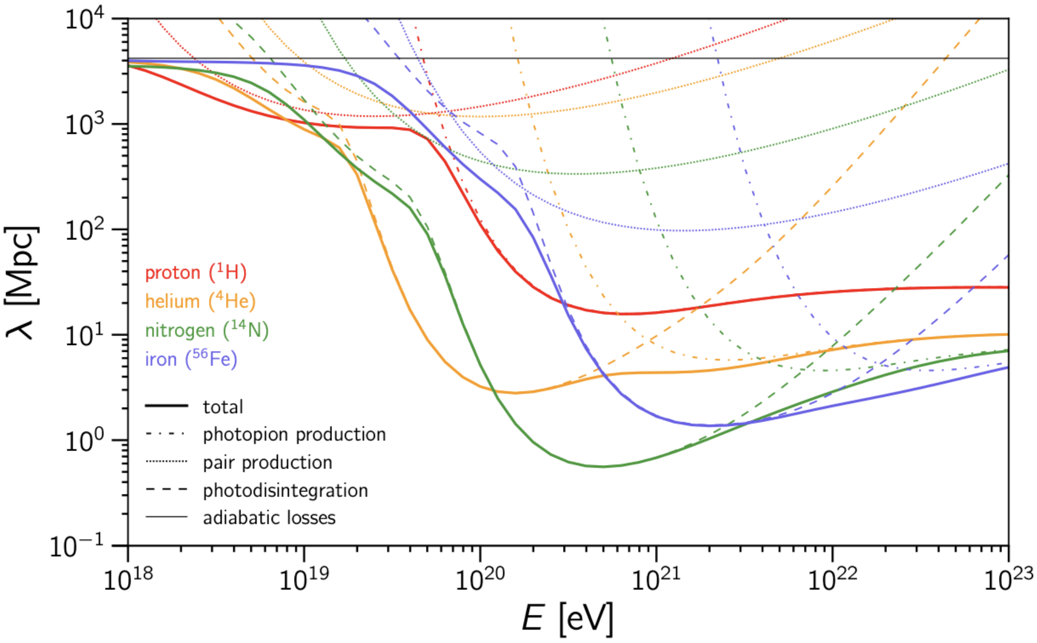

Figure 3.8: Energy-loss lengths for UHECR nuclei due to interactions with the CMB and EBL (403), as well as adiabatic losses from cosmic expansion. Figure reproduced from (281).

production at $E_p \gtrsim 5 \times 10^{19}$ eV and pair production below that. For heavier nuclei however, the effect of photomeson interactions is only felt at extremely high energies ($\gtrsim$ 1 ZeV for helium, $\gtrsim$ 20 ZeV for iron), and the main interaction in most of the UHE range is photodisintegration. With this picture in mind, we expect a nitrogen nucleus emitted at 10^{21} eV, for example, to immediately undergo successive photodisintegrations with the CMB until 14 protons are left, with energy $E_p \sim 10^{21}/14$ eV, which then suffer photomeson, pair production, and adiabatic energy losses until they reach the Earth.

All of these interactions between CRs and radiation fields end up producing secondary particles. Those which are stable may also reach the Earth and give us important information about the journey of primary CRs en route to us. Cosmogenic neutrinos arise from (i) the decay of charged pions in photopion production, (ii) the decay of neutrons also coming from photopion production, and (iii) the decay of unstable nuclei after photodisintegration reactions. The first case produces neutrinos at an energy a few percent that of the parent nucleon, whereas the other two cases yield much less energetic neutrinos ($\lesssim 0.1\%$ of the decaying nucleon's energy). As a result, cosmogenic neutrino flux predictions usually show a two-bump feature: a small bump at $\sim$ 10 PeV from nuclear decay and a large bump at $\sim$ EeV or above from pion decay (404). Simultaneously, electrons and photons are generated in (i) neutral pion decays, (ii) charged pion decays (from the subsequent decay of $\mu^{\pm}$), (iii) decays of excited nuclei from photodisintegration, and (*iv*) Bethe-Heitler pair production. When considering UHECRs, all of these EM secondaries are so energetic that they should still undergo EM cascading before reaching the Earth. Since the UHECR sources are unknown to us, the resulting cosmogenic γ-ray flux should constitute a diffuse contribution to the EGB.

3.2.3
Simulations with CRPropa 3.2

It should be clear by now that the problem of UHECR propagation and production of secondaries is quite complex. In order to get precise predictions for their fluxes at the Earth, compatible with the high precision of our current multi-messenger detectors, one requires the precision of numerical simulations. For this purpose, we have chosen to use the publicly available Monte Carlo code CRPropa 3.2 (354).

CRPropa provides a sophisticated platform to model the intricate interactions between UHECRs and the various astrophysical environments they encounter throughout their cosmic journey. In its latest version (3.2), it contains interaction modules for all relevant processes in UHECR and secondary propagation; see Figure 4 in (354). In particular, it contains EPP, ICS, ETP, and DPP modules necessary to simulate EM cascades within its own framework, unlike previous versions which relied on external (and somewhat unreliable) cascading codes (405). Additionally, CRPropa 3.2 uses a thinning procedure to deal with the large photon/electron multiplicities that arise in EM cascades, saving it from having to track all particles individually and improving computational time.

CRPropa works in the following way: we give it a set of source-related input parameters (redshift distribution, UHECR emission spectrum and composition), choice of photon backgrounds (we include the CMB, along with the EBL model by Gilmore *et al.* (403) in our simulations[6]), select the particle interaction modules included in the simulation, and choose a number of injected CRs, N_{part}, into the Monte Carlo simulation. The example below contains a Python code that simulates UHECR propagation for $N_{\text{part}} = 10^5$ and records the resulting spectra/composition at $z = 0$, illustrating how these inputs are fed into CRPropa:

Code 1: Example CRPropa simulation code for UHECR propagation

```python
# Importing CRPropa3
from crpropa import *

```

---

[6] We have tested that other EBL models have no noticeable effects on our results

```
# Creating sources
source = Source()
source.add(SourceParticleType(nucleusId(56, 26))) # pure iron
    composition
source.add(SourcePowerLawSpectrum(0.01*EeV, 1000*EeV, -1)) #
    E^-1 spectrum from 0.01 EeV to 1000 EeV
source.add(SourceUniform1D(0*Mpc, redshift2ComovingDistance
    (6))) # uniform source distribution between z=0 and z=6
source.add(SourceRedshift1D()) # positions z=0 at origin

# Setting up simulation
sim = ModuleList()
sim.add(SimplePropagation(0.1*kpc,10*kpc)) # simulation
    module for 1D propagation without magnetic fields,
    limiting propagation stepsize to [0.1,10] kpc
sim.add(Redshift()) # adding cosmological redshift
sim.add(MinimumEnergy(0.01*TeV)) # mininum energy in
    simulation: particles below 0.01 TeV are not recorded
# Turning on interactions with different photon backgrounds
sim.add(ElectronPairProduction(CMB()))
sim.add(ElectronPairProduction(IRB_Gilmore12()))
sim.add(PhotoPionProduction(CMB()))
sim.add(PhotoPionProduction(IRB_Gilmore12()))
sim.add(PhotoDisintegration(CMB()))
sim.add(PhotoDisintegration(IRB_Gilmore12()))
sim.add(NuclearDecay())

# Creating an observer that detects all particles
obs = Observer()
obs.add(ObserverPoint()) # places observer at origin

# Creating output file
output = TextOutput("output.txt", Output.Event1D)
output.enable(Output.SourceEnergyColumn) # saving energy of
    original (emitted) CR
output.enable(Output.CurrentEnergyColumn) # saving energy
    upon arrival at the Observer
output.enable(Output.CurrentIdColumn) # saving type of
    particle upon arrival
output.enable(Output.SourcePositionColumn) # saving position/
    distance of the source
obs.onDetection(output)
sim.add(obs)

#Running the simulation
sim.run(source, 100000) # injected particles: N_part = 100000
```

As can be seen, the code has a simple structure: import the CRPropa module, set the source parameters, set the interactions, set observers which detect particles, create output files, run. In Code 1 above, the Observer is detecting all particles (primary and secondary), but it is usually more convenient to define different observers to detect different types of particles, *e.g.* one observer for nuclei, another for photons, another for neutrinos, etc. For example, see the code excerpt below, where we not only create multiple observers for different particles, but also customize the content of each output file:

Code 2: Creating observers and output files for different particles

```
# Observer for all particles
obs = Observer()
obs.add(ObserverPoint()) # places observer at z=0
output = TextOutput("all.txt", Output.Event1D)
output.disableAll() # disables all default information saved
    in output file (useful to save memory space)
output.enable(Output.SourceEnergyColumn)
output.enable(Output.CurrentEnergyColumn)
output.enable(Output.CurrentIdColumn)
output.enable(Output.SourcePositionColumn)
obs.onDetection(output)
sim.add(obs)

# Observer for nuclei
nuclobs = Observer()
nuclobs.add(ObserverPoint())
nuclobs.add(ObserverPhotonVeto()) # no photons
nuclobs.add(ObserverElectronVeto()) # no electrons/positrons
nuclobs.add(ObserverNeutrinoVeto()) # no neutrinos
nucloutput = TextOutput("nucl.txt", Output.Event1D)
nucloutput.enable(Output.CreatedPositionColumn) # position
    [Mpc] where the particle was created; if particle survived
     directly from source, this is simply the source position
nucloutput.enable(Output.CreatedEnergyColumn) # energy [EeV]
    of particle when it was created
nuclobs.onDetection(nucloutput)
sim.add(nuclobs)

# Observer for photons
photonobs = Observer()
photonobs.add(ObserverPoint())
photonobs.add(ObserverNucleusVeto()) # no nuclei
photonobs.add(ObserverNeutrinoVeto())
photonobs.add(ObserverElectronVeto())
```

```
photonoutput = TextOutput("photons.txt", Output.Event1D)
photonoutput.enableAll() # include all output information
photonobs.onDetection(photonoutput)
sim.add(photonobs)
```

The outputs are file containing all the particles detected by each Observer, as well as whatever information about these particles we choose to include (initial and final energies, positions, etc). In running the simulation, we set the final parameter N_{part}, which is proportional to the running time (if not parallelized) and the output file size; the more particles injected, the more particles produced during propagation and detected at the Earth.

After the running of the code, we can manipulate the output file and extract the final energy spectrum and composition from the information contained in it. This is done by separating the final particles into energy bins and creating a histogram. We can then divide the number of particles $\mathrm{d}N$ in each bin by their bin widths $\mathrm{d}E$ and obtain the spectrum $\mathrm{d}N/\mathrm{d}E$ by interpolating over all bins. This can be interpreted as an isotropic flux if we divide by a unit area, a unit time and a unit solid angle, which should just affect the overall normalization, without modifying its shape/energy-dependence. With that said, the overall normalization is always left as a free parameter since it depends on N_{part}. We later normalize the resulting fluxes to match our UHECR observations.

Some caveats regarding CRPropa's functionality and limitations are in order. These will hopefully help the reader interested in using the code for their own simulations.

- It seems to always be necessary to include an observer that detects all particles. The reason for this requirement is unknown, but the code shows defective outputs when this observer is absent.
- The order of setup commands (source setup, interactions modules, creating observers, etc.) in the code is important! For safety, follow the order used in Code 1.
- It is possible to define observers that detect particles at their point of creation, rather than at $z = 0$, by using `ObserverDetectAll()` rather than `ObserverPoint()`. Be caferul, however, that detecting particles will, by default, remove them from the simulation. To avoid this and make sure these particles (or their secondaries) also reach observers placed at $z = 0$, the user must include `obs.setDeactivateOnDetection(False)` after `obs.onDetection(output)`.

- The output file size can be an issue in CRPropa, exceeding 10 GB in some cases, which is why it is important to control $N_{\rm part}$, especially when detecting electrons and positrons.
- Although the module `SimplePropagation` has by default minimum and maximum stepsizes of 0.1 kpc and 1 Gpc, it will always try to pick the largest possible propagation step. This may lead to problems if the energy-loss length of any interaction is larger than the stepsize used by the code. For safety, we set the maximum stepsize to 10 kpc in all our simulations, which is smaller than or comparable to the energy-loss length for all processes involved. Of course, this comes at a huge cost of computational time.
- We have not included the presence of the CRB in our simulations, since their implementation seems to be problematic in version 3.2 (due to missing files in the CRPropa library).
- The more recent CRBeam code (336) has pointed out some discrepancies with CRPropa results, which they traced back to issues with CRPropa's implementation of EBL redshift evolution and with their pre-computed tables for the energy distribution of secondaries. This should not affect significantly the conclusions of this work; the consequence of these predicaments is just a mild overestimation of cascaded γ-ray fluxes. Also, note that the EBL redshift evolution is still quite uncertain, showing high variability among different models in the literature.
- Although CRPropa's documentation includes modules that allow us to set arbitrary emission spectra and source distributions, we could not find any explanation of how to implement them in simulation. The only available options that seem to work reliably are using `SourcePowerLawSpectrum(Emin, Emax, s)` for a power-law spectrum E^s between $E_{\rm min}$ and $E_{\rm max}$ and `SourceUniform1D(dc,min, dc,max)` for a homogeneous distribution between comoving distances $d_{c,\rm min}$ and $d_{c,\rm max}$.

The last item in the list above is quite inconvenient, as we would like to test several different assumptions for the injection spectra and, especially, the redshift evolution of UHECR sources. In order to overcome this, we have devised a method to modify the spectrum and distribution *after* performing the simulations. We start by running the code for a large number of particles, assuming an E^{-1} power-law emission spectrum within a large range $[E_{\rm min}, E_{\rm max}]$, so that particles are injected uniformly[7] across all energies of interest, and assuming a uniform source evolution between $z = [0, 8]$ (we neglect UHECR

---

[7] In other words, the differential number of particles in $[E, E+{\rm d}E]$, given by $({\rm d}N/{\rm d}E)\,{\rm d}E$, is constant.

production from sources outside of this range). Once the output file is produced, instead of making a simple histogram of its particles, as previously described, we implement a *weighted* histogram instead. The weight of particle i in the output file, w_i, is given by

$$w_i = E_{0,i} \times \frac{\mathrm{d}N_{\mathrm{inj}}}{\mathrm{d}E_0}(E_{0,i}) \times f(z_{0,i}) \;, \tag{3-10}$$

where $\frac{\mathrm{d}N_{\mathrm{inj}}}{\mathrm{d}E_0}(E_0)$ is the desired injection spectrum, $f(z)$ is the desired redshift evolution, $E_{0,i}$ and $z_{0,i}$ are the initial energy and redshift of the injected CR that produced particle i (it can be the particle itself) and the factor of $E_{0,i}$ at the start compensates for the default E^{-1} spectrum used in the simulation. Note that we have control of CRPropa to provide us with each $E_{0,i}$ and $z_{0,i}$ in the output files.

Effectively, what we are doing is transforming that one initial CR that produced particle i into w_i identical CRs, which would then produce w_i particles identical to particle i. Since both the emission spectrum and the z-distribution are proportional to the normalization (*i.e.* the number of injected CRs, which is what the weighting changes) at each energy and redshift, this weighting procedure is equivalent to changing these initial conditions altogether. An advantage that comes with this weighting method is that scanning over several parameters, *e.g.* redshift evolution, spectral index of sources, etc., can be done by running CRPropa with our default parameters only once, and then changing the weights post-simulation, saving a lot of time.

One final example of code is shown below. In fact, this is the code used for our simulations of cosmogenic γ-ray fluxes at the Earth. Notice that we control the particles kept track by CRPropa after each interaction (we deactivate neutrinos to save computational time). We also inject a very small number of particles per γ-rays Monte Carlo simulation. This is because these simulations take a lot of time to run, even for this small number of particles. For example, the code below can take between 5 – 10 days to run (on a Macbook Pro M1), depending on the initial energy/position of the injected He nuclei. For iron nuclei, a single particle can take over a month to simulate!

Code 3: Final code used for γ-ray simulations

```
from crpropa import *

# Choosing what particles we keep track in the simulation
electrons = True
photons = True
neutrinos = False
antinucleons = True
```

```
# Creating sources
source = Source()
source.add(SourceParticleType(nucleusId(4, 2))) #protons:(1,1), He:(4,2), N:(14,7), Si:(28,14), Fe:(56,26)
source.add(SourcePowerLawSpectrum(0.01*EeV, (10**3.5)*EeV, -1)) #dNdE(Emin, Emax, alpha); keep alpha=-1 and the range [Emin,Emax] large (they will be adjusted later in weighting to match any spectrum we want)
source.add(SourceUniform1D(0, redshift2ComovingDistance(8))) #uniform F(z) between z=0 and z=8 (also adjusted in weighting); redshift2ComovingDistance(z) redshift conversion already gives d_c in Mpc
source.add(SourceRedshift1D()) # positions z=0 at origin; must be added after SourceUniform1D

# Setting up simulation
sim = ModuleList()
sim.setShowProgress(True)
sim.add(SimplePropagation(0.1*kpc, 10*kpc))
sim.add(Redshift())
sim.add(MinimumEnergy(10*GeV)) # keeping track of EM cascades below 10 GeV takes extremely long...

# Interaction modules format: (bkg, secondary particles)
sim.add(ElectronPairProduction(CMB(), electrons))
sim.add(ElectronPairProduction(IRB_Gilmore12(), electrons))
sim.add(PhotoPionProduction(CMB(), photons, neutrinos, electrons, antinucleons))
sim.add(PhotoPionProduction(IRB_Gilmore12(), photons, neutrinos, electrons, antinucleons))
sim.add(PhotoDisintegration(CMB(), photons))
sim.add(PhotoDisintegration(IRB_Gilmore12(), photons))
sim.add(NuclearDecay(electrons, photons, neutrinos))
sim.add(ElasticScattering(CMB()))
#EM Cascade interactions. Format: (photon bkg, secondary particles, thinning). We use maximal thinning (=1).
sim.add(EMInverseComptonScattering(CMB(), photons, 1))
sim.add(EMInverseComptonScattering(IRB_Gilmore12(), photons, 1))
sim.add(EMPairProduction(CMB(), electrons, 1))
sim.add(EMPairProduction(IRB_Gilmore12(), electrons, 1))
sim.add(EMDoublePairProduction(CMB(), electrons, 1))
sim.add(EMDoublePairProduction(IRB_Gilmore12(), electrons, 1))
sim.add(EMTripletPairProduction(CMB(), electrons, 1))
sim.add(EMTripletPairProduction(IRB_Gilmore12(), electrons, 1))
```

```

# Observer for all particles that reach z=0
obs = Observer()
obs.add(ObserverPoint())
output = TextOutput("He-all.txt", Output.Event1D)
output.disableAll()
output.enable(Output.SourceEnergyColumn)
output.enable(Output.CurrentEnergyColumn)
output.enable(Output.CurrentIdColumn)
output.enable(Output.SourcePositionColumn)
obs.onDetection(output)
sim.add(obs)

# Observer for nuclei
nuclobs = Observer()
nuclobs.add(ObserverPoint())
nuclobs.add(ObserverPhotonVeto())
nuclobs.add(ObserverElectronVeto())
nuclobs.add(ObserverNeutrinoVeto())
nucloutput = TextOutput("He-nucl.txt", Output.Event1D)
nucloutput.enable(Output.SourcePositionColumn) # for
    implementing weights (to have arbitrary z-distribution)
nuclobs.onDetection(nucloutput)
sim.add(nuclobs)

# Observer for photons
photonobs = Observer()
photonobs.add(ObserverPoint())
photonobs.add(ObserverNucleusVeto())
photonobs.add(ObserverNeutrinoVeto())
photonobs.add(ObserverElectronVeto())
photonoutput = TextOutput("He-gamma.txt", Output.Event1D)
photonoutput.disableAll()
photonoutput.enable(Output.SourcePositionColumn) # for
    implementing weights (to have arbitrary z-distribution)
photonoutput.enable(Output.SourceEnergyColumn) # for
    implementing weights (to have arbitrary inj. spectrum)
photonoutput.enable(Output.CurrentEnergyColumn)
photonoutput.enable(Output.WeightColumn) # weight of each
    particle induced by thinning procedure; we multiply this
    in the weight w_i of each particle during the post-
    simulation weighting procedure
photonobs.onDetection(photonoutput)
sim.add(photonobs)

sim.run(source, 10, True)
```

In Section 3.4, we will show some preliminary results of our CRPropa simulations. For the moment, let us talk about the γ rays associated to the last messenger on our list: neutrinos.

3.3
The Electromagnetic Counterpart of Astrophysical Neutrinos

In this section, we shall describe our model-independent methodology for calculating the γ-ray flux associated to the IceCube neutrino observations. This methodology was developed in (19) and refined in (20), and assumes that the astrophysical neutrino sources are transparent to the escape of high-energy γ rays. This picture is, of course, disfavored by multi-messenger considerations (19, 20, 406, 407), but it is not yet set in stone.

The first step will be to describe IceCube's observations of astrophysical neutrinos. This requires understanding how the detector works, what signals do neutrinos produce within it and a brief understanding of the atmospheric backgrounds dominating the flux below $\sim$ 200 TeV. We will then present several datasets created by the IceCube collaboration, each with its own best fit for the astrophysical neutrino flux. Finally, we describe a systematic approach to calculating the γ-ray fluxes at the Earth corresponding to these neutrino observations.

3.3.1
IceCube and its Astrophysical Neutrino Observations

The *IceCube Neutrino Observatory* (408) is currently the largest and most important experiment with the goal of measuring the diffuse flux of astrophysical neutrinos at $\gtrsim$ TeV energies. It is located near the South Pole and is comprised of detectors above and below the surface. Its underground array consists of 86 strings carrying 60 digital optical modules (DOMs) each, which have been deployed deep within the clear Antarctic ice, between 1450 – 2450 m in depth. These are arranged in a hexagonal array with a 125 m spacing between strings, and a 17 m vertical spacing between DOMs in each string, covering a total fiducial volume of $\sim 1\ \text{km}^3$. This large instrumented volume is optimized for detecting neutrinos with energies above $\gtrsim$ 100 GeV. The symmetrical structure is broken by a tighter arrangement of strings and DOMs around the center of the detector, known as DeepCore (409). This densely instrumented region is optimized for detecting atmospheric neutrinos down to $\sim$ a few GeV. On the surface, IceCube has an array of ice-Cherenkov tanks spanning an area of $\sim 1\ \text{km}^2$ known as IceTop (410). Its goal is to detect CR-induced EASs produced in the atmosphere, as well as to serve as a veto

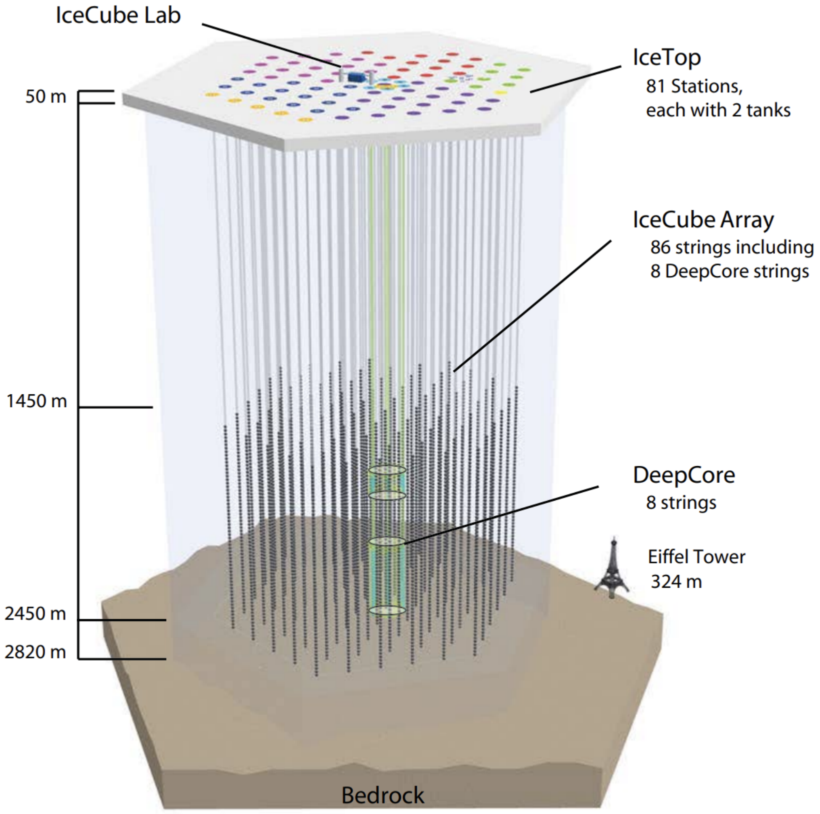

Figure 3.9: The IceCube Detector with its components DeepCore and IceTop. Figure from (411).

against the atmospheric background in the underground detector. All of these structures can be visualized in Figure 3.9.

Three years after its completion and inauguration in December 2010, IceCube reported its first direct evidence for the existence of an astrophysical neutrino flux (412), with the observation of two $\sim$ PeV-energy neutrinos affectionately named "Bert" and "Ernie". Soon after, an improved sensitivity and an extended energy coverage down to ~ 30 TeV allowed them to claim 26 additional events (413), increasing the confidence of an astrophysical flux interpretation to $\sim 4\sigma$. All of the reported events so far had something in common: the interaction vertex between the neutrino and the ice nucleus was located within detector's fiducial volume. IceCube eventually extended their searches to include signals coming from interactions outside the detector (414), finally increasing the confidence in an astrophysical excess beyond the discovery threshold: 6.7σ (415). Currently, IceCube data is consistent with an isotropic, diffuse flux of neutrinos in the few TeV – few PeV range, with an approximately equal flavor composition. Isotropy indicates that these neutrinos must have an extragalactic origin (416) (neglecting the Galactic component, which has recently been detected at a 4.5σ level (216)).

The all-flavor astrophysical neutrino flux is usually fitted by a power law,

$$\Phi_\nu(E_\nu) = \Phi_{\rm astro} \times 10^{-18} \left(\frac{E_\nu}{100\ \rm TeV}\right)^{-\gamma_{\rm astro}} , \qquad \text{for } E_\nu \geq E_{\rm th} \ , \tag{3-11}$$

with a normalization $\Phi_{\rm astro}$ $[\rm GeV^{-1}\,cm^{-2}\,s^{-1}\,sr^{-1}]$ and a spectral index $\gamma_{\rm astro}$ left as free parameters, adjusted to our observations. The fit is only performed above a threshold energy $E_{\rm th}$ to avoid atmospheric background contamination (see Section 3.3.1.2). This functional form is not only motivated by the data itself, but also by the standard multi-messenger picture of diffusive shock acceleration followed by $pp/p\gamma$ interactions in astrophysical sources. Conversely, an accurate determination of $\Phi_{\rm astro}$ and $\gamma_{\rm astro}$ gives us valuable information about the particle acceleration and neutrino production mechanisms at their sources. IceCube classifies its events into many datasets, presented in Section 3.3.1.3, each preferring a unique $(\Phi_{\rm astro}, \gamma_{\rm astro})$ combination (see Figure 3.11). Building up to that, we now take a brief detour to discuss other aspects of IceCube's observations.

3.3.1.1
Event Morphologies

The DOMs at IceCube contain photomultipliers which detect the secondary Cherenkov photons produced from neutrino interactions with the surrounding ice or bedrock. Analysing the energy deposited by these photons, IceCube can extract the incoming neutrino energies and directions. Since neutrinos are not deflected by magnetic fields, these directions point directly back to their sources. The accuracy of event reconstruction depends on several factors such as the vertex location, the initial neutrino energy and the type of interaction with the medium surrounding the detector.

These interactions can be of two types[8]: NC or CC (see Section 1.1.3),

$$\overset{(-)}{\nu}_\ell + N \to \overset{(-)}{\nu}_\ell + N' \qquad \text{(NC)} \ , \tag{3-12}$$

$$\overset{(-)}{\nu}_\ell + N \to \ell^{-(+)} + N' \qquad \text{(CC)} \ , \tag{3-13}$$

where the subscript $\ell = e, \mu, \tau$ refers to a specific lepton flavor and N and N' are the initial and final hadronic states of the nucleus, respectively. All NC interactions, as well as CC interactions with $\overset{(-)}{\nu}_e$ or $\overset{(-)}{\nu}_\tau$ produce what is known as a *"cascade"* signal: a localized, nearly-spherical hadronic shower of particles. Meanwhile, CC $\overset{(-)}{\nu}_\mu$ interactions produce *"muon tracks"*: Cherenkov tracks left

[8] For the $\gtrsim 10$ GeV neutrinos considered at IceCube, these interactions occur within the regime of deep inelastic scattering (417), meaning that N and N' are necessarily different.

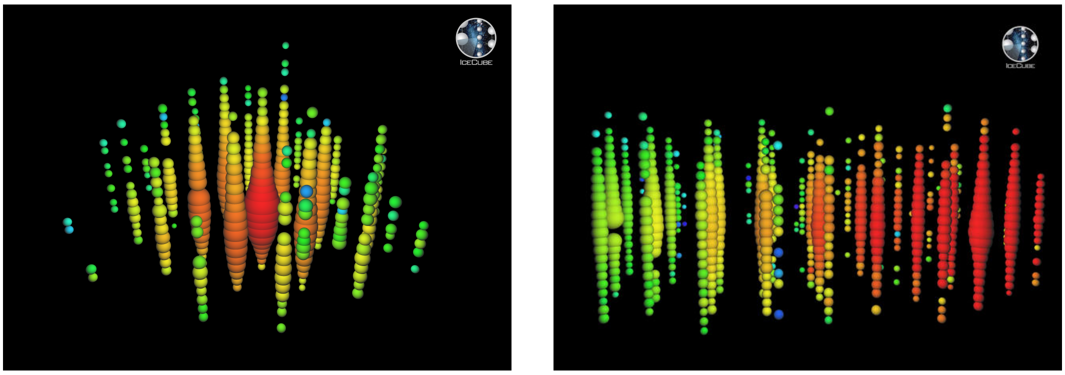

Figure 3.10: *Left*: Cascade event at IceCube from a 1.14 PeV event at IceCube. Each sphere represents a DOM in the detector, and the size of the spheres indicate the amount of Cherenkov light (energy) collected by each DOM. The colors represent time: red DOMs are triggered before orange/yellow/blue DOMs. *Right*: Muon track from a muon crossing IceCube from right to left (in the figure's orientation). This muon was produced in a CC interaction of an 880 TeV neutrino. These (and many more) pictures of events can be found in IceCube's official website (421).

by the final-state muon as it propagates through the detector[9].

Each of these two different morphologies, shown in Figure 3.10, have their advantages and disadvantages. Cascades are generally contained within the detector, conferring them an excellent calorimetric determination of the initial neutrino's energy, within $\sim 15\%$ of the true value (418). On the other hand, their angular resolution is limited ($> 8°$, (190)). These characteristics make cascades ideal for measuring the energy spectrum of the astrophysical neutrino flux. Meanwhile, muon tracks offer a great angular resolution ($< 1°$, (419)) while having poor energy reconstruction capabilities. This makes them ideal for point-source searches. Besides cascades and tracks, more exotic signatures can occur in the detector (420), the most famous one being the "double-bang" morphology from $\overset{(-)}{\nu}_\tau$ CC interactions at $\gtrsim 100$ TeV, which are beyond the scope of this thesis.

3.3.1.2
Atmospheric Muon and Neutrino Backgrounds

As we have seen in Figure 1.6, the atmospheric neutrino flux dominates over the astrophysical one at $\lesssim 200$ TeV. In fact, muon- and neutrino-induced atmospheric events at IceCube overshadow those from astrophysical origin by many orders of magnitude. As such, a good understanding of these backgrounds is crucial if we wish to measure the diffuse extragalactic flux down to $\sim$ TeV

---

[9] Muonic decays of τ leptons ($\tau^- \longrightarrow \nu_\tau + \mu^- + \bar{\nu}_\mu$, branching ratio $\sim 17\%$) produced in ν_τ CC interactions also produce muon tracks.

energies, an energy range which we will find to be quite important for our analysis in this work. In this section, we briefly comment on the origin of these atmospheric fluxes and how IceCube is able to filter them out.

When CRs interact with gas in the Earth's atmosphere, they produce copious amounts of muons and neutrinos in EASs. Atmospheric muons induce muon-track triggers at IceCube at a rate of 3000 Hz (422). There are three ways that one can eliminate/suppress this signal. The first is to consider only up-going tracks in the detector, since muons cannot traverse the Earth before decaying. This comes at the cost of missing nearly half of the sky, including the Galactic center. The second method is to impose a high-energy cut to the event selection criteria (423). This makes the analysis sensitive only to the energy range where the steep atmospheric flux is already very suppressed, but does not allow for a determination of the astrophysical flux in the TeV band. Lastly, it is also possible to filter out most of the entering atmospheric muon tracks by considering only events where the interaction vertex is inside the fiducial volume of the detector. That is, one should define a "veto region" containing DOMs around the edges of the detector such that any track/cascade signals starting in or crossing through that region get vetoed.

Atmospheric neutrinos are much less common (as expected, since neutrinos rarely interact with the detector), but they are still relevant (424) and more tricky to tag and eliminate. Most of them come from the decay of charged pions and kaons created in EASs, producing what is known as the "conventional" atmospheric neutrino flux. Let us briefly discuss its spectral shape. Incoming CRs below the knee follow an $\approx E^{-2.7}$ power-law spectrum. However, if secondary particles produced in EASs lose a significant fraction of their energy before decaying into neutrinos, the resulting neutrino spectrum should be softer than the CR one. Of course, this depends on the secondary particle's energy and incoming zenith angle (which determines the atmospheric column depth and distance that must be traversed). This problem has been treated analytically in (36, 94) and is usually solved numerically in Monte Carlo simulations (425, 426). The end result after zenith integration is an $\approx E_\nu^{-3.7}$ power law flux.

Heavier, charmed mesons (*e.g.* $D^{\pm,0}$) can also be produced in EASs, albeit at higher energies. Their decays results in an additional contribution to the atmospheric background known as the "prompt" atmospheric neutrino flux (427, 428). This name comes from the fact that these heavy mesons decay promptly after being created, without losing energy in scatterings. As such, they follow the CR $E^{-2.7}$ spectrum and eventually overtake the conventional neutrino flux as the dominant atmospheric component. This occurs well into the energy region dominated by the astrophysical flux ($\sim$ PeV energies, quite model dependent), which explains why the prompt flux has never been measured by IceCube (429).

Unlike atmospheric muons, these neutrinos are able to reach the IceCube detector from both hemispheres. A simple directional restriction cannot eliminate such a background. Instead, one must use the fact that these neutrinos are often accompanied by muons (from meson decays), which is never the case for astrophysical neutrinos, whose associated muons have decayed long ago. If a muon and a neutrino event are observed nearly simultaneously and side-by-side, they should be vetoed for safety. This “self-veto” method (430, 431) plays a crucial role for IceCube to select its signal events amidst so much noise coming from the atmosphere.

3.3.1.3
IceCube Datasets

Now that we have covered the common event morphologies and atmospheric background at IceCube, we are ready to present their main datasets, which they use to perform fits to the astrophysical neutrino flux. These samples are organized depending on the distinct background rejection methods adopted by the collaboration. We will not be concerned with the evolution of the datasets over the years (*e.g.* (432, 433, 434, 435)); instead, we just present here the most recent results available at the time of writing this thesis. A summary of the best-fit parameters for each of their single power-law fits using Eq. (3-11) is shown in Figure 3.11.

In no particular order, the datasets are:

– *High Energy Starting Events* (HESE): any event where the interaction vertex marking the origin of the signal is contained within the fiducial volume of the detector, *i.e.* excluding a veto region around the outer layer of the instrumented volume. As previously stated, this helps reduce the atmospheric muon background . The self-veto method is also used to tag neutrino signals within a small time window of a muon track as atmospheric. After collecting 7.5 years of data into their HESE sample (184), IceCube reports a single power-law fit as in Eq. (3-11) with best fit values $\Phi_{\rm astro} = 6.37^{+1.46}_{-1.62}$ and $\gamma_{\rm astro} = 2.87^{+0.20}_{-0.19}$, by using to Wilks' theorem in a frequentist analysis. The low-energy threshold used for the HESE dataset is $E_{\rm th} = 60$ TeV. Many different kinds of fits have also been performed, although there is no preference for them over the single power-law one. This is a common feature among all datasets presented here.

- *Cascades*: events with cascade morphology at IceCube, consisting mainly of electron and tau neutrinos. By construction, this eliminates most of the atmospheric muon background, while self veto is still required to suppress the atmospheric neutrino background. The main background is attributed to faint tracks, which deposit most of their energy in a single bremsstrahlung, mimicking a cascade-like event. With 6 years of cascade data (436), IceCube's power-law fit to Eq. (3-11) yields $\Phi_{\rm astro} = 3 \times 1.66^{+0.25}_{-0.27}$ and $\gamma_{\rm astro} = 2.57 \pm 0.07$, where the factor of 3 in the normalization approximately converts the per-flavor into to the all-flavor flux, since $(\nu_e : \nu_\mu : \nu_\tau)_\oplus \approx (1 : 1 : 1)$ is assumed. Slight variations arise from considering pp (just reported) and $p\gamma$ scenarios at the source. The threshold for this analysis is $E_{\rm th} = 16$ TeV.
- *Through-going muon tracks*: up-going track events from muon neutrinos arriving at the Earth through the Northern celestial hemisphere. The probability of neutrinos crossing the Earth's interior before reaching the detector depends on their energy and incoming zenith angle (437), with absorption kicking in above a few TeV. Naturally, neutrinos entering just below the horizon have a higher chance of surviving. Best-fit values for Eq. (3-11) with 9.5 years of data (438) indicate $\Phi_{\rm astro} = 3 \times 1.44^{+0.25}_{-0.26}$ and $\gamma_{\rm astro} = 2.37 \pm 0.09$, valid down to $E_{\rm th} = 15$ TeV.
- *Inelasticity*: The inelasticity (the ratio of hadronic cascade energy to total neutrino energy) distribution of neutrinos is well described within the SM framework in the deep inelastic scattering regime. Using inelasticity measurements of astrophysical neutrinos, one can characterize their energy spectrum using both muon tracks and cascades (439). Using 5 years of IceCube data (440), the astrophysical flux is found to be consistent with Eq. (3-11) with $\Phi_{\rm astro} = 3 \times 2.04^{+0.23}_{-0.21}$ and $\gamma_{\rm astro} = 2.62 \pm 0.07$ all the way down to $E_{\rm th} = 3.5$ TeV.
- *Enhanced Starting Track Event Selection* (ESTES): by taking advantage of muon-track morphologies for dynamic vetoes (441) and using sophisticated machine learning algorithms to better reduce atmospheric muon contamination, IceCube is now able to extend its astrophysical neutrino searches down into low TeV energies. The ESTES dataset takes advantage of fiducial-volume vetoing, self-vetoing, and boosted decision trees to build a highly pure sample of astrophysical neutrino candidates. With 10.3 years of data analyzed (442), they find $\Phi_{\rm astro} = 3 \times 1.68^{+0.19}_{-0.22}$ and $\gamma_{\rm astro} = 2.58^{+0.10}_{-0.09}$ for the parameters in Eq. (3-11), extending down to $E_{\rm th} = 3$ TeV.

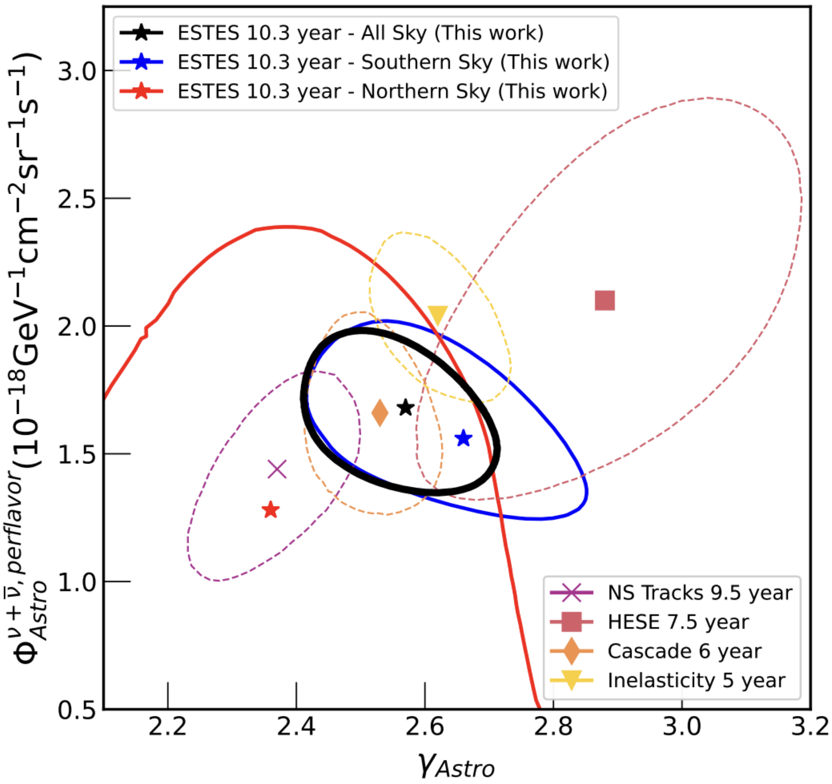

Figure 3.11: Best-fit parameters following Eq. (3-11) and their 68% confidence intervals for different IceCube datasets. The normalization corresponds to the per-flavor flux, which is defined to be 1/3 of the total, all-flavor one. The results are mostly consistent with each other. Figure from (442).

3.3.2
Corresponding Cascaded γ-ray Fluxes

We have seen that IceCube's astrophysical neutrino observations indicate the presence of a diffuse extragalactic flux (since it is approximately isotropic) with a power-law spectrum arriving at the Earth. If we assume a redshift distribution for these sources, we can reconstruct their emission spectra via Eq. (1-45). In particular, a power-law injection $\mathrm{d}N_\nu/\mathrm{d}\varepsilon_\nu = A\varepsilon_\nu^{-\gamma}$ gives us a power-law flux at the Earth with the same spectral index,

$$\Phi_\nu^{\mathrm{diff}}(E_\nu) = \frac{A}{4\pi}\left[\int_0^\infty \mathrm{d}z\,\frac{\mathcal{F}(z)}{H(z)}\,(1+z)^{-\gamma}\right] E_\nu^{-\gamma}\,, \tag{3-14}$$

just like the fit performed by IceCube using Eq. (3-11).

Given an emission spectrum of neutrinos, the corresponding γ-ray emission can be obtained through Eq. (1-37), assuming a pp or $p\gamma$ for these particles. As long as there is no intra-source absorption of γ rays, these will cascade down to sub-TeV energies during cosmological propagation, becoming a diffuse EGB contribution. For the purpose of our analysis, we wish to be as conservative as possible in order to obtain robust constraints. This requires assuming the lowest possible neutrino/γ-ray emission at their sources, while still interpreting IceCube data. A simple power-law injection $\mathrm{d}N_\nu/\mathrm{d}\varepsilon_\nu = A\varepsilon_\nu^{-\gamma}$, is not the best we can do. Since IceCube is not sensitive to the astrophysical flux below E_{th} (whose exact value depends on the dataset considered), we can assume a break in the power law below this energy, to suppress any emission beyond what is really necessary to account for their observations.

Inspired by the $p\gamma$-threshold break (discussed in Section 1.3.2.2), we then assume

$$\frac{\mathrm{d}N_\nu}{\mathrm{d}\varepsilon_\nu}(\varepsilon_\nu) = \begin{cases} B & \varepsilon_\nu < \varepsilon_{\mathrm{br}} \\ A\ \varepsilon_\nu^{-\gamma} & \varepsilon_{\mathrm{br}} < \varepsilon_\nu < \varepsilon_{\mathrm{cut}} \\ 0 & \varepsilon_\nu > \varepsilon_{\mathrm{cut}} \end{cases} , \tag{3-15}$$

where A and B are normalization constants satisfying $B = A\varepsilon_{\mathrm{br}}^{-s_h}$ for continuity at $\varepsilon_\nu = \varepsilon_{\mathrm{br}}$. We also impose a sharp cutoff at $\varepsilon_{\mathrm{cut}} = 10$ PeV because IceCube has not seen any neutrinos with higher energy. Although the IceCube dataset fits do not extend up to such a high energy, the flux is so low that this assumption simply does not affect our results. In fact, the most important factors determining a large γ-ray flux at the Earth are the spectral index γ and the break energy position $\varepsilon_{\mathrm{br}}$.

We can associate our parameters to the ones introduced in the IceCube fit (3-11). The spectral indices equal ($\gamma = \gamma_{\mathrm{astro}}$) and the normalizations are straightforwardly related by

$$\frac{A}{4\pi}\left[\int_0^\infty \mathrm{d}z\, \frac{\mathcal{F}(z)}{H(z)}\,(1+z)^{-\gamma}\right] = \Phi_{\mathrm{astro}} \times 10^{-8}\left(\frac{1}{100\ \mathrm{TeV}}\right)^{-\gamma} . \tag{3-16}$$

However, the break energy $\varepsilon_{\mathrm{br}}$ at the source does not reflect exactly the position of the spectral break at the Earth. For a point source at redshift z, we expect the break at the Earth to be $E_{\mathrm{br}} = \varepsilon_{\mathrm{br}}/(1+z)$ due to cosmological redshifting. If we have a distribution of sources, this break will be smoothed out at the Earth, in contrast to the sharp break occurring at the sources. Of course, since IceCube does not observe a break in the true spectrum with any relevant statistical significance, we must have $E_{\mathrm{br}} \leq E_{\mathrm{th}}$. Although E_{th} varies between datasets, they are all detecting the same astrophysical neutrino flux. As such, we can consider the smallest value $E_{\mathrm{th}} = 3$ TeV for the ESTES dataset.

The general procedure should be clear at this point:

1. Assume a distribution of astrophysical neutrino sources with redshift, $\mathcal{F}(z)$.

2. Assume a set of parameters A, γ, $\varepsilon_{\mathrm{br}}$, and $\varepsilon_{\mathrm{cut}}$ in Eq. (3-15) consistent with IceCube observations at the Earth (using Eq. (1-45)). The corre-

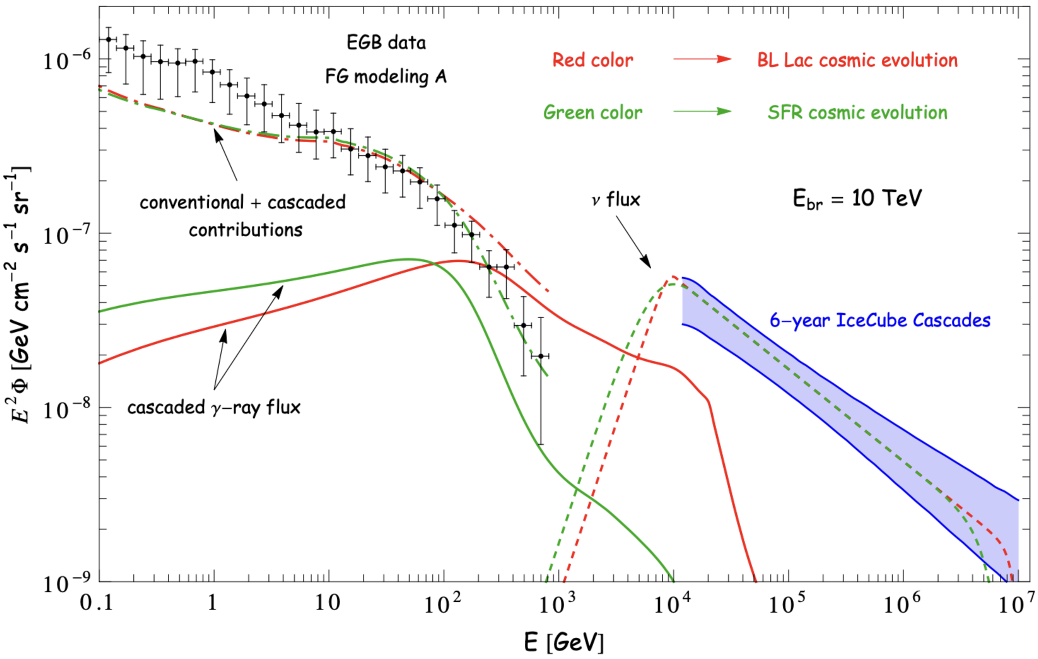

Figure 3.12: Neutrino fluxes (dashed lines) from the broken-power-law spectrum given in Eq. (3-15), with best-fit parameters from IceCube's Cascades dataset (blue band represents the 1σ confidence level uncertainty in these parameters) and $E_{\mathrm{br}} = 10$ TeV at the Earth, for two different source distribution ("cosmic evolution") assumptions. Their corresponding cascaded γ-ray fluxes are shown by solid lines. Adding the conventional contributions, we obtain the dot-dashed lines, which fail to provide good fits to the EGB data points, leading to a tension. Figure from (20).

sponding γ-ray emission is given by Eq. (1-37).

3. Simulate cosmological EM cascades to obtain the final contribution to the EGB from the IceCube neutrino sources.

These simulations have already been performed by the author of this thesis and published in (20, 19). Figure 3.12 shows couple of examples assuming a break energy (at the Earth) of $E_{\mathrm{br}} = 10$ TeV and best-fit the normalization/spectral index from IceCube's Cascades dataset. The neutrino (dashed lines) and γ-ray (solid lines) fluxes at the Earth are obtained for source redshift evolutions following the star formation rate (443) (red) or the BL Lac distribution (156) (green). Unfortunately, they were done using the code γ-Cascade V3 which, as described in Section 2.3, had some innacuracies, overestimating the flux from EM cascades around 100 GeV – 1 TeV. This led to an overestimation of the tension with *Fermi*-LAT data, which served as justification for the (now mainstream) picture that IceCube sources are γ-ray opaque. This project reevaluates these fluxes using the much improved γ-Cascade V4.

3.4
Analysis Method and Preliminary Results

It is time to gather our thoughts. There are three separate and non-overlapping contributions to the EGB: the conventional flux from known sources emitting mostly at sub-TeV energies, the cosmogenic flux from UHECR propagation, and the γ-ray counterpart of astrophysical neutrinos at $>$ TeV energies. This last one is only expected if their sources are not γ-ray opaque. We wish to add all of these components and perform a fit to *Fermi*-LAT's EGB data. Overshoots indicate that we are overestimating one of these three contributions. Undershoots indicate that our knowledge of the sources producing the EGB is incomplete.

The flexibility of the fit depends on the uncertainty in the estimations of conventional contributions and the freedom of parameters that control the cosmogenic and neutrino-counterpart fluxes. To quantify the goodness-of-fit, we introduce the chi-squared statistic

$$\chi^2 = \min_{\{\mathcal{A}_j\}} \left[\sum_i \frac{\left(F_{i,\mathrm{EGB}} - \sum_j \mathcal{A}_j F_{i,j} - F_{i,\mathrm{cr}} - F_{i,\nu}\right)^2}{\sigma_i^2} + \sum_j \frac{(\mathcal{A}_j - 1)^2}{\sigma_{\mathcal{A}_j}^2} \right] . \tag{3-17}$$

The terms in this equation are as follows:

- $F_{i,\mathrm{EGB}}$ is the EGB intensity at energy bin i, as reported by *Fermi*-LAT, with error σ_i;
- $F_{i,j}$ is the intensity at bin i of the conventional contribution j to the EGB, where j represents blazars, RGs or SFGs;
- $F_{i,\mathrm{cr}}$ is the intensity at bin i of the cosmogenic contribution from UHECR propagation secondaries;
- $F_{i,\nu}$ is the intensity at bin i of the γ-ray flux coming from the astrophysical neutrino sources;
- $\mathcal{A}_j$ is a nuisance parameter to account for our uncertainty on the normalization of conventional contribution j;
- $\sigma_{\mathcal{A}_j}^2$ is the average normalization uncertainty of the conventional astrophysical contribution j over all bins. It shows up in the pull-terms of the chi-squared (3-17), assumed to be Gaussian.

Minimization over the set of nuisance parameters $\{\mathcal{A}_j\}$ is performed in order to find the χ^2 for each choice of parameters. Although it is not written explicitly, the free-parameter dependencies are included in $F_{i,\mathrm{cr}}$ and $F_{i,\nu}$, associated to the composition, spectrum and redshift evolution of UHECR sources, as well as the spectrum and evolution of astrophysical neutrino sources.

After scanning over the entire parameter space, we can identify the smallest chi-squared, χ^2_{min}, and obtain constraints on each scenario by imposing $\Delta\chi^2 = \chi^2 - \chi^2_{\text{min}} < q$. The value of q depends on the desired confidence level and on the number of free parameters in the analysis (273). The outcome of this χ^2 analysis is to hopefully establish joint constraints on the composition of UHECRs together with the γ-ray emission from the IceCube sources.

As far as we know, such a multi-messenger interplay has never been considered in the literature. A similar study was recently carried out in (444), although their analysis has some important qualitative differences from ours:

1. Their focus was to study the influence of the UHECR source environment in interpreting the TA/PAO and IceCube data. This adds an unnecessary level of complexity with respect to our analysis by assuming unknown source features. Our method has the advantage of being completely model independent; we do not make any claims regarding the acceleration and reprocessing of particles inside the source, only on their possible emission spectra and composition, which we have more direct access to.

2. They consider that the UHECR sources also produce primary neutrinos at $\gtrsim$ PeV energies. Their idea is to perform a fit to the IceCube data using this flux associated to UHECR production, which is only substantial above a few hundreds of TeVs. Consequently, their only constraints come from the $\gtrsim 10^{15.9}$ eV upper limits on the neutrino flux (445) and a few new data points from a Glashow resonance event (272). Accommodating the low-energy part of the IceCube data requires introducing an additional neutrino component, in principle independent of UHECRs.

3. It is argued in (444) that neutrino constraints are much stronger than those coming from γ rays. This is used as a justification to ignore γ rays altogether in their analysis. However, this only happens because they do not consider the γ-ray component coming from the "non-UHECR" neutrino sources mentioned in the last point. If the IceCube neutrino sources are not completely opaque, their γ-ray emission narrows the allowed parameter space significantly, as show in (20, 19). Certainly, γ-ray limits cannot be ignored.

With that said, we remind the reader that final results for this work are still under preparation. This is due to two factors: (*i*) CRPropa simulations of EM cascades for heavy nuclei take a very long time. Currently, we still lack a few particles for Monte Carlo convergence to be achieved. Also, (*ii*) we await on the completion and release of γ-Cascade V4 (which should be quite soon!)

to calculate the γ-ray cascaded fluxes associated to astrophysical neutrinos. Still, we present some preliminary results from CRPropa simulations below.

In order to check the validity of our UHECR simulations, as well as our post-processing weighting procedure in Eq. (3-10), we attempt to reproduce a result similar to that in Figure 4a from (52). Our CRPropa simulations outcome is shown in Figure 3.13. It shows the UHECR flux at the Earth from an energy-dependent mixed-composition emission of CRs at their sources (see colored curves in the bottom panel of Figure 3 in (52)), distributed following the star-formation rate (443). Atomic masses are grouped into 4 categories: $1 \leq A \leq 2$, $3 \leq A \leq 6$, $7 \leq A \leq 19$ and $20 \leq A \leq 39$, both at emission and detection. In order to reproduce exactly Figure 4a in (52), we would need to know their exact composition escaping the UHECR sources, which is inaccessible from their Figure 3 due to this mass grouping. Instead, we expect to produce similar results by assuming $1 \leq A \leq 2$ as pure proton, $3 \leq A \leq 6$ as pure helium, $7 \leq A \leq 19$ as pure nitrogen and $20 \leq A \leq 39$ as pure silicon at emission. After the simulation is complete, CRPropa outputs several different CR nuclei, which we once again group in the same way for display in Figure 3.13. We include the "galactic" contribution from (52) in the total flux (black line), in order to better interpret the PAO data points. Clearly, we still require more particles for Monte Carlo convergence of heavy nuclei[10]. The good news is that the result resembles closely the result from (52), which is a sign that our simulations are being done correctly and that our weighting procedure works well.

Besides CR-only simulations, it is interesting to check if we can correctly propagate secondaries using CRPropa. For that, we seek to perform a simulation of a pure proton injection spectrum interpreting the PAO data, and obtain its corresponding cascaded cosmogenic γ-ray flux. This is done using a similar script to the one presented in Code 3. Conveniently, such a simulation was already performed in (447) by using their own CR propagation codes. In Figure 3.14, we aim to reproduce the upper left panel of Figure 4 in (447), using their injection spectrum and redshift distribution. Unfortunately, due to CRPropa's bad computational time efficiency for EM cascades below 10 GeV, we are not able to obtain the flux below this energy. At face value, we see quite a good agreement between our (solid) and their (dashed) final CR fluxes at the Earth, with only a small difference near the low-energy tails of the spectra. Our cascaded γ-ray flux is a factor ~ 2 lower than that from (447). This is

---

[10] These results were obtained after CRPropa simulations of 10^7 proton, 10^7 helium, 2×10^6 nitrogen, and 4×10^5 silicon primary CRs, injected uniformly in energy between $[10^{-2}, 10^{3.5}]$ EeV and in redshift between $z \in [0, 8]$, as described in Section 3.2.3. The emission spectrum and redshift distribution were adjusted later with weighting.

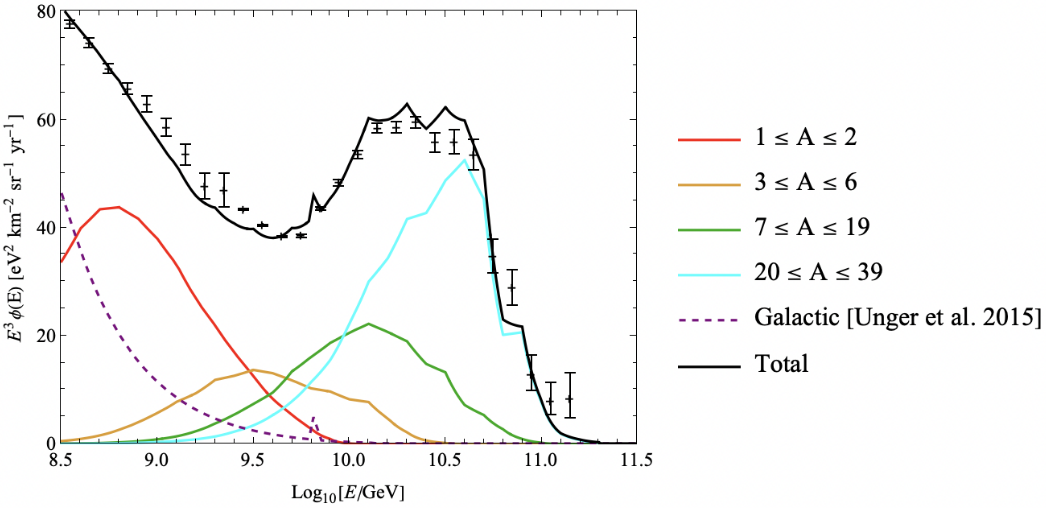

Figure 3.13: CRPropa simulation of CRs emitted with an energy-dependent mixed composition from sources following the star-formation-rate evolution. Different colored curves represent groups of nuclei with similar atomic masses according to the legend. The black curve is the sum of these components, together with the galactic component (purple dashed line) from Figure 4a in (52). Data points are from recent PAO data (446), and uncertainties are statistical only. See main text for more details.

likely due to different treatments of EM cascades between both codes, which could potentially affect the quantitative results of the EGB fit analysis, which is the main goal of this work. In order to truly verify the validity of our γ-ray simulations with CRPropa, a cross-check with an independent third result is required.

Another conclusion we can get from Figure 3.14 is that, in the most optimistic scenario where the UHECR flux is entirely comprised of protons, its corresponding γ-ray flux is comparable to the EGB data. Of course, this does not reflect reality, and heavier nuclei are indeed expected to produce a lower photon yield (374, 448). This is due to the way CR interactions with the CMB scale with atomic mass A. Additionally, other factors such as redshift distribution of sources and IGMF strength also plays a role in increasing/decreasing this EGB contribution (376). Still, one can be optimistic that including this component into the analysis could potentially lead to interesting constraints on the UHECR composition at their sources.

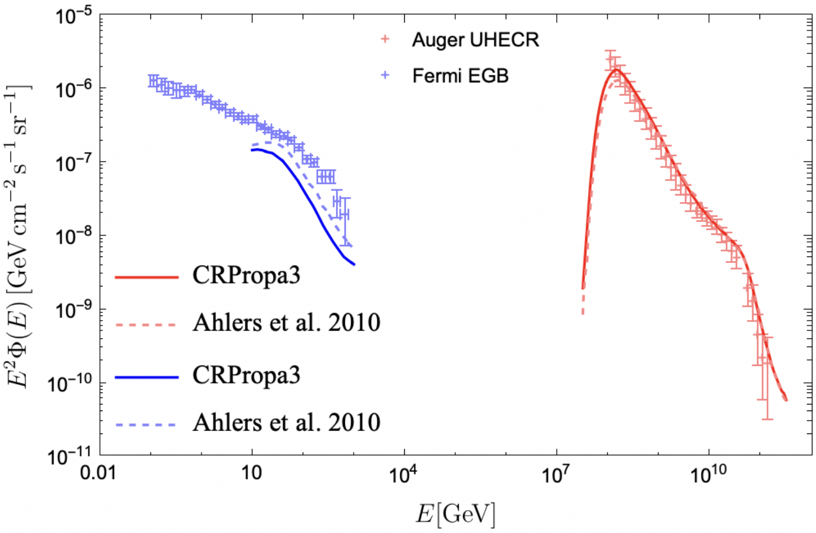

Figure 3.14: Results from CRPropa simulations of UHECR protons and their EM cascade secondaries, shown as solid lines. This is in relatively good agreement with independent results from (447) (dashed lines), the main difference being a factor ~ 2 between the γ-ray fluxes. EGB (blue data points) and PAO (red data points) measurements are also shown for reference.

4
The Flavor Composition of Supernova Neutrinos

This chapter takes a detour from the $>$ TeV Universe which has been to focus of this thesis so far. Instead, we consider neutrinos coming from SNe, typically found to be around the 10 MeV band, as can be seen in Figure 1.6. Neutrinos are crucial for our current understanding of stellar collapse, SN dynamics, and the formation of compact remnants after the explosion. As such, these messengers have been extensively studied in the literature, together with their EM counterparts. For a comprehensive review on the subject, see (449).

Our particular interest shall be on the evolution and composition of SN neutrinos in flavor-space. We present here the results from (3), where we show that standard matter effects, described in Section 1.4.2, in the outer layers of core-collapse SNe significantly constrain the flavor content of the neutrino flux at the Earth. Our limits are robust with respect to the enormous uncertainties originating from self-induced flavor conversions in the supernova core.

4.1
Self-Induced Flavor Conversions

During a core-collapse SN event, the immense gravitational binding energy of the progenitor star is predominantly liberated through a rapid emission of neutrinos, typically lasting around 10 seconds (450, 451). After being generated in the SN core, these neutrinos traverse the mantle and envelope, where they are thought to be pivotal in driving the explosion by reviving the stalled shock wave after the collapse (452, 453).

In 1987, the detection of a few tens of SN neutrinos coming from the Large Magellanic Cloud confirmed the basic features of the core-collapse models, such as the mean energy and the duration of the neutrino burst (91, 92, 93) (see (454) for a recent analysis). Nevertheless, the intricacies of the SN physics remain a challenge, largely due to the uncertainties surrounding neutrino flavor transformations in the core (455, 456, 457, 458). In such a neutrino-dense environment, the coherent forward scattering of neutrinos onto each other gives rise to collective effects that drive a nonlinear flavor evolution (449, 459, 460, 461, 462). These *self-induced conversions* are referred to as “slow” or “fast” depending on the characteristic spatial scale in which they manifest. Slow self-induced conversions develop over a length scale governed by the vacuum oscillation frequency, which is on the order of a few kilometers for typical SN neutrino energies (449, 461). These conversions take place in an intermediate zone situated $\sim$ 100 km away from the neutrino decoupling region, but before the standard matter-induced resonant neutrino conversion occurs (84, 85, 278, 279). Conversely, fast self-induced conversions have characteristic scales as small as centimeters and could significantly influence the flavor evolution, energy spectrum, and angular distribution of each neutrino species near the decoupling region (463, 464, 465, 466, 467). In addition, it was recently found that coherent flavor conversion can also be induced by incoherent collisions in the SN environment (468). The lack of a full solution to the quantum kinetic equations governing this collective behavior leads to unpredictable consequences for the SN dynamics (457, 458) and, ultimately, for the neutrino signal detected at the Earth (469).

Amidst this conundrum, it is natural to wonder if a meaningful improvement in our understanding of the core-collapse phenomenon and neutrino propagation will be possible from, even after the observation of the next galactic SN. In the next sections, we show that many features of the neutrino flux coming to the Earth can be understood by adopting a completely agnostic approach to the flavor composition emerging from the SN core, where collective effects dominate. If confirmed by the next SN observation, these predictions will not only validate our fundamental understanding of the SN dynamics and neutrino conversion in the outermost layers, but also elucidate crucial properties of the neutrino fluxes emerging from the region of self-induced conversions.

4.2
Matter Effects in Supernovae

In Section 1.4.2, we described the appearance of new matter eigenstates of the two-neutrino-flavor Hamiltonian (1-59), due to the presence of dense matter. The equation determining the evolution of the system was given by Eq. (1-57), including a vacuum term and a matter term. This equation is, in fact, a simplified version of the complete expression that takes into account neutrino-neutrino interactions, advection, and collisions (470, 471, 472, 473). By solving Eq. (1-57) under a varying electron density $n_e(x)$, we identified the MSW resonance (84, 85, 278, 279) occurring around a specific density, which allows neutrinos to convert from one matter eigenstate to another, depending on the characteristics of the physical region where this resonance takes place. We also briefly commented on the generalization of these phenomena to the three-flavor case, where two possible resonances exist.

Let us now consider the more realistic scenario of flavor evolution taking place inside SNe. Let $\rho_m(r)$ be the density of matter, assumed to be spherically symmetric in a SN explosion. Recall it is related to the electron number density through $n_e \approx \rho_m Y_e / m_N$, where Y_e is the electron fraction in the medium and m_N is the mass of a nucleon. As neutrinos propagate outward towards vacuum, ρ_m gradually decreases and they encounter the two resonance layers where effective flavor conversions can occur. These are called the H- and L-resonances, occurring when the following conditions are satisfied:

$$\sqrt{2} G_F \frac{Y_e}{m_N} \rho_m^{\text{res}} = \frac{\Delta m_{i1}^2 \cos 2\theta_{1i}}{2E} \ , \tag{4-1}$$

where res $= H(L)$ corresponds to $i = 3(2)$. For efficient flavor conversion, adiabaticity must be satisfied at the resonance layers. The degree of adiabaticity can be estimated by considering the parameter

$$\gamma = \frac{\Delta m_{i1}^2 \sin^2 2\theta_{1i}}{2E \cos 2\theta_{1i}} \left(\frac{1}{Y_e \rho_m^{\text{res}}} \left| \frac{d(Y_e \rho_m)}{dr} \right|_{\text{res}} \right)^{-1} \ , \tag{4-2}$$

and propagation is adiabatic for $\gamma > 1$ (474).

At densities above ρ_m^H, V_e dominates in Eq. (1-55) and vacuum mixing is suppressed. As a result, the ν_e effectively decouples from the other flavors (*i.e.* does not oscillate anymore) and behaves as the heaviest eigenstate in matter, which corresponds to $\nu_{\mathrm{M},3}$ if neutrino masses follow NO, or $\nu_{\mathrm{M},2}$ in the IO scenario. The other flavors are equally affected by matter and oscillate among themselves with frequency given by the vacuum terms, showing a near maximal mixing ($\theta_{23} \approx 49°$). Therefore, the eigenstates of the $\nu_\mu - \nu_\tau$ subspace at $\rho_m \gg \rho_m^H$ are given by approximately equal mixtures of ν_μ and ν_τ. In NO, these matter eigenstates are $\nu_{\mathrm{M},1}$ and $\nu_{\mathrm{M},2}$, while in IO, they are $\nu_{\mathrm{M},1}$ and $\nu_{\mathrm{M},3}$. Thus, any quantity of $|\nu_\mu\rangle$ and $|\nu_\tau\rangle$ eigenstates emerging from the region of self-induced flavor conversions would manifest itself, in the region of standard matter effects, by two out of the three matter eigenstates being present in roughly equal amounts.

4.3

A Systematic Approach to Supernova Neutrino Flavor Evolution

Depending on the mechanisms governing flavor dynamics of self-induced conversions, we can expect neutrino flavor coherence to be either maintained or lost. This separates our problem into two possible scenarios: neutrinos leave the region of collective effects either as flavor eigenstates or as matter eigenstates. To account for our present uncertainty regarding this issue, we assume these eigenstates are present in arbitrary relative proportions. With these considerations, our results become completely agnostic with respect to the outcome of self-induced conversions. Let us now study each case separately.

4.3.1
Case 1: Flavor Coherence from Collective Effects

We start by considering all possible flavor ratio configurations leaving the region of self-induced conversions, before the onset of standard matter effects. Once neutrinos reach the boundary between these regions, any superposition of electron neutrinos with other flavors is quickly destroyed (it becomes the heaviest matter eigenstate), while the $\nu_\mu - \nu_\tau$ subspace retains its flavor superposition.

The $\nu_\mu - \nu_\tau$ subspace of the density matrix corresponding to the k-th neutrino exiting the collective effects region is

$$\rho^k_{\nu_x} = \begin{pmatrix} \alpha_k^2 & \alpha_k\beta_k e^{-i\phi_k} \\ \alpha_k\beta_k e^{i\phi_k} & \beta_k^2 \end{pmatrix} . \tag{4-3}$$

Here, α_k, β_k, and ϕ_k are real numbers, subject to the condition $\alpha_k^2 + \beta_k^2 = 1$. Assuming an emission of 10^{58} neutrinos over the 10-second duration of a galactic SN burst (475), at a distance of 10 kpc, we estimate the flux reaching us to be approximately 10^{15} neutrinos per square meter per second. k ranges from 1 to N, where N represents the number of non-electron neutrinos with a specific energy composing this flux at the Earth.

The density matrix for the ensemble of N neutrinos is

$$\rho_{\nu_x} = \frac{1}{N}\sum_{k=1}^{N} \begin{pmatrix} \alpha_k^2 & \alpha_k\beta_k e^{-i\phi_k} \\ \alpha_k\beta_k e^{i\phi_k} & \beta_k^2 \end{pmatrix} . \tag{4-4}$$

Since N is very large, we assume for simplicity that the off-diagonal elements of Eq. (4-4) average to zero, due to the many oscillatory terms composing the sum[1]. Later, we discuss situations in which the assumption of vanishing off-diagonal terms is not valid. Note that α_k, β_k, and ϕ_k depend on the production point, energy, direction and evolution of each neutrino under self-induced interactions. These can be incredibly diverse – almost random – for each of the N neutrinos in the ensemble (477), causing the superposition between ν_μ and ν_τ to be effectively destroyed. Therefore, before entering the region of standard matter effects, the neutrino ensemble's density matrix becomes diagonal in the flavor basis and can be described as composed of the various flavor eigenstates in arbitrary proportions.

Let us focus our attention for the moment only on neutrinos (antineutrinos are discussed in Section 4.3.3). Assuming adiabaticity of neutrino propagation, the relative proportions between the (vacuum) mass eigenstates that

---

[1] The density matrix in Eq. (4-3) corresponds to the pure state $|\nu_x\rangle = \alpha_k|\nu_\mu\rangle + \beta_k e^{i\phi_k}|\nu_\tau\rangle$. However, the argument still applies to states with intermediate level of coherence if the off-diagonal terms retain some degree of oscillatory behavior (476).

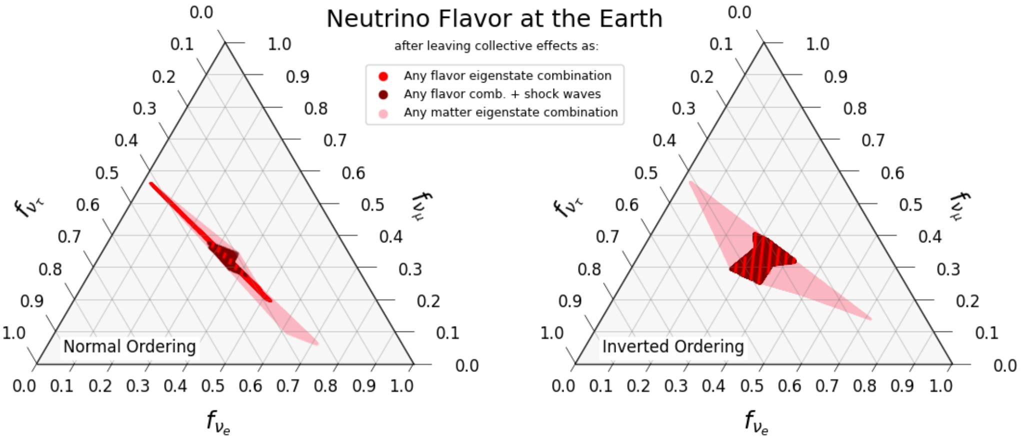

Figure 4.1: Allowed regions for the flavor composition of SN neutrinos arriving at the Earth in the NO (left) and IO (right) scenarios. *Red*: Assuming the flux emerging from collective effects is composed of flavor eigenstates in an arbitrary flavor ratio configuration, and propagation in the outer layers is adiabatic. *Maroon*: Assuming the flux emerging from collective effects in an arbitrary flavor ratio configuration, but there is non-adiabatic propagation through the H-resonance (from the presence of shock waves). *Pink*: Assuming a flux of matter eigenstates in arbitrary amounts emerging from collective effects (for instance, due to wave packet decoherence). Stripes are used for overlapping regions. We consider the 3σ range of variability for the parameters θ_{12} and θ_{13}, which affect the fraction of electron flavor f_{ν_e}. Figure from (3).

reach the Earth are identical to those of matter eigenstates propagating in the SN outer layers ($\nu_{\mathrm{M},i} \to \nu_i$). Recall that flavor coherence between ν_μ and ν_τ implies that two of the matter eigenstates are produced in roughly equal amounts due to their maximal mixing. After some calculations, we find after that the possible range of the electron neutrino fraction f_{ν_e} at the Earth can be constrained to

$$f^{NO}_{\nu_e} \lesssim 0.5 \ , \qquad f^{IO}_{\nu_e} \approx 1/3 \ , \tag{4-5}$$

depending on the mass ordering assumed. This result corresponds to the red-shaded region in Figure 4.1.

To better understand the emergence of these constraints, we characterize the evolution within the zone of standard matter effects in terms of flavor ratios $(f_{\nu_e}, f_{\nu_\mu}, f_{\nu_\tau})$. Assuming NO and adiabatic propagation, it follows that an initially produced ν_e arrives at the Earth as ν_3 (478):

$$(1,0,0)_{SN} \to \left(|U_{e3}|^2 \, , |U_{\mu 3}|^2 \, , |U_{\tau 3}|^2\right)_{\oplus} \ . \tag{4-6}$$

Conversely, either of the non-electron flavors, ν_μ or ν_τ, arrive at the Earth as approximately equal mixtures of ν_1 and ν_2. Therefore,

$$\begin{gathered}(0,1,0)_{SN} \quad \text{or} \quad (0,0,1)_{SN} \rightarrow \\ \frac{1}{2}\left(|U_{e1}|^2+|U_{e2}|^2, |U_{\mu1}|^2+|U_{\mu2}|^2, |U_{\tau1}|^2+|U_{\tau2}|^2\right)_{\oplus} \ . \end{gathered} \tag{4-7}$$

For any initial combination $(a,b,c)_{SN}$, we obtain on Earth the ν_e fraction

$$f_{\nu_e}^{NO} = a\,|U_{e3}|^2 + b\frac{|U_{e1}|^2+|U_{e2}|^2}{2} + c\frac{|U_{e1}|^2+|U_{e2}|^2}{2} \ . \tag{4-8}$$

Because of the unitarity of the PMNS matrix and $a+b+c=1$, Eq. (4-8) simplifies to

$$f_{\nu_e}^{NO} = \frac{1}{2}\left(1-|U_{e3}|^2\right) + \frac{a}{2}\left(3\,|U_{e3}|^2-1\right) \ , \tag{4-9}$$

Considering $|U_{e3}|^2 \approx 0.02 \ll 1$ (275), we obtain

$$f_{\nu_e}^{NO} \approx \frac{(1-a)}{2} \lesssim 0.5 \ . \tag{4-10}$$

In the IO scenario, the argument mirrors the one between Eqz. (4-6)–(4-9), with the interchange of the PMNS matrix elements $U_{\alpha3}$ and $U_{\alpha2}$ for any flavor α. Thus, by replacing U_{e3} with U_{e2} in Eq. (4-9), we have

$$f_{\nu_e}^{IO} = \frac{1}{2}\left(1-|U_{e2}|^2\right) + \frac{a}{2}\left(3\,|U_{e2}|^2-1\right) \ . \tag{4-11}$$

Assuming $|U_{e2}|^2 \approx 1/3$ (275), we obtain[2]

$$f_{\nu_e}^{IO} \approx \frac{1}{3} \ . \tag{4-12}$$

The red-shaded regions in Figure 4.1 correspond to $f_{\nu_e}^{NO}$ and $f_{\nu_e}^{IO}$ after varying θ_{12} and θ_{13} within their 3σ allowed range and using the best-fit values for the other oscillation parameters (we have explicitly checked that the impact of θ_{23} and δ_{CP} on the allowed f_{ν_e} range is less than 10%) (275).

The results in Eqs. (4-10) and (4-12) are applicable to neutrinos of any energy and at any instant in time during the SN event. Nonetheless, exceptions may be possible in the presence of strong shock waves, leading to the modification of Eq. (4-10) at certain parts of the energy spectrum. Shock waves affect the matter profile and can lead to two interesting effects: the creation of multiple H- and L- resonances (479, 480), and the loss of adiabaticity during MSW resonances. This latter consequence can lead to transitions between different matter eigenstates, as described in Section 1.4.2.

If an even number of H-resonances are non-adiabatic, results do not change (neglecting phase effects (481)). However, if an odd number of the

---

[2] According to Eqs. (4-11) and (4-12), any initial flavor configuration in the solar core leads to $f_{\nu_e} \approx 1/3$ at the Earth for both mass orderings.

H-resonances are non-adiabatic, the outcome is modified in the NO scenario, since a $\nu_{\mathrm{M},3} \leftrightarrow \nu_{\mathrm{M},2}$ transition that happens at one of the resonance layers is not reverted by another transition of the same type. It is straightforward to determine the consequence of an odd number of non-adiabatic H-resonances: $\nu_{\mathrm{M},3} \leftrightarrow \nu_{\mathrm{M},2}$ transitions imply that matrix elements $U_{\alpha 3}$ and $U_{\alpha 2}$ should be interchanged in Eqs. (4-6)–(4-9). The argument becomes similar to the one that leads to Eqs. (4-11) and Eq. (4-12), resulting in

$$f_{\nu_e}^{NO}(\text{non-adiabatic } H) \approx \frac{1}{3} \ . \tag{4-13}$$

Because the position of the H-resonance is energy dependent, the portion of the energy spectrum influenced by the transient non-adiabaticity provides information about the location of the shock wave front (479, 480). Thus, we can track the motion of the shock wave through the H-resonance layers using flavor ratios if neutrino masses follow NO: during the shock's transit through that region, f_{ν_e} converges to 1/3 in the corresponding part of the energy spectrum. In the IO scenario, the H-resonance does not occur in the neutrino channel, but in antineutrinos instead. Therefore, the result is identical to the adiabatic case:

$$f_{\nu_e}^{IO}(\text{non-adiabatic } H) \approx \frac{1}{3} \ . \tag{4-14}$$

The impact of the non-adiabatic H-resonance in neutrino propagation is illustrated by the maroon regions in Figure 4.1. Once again, we vary only θ_{12} and θ_{13} within their 3σ uncertainties. We conclude that the presence of shock wave fronts at the H-resonance(s) causes the neutrino system to converge to $f_{\nu_e} \approx 1/3$ at the Earth for both mass orderings. Although shock wave fronts can also penetrate the L-resonance layer, adiabaticity is never strongly violated there (449). Even in cases where such violations may happen, they typically occur at later times (beyond 10 seconds post-bounce) (480), so we do not consider them here.

4.3.2
Case 2: Flavor Decoherence from Collective Effects

All the derived results so far relied on the assumption that the off-diagonal elements in Eq. (4-4) are negligible. However, there are physical situations of interest in which Eq. (4-4) is not diagonal. For instance, the outcome of collective effects could be eigenstates in neutrino-neutrino potentials that adiabatically transform into matter eigenstates in the usual matter potentials. In such a situation, the density matrix for N neutrinos would be diagonal in the matter eigenstates basis, but not in the flavor basis (482). The matter eigenstates $\nu_{\mathrm{M},i}$ would arise in any relative amounts with no correlations between any two of them in principle, and results would differ drastically from the previous section.

Another interesting situation would happen if some unknown physical mechanism restricts the allowed values of all parameters in Eq. 4-4. In this case, the fractions of $\nu_{\mathrm{M},1}$, $\nu_{\mathrm{M},2}$ and $\nu_{\mathrm{M},3}$ that enter the region of standard matter effects are strongly dependent on the specific values of α_k, β_k and ϕ_k. If the range of values for these parameters is unknown or varies significantly over time, the initial relative fractions of each matter eigenstate would also appear to be somewhat arbitrary.

Within the scenarios described in this section, the outcome of collective effects is better formulated in terms of matter eigenstates rather than flavor eigenstates, and there are no MSW resonances. Once these matter eigenstates convert to mass eigenstates in vacuum, the situation resembles the usual picture of wave-packet decoherence of neutrino oscillations in vacuum and matter (483). Nevertheless, we can still constrain the flavor composition on Earth in terms of f_{ν_e}. By considering these eigenstates to leave the collective effects region and, subsequently, arrive at Earth in arbitrary relative proportions of ν_i, we find that $f_{\nu_e} \lesssim 0.7$ for both mass orderings[3]. These constraints are depicted as pink-shaded regions in the flavor triangles of Figure 4.1. The results are not as constraining as in the previous section. This is because those cases end up being a particular subset of the possibilities considered in this section.

4.3.3
Supernova Antineutrino Flavor Ratios

For antineutrinos, recall that the sign of the matter potential is reversed in the Hamiltonian (1-55), $V_e \to -V_e$. In the two-flavor scenario considered in Section 1.4.2, this would modify Eqs. (1-65) and (1-66) such that $\theta_{\mathrm{M}} \approx 0$ and $|\nu_e\rangle \approx |\nu_{\mathrm{M},1}\rangle$.

Let us discuss the consequences of this in the three-flavor SN system. At $\rho_m \gg \rho_m^H$, we end up having $\bar{\nu}_e \approx \bar{\nu}_{\mathrm{M},1}$ for NO, and the possible fraction of electron antineutrinos on Earth is given by Eq. (4-9) with $|U_{e1}|^2$ in place of $|U_{e3}|^2$,

$$f_{\bar{\nu}_e}^{NO} = \frac{1}{2}\left(1 - |U_{e1}|^2\right) + \frac{a}{2}\left(3\,|U_{e1}|^2 - 1\right) \ . \tag{4-15}$$

Considering that $|U_{e1}|^2 \approx 2/3$ (275), we have

$$\frac{1}{6} \lesssim f_{\bar{\nu}_e}^{NO} \lesssim \frac{2}{3} \ . \tag{4-16}$$

---

[3] This constraint applies to any alternative scenario affecting neutrino propagation (*e.g.* hydrodynamic turbulence (484)).

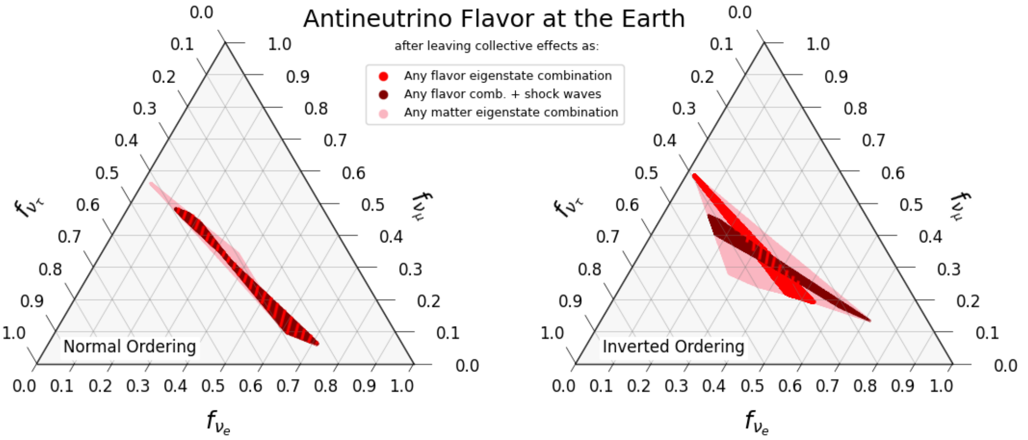

Figure 4.2: Same as Figure 4.1, but for antineutrinos (3).

Eq. (4-16) is applicable even in the presence of shock waves. On the other hand, for IO, $\bar{\nu}_e \approx \bar{\nu}_{\mathrm{M},3}$ above the H-resonance density, and $f^{IO}_{\bar{\nu}_e}$ is described by Eq. (4-9), leading to

$$f^{IO}_{\bar{\nu}_e} \lesssim 0.5 \; . \tag{4-17}$$

If the H-resonance is non-adiabatic, transitions $\bar{\nu}_{\mathrm{M},3} \to \bar{\nu}_{\mathrm{M},1}$ modify the allowed regions for $f^{IO}_{\bar{\nu}_e}$, which will then be given by Eq. (4-15). Therefore,

$$\frac{1}{6} \lesssim f^{IO}_{\bar{\nu}_e}(\text{non-adiabatic } H) \lesssim \frac{2}{3} \; . \tag{4-18}$$

In case antineutrinos emerge from the core as incoherent matter eigenstates, we have $f_{\bar{\nu}_e} \lesssim 0.7$ for both mass orderings. These results are depicted in Fig. 4.2.

4.4
Summary and Future Prospects

We have shown that the flavor composition of SN neutrinos reaching the Earth can be theoretically constrained, even when assuming complete uncertainty about the neutrino state that emerges from the innermost regions dominated by self-induced conversions. Under certain conditions, the neutrino flux can be viewed as composed of flavor eigenstates in an arbitrary flavor ratio configuration. If this scenario occurs, we predict that the proportion of ν_e is always smaller than 0.5 for NO, whereas, for IO, we expect $f_{\nu_e} \approx 1/3$. However, in the opposite case in which neutrinos come out from self-induced conversions as fluxes of matter eigenstates (for instance, due to wave-packet decoherence), we obtain $f_{\nu_e} \lesssim 0.7$.

Ultimately, we advocate for a phenomenological approach to comprehensively address the intricacies of neutrino flavor conversion in SN environments. Experimental challenges along the way include distinguishing between ν_x and $\bar{\nu}_x$ in neutral current scatterings (485). This approach can also be extended to accommodate non-standard scenarios, potentially unveiling novel phenomena underlying the physics of neutrino masses and mixing (486, 487).

5
Bibliography

1 CAPANEMA, A.; ESMAEILI, A.; ESMAILI, A. Evaporating primordial black holes in gamma ray and neutrino telescopes. **JCAP**, v. 12, n. 12, p. 051, 2021.

2 ESMAEILI, A. et al. Ultrahigh energy neutrinos from high-redshift electromagnetic cascades. **Phys. Rev. D**, v. 106, n. 123016, 2022.

3 CAPANEMA, A.; PORTO, Y.; SAEZ, M. M. The Flavor Composition of Supernova Neutrinos. 3 2024.

4 TOMPKINS, S. A. et al. The cosmic radio background from 150 MHz to 8.4 GHz and its division into AGN and star-forming galaxy flux. **MNRAS**, v. 521, p. 332–353, 1 2023.

5 WEINBERG, S. **Cosmology**. Great Clarendon Street, Oxford OX2 6DP: Oxford University Press, 2008. ISBN 978-0-19-852682-7.

6 HILL, R.; MASUI, K. W.; SCOTT, D. The Spectrum of the Universe. **Appl. Spectrosc.**, v. 72, n. 5, p. 663–688, 2018.

7 COORAY, A. Extragalactic backgroundlight measurements and applications. **R. Soc. open sci.**, v. 3, n. 3, p. 150555, 2016.

8 BEREZINSKY, V.; KALASHEV, O. High energy electromagnetic cascades in extragalactic space: physics and features. **Phys. Rev. D**, v. 94, n. 2, p. 023007, 2016.

9 GOULD, R. J.; SCHREDER, G. P. Opacity of the Universe to High-Energy Photons. **Phys. Rev.**, v. 155, p. 1408–1411, 1967.

10 BEREZINSKY, V. Inverse Compton effect, pair production and penetration of high energy electrons and photons through the metagalactics. **Yad. Fiz.**, v. 11, p. 399–410, 1970.

11 AHARONIAN, F. A.; COPPI, P. S.; VOELK, H. J. Very high-energy gamma-rays from AGN: Cascading on the cosmic background radiation fields and the formation of pair halos. **Astrophys. J. Lett.**, v. 423, p. L5–L8, 1994.

12 AARTSEN, M. G. et al. IceCube-Gen2: the window to the extreme Universe. **J. Phys. G**, v. 48, n. 6, p. 060501, 2021.

13 PUNCH, M. et al. Detection of TeV photons from the active galaxy Markarian 421. **Nature**, v. 358, p. 477–478, 1992.

14 GRÉAUX, L. et al. STeVECat, the Spectral TeV Extragalactic Catalog. **PoS**, Gamma2022, p. 171, 2023.

15 CAO, Z. et al. Ultrahigh-energy photons up to 1.4 petaelectronvolts from 12 γ-ray Galactic sources. **Nature**, v. 594, n. 7861, p. 33–36, 2021.

16 AMENOMORI, M. et al. First Detection of sub-PeV Diffuse Gamma Rays from the Galactic Disk: Evidence for Ubiquitous Galactic Cosmic Rays beyond PeV Energies. **Phys. Rev. Lett.**, v. 126, n. 14, p. 141101, 2021.

17 ACKERMANN, M. et al. The spectrum of isotropic diffuse gamma-ray emission between 100 MeV and 820 GeV. **Astrophys. J.**, v. 799, p. 86, 2015.

18 ACKERMANN, M. et al. Unresolved Gamma-Ray Sky through its Angular Power Spectrum. **Phys. Rev. Lett.**, v. 121, n. 24, p. 241101, 2018.

19 CAPANEMA, A.; ESMAILI, A.; MURASE, K. New constraints on the origin of medium-energy neutrinos observed by IceCube. **Phys. Rev. D**, v. 101, n. 10, p. 103012, 2020.

20 CAPANEMA, A.; ESMAILI, A.; SERPICO, P. D. Where do IceCube neutrinos come from? Hints from the diffuse gamma-ray flux. **JCAP**, v. 02, p. 037, 2021.

21 HESS, V. F. Über Beobachtungen der durchdringenden Strahlung bei sieben Freiballonfahrten. **Phys. Z.**, v. 13, p. 1084–1091, 1912.

22 MILLIKAN, R. A.; CAMERON, G. H. The Origin of the Cosmic Rays. **Phys. Rev.**, v. 32, n. 4, p. 533–557, 1928.

23 JOHNSON, T. H. The Azimuthal Asymmetry of the Cosmic Radiation. **Phys. Rev.**, v. 43, n. 10, p. 834–835, 1933.

24 ALVAREZ, L.; COMPTON, A. H. A Positively Charged Component of Cosmic Rays. **Phys. Rev.**, v. 43, n. 10, p. 835–836, 1933.

25 ROSSI, B. Directional Measurements on the Cosmic Rays Near the Geomagnetic Equator. **Phys. Rev.**, v. 45, n. 3, p. 212–214, 1934.

26 ROSSI, B. Absorptionsmessungen der durchdringenden Korpuskularstrahlung in einem Meter Blei. **Die Naturwissenschaften**, v. 20, n. 4, p. 65, 1932.

27 MAURIN, D. et al. Cosmic-Ray Database Update: Ultra-High Energy, Ultra-Heavy, and Antinuclei Cosmic-Ray Data (CRDB v4.0). **Universe**, v. 6, n. 8, p. 102, 2020.

28 MAURIN, D. et al. A cosmic-ray database update: CRDB v4.1. **Eur. Phys. J. C**, v. 83, n. 10, p. 971, 2023.

29 LINSLEY, J.; SCARSI, L.; ROSSI, B. Extremely energetic cosmic-ray event. **Phys. Rev. Lett.**, v. 6, p. 485–487, 1961.

30 LINSLEY, J. Evidence for a primary cosmic-ray particle with energy 10**20-eV. **Phys. Rev. Lett.**, v. 10, p. 146–148, 1963.

31 PARKER, E. N. The passage of energetic charged particles through interplanetary space. **Planet. Space Sci.**, v. 13, n. 1, p. 9–49, 1965.

32 GLEESON, L. J.; AXFORD, W. I. Solar Modulation of Galactic Cosmic Rays. **Astrophys. J.**, v. 154, p. 1011, 1968.

33 GABICI, S. Low-energy cosmic rays: regulators of the dense interstellar medium. **Astron. Astrophys. Rev.**, v. 30, n. 1, p. 4, 2022.

34 GREISEN, K. End to the cosmic ray spectrum? **Phys. Rev. Lett.**, v. 16, p. 748–750, 1966.

35 ZATSEPIN, G. T.; KUZMIN, V. A. Upper limit of the spectrum of cosmic rays. **JETP Lett.**, v. 4, p. 78–80, 1966.

36 GAISSER, T. K.; ENGEL, R.; RESCONI, E. **Cosmic Rays and Particle Physics: 2nd Edition**. [S.l.]: Cambridge University Press, 2016. ISBN 978-0-521-01646-9.

37 HILLAS, A. M. The Origin of Ultrahigh-Energy Cosmic Rays. **Ann. Rev. Astron. Astrophys.**, v. 22, p. 425–444, 1984.

38 ACKERMANN, M. et al. Fermi-LAT Observations of the Diffuse Gamma-Ray Emission: Implications for Cosmic Rays and the Interstellar Medium. **Astrophys. J.**, v. 750, p. 3, 2012.

39 AAB, A. et al. Observation of a Large-scale Anisotropy in the Arrival Directions of Cosmic Rays above 8×10^{18} eV. **Science**, v. 357, n. 6537, p. 1266–1270, 2017.

40 AAB, A. et al. Large-scale cosmic-ray anisotropies above 4 EeV measured by the Pierre Auger Observatory. **Astrophys. J.**, v. 868, n. 1, p. 4, 2018.

41 GOLUP, G. An update on the arrival direction studies made with data from the Pierre Auger Observatory. **PoS**, ICRC2023, p. 252, 2023.

42 EVOLI, C. **The Cosmic-Ray Energy Spectrum**. Zenodo, 2020. Disponível em: <https://doi.org/10.5281/zenodo.4396125>.

43 KULIKOV, G. V.; KHRISTIANSEN, G. B. On the Size Spectrum of Extensive Air Showers. **JETP**, v. 8, n. 3, p. 441–444, 1959.

44 PETERS, B. Primary cosmic radiation and extensive air showers. **Nuovo Cim.**, v. 22, n. 4, p. 800–819, 1961.

45 HOERANDEL, J. R. On the knee in the energy spectrum of cosmic rays. **Astropart. Phys.**, v. 19, p. 193–220, 2003.

46 LINSLEY, J. Primary cosmic rays of energy 10**17 to 10**20-eV: The energy spectrum and arrival directions. In: **8th International Cosmic Ray Conference**. [S.l.: s.n.], 1963.

47 GIACINTI, G. et al. Cosmic Ray Anisotropy as Signature for the Transition from Galactic to Extragalactic Cosmic Rays. **JCAP**, v. 07, p. 031, 2012.

48 AAB, A. et al. Depth of maximum of air-shower profiles at the Pierre Auger Observatory. II. Composition implications. **Phys. Rev. D**, v. 90, n. 12, p. 122006, 2014.

49 BELLIDO, J. Depth of maximum of air-shower profiles at the Pierre Auger Observatory: Measurements above $10^{17.2}$ eV and Composition Implications. **PoS**, ICRC2017, p. 506, 2018.

50 HALIM, A. A. et al. Constraining the sources of ultra-high-energy cosmic rays across and above the ankle with the spectrum and composition data measured at the Pierre Auger Observatory. **JCAP**, v. 05, p. 024, 2023.

51 GLOBUS, N.; ALLARD, D.; PARIZOT, E. A complete model of the cosmic ray spectrum and composition across the Galactic to extragalactic transition. **Phys. Rev. D**, v. 92, n. 2, p. 021302, 2015.

52 UNGER, M.; FARRAR, G. R.; ANCHORDOQUI, L. A. Origin of the ankle in the ultrahigh energy cosmic ray spectrum, and of the extragalactic protons below it. **Phys. Rev. D**, v. 92, n. 12, p. 123001, 2015.

53 KACHELRIESS, M. et al. Minimal model for extragalactic cosmic rays and neutrinos. **Phys. Rev. D**, v. 96, n. 8, p. 083006, 2017.

54 BEREZINSKY, V. S.; GRIGOR'EVA, S. I. A Bump in the ultrahigh-energy cosmic ray spectrum. **Astron. Astrophys.**, v. 199, p. 1–12, 1988.

55 BEREZINSKY, V.; GAZIZOV, A. Z.; GRIGORIEVA, S. I. On astrophysical solution to ultrahigh-energy cosmic rays. **Phys. Rev. D**, v. 74, p. 043005, 2006.

56 MAYOTTE, E. W. et al. Measurement of the mass composition of ultra-high-energy cosmic rays at the Pierre Auger Observatory. **PoS**, ICRC2023, p. 365, 2023.

57 AAB, A. et al. Features of the Energy Spectrum of Cosmic Rays above 2.5×10^{18} eV Using the Pierre Auger Observatory. **Phys. Rev. Lett.**, v. 125, n. 12, p. 121106, 2020.

58 BIRD, D. J. et al. Detection of a cosmic ray with measured energy well beyond the expected spectral cutoff due to cosmic microwave radiation. **Astrophys. J.**, v. 441, p. 144–150, 1995.

59 HAYASHIDA, N. et al. Observation of a very energetic cosmic ray well beyond the predicted 2.7-K cutoff in the primary energy spectrum. **Phys. Rev. Lett.**, v. 73, p. 3491–3494, 1994.

60 SAKAKI, N. et al. Cosmic ray energy spectrum above 3 x 10**18-eV observed with AGASA. In: **27th International Cosmic Ray Conference**. [S.l.: s.n.], 2001.

61 ABBASI, R. U. et al. An extremely energetic cosmic ray observed by a surface detector array. **Science**, v. 382, n. 6673, p. abo5095, 2023.

62 TOMASSETTI, N.; OLIVA, A. Production of cosmic-ray antinuclei in the Galaxy and background for dark matter searches. **PoS**, EPS-HEP2017, p. 620, 2017.

63 DIESING, R.; CAPRIOLI, D. Nonsecondary origin of cosmic ray positrons. **Phys. Rev. D**, v. 101, n. 10, p. 103030, 2020.

64 EVOLI, C. et al. Galactic factories of cosmic-ray electrons and positrons. **Phys. Rev. D**, v. 103, n. 8, p. 083010, 2021.

65 SERPICO, P. D. Astrophysical models for the origin of the positron 'excess'. **Astropart. Phys.**, v. 39-40, p. 2–11, 2012.

66 PLOTKO, P. et al. Differences between the Pierre Auger Observatory and Telescope Array Spectra: Systematic Effects or Indication of a Local Source of Ultra-high-energy Cosmic Rays? **Astrophys. J.**, v. 953, n. 2, p. 129, 2023.

67 AAB, A. et al. Measurement of the cosmic-ray energy spectrum above 2.5×10^{18} eV using the Pierre Auger Observatory. **Phys. Rev. D**, v. 102, n. 6, p. 062005, 2020.

68 IVANOV, D. Energy Spectrum Measured by the Telescope Array. **PoS**, ICRC2019, p. 298, 2020.

69 TSUNESADA, Y. Joint analysis of the energy spectrum of ultra-high-energy cosmic rays as measured at the Pierre Auger Observatory and the Telescope Array. **PoS**, ICRC2021, p. 337, 2021.

70 AAB, A. et al. Evidence for a mixed mass composition at the 'ankle' in the cosmic-ray spectrum. **Phys. Lett. B**, v. 762, p. 288–295, 2016.

71 YUSHKOV, A. Mass Composition of Cosmic Rays with Energies above $10^{17.2}$ eV from the Hybrid Data of the Pierre Auger Observatory. **PoS**, ICRC2019, p. 482, 2020.

72 BERGMAN, D. et al. Testing the Compatibility of the Depth of the Shower Maximum Measurements performed at Telescope Array and the Pierre Auger Observatory - Auger-TA Mass Composition Working Group Report. **EPJ Web Conf.**, v. 283, p. 02008, 2023.

73 GARIAZZO, S. Neutrino masses in cosmology. In: **21st Lomonosov Conference on Elementary Particle Physics**. [S.l.: s.n.], 2024.

74 GIUNTI, C.; KIM, C. W. **Fundamentals of Neutrino Physics and Astrophysics**. [S.l.]: Oxford University Press, 2007. ISBN 978-0-19-850871-7.

75 COWAN, C. L. et al. Detection of the free neutrino: A Confirmation. **Science**, v. 124, p. 103–104, 1956.

76 WU, C. S. et al. Experimental Test of Parity Conservation in β Decay. **Phys. Rev.**, v. 105, p. 1413–1414, 1957.

77 PONTECORVO, B. M. **Inverse β Process**. 1946. Disponível em: <https://centropontecorvo.df.unipi.it/Articles/Inverse_beta_process_Report_PD205-1946.pdf>.

78 BAHCALL, J. N. Solar neutrinos. I: Theoretical. **Phys. Rev. Lett.**, v. 12, p. 300–302, 1964.

79 DAVIS JR., R.; HARMER, D. S.; HOFFMAN, K. C. Search for neutrinos from the sun. **Phys. Rev. Lett.**, v. 20, p. 1205–1209, 1968.

80 MAKI, Z.; NAKAGAWA, M.; SAKATA, S. Remarks on the unified model of elementary particles. **Prog. Theor. Phys.**, v. 28, p. 870–880, 1962.

81 PONTECORVO, B. Neutrino Experiments and the Problem of Conservation of Leptonic Charge. **Zh. Eksp. Teor. Fiz.**, v. 53, p. 1717–1725, 1967.

82 AHMAD, Q. R. et al. Measurement of the rate of $\nu_e + d \to p + p + e^-$ interactions produced by ^{8}B solar neutrinos at the Sudbury Neutrino Observatory. **Phys. Rev. Lett.**, v. 87, p. 071301, 2001.

83 AHMAD, Q. R. et al. Direct evidence for neutrino flavor transformation from neutral current interactions in the Sudbury Neutrino Observatory. **Phys. Rev. Lett.**, v. 89, p. 011301, 2002.

84 WOLFENSTEIN, L. Neutrino Oscillations in Matter. **Phys. Rev. D**, v. 17, p. 2369–2374, 1978.

85 MIKHEYEV, S. P.; SMIRNOV, A. Y. Resonance Amplification of Oscillations in Matter and Spectroscopy of Solar Neutrinos. **Sov. J. Nucl. Phys.**, v. 42, p. 913–917, 1985.

86 GUARINI, E. **Exploring the High-Energy Transient Universe with Neutrinos**. Tese (PhD Thesis) — Niels Bohr Institute, January 2024. Available at <https://nbi.ku.dk/english/theses/phd-theses/ersilia-guarini/>.

87 VITAGLIANO, E.; TAMBORRA, I.; RAFFELT, G. Grand Unified Neutrino Spectrum at Earth: Sources and Spectral Components. **Rev. Mod. Phys.**, v. 92, p. 45006, 2020.

88 DOLGOV, A. D. Neutrinos in cosmology. **Phys. Rept.**, v. 370, p. 333–535, 2002.

89 CAPANEMA, A. **Cascaded gamma-ray Counterpart of the IceCube Neutrinos**. Dissertação (Master's thesis) — Pontifícia Universidade Católica do Rio de Janeiro, Rio de Janeiro, RJ - Brazil, September 2020. Available at <https://www.maxwell.vrac.puc-rio.br/colecao.php?strSecao=resultado&nrSeq=52189@2>.

90 VITAGLIANO, E.; REDONDO, J.; RAFFELT, G. Solar neutrino flux at keV energies. **JCAP**, v. 12, p. 010, 2017.

91 HIRATA, K. et al. Observation of a Neutrino Burst from the Supernova SN 1987a. **Phys. Rev. Lett.**, v. 58, p. 1490–1493, 1987.

92 BIONTA, R. M. et al. Observation of a Neutrino Burst in Coincidence with Supernova SN 1987a in the Large Magellanic Cloud. **Phys. Rev. Lett.**, v. 58, p. 1494, 1987.

93 ALEKSEEV, E. N. et al. Detection of the Neutrino Signal From SN1987A in the LMC Using the Inr Baksan Underground Scintillation Telescope. **Phys. Lett. B**, v. 205, p. 209–214, 1988.

94 LIPARI, P. Lepton spectra in the earth's atmosphere. **Astropart. Phys.**, v. 1, p. 195–227, 1993.

95 ACHAR, C. V. et al. Detection of muons produced by cosmic ray neutrinos deep underground. **Phys. Lett.**, v. 18, p. 196–199, 1965.

96 REINES, F. et al. Evidence for high-energy cosmic ray neutrino interactions. **Phys. Rev. Lett.**, v. 15, p. 429–433, 1965.

97 FUKUDA, Y. et al. Evidence for oscillation of atmospheric neutrinos. **Phys. Rev. Lett.**, v. 81, p. 1562–1567, 1998.

98 BHATTACHARYA, A. et al. Prompt atmospheric neutrino fluxes: perturbative QCD models and nuclear effects. **JHEP**, v. 11, p. 167, 2016.

99 KHEIRANDISH, A. Identifying Galactic sources of high-energy neutrinos. **Astrophys. Space Sci.**, v. 365, n. 6, p. 108, 2020.

100 ABBASI, R. et al. IceCat-1: The IceCube Event Catalog of Alert Tracks. **Astrophys. J. Suppl.**, v. 269, n. 1, p. 25, 2023.

101 BEREZINSKY, V. S.; ZATSEPIN, G. T. Cosmic rays at ultrahigh-energies (neutrino?). **Phys. Lett. B**, v. 28, p. 423–424, 1969.

102 BEREZINSKY, V. S.; SMIRNOV, A. Y. Cosmic neutrinos of ultra-high energies and detection possibility. **Astrophys. Space Sci.**, v. 32, p. 461–482, 1975.

103 AHLERS, M.; HALZEN, F. Minimal Cosmogenic Neutrinos. **Phys. Rev. D**, v. 86, p. 083010, 2012.

104 AGERON, M. et al. ANTARES: the first undersea neutrino telescope. **Nucl. Instrum. Meth. A**, v. 656, p. 11–38, 2011.

105 FUSCO, L. A. Overview of the results from the ANTARES neutrino telescope. **J. Phys. Conf. Ser.**, v. 2429, n. 1, p. 012027, 2023.

106 ADRIAN-MARTINEZ, S. et al. Letter of intent for KM3NeT 2.0. **J. Phys. G**, v. 43, n. 8, p. 084001, 2016.

107 DRAKOPOULOU, E. KM3NeT: Status and physics results. **Nucl. Instrum. Meth. A**, v. 1056, p. 168592, 2023.

108 AIELLO, S. et al. Astronomy potential of KM3NeT/ARCA. 2 2024.

109 MORSE, R. et al. The AMANDA neutrino astronomy project. In: **5th International Symposium on Neutrino Telescopes**. [S.l.: s.n.], 1993.

110 HILL, G. C. Neutrino astronomy with IceCube and AMANDA. **Nucl. Phys. B Proc. Suppl.**, v. 221, p. 103–109, 2011.

111 AVRORIN, A. D. et al. Baikal-GVD: status and prospects. **EPJ Web Conf.**, v. 191, p. 01006, 2018.

112 AYNUTDINOV, V. M. et al. Large neutrino telescope Baikal-GVD: recent status. **PoS**, ICRC2023, p. 976, 2023.

113 GORHAM, P. W. et al. The Antarctic Impulsive Transient Antenna Ultra-high Energy Neutrino Detector Design, Performance, and Sensitivity for 2006-2007 Balloon Flight. **Astropart. Phys.**, v. 32, p. 10–41, 2009.

114 ASKAR'YAN, G. A. Excess negative charge of an electron-photon shower and its coherent radio emission. **Zh. Eksp. Teor. Fiz.**, v. 41, p. 616–618, 1961.

115 NIZ, J. A.-M. et al. Askaryan radiation from neutrino-induced showers in ice. **Phys. Rev. D**, v. 101, n. 8, p. 083005, 2020.

116 GORHAM, P. W. et al. Constraints on the ultrahigh-energy cosmic neutrino flux from the fourth flight of ANITA. **Phys. Rev. D**, v. 99, n. 12, p. 122001, 2019.

117 GORHAM, P. W. et al. Characteristics of Four Upward-pointing Cosmic-ray-like Events Observed with ANITA. **Phys. Rev. Lett.**, v. 117, n. 7, p. 071101, 2016.

118 GORHAM, P. W. et al. Observation of an Unusual Upward-going Cosmic-ray-like Event in the Third Flight of ANITA. **Phys. Rev. Lett.**, v. 121, n. 16, p. 161102, 2018.

119 GORHAM, P. W. et al. Unusual Near-Horizon Cosmic-Ray-like Events Observed by ANITA-IV. **Phys. Rev. Lett.**, v. 126, n. 7, p. 071103, 2021.

120 PRECHELT, R. et al. Analysis of a tau neutrino origin for the near-horizon air shower events observed by the fourth flight of the Antarctic Impulsive Transient Antenna. **Phys. Rev. D**, v. 105, n. 4, p. 042001, 2022.

121 BERTóLEZ-MARTíNEZ, T. et al. IceCube and the origin of ANITA-IV events. **JHEP**, v. 07, p. 005, 2023.

122 AGOSTINI, M. et al. The Pacific Ocean Neutrino Experiment. **Nature Astron.**, v. 4, n. 10, p. 913–915, 2020.

123 ROMERO-WOLF, A. et al. An Andean Deep-Valley Detector for High-Energy Tau Neutrinos. In: **Latin American Strategy Forum for Research Infrastructure**. [S.l.: s.n.], 2020.

124 YE, Z. P. et al. A multi-cubic-kilometre neutrino telescope in the western Pacific Ocean. **Nature Astron.**, v. 7, n. 12, p. 1497–1505, 2023.

125 OTTE, A. N. et al. Trinity: An Air-Shower Imaging System for the Detection of Ultrahigh Energy Neutrinos. **PoS**, ICRC2019, p. 976, 2020.

126 MARINELLI, A.; MIGLIOZZI, P.; SIMONELLI, A. Acoustic neutrino detection in a Adriatic multidisciplinary observatory (ANDIAMO). **Astropart. Phys.**, v. 143, p. 102760, 2022.

127 ALLISON, P. et al. Design and Initial Performance of the Askaryan Radio Array Prototype EeV Neutrino Detector at the South Pole. **Astropart. Phys.**, v. 35, p. 457–477, 2012.

128 WISSEL, S. et al. Concept Study for the Beamforming Elevated Array for Cosmic Neutrinos (BEACON). **PoS**, ICRC2019, p. 1033, 2020.

129 NIZ, J. A.-M. et al. The Giant Radio Array for Neutrino Detection (GRAND): Science and Design. **Sci. China Phys. Mech. Astron.**, v. 63, n. 1, p. 219501, 2020.

130 OLINTO, A. V. et al. The POEMMA (Probe of Extreme Multi-Messenger Astrophysics) observatory. **JCAP**, v. 06, p. 007, 2021.

131 ABARR, Q. et al. The Payload for Ultrahigh Energy Observations (PUEO): a white paper. **JINST**, v. 16, n. 08, p. P08035, 2021.

132 PROHIRA, S. et al. The Radar Echo Telescope for Cosmic Rays: Pathfinder experiment for a next-generation neutrino observatory. **Phys. Rev. D**, v. 104, n. 10, p. 102006, 2021.

133 AGUILAR, J. A. et al. Design and Sensitivity of the Radio Neutrino Observatory in Greenland (RNO-G). **JINST**, v. 16, n. 03, p. P03025, 2021. [Erratum: JINST 18, E03001 (2023)].

134 WANG, S.-H. et al. TAROGE-M: radio antenna array on antarctic high mountain for detecting near-horizontal ultra-high energy air showers. **JCAP**, v. 11, p. 022, 2022.

135 MURASE, K.; BARTOS, I. High-Energy Multimessenger Transient Astrophysics. **Ann. Rev. Nucl. Part. Sci.**, v. 69, p. 477–506, 2019.

136 RONCHINI, S. et al. Perspectives for multimessenger astronomy with the next generation of gravitational-wave detectors and high-energy satellites. **Astron. Astrophys.**, v. 665, p. A97, 2022.

137 CHRISTENSEN, N. L. Multimessenger Astronomy. In: **46th Rencontres de Moriond on Gravitational Waves and Experimental Gravity**. [S.l.: s.n.], 2011. p. 35–42.

138 CARROLL, S. M. **Spacetime and Geometry: An Introduction to General Relativity**. [S.l.]: Cambridge University Press, 2019. ISBN 978-0-8053-8732-2, 978-1-108-48839-6, 978-1-108-77555-7.

139 EINSTEIN, A. Approximative Integration of the Field Equations of Gravitation. **Sitzungsber. Preuss. Akad. Wiss. Berlin (Math. Phys.)**, v. 1916, p. 688–696, 1916.

140 EINSTEIN, A. Über Gravitationswellen. **Sitzungsber. Preuss. Akad. Wiss. Berlin (Math. Phys.)**, v. 1918, p. 154–167, 1918.

141 ABBOTT, B. P. et al. Observation of Gravitational Waves from a Binary Black Hole Merger. **Phys. Rev. Lett.**, v. 116, n. 6, p. 061102, 2016.

142 HARTLE, J. B. **Gravity: An introduction to Einstein's general relativity**. [S.l.]: Pearson New International Edition, 2014. ISBN 978-1-292-03914-5.

143 AGAZIE, G. et al. The NANOGrav 15 yr Data Set: Evidence for a Gravitational-wave Background. **Astrophys. J. Lett.**, v. 951, n. 1, p. L8, 2023.

144 ANTONIADIS, J. et al. The second data release from the European Pulsar Timing Array - III. Search for gravitational wave signals. **Astron. Astrophys.**, v. 678, p. A50, 2023.

145 REARDON, D. J. et al. Search for an Isotropic Gravitational-wave Background with the Parkes Pulsar Timing Array. **Astrophys. J. Lett.**, v. 951, n. 1, p. L6, 2023.

146 XU, H. et al. Searching for the Nano-Hertz Stochastic Gravitational Wave Background with the Chinese Pulsar Timing Array Data Release I. **Res. Astron. Astrophys.**, v. 23, n. 7, p. 075024, 2023.

147 MOORE, C. J.; COLE, R. H.; BERRY, C. P. L. Gravitational-wave sensitivity curves. **Class. Quant. Grav.**, v. 32, n. 1, p. 015014, 2015.

148 ABBOTT, B. P. et al. Gravitational Waves and Gamma-rays from a Binary Neutron Star Merger: GW170817 and GRB 170817A. **Astrophys. J. Lett.**, v. 848, n. 2, p. L13, 2017.

149 COULTER, D. A. et al. Swope Supernova Survey 2017a (SSS17a), the Optical Counterpart to a Gravitational Wave Source. **Science**, v. 358, p. 1556, 2017.

150 ANTONUCCI, R. Unified models for active galactic nuclei and quasars. **Ann. Rev. Astron. Astrophys.**, v. 31, p. 473–521, 1993.

151 SANDERS, N. **Guide to Classification of Galaxies and AGNs**. Astrobites, 2011. Disponível em: <https://astrobites.org/guides/galaxy-and-agn-types/>.

152 BIANCHI, S.; MAIOLINO, R.; RISALITI, G. AGN Obscuration and the Unified Model. **Adv. Astron.**, v. 2012, p. 782030, 2012.

153 BLANDFORD, R.; MEIER, D.; READHEAD, A. Relativistic Jets from Active Galactic Nuclei. **Ann. Rev. Astron. Astrophys.**, v. 57, p. 467–509, 2019.

154 CAO, G. et al. Progress in multi-messenger observations and emission models of blazars. **New Astron. Rev.**, v. 98, p. 101693, 2024.

155 URRY, C. M.; PADOVANI, P. Unified schemes for radio-loud active galactic nuclei. **Publ. Astron. Soc. Pac.**, v. 107, p. 803, 1995.

156 AJELLO, M. et al. The Cosmic Evolution of Fermi BL Lacertae Objects. **Astrophys. J.**, v. 780, p. 73, 2014.

157 AJELLO, M. et al. The Luminosity Function of Fermi-detected Flat-Spectrum Radio Quasars. **Astrophys. J.**, v. 751, p. 108, 2012.

158 AJELLO, M. et al. The Fourth Catalog of Active Galactic Nuclei Detected by the Fermi Large Area Telescope: Data Release 3. **Astrophys. J. Suppl.**, v. 263, n. 2, p. 24, 2022.

159 ELIA, D. et al. The Star Formation Rate of the Milky Way as Seen by Herschel. **Astrophys. J.**, v. 941, n. 2, p. 162, 2022.

160 AJELLO, M. et al. The γ-Ray Emission of Star-forming Galaxies. **Astrophys. J.**, v. 894, n. 2, p. 88, 2020.

161 ROTH, M. A. et al. The diffuse γ-ray background is dominated by star-forming galaxies. **Nature**, v. 597, n. 7876, p. 341–344, 2021.

162 BYKOV, A. M. et al. High-Energy Particles and Radiation in Star-Forming Regions. **Space Sci. Rev.**, v. 216, n. 3, p. 42, 2020.

163 MANNUCCI, F. et al. The infrared supernova rate in starburst galaxies. **Astron. Astrophys.**, v. 401, p. 519–530, 2003.

164 ABDOLLAHI, S. et al. $Fermi$ Large Area Telescope Fourth Source Catalog. **Astrophys. J. Suppl.**, v. 247, n. 1, p. 33, 2020.

165 BAADE, W.; ZWICKY, F. Cosmic Rays from Super-Novae. **Proc. Nat. Acad. Sci.**, v. 20, n. 5, p. 259, 1934.

166 ACKERMANN, M. et al. Detection of the Characteristic Pion-Decay Signature in Supernova Remnants. **Science**, v. 339, p. 807, 2013.

167 SVESHNIKOVA, L. G. The knee in galactic cosmic ray spectrum and variety in supernovae. **Astron. Astrophys.**, v. 409, p. 799–808, 2003.

168 WANG, X.-Y. et al. High-energy Cosmic Rays and Neutrinos from Semi-relativistic Hypernovae. **Phys. Rev. D**, v. 76, p. 083009, 2007.

169 CAO, Z. et al. Peta–electron volt gamma-ray emission from the Crab Nebula. **Science**, v. 373, n. 6553, p. 425–430, 2021.

170 BUCCIANTINI, N.; ARONS, J.; AMATO, E. Modeling the spectral evolution of PWNe inside SNRs. **Mon. Not. Roy. Astron. Soc.**, v. 410, p. 381, 2011.

171 KOTERA, K.; AMATO, E.; BLASI, P. The fate of ultrahigh energy nuclei in the immediate environment of young fast-rotating pulsars. **JCAP**, v. 08, p. 026, 2015.

172 CHANDRASEKHAR, S. The maximum mass of ideal white dwarfs. **Astrophys. J.**, v. 74, p. 81–82, 1931.

173 JANKA, H.-T. Neutrino emission from supernovae. In: ______. **Handbook of Supernovae**. [S.l.: s.n.], 2017. p. 1575–1604.

174 MEZZACAPPA, A.; ZANOLIN, M. Gravitational Waves from Neutrino-Driven Core Collapse Supernovae: Predictions, Detection, and Parameter Estimation. 1 2024.

175 MICELI, D.; NAVA, L. Gamma-Ray Bursts Afterglow Physics and the VHE Domain. **Galaxies**, v. 10, n. 3, p. 66, 2022.

176 HJORTH, J. et al. A Very energetic supernova associated with the gamma-ray burst of 29 March 2003. **Nature**, v. 423, p. 847–850, 2003.

177 TROJA, E. et al. A nearby long gamma-ray burst from a merger of compact objects. **Nature**, v. 612, n. 7939, p. 228–231, 2022.

178 FAZI, G. G. (Ed.). **The Encyclopedia of Cosmology**. [S.l.]: World Scientific, 2023. ISBN 978-981-12-8969-9, 978-981-12-8971-2.

179 SEDDA, M. A.; BORTOLAS, E.; SPERA, M. (Ed.). **Black Holes in the Era of Gravitational-Wave Astronomy**. Amsterdam: Elsevier, 2024. ISBN 978-0-323-95636-9, 978-0-323-95637-6.

180 COLLE, F. D.; LU, W. Jets from Tidal Disruption Events. **New Astron. Rev.**, v. 89, p. 101538, 2020.

181 LUNARDINI, C. Neutrinos from Tidal Disruption Events. **PoS**, ICRC2019, p. 949, 2020.

182 PIRAN, T.; BENIAMINI, P. Ultra high energy cosmic rays from tidal disruption events. **JCAP**, v. 11, p. 049, 2023.

183 MURASE, K. et al. High-Energy Neutrino and Gamma-Ray Emission from Tidal Disruption Events. **Astrophys. J.**, v. 902, n. 2, p. 108, 2020.

184 ABBASI, R. et al. The IceCube high-energy starting event sample: Description and flux characterization with 7.5 years of data. **Phys. Rev. D**, v. 104, p. 022002, 2021.

185 AAB, A. et al. An Indication of anisotropy in arrival directions of ultra-high-energy cosmic rays through comparison to the flux pattern of extragalactic gamma-ray sources. **Astrophys. J. Lett.**, v. 853, n. 2, p. L29, 2018.

186 ABREU, P. et al. The ultra-high-energy cosmic-ray sky above 32 EeV viewed from the Pierre Auger Observatory. **PoS**, ICRC2021, p. 307, 2021.

187 ALVAREZ, E. et al. Searches for correlation between UHECR events and high-energy gamma-ray Fermi-LAT data. **JCAP**, v. 12, p. 023, 2016.

188 ALBERT, A. et al. Search for Spatial Correlations of Neutrinos with Ultra-high-energy Cosmic Rays. **Astrophys. J.**, v. 934, n. 2, p. 164, 2022.

189 PARTENHEIMER, A. et al. Ultra-high-energy Cosmic Ray Sources can be Gamma-ray Dim. 4 2024.

190 AARTSEN, M. G. et al. Search for Sources of Astrophysical Neutrinos Using Seven Years of IceCube Cascade Events. **Astrophys. J.**, v. 886, p. 12, 2019.

191 AARTSEN, M. G. et al. Time-Integrated Neutrino Source Searches with 10 Years of IceCube Data. **Phys. Rev. Lett.**, v. 124, n. 5, p. 051103, 2020.

192 AARTSEN, M. G. et al. IceCube Search for High-Energy Neutrino Emission from TeV Pulsar Wind Nebulae. **Astrophys. J.**, v. 898, n. 2, p. 117, 2020.

193 ABBASI, R. et al. Evidence for neutrino emission from the nearby active galaxy NGC 1068. **Science**, v. 378, n. 6619, p. 538–543, 2022.

194 ABBASI, R. et al. Searching for High-energy Neutrino Emission from Galaxy Clusters with IceCube. **Astrophys. J. Lett.**, v. 938, n. 2, p. L11, 2022.

195 ABBASI, R. et al. Search for Continuous and Transient Neutrino Emission Associated with IceCube's Highest-energy Tracks: An 11 yr Analysis. **Astrophys. J.**, v. 964, n. 1, p. 40, 2024.

196 ABBASI, R. et al. Search for Correlations of High-energy Neutrinos Detected in IceCube with Radio-bright AGN and Gamma-Ray Emission from Blazars. **Astrophys. J.**, v. 954, n. 1, p. 75, 2023.

197 PRIVON, G. C. et al. Search for high-energy neutrino emission from hard X-ray AGN with IceCube. **PoS**, ICRC2023, p. 1032, 2023.

198 ABBASI, R. et al. Constraining High-energy Neutrino Emission from Supernovae with IceCube. **Astrophys. J. Lett.**, v. 949, n. 1, p. L12, 2023.

199 ABBASI, R. et al. All-Sky Search for Transient Astrophysical Neutrino Emission with 10 Years of IceCube Cascade Events. 12 2023.

200 AARTSEN, M. G. et al. Multimessenger observations of a flaring blazar coincident with high-energy neutrino IceCube-170922A. **Science**, v. 361, n. 6398, p. eaat1378, 2018.

201 AARTSEN, M. G. et al. Neutrino emission from the direction of the blazar TXS 0506+056 prior to the IceCube-170922A alert. **Science**, v. 361, n. 6398, p. 147–151, 2018.

202 STEIN, R. et al. A tidal disruption event coincident with a high-energy neutrino. **Nature Astron.**, v. 5, n. 5, p. 510–518, 2021.

203 ACHTERBERG, A. et al. On the selection of AGN neutrino source candidates for a source stacking analysis with neutrino telescopes. **Astropart. Phys.**, v. 26, p. 282–300, 2006.

204 ABBASI, R. et al. Time-Integrated Searches for Point-like Sources of Neutrinos with the 40-String IceCube Detector. **Astrophys. J.**, v. 732, p. 18, 2011.

205 HUBER, M. Searches for steady neutrino emission from 3FHL blazars using eight years of IceCube data from the Northern hemisphere. **PoS**, ICRC2019, p. 916, 2020.

206 KHEIRANDISH, A.; WOOD, J. IceCube Search for Galactic Neutrino Sources based on HAWC Observations of the Galactic Plane. **PoS**, ICRC2019, p. 932, 2020.

207 AARTSEN, M. G. et al. The contribution of Fermi-2LAC blazars to the diffuse TeV-PeV neutrino flux. **Astrophys. J.**, v. 835, n. 1, p. 45, 2017.

208 ABBASI, R. et al. Search for Astrophysical Neutrinos from 1FLE Blazars with IceCube. **Astrophys. J.**, v. 938, n. 1, p. 38, 2022.

209 ABBASI, R. et al. Search for High-Energy Neutrinos from TDE-like Flares with IceCube. **PoS**, ICRC2023, p. 1478, 2023.

210 MCDONOUGH, K. et al. A Search for AGN sources of the IceCube Diffuse Neutrino Flux. 7 2023.

211 LIU, Q.; KHEIRANDISH, A. Searching for High-Energy Neutrino Emission from TeV Pulsar Wind Nebulae. **PoS**, ICRC2019, p. 944, 2020.

212 BOURI, S. et al. First Search for High-Energy Neutrino Emission from Galaxy Mergers. 4 2024.

213 PASUMARTI, V.; DESAI, S. A stacked search for spatial coincidences between IceCube neutrinos and radio pulsars. **JCAP**, v. 04, p. 010, 2024.

214 LUCARELLI, F. et al. Neutrino search from γ-ray bursts during the prompt and X-ray afterglow phases using 10 years of IceCube public data. **Astron. Astrophys.**, v. 672, p. A102, 2023.

215 STEIN, R. Search for Neutrinos from Populations of Optical Transients. **PoS**, ICRC2019, p. 1016, 2020.

216 ABBASI, R. et al. Observation of high-energy neutrinos from the Galactic plane. **Science**, v. 380, n. 6652, p. adc9818, 2023.

217 AMBROSONE, A. et al. Galactic diffuse neutrino emission from sources beyond the discovery horizon. **Phys. Rev. D**, v. 109, n. 4, p. 043007, 2024.

218 LIU, S. et al. Hadronic versus Leptonic Models for γ-Ray Emission from VER J2227+608. **Astrophys. J. Lett.**, v. 897, n. 2, p. L34, 2020.

219 PALIYA, V. S. et al. Leptonic and Hadronic Modeling of $Fermi$-LAT Hard Spectrum Quasars and Predictions for High-Energy Polarization. **Astrophys. J.**, v. 863, n. 1, p. 98, 2018.

220 GUÉPIN, C.; CERUTTI, B.; KOTERA, K. Proton acceleration in pulsar magnetospheres. **Astron. Astrophys.**, v. 635, p. A138, 2020.

221 FERMI, E. On the Origin of the Cosmic Radiation. **Phys. Rev.**, v. 75, p. 1169–1174, 1949.

222 SERPICO, P. D. **High energy physics processes in astrophysics**. 2019. Lecture Notes. Disponível em: <https://www.ictp-saifr.org/school-on-high-energy-astrophysics/>.

223 KACHELRIESS, M. Lecture notes on high energy cosmic rays. 1 2008.

224 LONGAIR, M. S. **High Energy Astrophysics (Third Edition)**. [S.l.]: Cambridge University Press, 2011. ISBN 978-0-521-75618-1.

225 KRYMSKII, G. F. A regular mechanism for the acceleration of charged particles on the front of a shock wave. **Sov. Phys. Dokl.**, v. 22, p. 327, 1977.

226 AXFORD, W. I.; LEER, E.; SKADRON, G. The acceleration of cosmic ray by shock waves. **15 international cosmic ray conference**, v. 11, p. 132–137, 1977.

227 BELL, A. R. The acceleration of cosmic rays in shock fronts – I. **Mon. Not. Roy. Astron. Soc.**, v. 182, n. 2, p. 147–156, 1978.

228 BLANDFORD, R. D.; OSTRIKER, J. P. Particle Acceleration by Astrophysical Shocks. **Astrophys. J. Lett.**, v. 221, p. L29–L32, 1978.

229 PADMANABHAN, T. **Theoretical Astrophysics Volume I: Astrophysical Processes**. [S.l.]: Cambridge University Press, 2000. ISBN 0 521 56240 6.

230 CAPRIOLI, D. Particle acceleration at shocks: An introduction. **Proc. Int. Sch. Phys. Fermi**, v. 208, p. 143–181, 2024.

231 BELL, A. R. Turbulent amplification of magnetic field and diffusive shock acceleration of cosmic rays. **Mon. Not. Roy. Astron. Soc.**, v. 353, n. 2, p. 550—-558, 2004.

232 ZIRAKASHVILI, V. N.; PTUSKIN, V. S. The influence of the Alfvénic drift on the shape of cosmic ray spectra in SNRs. **AIP Conf. Proc.**, v. 1085, n. 1, p. 336–339, 2009.

233 BLASI, P. et al. Collisionless shocks in a partially ionized medium: I. Neutral return flux and its effects on acceleration of test particles. **Astrophys. J.**, v. 755, p. 121, 2012.

234 BLASI, P. The Origin of Galactic Cosmic Rays. **Astron. Astrophys. Rev.**, v. 21, p. 70, 2013.

235 GIANNIOS, D. UHECRs from magnetic reconnection in relativistic jets. **Mon. Not. Roy. Astron. Soc.**, v. 408, p. 46, 2010.

236 RIEGER, F. M.; DUFFY, P. Shear acceleration in relativistic astrophysical jets. **Astrophys. J.**, v. 617, p. 155–161, 2004.

237 ENGEL, R. et al. Proton proton cross-section at $\sqrt{s}$ similar to 30-TeV. **Phys. Rev. D**, v. 58, p. 014019, 1998.

238 HANHART, C. et al. Role of the Delta isobar in the reaction N N —> N N pi near threshold. **Phys. Lett. B**, v. 444, p. 25–31, 1998.

239 KAMAE, T. et al. Parameterization of Gamma, e+/- and Neutrino Spectra Produced by p-p Interaction in Astronomical Environment. **Astrophys. J.**, v. 647, p. 692–708, 2006. [Erratum: Astrophys.J. 662, 779 (2007)].

240 HARDIE, J. G. et al. Kinematically complete measurement of p p –> p n pi+ near threshold. **Phys. Rev. C**, v. 56, p. 20–37, 1997.

241 LINDENBAUM, S. J.; STERNHEIMER, R. M. Isobaric nucleon model for pion production in nucleon-nucleon collisions. **Phys. Rev.**, v. 105, p. 1874–1879, 1957.

242 NORBURY, J. W. **Pion Total Cross Section in Nucleon - Nucleon Collisions**. [S.l.], 2009. Disponível em: <https://ntrs.nasa.gov/citations/20090042822>.

243 NORBURY, J. W.; TOWNSEND, L. W. Parameterized total cross-sections for pion production in nuclear collisions. **Nucl. Instrum. Meth. B**, v. 254, p. 187–192, 2007.

244 FEYNMAN, R. P. Very high-energy collisions of hadrons. **Phys. Rev. Lett.**, v. 23, p. 1415–1417, 1969.

245 LIPARI, P. Hadronic interactions modeling, and the calculation of the inclusive fluxes of atmospheric muons and neutrinos. **Nucl. Phys. B Proc. Suppl.**, v. 175-176, p. 96–103, 2008.

246 KOBA, Z.; NIELSEN, H. B.; OLESEN, P. Scaling of multiplicity distributions in high-energy hadron collisions. **Nucl. Phys. B**, v. 40, p. 317–334, 1972.

247 HEGYI, S. KNO scaling 30 years later. **Nucl. Phys. B Proc. Suppl.**, v. 92, p. 122–129, 2001.

248 DOKSHITZER, Y. L. Improved QCD treatment of the KNO phenomenon. **Phys. Lett. B**, v. 305, p. 295–301, 1993.

249 SJOSTRAND, T.; ZIJL, M. van. A Multiple Interaction Model for the Event Structure in Hadron Collisions. **Phys. Rev. D**, v. 36, p. 2019, 1987.

250 ALEXOPOULOS, T. et al. The role of double parton collisions in soft hadron interactions. **Phys. Lett. B**, v. 435, p. 453–457, 1998.

251 KAMAE, T.; ABE, T.; KOI, T. Diffractive interaction and scaling violation in p p —> pi0 interaction and GeV excess in galactic diffuse gamma-ray spectrum of EGRET. **Astrophys. J.**, v. 620, p. 244–256, 2005.

252 RIEHN, F. et al. Hadronic interaction model Sibyll 2.3d and extensive air showers. **Phys. Rev. D**, v. 102, n. 6, p. 063002, 2020.

253 OSTAPCHENKO, S. QGSJET-III model of high energy hadronic interactions: The formalism. **Phys. Rev. D**, v. 109, n. 3, p. 034002, 2024.

254 PIEROG, T. et al. EPOS LHC: Test of collective hadronization with data measured at the CERN Large Hadron Collider. **Phys. Rev. C**, v. 92, n. 3, p. 034906, 2015.

255 ROULET, E.; VISSANI, F. On the energy of the protons producing the very high-energy astrophysical neutrinos. **JCAP**, v. 03, p. 050, 2021.

256 KELNER, S. R.; AHARONIAN, F. A.; BUGAYOV, V. V. Energy spectra of gamma-rays, electrons and neutrinos produced at proton-proton interactions in the very high energy regime. **Phys. Rev. D**, v. 74, p. 034018, 2006. [Erratum: Phys.Rev.D 79, 039901 (2009)].

257 AHARONIAN, F. A.; ATOYAN, A. M. Broad-band diffuse gamma-ray emission of the galactic disk. **Astron. Astrophys.**, v. 362, p. 937, 2000.

258 STECKER, F. W. Effect of photomeson production by the universal radiation field on high-energy cosmic rays. **Phys. Rev. Lett.**, v. 21, p. 1016–1018, 1968.

259 MANNHEIM, K.; BIERMANN, P. L. Photomeson production in active galactic nuclei. **Astron. Astrophys.**, v. 221, p. 211–220, 1989.

260 STECKER, F. W. Ultrahigh energy photons, electrons and neutrinos, the microwave background, and the universal cosmic ray hypothesis. **Astrophys. Space Sci.**, v. 20, p. 47–57, 1973.

261 HUMMER, S. et al. Simplified models for photohadronic interactions in cosmic accelerators. **Astrophys. J.**, v. 721, p. 630–652, 2010.

262 MUCKE, A. et al. SOPHIA: Monte Carlo simulations of photohadronic processes in astrophysics. **Comput. Phys. Commun.**, v. 124, p. 290–314, 2000.

263 MUCKE, A. et al. On photohadronic processes in astrophysical environments. **Publ. Astron. Soc. Austral.**, v. 16, p. 160, 1999.

264 FIORILLO, D. F. G. et al. Unified thermal model for photohadronic neutrino production in astrophysical sources. **JCAP**, v. 07, p. 028, 2021.

265 KELNER, S. R.; AHARONIAN, F. A. Energy spectra of gamma-rays, electrons and neutrinos produced at interactions of relativistic protons with low energy radiation. **Phys. Rev. D**, v. 78, p. 034013, 2008. [Erratum: Phys.Rev.D 82, 099901 (2010)].

266 MURASE, K.; FUKUGITA, M. Energetics of High-Energy Cosmic Radiations. **Phys. Rev. D**, v. 99, n. 6, p. 063012, 2019.

267 WAXMAN, E.; BAHCALL, J. High energy neutrinos from astrophysical sources: An upper bound. **Phys. Rev. D**, APS, v. 59, n. 023002, p. 8, 1998.

268 WAXMAN, E. Cosmological origin for cosmic rays above 10^{19} ev. **Astrophys. J.**, IOP, v. 452, n. 1, p. L1–L4, 1995.

269 BAHCALL, J.; WAXMAN, E. High energy astrophysical neutrinos: The upper bound is robust. **Phys. Rev. D**, APS, v. 64, n. 023002, p. 8, 2001.

270 MURASE, K.; BEACOM, J. F. Neutrino Background Flux from Sources of Ultrahigh-Energy Cosmic-Ray Nuclei. **Phys. Rev. D**, v. 81, p. 123001, 2010.

271 GLASHOW, S. L. Resonant Scattering of Antineutrinos. **Phys. Rev.**, v. 118, p. 316–317, 1960.

272 AARTSEN, M. G. et al. Detection of a particle shower at the Glashow resonance with IceCube. **Nature**, v. 591, n. 7849, p. 220–224, 2021. [Erratum: Nature 592, E11 (2021)].

273 WORKMAN, R. L. et al. Review of Particle Physics. **PTEP**, v. 2022, p. 083C01, 2022.

274 GIUNTI, C. No Effect of Majorana Phases in Neutrino Oscillations. **Phys. Lett. B**, v. 686, p. 41–43, 2010.

275 SALAS, P. F. de et al. 2020 global reassessment of the neutrino oscillation picture. **JHEP**, v. 02, p. 071, 2021.

276 KRUPPKE, D. **On Theories of Neutrino Oscillations: A Summary and Characterisation of the Problematic Aspects**. Dissertação (Mestrado) — Bielefeld U., 2007.

277 BUSTAMANTE, M.; AHLERS, M. Inferring the flavor of high-energy astrophysical neutrinos at their sources. **Phys. Rev. Lett.**, v. 122, n. 24, p. 241101, 2019.

278 MIKHEEV, S. P.; SMIRNOV, A. Y. Resonant amplification of neutrino oscillations in matter and solar neutrino spectroscopy. **Nuovo Cim. C**, v. 9, p. 17–26, 1986.

279 MIKHEEV, S. P.; SMIRNOV, A. Y. Neutrino Oscillations in an Inhomogeneous Medium: Adiabatic Regime. **Sov. Phys. JETP**, v. 65, p. 230–236, 1987.

280 BOTELLA, F. J.; LIM, C. S.; MARCIANO, W. J. Radiative Corrections to Neutrino Indices of Refraction. **Phys. Rev. D**, v. 35, p. 896, 1987.

281 ADDAZI, A. et al. Quantum gravity phenomenology at the dawn of the multi-messenger era—A review. **Prog. Part. Nucl. Phys.**, v. 125, p. 103948, 2022.

282 AKRAMI, Y. et al. Planck 2018 results. VII. Isotropy and Statistics of the CMB. **Astron. Astrophys.**, v. 641, p. A7, 2020.

283 FIXSEN, D. J. The Temperature of the Cosmic Microwave Background. **Astrophys. J.**, v. 707, p. 916–920, 2009.

284 PENZIAS, A. A.; WILSON, R. W. A Measurement of excess antenna temperature at 4080-Mc/s. **Astrophys. J.**, v. 142, p. 419–421, 1965.

285 AGHANIM, N. et al. Planck 2018 results. I. Overview and the cosmological legacy of Planck. **Astron. Astrophys.**, v. 641, p. A1, 2020.

286 PARTRIDGE, R. B.; PEEBLES, P. J. E. Are young galaxies visible? ii. the integrated background. **Astrophys. J.**, v. 148, p. 377, 1967.

287 HAUSER, M. G.; DWEK, E. The cosmic infrared background: measurements and implications. **Ann. Rev. Astron. Astrophys.**, v. 39, p. 249–307, 2001.

288 DOMINGUEZ, A. et al. Extragalactic Background Light Inferred from AEGIS Galaxy SED-type Fractions. **Mon. Not. Roy. Astron. Soc.**, v. 410, p. 2556, 2011.

289 SALDANA-LOPEZ, A. et al. An observational determination of the evolving extragalactic background light from the multiwavelength HST/CANDELS survey in the Fermi and CTA era. **Mon. Not. Roy. Astron. Soc.**, v. 507, n. 4, p. 5144–5160, 2021.

290 HAUSER, M. G. et al. The COBE diffuse infrared background experiment search for the cosmic infrared background. 1. Limits and detections. **Astrophys. J.**, v. 508, p. 25, 1998.

291 ACCIARI, V. A. et al. Measurement of the extragalactic background light using MAGIC and Fermi-LAT gamma-ray observations of blazars up to z = 1. **Mon. Not. Roy. Astron. Soc.**, v. 486, n. 3, p. 4233–4251, 2019.

292 LAUER, T. R. et al. New Horizons Observations of the Cosmic Optical Background. **Astrophys. J.**, v. 906, n. 2, p. 77, 2021.

293 LAUER, T. R. et al. Anomalous Flux in the Cosmic Optical Background Detected with New Horizons Observations. **Astrophys. J. Lett.**, v. 927, n. 1, p. L8, 2022.

294 NITU, I. C. et al. An updated estimate of the cosmic radio background and implications for ultra-high-energy photon propagation. **Astropart. Phys.**, v. 126, p. 102532, 2021.

295 FIXSEN, D. J. et al. ARCADE 2 Measurement of the Extra-Galactic Sky Temperature at 3-90 GHz. **Astrophys. J.**, v. 734, p. 5, 2011.

296 PROTHEROE, R. J.; BIERMANN, P. L. A New estimate of the extragalactic radio background and implications for ultrahigh-energy gamma-ray propagation. **Astropart. Phys.**, v. 6, p. 45–54, 1996. [Erratum: Astropart.Phys. 7, 181 (1997)].

297 BRAY, J. D.; SCAIFE, A. M. M. An upper limit on the strength of the extragalactic magnetic field from ultra-high-energy cosmic-ray anisotropy. **Astrophys. J.**, v. 861, n. 1, p. 3, 2018.

298 NERONOV, A. et al. Degree-scale GeV 'jets' from active and dead TeV blazars. **Astrophys. J. Lett.**, v. 719, p. L130, 2010.

299 VALLéE, J. P. Observations of the Magnetic Fields Inside and Outside the Milky Way, Starting with Globules ($\sim$ 1 parsec), Filaments, Clouds, Superbubbles, Spiral Arms, Galaxies, Superclusters, and Ending with the Cosmological Universe's Background Surface (at $\sim$ 8 Teraparsecs). **Fund. of Cosmic. Phys.**, v. 19, p. 1–89, 1997.

300 WIDROW, L. M. Origin of galactic and extragalactic magnetic fields. **Rev. Mod. Phys.**, v. 74, p. 775–823, 2002.

301 SIGL, G. **Astroparticle Physics: Theory and Phenomenology**. [S.l.]: Atlantis Press, 2017. v. 1. (Atlantis Studies in Astroparticle Physics and Cosmology, v. 1). ISBN 978-94-6239-242-7, 978-94-6239-243-4.

302 UNGER, M.; FARRAR, G. R. The Coherent Magnetic Field of the Milky Way. 11 2023.

303 JANSSON, R.; FARRAR, G. R. A New Model of the Galactic Magnetic Field. **Astrophys. J.**, v. 757, p. 14, 2012.

304 HAVERKORN, M. et al. The outer scale of turbulence in the magneto-ionized Galactic interstellar medium. **Astrophys. J.**, v. 680, p. 362, 2008.

305 DURRER, R.; NERONOV, A. Cosmological Magnetic Fields: Their Generation, Evolution and Observation. **Astron. Astrophys. Rev.**, v. 21, p. 62, 2013.

306 NERONOV, A.; VOVK, I. Evidence for strong extragalactic magnetic fields from Fermi observations of TeV blazars. **Science**, v. 328, p. 73–75, 2010.

307 PAOLETTI, D.; FINELLI, F. CMB Constraints on a Stochastic Background of Primordial Magnetic Fields. **Phys. Rev. D**, v. 83, p. 123533, 2011.

308 PLAGA, R. Detecting intergalactic magnetic fields using time delays in pulses of γ-rays. **Nature**, v. 374, n. 6521, p. 430–432, 1995.

309 HUANG, Y.-Y. et al. Constraints on the Intergalactic Magnetic Field Strength from γ-Ray Observations of GRB 221009A. **Astrophys. J. Lett.**, v. 955, n. 1, p. L10, 2023.

310 MICELI, D.; VELA, P. D.; PRANDINI, E. Prospects for detection of the pair-echo emission from TeV gamma-ray bursts. 5 2024.

311 FINKE, J.; REYES, L.; GEORGANOPOULOS, M. Constraints on the Intergalactic Magnetic Field from Gamma-Ray Observations of Blazars. **eConf**, C121028, p. 365, 2012.

312 BREIT, G.; WHEELER, J. A. Collision of two light quanta. **Phys. Rev.**, v. 46, p. 1087–1091, 1934.

313 JAUCH, J. M.; ROHRLICH, F. **The Theory of Photons and Electrons: The Relativistic Quantum Field Theory of Charged Particles with Spin One-half**. 1st. ed. Cambridge, MA: Addison-Wesley, 1955.

314 CANNONI, M. Lorentz invariant relative velocity and relativistic binary collisions. **Int. J. Mod. Phys. A**, v. 32, n. 02n03, p. 1730002, 2017.

315 GOULD, R. J.; SCHRéDER, G. P. Pair production in photon-photon collisions. **Phys. Rev.**, v. 155, n. 5, p. 1404–1407, 1967.

316 AGARONYAN, F. A.; ATOYAN, A. M.; NAGAPETYAN, A. M. Photoproduction of electron-positron pairs in compact x-ray sources. **Astrophysics**, v. 19, p. 187–194, 1983.

317 BOTTCHER, M.; SCHLICKEISER, R. The Pair production spectrum from photon-photon annihilation. **Astron. Astrophys.**, v. 325, p. 866, 1997.

318 LEE, S. On the propagation of extragalactic high-energy cosmic and gamma-rays. **Phys. Rev. D**, v. 58, p. 043004, 1998.

319 AHARONIAN, F. A.; KRIRILLOV-UGRIUMOV, V. G.; VARDANIAN, V. V. Formation of relativistic electron-photon showers in compact x-ray sources. **Astrophys. Spa. Sci.**, v. 115, n. 2, p. 201–225, 1985.

320 ZDZIARSKI, A. A. Saturated pair-photon cascades on isotropic background photons. **Astrophys. J.**, v. 335, p. 786–802, 1988.

321 JONES, F. C. Calculated Spectrum of Inverse-Compton-Scattered Photons. **Phys. Rev.**, v. 167, p. 1159–1169, 1968.

322 BELMONT, R. Numerical computation of isotropic Compton scattering. **Astron. Astrophys.**, v. 506, p. 589, 2009.

323 SARKAR, A.; CHLUBA, J.; LEE, E. Dissecting the Compton scattering kernel I: Isotropic media. **Mon. Not. Roy. Astron. Soc.**, v. 490, n. 3, p. 3705–3726, 2019.

324 AGARONYAN, F. A.; ATOYAN, A. M. Compton scattering of relativistic electrons in compact x-ray sources. **Astrophys. and Spa. Sci.**, v. 79, n. 2, p. 321–336, 1981.

325 BLUMENTHAL, G. R.; GOULD, R. J. Bremsstrahlung, synchrotron radiation, and compton scattering of high-energy electrons traversing dilute gases. **Rev. Mod. Phys.**, v. 42, p. 237–270, 1970.

326 ATHAR, H.; LIN, G.-L.; TSENG, J.-J. Muon pair production by electron photon scatterings. **Phys. Rev. D**, v. 64, p. 071302, 2001.

327 WANG, K. et al. Neutrino Production in Electromagnetic Cascades: An extra component of cosmogenic neutrino at ultrahigh energies. **Phys. Rev. D**, v. 95, n. 6, p. 063010, 2017.

328 BROWN, R. W. et al. Role of γ+γ→e++e−+e++e− in Photoproduction, Colliding Beams, and Cosmic Photon Absorption. **Phys. Rev. D**, v. 8, n. 9, p. 3083, 1973.

329 DEMIDOV, S. V.; KALASHEV, O. E. Double Pair Production by Ultra High Energy Cosmic Ray Photons. **J. Exp. Theor. Phys.**, v. 108, p. 764–769, 2009.

330 BORSELLINO, A. Sulle coppie di elettroni create da raggi γ in presenza di elettroni. **Nuovo Cim.**, v. 4, p. 112–130, 1947.

331 HAUG, E. Bremsstrahlung and Pair Production in the Field of Free Electrons. **Z. Naturforsch. A**, v. 30, p. 1099–1113, 1975.

332 MASTICHIADIS, A. Relativistic electrons in photon fields: effects of triplet pair production on inverse Compton gamma-ray spectra. **MNRAS**, v. 253, p. 235–244, 11 1991.

333 HAUG, E. SIMPLE ANALYTIC EXPRESSIONS FOR THE TOTAL CROSS-SECTION FOR GAMMA E PAIR PRODUCTION. **Z. Naturforsch. A**, v. 36, p. 413–414, 1981.

334 MASTICHIADIS, A.; PROTHEROE, R. J.; SZABO, A. P. The effect of triplet production on pair-Compton cascades in thermal radiation. **Mon. Not. Roy. Astron. Soc.**, v. 266, p. 910, 1994.

335 BLANCO, C. γ-cascade: a simple program to compute cosmological gamma-ray propagation. **JCAP**, v. 01, p. 013, 2019.

336 KALASHEV, O. et al. Modeling the propagation of very-high-energy γ-rays with the CRbeam code: Comparison with CRPropa and ELMAG codes. **Astron. Astrophys.**, v. 675, p. A132, 2023.

337 BLYTT, M.; KACHELRIESS, M.; OSTAPCHENKO, S. ELMAG 3.01: A three-dimensional Monte Carlo simulation of electromagnetic cascades on the extragalactic background light and in magnetic fields. 9 2019.

338 ESMAEILI, A.; ESMAILI, A.; SERPICO, P. D. Neutrinos from muon-rich ultra high energy electromagnetic cascades: The MUNHECA code. **Comput. Phys. Commun.**, v. 299, p. 109154, 2024.

339 ADE, P. A. R. et al. Planck 2015 results. XIX. Constraints on primordial magnetic fields. **Astron. Astrophys.**, v. 594, p. A19, 2016.

340 JOHN, I.; LINDEN, T. Pulsars do not produce sharp features in the cosmic-ray electron and positron spectra. **Phys. Rev. D**, v. 107, n. 10, p. 103021, 2023.

341 FINKE, J. D. et al. Modeling the Extragalactic Background Light and the Cosmic Star Formation History. **Astrophys. J.**, v. 941, n. 1, p. 33, 2022.

342 FRANCESCHINI, A.; RODIGHIERO, G. The extragalactic background light revisited and the cosmic photon-photon opacity. **Astron. Astrophys.**, v. 603, p. A34, 2017.

343 BOYER, J. et al. Two photon production of pion pairs. **Phys. Rev. D**, v. 42, p. 1350–1367, 1990.

344 MORGAN, D.; PENNINGTON, M. R. Low-energy $\gamma\gamma \to \pi\pi$ Cross-section and the QED Born Amplitude. **Phys. Lett. B**, v. 192, p. 207–211, 1987.

345 WHALLEY, M. R. A Compilation of data on two photon reactions. **J. Phys. G**, v. 27, p. A1–A121, 2001.

346 MORGAN, D.; PENNINGTON, M. R.; WHALLEY, M. R. A Compilation of data on two photon reactions leading to hadron final states. **J. Phys. G: Nucl. Part. Phys., Volume 20, Number 8A**, v. 20, n. A1, 1994.

347 POMAKOV, V. et al. The redshift evolution of extragalactic magnetic fields. **Mon. Not. Roy. Astron. Soc.**, v. 515, n. 1, p. 256–270, 2022.

348 LI, Z.; WAXMAN, E. EeV neutrinos associated with UHECR sources. In: **32nd International Cosmic Ray Conference**. [S.l.: s.n.], 2007. v. 8, p. 262.

349 WOODS, T. E. et al. Titans of the Early Universe: The Prato Statement on the Origin of the First Supermassive Black Holes. **Publ. Astron. Soc. Austral.**, v. 36, p. e027, 2019.

350 INAYOSHI, K.; VISBAL, E.; HAIMAN, Z. The Assembly of the First Massive Black Holes. **Ann. Rev. Astron. Astrophys.**, v. 58, p. 27–97, 2020.

351 MANNUCCI, F. et al. A fundamental relation between mass, SFR and metallicity in local and high redshift galaxies. **Mon. Not. Roy. Astron. Soc.**, v. 408, p. 2115, 2010.

352 KACHELRIESS, M. The rise and fall of top-down models as main UHECR sources. In: **20th Rencontres de Blois on Challenges in Particle Astrophysics**. [S.l.: s.n.], 2008. p. 215–224.

353 GUÉPIN, C. et al. Indirect dark matter searches at ultrahigh energy neutrino detectors. **Phys. Rev. D**, v. 104, n. 8, p. 083002, 2021.

354 BATISTA, R. A. et al. CRPropa 3.2 — an advanced framework for high-energy particle propagation in extragalactic and galactic spaces. **JCAP**, v. 09, p. 035, 2022.

355 ACKERMANN, M. et al. A method to analyze the diffuse gamma-ray emission with the Fermi Large Area Telescope. **AIP Conf. Proc.**, v. 1085, n. 1, p. 763–766, 2009.

356 BALLET, J. et al. Fermi Large Area Telescope Fourth Source Catalog Data Release 4 (4FGL-DR4). 7 2023.

357 AJELLO, M. et al. The Fourth Catalog of Active Galactic Nuclei Detected by the Fermi Large Area Telescope. **Astrophys. J.**, v. 892, p. 105, 2020.

358 MAURO, M. D.; DONATO, F. Composition of the Fermi-LAT isotropic gamma-ray background intensity: Emission from extragalactic point sources and dark matter annihilations. **Phys. Rev. D**, v. 91, n. 12, p. 123001, 2015.

359 AJELLO, M. et al. The Origin of the Extragalactic Gamma-Ray Background and Implications for Dark-Matter Annihilation. **Astrophys. J. Lett.**, v. 800, n. 2, p. L27, 2015.

360 CALORE, F.; MAURO, M. D.; DONATO, F. Diffuse gamma-ray emission from galactic pulsars. **Astrophys. J.**, v. 796, p. 1, 2014.

361 CERRUTI, M. Leptonic and Hadronic Radiative Processes in Supermassive-Black-Hole Jets. **Galaxies**, v. 8, n. 4, p. 72, 2020.

362 QU, Y.; ZENG, H.; YAN, D. Gamma-ray luminosity function of bl lac objects and contribution to the extragalactic gamma-ray background. **Mon. Not. Roy. Astron. Soc.**, v. 490, n. 1, p. 758–765, 2019.

363 MAURO, M. D. et al. Diffuse γ-ray emission from unresolved BL Lac objects. **Astrophys. J.**, v. 786, p. 129, 2014.

364 KORSMEIER, M. et al. Flat-spectrum Radio Quasars and BL Lacs Dominate the Anisotropy of the Unresolved Gamma-Ray Background. **Astrophys. J.**, v. 933, n. 2, p. 221, 2022.

365 ZENG, H.; YAN, D.; ZHANG, L. Gamma-ray luminosity function of BL Lac objects. **Mon. Not. Roy. Astron. Soc.**, v. 441, p. 1760–1768, 2014.

366 MAURO, M. D. et al. Diffuse γ-ray emission from misaligned active galactic nuclei. **Astrophys. J.**, v. 780, p. 161, 2014.

367 INOUE, Y. Contribution of the Gamma-ray Loud Radio Galaxies Core Emissions to the Cosmic MeV and GeV Gamma-Ray Background Radiation. **Astrophys. J.**, v. 733, p. 66, 2011.

368 HOOPER, D.; LINDEN, T.; LOPEZ, A. Radio Galaxies Dominate the High-Energy Diffuse Gamma-Ray Background. **JCAP**, v. 08, p. 019, 2016.

369 TAMBORRA, I.; ANDO, S.; MURASE, K. Star-forming galaxies as the origin of diffuse high-energy backgrounds: Gamma-ray and neutrino connections, and implications for starburst history. **JCAP**, v. 09, p. 043, 2014.

370 UEDA, Y. et al. Cosmological evolution of the hard x-ray AGN luminosity function and the origin of the hard x-ray background. **Astrophys. J.**, v. 598, p. 886–908, 2003.

371 ACKERMANN, M. et al. GeV Observations of Star-forming Galaxies with \textitFermi LAT. **Astrophys. J.**, v. 755, p. 164, 2012.

372 LINDEN, T. Star-Forming Galaxies Significantly Contribute to the Isotropic Gamma-Ray Background. **Phys. Rev. D**, v. 96, n. 8, p. 083001, 2017.

373 CHOLIS, I.; HOOPER, D.; MCDERMOTT, S. D. Dissecting the Gamma-Ray Background in Search of Dark Matter. **JCAP**, v. 02, p. 014, 2014.

374 AHLERS, M.; SALVADO, J. Cosmogenic gamma-rays and the composition of cosmic rays. **Phys. Rev. D**, v. 84, p. 085019, 2011.

375 BLANCO, C.; HOOPER, D. Constraints on Decaying Dark Matter from the Isotropic Gamma-Ray Background. **JCAP**, v. 03, p. 019, 2019.

376 MUZIO, M. S.; UNGER, M.; FARRAR, G. R. Progress towards characterizing ultrahigh energy cosmic ray sources. **Phys. Rev. D**, v. 100, n. 10, p. 103008, 2019.

377 BATISTA, R. A. et al. Cosmogenic photon and neutrino fluxes in the Auger era. **JCAP**, v. 01, p. 002, 2019.

378 ABRAHAM, J. et al. Measurement of the Depth of Maximum of Extensive Air Showers above 10^{18} eV. **Phys. Rev. Lett.**, v. 104, p. 091101, 2010.

379 ABREU, P. et al. Interpretation of the Depths of Maximum of Extensive Air Showers Measured by the Pierre Auger Observatory. **JCAP**, v. 02, p. 026, 2013.

380 ABBASI, R. U. et al. Mass composition of ultrahigh-energy cosmic rays with the Telescope Array Surface Detector data. **Phys. Rev. D**, v. 99, n. 2, p. 022002, 2019.

381 ABREU, P. et al. The Pierre Auger Observatory II: Studies of Cosmic Ray Composition and Hadronic Interaction models. In: **32nd International Cosmic Ray Conference**. [S.l.: s.n.], 2011. v. 3, p. 208.

382 AAB, A. et al. Azimuthal Asymmetry in the Risetime of the Surface Detector Signals of the Pierre Auger Observatory. **Phys. Rev. D**, v. 93, n. 7, p. 072006, 2016.

383 AAB, A. et al. Inferences on mass composition and tests of hadronic interactions from 0.3 to 100 EeV using the water-Cherenkov detectors of the Pierre Auger Observatory. **Phys. Rev. D**, v. 96, n. 12, p. 122003, 2017.

384 SáNCHEZ-LUCAS, P. **The $\langle\Delta\rangle$ Method: an estimator for the mass composition of ultra-high-energy cosmic rays**. Tese (PhD Thesis) — Universidad de Granada, November 2016. Available at <https://hera.ugr.es/tesisugr/26357422.pdf>.

385 ZHEZHER, Y. Cosmic-ray mass composition with the TA SD 12-year data. **PoS**, ICRC2021, p. 300, 2021.

386 BETHE, H.; HEITLER, W. On the Stopping of fast particles and on the creation of positive electrons. **Proc. Roy. Soc. Lond. A**, v. 146, p. 83–112, 1934.

387 RACAH, G. Sopra L'irradiazione Nell'urto di Particelle Veloci. **Nuovo Cim.**, v. 11, p. 461–476, 1934.

388 BLUMENTHAL, G. R. Energy loss of high-energy cosmic rays in pair-producing collisions with ambient photons. **Phys. Rev. D**, v. 1, p. 1596–1602, 1970.

389 MOTZ, J. W.; OLSEN, H. A.; KOCH, H. W. Pair production by photons. **Rev. Mod. Phys.**, v. 41, p. 581–639, 1969.

390 CHODOROWSKI, M. J.; ZDZIARSKI, A. A.; SIKORA, M. Reaction Rate and Energy-Loss Rate for Photopair Production by Relativistic Nuclei. **Astrophys. J.**, v. 400, p. 181–185, 1992.

391 RACHEN, J. P.; BIERMANN, P. L. Extragalactic ultrahigh-energy cosmic rays. 1. Contribution from hot spots in FR-II radio galaxies. **Astron. Astrophys.**, v. 272, p. 161–175, 1993.

392 PROTHEROE, R. J.; JOHNSON, P. A. Propagation of ultrahigh-energy protons over cosmological distances and implications for topological defect models. **Astropart. Phys.**, v. 4, p. 253, 1996.

393 BALDWIN, G. C.; KLAIBER, G. S. Photo-Fission in Heavy Elements. **Phys. Rev.**, v. 71, p. 3–10, 1947.

394 BALDWIN, G. C.; KLAIBER, G. S. X-Ray Yield Curves for γ-n Reactions. **Phys. Rev.**, v. 73, p. 1156–1163, 1948.

395 GOLDHABER, M.; TELLER, E. On nuclear dipole vibrations. **Phys. Rev.**, v. 74, p. 1046–1049, 1948.

396 MOREJON, L. et al. Improved photomeson model for interactions of cosmic ray nuclei. **JCAP**, v. 11, p. 007, 2019.

397 PUGET, J. L.; STECKER, F. W.; BREDEKAMP, J. H. Photonuclear Interactions of Ultrahigh-Energy Cosmic Rays and their Astrophysical Consequences. **Astrophys. J.**, v. 205, p. 638–654, 1976.

398 STECKER, F. W.; SALAMON, M. H. Photodisintegration of ultrahigh-energy cosmic rays: A New determination. **Astrophys. J.**, v. 512, p. 521–526, 1999.

399 KONING, A. J.; HILAIRE, S.; DUIJVESTIJN, M. C. TALYS: Comprehensive Nuclear Reaction Modeling. **AIP Conf. Proc.**, v. 769, n. 1, p. 1154, 2005.

400 AGOSTINELLI, S. et al. GEANT4–a simulation toolkit. **Nucl. Instrum. Meth. A**, v. 506, p. 250–303, 2003.

401 FERRARI, A. et al. FLUKA: A multi-particle transport code (Program version 2005). 10 2005.

402 BATISTA, R. A.; SIGL, G. Diffusion of cosmic rays at EeV energies in inhomogeneous extragalactic magnetic fields. **JCAP**, v. 11, p. 031, 2014.

403 GILMORE, R. C. et al. Semi-analytic modeling of the EBL and consequences for extragalactic gamma-ray spectra. **Mon. Not. Roy. Astron. Soc.**, v. 422, p. 3189, 2012.

404 AVE, M. et al. Ultra-high energy cosmic rays and cosmogenic neutrinos. **Nucl. Phys. B Proc. Suppl.**, v. 136, p. 159–168, 2004.

405 BATISTA, R. A. et al. CRPropa 3 - a Public Astrophysical Simulation Framework for Propagating Extraterrestrial Ultra-High Energy Particles. **JCAP**, v. 05, p. 038, 2016.

406 FANG, K.; GALLAGHER, J. S.; HALZEN, F. The TeV Diffuse Cosmic Neutrino Spectrum and the Nature of Astrophysical Neutrino Sources. **Astrophys. J.**, v. 933, n. 2, p. 190, 2022.

407 MURASE, K.; GUETTA, D.; AHLERS, M. Hidden Cosmic-Ray Accelerators as an Origin of TeV-PeV Cosmic Neutrinos. **Phys. Rev. Lett.**, v. 116, n. 7, p. 071101, 2016.

408 AARTSEN, M. G. et al. The IceCube Neutrino Observatory: Instrumentation and Online Systems. **JINST**, v. 12, n. 03, p. P03012, 2017. [Erratum: JINST 19, E05001 (2024)].

409 ABBASI, R. et al. The Design and Performance of IceCube DeepCore. **Astropart. Phys.**, v. 35, p. 615–624, 2012.

410 ABBASI, R. et al. IceTop: The surface component of IceCube. **Nucl. Instrum. Meth. A**, v. 700, p. 188–220, 2013.

411 PANDYA, H.; GRIFFITH, Z. Search for diffuse gamma-ray emission from the Galactic plane with IceCube. **PoS**, ICRC2017, p. 705, 2018.

412 AARTSEN, M. G. et al. First observation of PeV-energy neutrinos with IceCube. **Phys. Rev. Lett.**, v. 111, p. 021103, 2013.

413 AARTSEN, M. G. et al. Evidence for High-Energy Extraterrestrial Neutrinos at the IceCube Detector. **Science**, v. 342, p. 1242856, 2013.

414 AARTSEN, M. G. et al. Search for a diffuse flux of astrophysical muon neutrinos with the IceCube 59-string configuration. **Phys. Rev. D**, v. 89, n. 6, p. 062007, 2014.

415 HAACK, C.; WIEBUSCH, C. A measurement of the diffuse astrophysical muon neutrino flux using eight years of IceCube data. **PoS**, ICRC2017, p. 1005, 2018.

416 AARTSEN, M. G. et al. Observation of High-Energy Astrophysical Neutrinos in Three Years of IceCube Data. **Phys. Rev. Lett.**, v. 113, p. 101101, 2014.

417 FORMAGGIO, J. A.; ZELLER, G. P. From eV to EeV: Neutrino Cross Sections Across Energy Scales. **Rev. Mod. Phys.**, v. 84, p. 1307–1341, 2012.

418 AARTSEN, M. G. et al. Energy Reconstruction Methods in the IceCube Neutrino Telescope. **JINST**, v. 9, p. P03009, 2014.

419 AARTSEN, M. G. et al. Searches for Extended and Point-like Neutrino Sources with Four Years of IceCube Data. **Astrophys. J.**, v. 796, n. 2, p. 109, 2014.

420 COWEN, D. F. Tau neutrinos in IceCube. **J. Phys. Conf. Ser.**, v. 60, p. 227–230, 2007.

421 COLLABORATION, I. **IceCube Media Gallery**. 2024. IceCube. Disponível em: <https://icecube.wisc.edu/gallery>.

422 AARTSEN, M. G. et al. Characterization of the Atmospheric Muon Flux in IceCube. **Astropart. Phys.**, v. 78, p. 1–27, 2016.

423 ABBASI, R. et al. Extending the search for neutrino point sources with IceCube above the horizon. **Phys. Rev. Lett.**, v. 103, p. 221102, 2009.

424 AARTSEN, M. G. et al. Development of a General Analysis and Unfolding Scheme and its Application to Measure the Energy Spectrum of Atmospheric Neutrinos with IceCube. **Eur. Phys. J. C**, v. 75, n. 3, p. 116, 2015.

425 HECK, D. et al. CORSIKA: A Monte Carlo code to simulate extensive air showers. 2 1998.

426 HONDA, M. et al. Calculation of atmospheric neutrino flux using the interaction model calibrated with atmospheric muon data. **Phys. Rev. D**, v. 75, p. 043006, 2007.

427 GONDOLO, P.; INGELMAN, G.; THUNMAN, M. Charm production and high-energy atmospheric muon and neutrino fluxes. **Astropart. Phys.**, v. 5, p. 309–332, 1996.

428 PASQUALI, L.; RENO, M. H.; SARCEVIC, I. Lepton fluxes from atmospheric charm. **Phys. Rev. D**, v. 59, p. 034020, 1999.

429 BOETTCHER, J. et al. Search for the Prompt Atmospheric Neutrino Flux in IceCube. **PoS**, ICRC2023, p. 1068, 2023.

430 SCHONERT, S. et al. Vetoing atmospheric neutrinos in a high energy neutrino telescope. **Phys. Rev. D**, v. 79, p. 043009, 2009.

431 GAISSER, T. K. et al. Generalized self-veto probability for atmospheric neutrinos. **Phys. Rev. D**, v. 90, n. 2, p. 023009, 2014.

432 KOPPER, C.; GIANG, W.; KURAHASHI, N. Observation of Astrophysical Neutrinos in Four Years of IceCube Data. **PoS**, ICRC2015, p. 1081, 2016.

433 KOPPER, C. Observation of Astrophysical Neutrinos in Six Years of IceCube Data. **PoS**, ICRC2017, p. 981, 2018.

434 NIEDERHAUSEN, H. M.; LESIAK-BZDAK, M.; STOESSL, A. High energy astrophysical neutrino flux characteristics for neutrino-induced cascades using IC79 and IC86-string IceCube conf. **PoS**, ICRC2015, p. 1109, 2016.

435 NIEDERHAUSEN, H. M.; XU, Y. High Energy Astrophysical Neutrino Flux Measurement Using Neutrino-induced Cascades Observed in 4 Years of IceCube Data. **PoS**, ICRC2017, p. 968, 2018.

436 AARTSEN, M. G. et al. Characteristics of the diffuse astrophysical electron and tau neutrino flux with six years of IceCube high energy cascade data. **Phys. Rev. Lett.**, v. 125, n. 12, p. 121104, 2020.

437 AARTSEN, M. G. et al. Measurement of the multi-TeV neutrino cross section with IceCube using Earth absorption. **Nature**, v. 551, p. 596–600, 2017.

438 ABBASI, R. et al. Improved Characterization of the Astrophysical Muon–neutrino Flux with 9.5 Years of IceCube Data. **Astrophys. J.**, v. 928, n. 1, p. 50, 2022.

439 BINDER, G. A. **Measurements of the Flavor Composition and Inelasticity Distribution of High-Energy Neutrino Interactions in IceCube**. Tese (Doutorado) — UC, Berkeley, 2017.

440 AARTSEN, M. G. et al. Measurements using the inelasticity distribution of multi-TeV neutrino interactions in IceCube. **Phys. Rev. D**, v. 99, n. 3, p. 032004, 2019.

441 JERO, K. Z. **A New Window for Detecting Astrophysical Neutrinos**. Tese (Doutorado) — University of Wisconsin, Madison, 2017.

442 ABBASI, R. et al. Characterization of the Astrophysical Diffuse Neutrino Flux using Starting Track Events in IceCube. 2 2024.

443 YUKSEL, H. et al. Revealing the High-Redshift Star Formation Rate with Gamma-Ray Bursts. **Astrophys. J. Lett.**, v. 683, p. L5–L8, 2008.

444 MUZIO, M. S.; FARRAR, G. R.; UNGER, M. Probing the environments surrounding ultrahigh energy cosmic ray accelerators and their implications for astrophysical neutrinos. **Phys. Rev. D**, v. 105, n. 2, p. 023022, 2022.

445 AARTSEN, M. G. et al. Differential limit on the extremely-high-energy cosmic neutrino flux in the presence of astrophysical background from nine years of IceCube data. **Phys. Rev. D**, v. 98, n. 6, p. 062003, 2018.

446 ABREU, P. et al. The energy spectrum of cosmic rays beyond the turn-down around 10^{17} eV as measured with the surface detector of the Pierre Auger Observatory. **Eur. Phys. J. C**, v. 81, n. 11, p. 966, 2021.

447 AHLERS, M. et al. GZK Neutrinos after the Fermi-LAT Diffuse Photon Flux Measurement. **Astropart. Phys.**, v. 34, p. 106–115, 2010.

448 KALASHEV, O. E.; SEMIKOZ, D. V.; SIGL, G. Ultra-High Energy Cosmic Rays and the GeV-TeV Diffuse Gamma-Ray Flux. **Phys. Rev. D**, v. 79, p. 063005, 2009.

449 MIRIZZI, A. et al. Supernova Neutrinos: Production, Oscillations and Detection. **Riv. Nuovo Cim.**, v. 39, n. 1-2, p. 1–112, 2016.

450 COLGATE, S. A.; WHITE, R. H. The Hydrodynamic Behavior of Supernovae Explosions. **Astrophys. J.**, v. 143, p. 626, 1966.

451 ARNETT, W. D. Gravitational collapse and weak interactions. **Can. J. Phys.**, v. 44, p. 2553–2594, 1966.

452 WILSON, J. R. Supernovae and Post-Collapse Behavior. **Numerical Astrophysics**, p. 422, 1985.

453 BETHE, H. A.; WILSON, J. R. Revival of a stalled supernova shock by neutrino heating. **Astrophys. J.**, v. 295, p. 14–23, 1985.

454 FIORILLO, D. F. G. et al. Supernova simulations confront SN 1987A neutrinos. **Phys. Rev. D**, v. 108, n. 8, p. 083040, 2023.

455 TAMBORRA, I.; SHALGAR, S. New Developments in Flavor Evolution of a Dense Neutrino Gas. **Ann. Rev. Nucl. Part. Sci.**, v. 71, p. 165–188, 2021.

456 EHRING, J. et al. Fast neutrino flavor conversion in core-collapse supernovae: A parametric study in 1D models. **Phys. Rev. D**, v. 107, n. 10, p. 103034, 2023.

457 EHRING, J. et al. Fast Neutrino Flavor Conversions Can Help and Hinder Neutrino-Driven Explosions. **Phys. Rev. Lett.**, v. 131, n. 6, p. 061401, 2023.

458 NAGAKURA, H. Roles of Fast Neutrino-Flavor Conversion on the Neutrino-Heating Mechanism of Core-Collapse Supernova. **Phys. Rev. Lett.**, v. 130, n. 21, p. 211401, 2023.

459 PANTALEONE, J. T. Neutrino oscillations at high densities. **Phys. Lett. B**, v. 287, p. 128–132, 1992.

460 PANTALEONE, J. T. Dirac neutrinos in dense matter. **Phys. Rev. D**, v. 46, p. 510–523, 1992.

461 DUAN, H.; FULLER, G. M.; QIAN, Y.-Z. Collective Neutrino Oscillations. **Ann. Rev. Nucl. Part. Sci.**, v. 60, p. 569–594, 2010.

462 CHAKRABORTY, S. et al. Collective neutrino flavor conversion: Recent developments. **Nucl. Phys. B**, v. 908, p. 366–381, 2016.

463 CHAKRABORTY, S. et al. Self-induced neutrino flavor conversion without flavor mixing. **JCAP**, v. 03, p. 042, 2016.

464 SAWYER, R. F. Speed-up of neutrino transformations in a supernova environment. **Phys. Rev. D**, v. 72, p. 045003, 2005.

465 SAWYER, R. F. The multi-angle instability in dense neutrino systems. **Phys. Rev. D**, v. 79, p. 105003, 2009.

466 SAWYER, R. F. Neutrino cloud instabilities just above the neutrino sphere of a supernova. **Phys. Rev. Lett.**, v. 116, n. 8, p. 081101, 2016.

467 IZAGUIRRE, I.; RAFFELT, G.; TAMBORRA, I. Fast Pairwise Conversion of Supernova Neutrinos: A Dispersion-Relation Approach. **Phys. Rev. Lett.**, v. 118, n. 2, p. 021101, 2017.

468 JOHNS, L. Collisional Flavor Instabilities of Supernova Neutrinos. **Phys. Rev. Lett.**, v. 130, n. 19, p. 191001, 2023.

469 ABBAR, S.; VOLPE, M. C. Using Bayesian Inference to Distinguish Neutrino Flavor Conversion Scenarios via a Prospective Supernova Neutrino Signal. 1 2024.

470 SIGL, G.; RAFFELT, G. General kinetic description of relativistic mixed neutrinos. **Nucl. Phys. B**, v. 406, p. 423–451, 1993.

471 CARDALL, C. Y. Liouville equations for neutrino distribution matrices. **Phys. Rev. D**, v. 78, p. 085017, 2008.

472 FIORILLO, D. F. G.; RAFFELT, G. G.; SIGL, G. Collective neutrino-antineutrino oscillations in dense neutrino environments? **Phys. Rev. D**, v. 109, n. 4, p. 043031, 2024.

473 FIORILLO, D. F. G.; RAFFELT, G. G.; SIGL, G. Inhomogeneous Kinetic Equation for Mixed Neutrinos: Tracing the Missing Energy. 1 2024.

474 DIGHE, A. S.; SMIRNOV, A. Y. Identifying the neutrino mass spectrum from the neutrino burst from a supernova. **Phys. Rev. D**, v. 62, p. 033007, 2000.

475 ATHAR, M. S. et al. Status and perspectives of neutrino physics. **Prog. Part. Nucl. Phys.**, v. 124, p. 103947, 2022.

476 KERSTEN, J.; SMIRNOV, A. Y. Decoherence and oscillations of supernova neutrinos. **Eur. Phys. J. C**, v. 76, n. 6, p. 339, 2016.

477 HANSEN, R. S. L.; SMIRNOV, A. Y. Neutrino conversion in a neutrino flux: Towards an effective theory of collective oscillations. **JCAP**, v. 04, p. 057, 2018.

478 DEV, P. S. B.; JANA, S.; PORTO, Y. Flavor Matters, but Matter Flavors: Matter Effects on Flavor Composition of Astrophysical Neutrinos. 12 2023.

479 SCHIRATO, R. C.; FULLER, G. M. Connection between supernova shocks, flavor transformation, and the neutrino signal. 5 2002.

480 TOMAS, R. et al. Neutrino signatures of supernova shock and reverse shock propagation. **JCAP**, v. 09, p. 015, 2004.

481 DASGUPTA, B.; DIGHE, A. Phase effects in neutrino conversions during a supernova shock wave. **Phys. Rev. D**, v. 75, p. 093002, 2007.

482 AKHMEDOV, E.; KOPP, J.; LINDNER, M. Collective neutrino oscillations and neutrino wave packets. **JCAP**, v. 09, p. 017, 2017.

483 PORTO-SILVA, Y. P.; SMIRNOV, A. Y. Coherence of oscillations in matter and supernova neutrinos. **JCAP**, v. 06, p. 029, 2021.

484 MUKHOPADHYAY, M.; SEN, M. On probing turbulence in core-collapse supernovae in upcoming neutrino detectors. 10 2023.

485 JACHOWICZ, N. et al. Identifying neutrinos and antineutrinos in neutral-current scattering reactions. **Phys. Rev. Lett.**, v. 93, p. 082501, 2004.

486 JANA, S.; PORTO-SILVA, Y. P.; SEN, M. Exploiting a future galactic supernova to probe neutrino magnetic moments. **JCAP**, v. 09, p. 079, 2022.

487 JANA, S.; PORTO, Y. Resonances of Supernova Neutrinos in Twisting Magnetic Fields. **Phys. Rev. Lett.**, v. 132, n. 10, p. 101005, 2024.

488 ZEL'DOVICH, Y. B.; NOVIKOV, I. D. The Hypothesis of Cores Retarded during Expansion and the Hot Cosmological Model. **Sov. Astron.**, v. 10, p. 602, 1967.

489 HAWKING, S. W. Black hole explosions. **Nature**, v. 248, p. 30–31, 1974.

490 HAWKING, S. W. Particle Creation by Black Holes. **Commun. Math. Phys.**, v. 43, p. 199–220, 1975. [Erratum: Commun.Math.Phys. 46, 206 (1976)].

491 PAGE, D. N. Particle Emission Rates from a Black Hole: Massless Particles from an Uncharged, Nonrotating Hole. **Phys. Rev. D**, v. 13, p. 198–206, 1976.

492 HECKLER, A. F. On the formation of a Hawking radiation photosphere around microscopic black holes. **Phys. Rev. D**, v. 55, p. 480–488, 1997.

493 HECKLER, A. F. Calculation of the emergent spectrum and observation of primordial black holes. **Phys. Rev. Lett.**, v. 78, p. 3430–3433, 1997.

494 MACGIBBON, J. H.; CARR, B. J.; PAGE, D. N. Do Evaporating Black Holes Form Photospheres? **Phys. Rev. D**, v. 78, p. 064043, 2008.

495 ARBEY, A.; AUFFINGER, J. BlackHawk: A public code for calculating the Hawking evaporation spectra of any black hole distribution. **Eur. Phys. J. C**, v. 79, n. 8, p. 693, 2019.

496 BAKER, M. J.; THAMM, A. Probing the particle spectrum of nature with evaporating black holes. **SciPost Phys.**, v. 12, n. 5, p. 150, 2022.

497 HALZEN, F.; KESZTHELYI, B.; ZAS, E. Neutrinos from primordial black holes. **Phys. Rev. D**, v. 52, p. 3239–3247, 1995.

498 DAVE, P.; TABOADA, I. Neutrinos from Primordial Black Hole Evaporation. **PoS**, ICRC2019, p. 863, 2021.

499 ALBERT, A. et al. Constraining the Local Burst Rate Density of Primordial Black Holes with HAWC. **JCAP**, v. 04, p. 026, 2020.

500 PAGE, D. N. Particle Emission Rates from a Black Hole. 2. Massless Particles from a Rotating Hole. **Phys. Rev. D**, v. 14, p. 3260–3273, 1976.

A

Neutrino Spectra from Muon Decay

Muon decay generates a neutrino spectrum whose shape depends on the energy distribution of produced μ^+ and μ^-; for a monoenergetic UHE photon, their distribution is given by $\mathrm{d}N_{\mu^\pm}/\mathrm{d}E_{\mu^\pm} \equiv (1/\sigma_{\mathrm{MPP}})\mathrm{d}\sigma_{\mathrm{MPP}}/\mathrm{d}E_{\mu^\pm}$. The total (all flavor) neutrino spectrum $\mathrm{d}N_\nu/\mathrm{d}E_\nu$ from the decay of $\mu^\pm$ with spectrum $\mathrm{d}N_{\mu^\pm}/\mathrm{d}E_{\mu^\pm}$ can be written as (94)

$$\begin{aligned}\frac{\mathrm{d}N_\nu}{\mathrm{d}E_\nu}(E_\nu) = \int_{E_{\mu,\min}}^{E_{\mu,\max}} \mathrm{d}E_\mu\, \frac{\mathrm{d}N_{\mu^\pm}}{\mathrm{d}E_{\mu^\pm}}(E_\mu) \\ \times \left[F_{\mu^\pm\to\overset{(-)}{\nu}_\mu}(E_\mu;E_\nu) + F_{\mu^\pm\to\overset{(-)}{\nu}_e}(E_\mu;E_\nu)\right] \ , \qquad \text{(A-1)}\end{aligned}$$

where

$$F_{a\to b}(E_a;E_b) = \frac{1}{E_a}F_{a\to b}\left(\frac{E_b}{E_a}\right) \ , \qquad \text{(A-2)}$$

and for unpolarized muons one has

$$F_{\mu^\pm\to\overset{(-)}{\nu}_\mu}(y) = \frac{5}{3} - 3y^2 + \frac{4}{3}y^3 \ , \qquad \text{(A-3)}$$

and

$$F_{\mu^\pm\to\overset{(-)}{\nu}_e}(y) = 2 - 6y^2 + 4y^3 \ . \qquad \text{(A-4)}$$

From these relations we can estimate the total energy drainage from the initial photon to neutrinos. By a simple inspection of the above formulae, on the average $\sim 65\%$ of the energy of a photon at the time of MPP goes to neutrinos.

In Figures 2.18 and 2.19, we also show the neutrino spectra from a monoenergetic charged pion decay. Given a pion spectrum $\mathrm{d}N_{\pi^\pm}/\mathrm{d}E_{\pi^\pm}$, there are two contributions to the final neutrino flux: (i) the (anti)muon neutrino emitted directly from the pion decay $\pi^\pm \to \mu^\pm\nu_\mu(\bar{\nu}_\mu)$,

$$\frac{\mathrm{d}N_\nu}{\mathrm{d}E_\nu}(E_\nu) = \int_{E_{\pi,\min}}^{E_{\pi,\max}} \mathrm{d}E_\pi\, \frac{\mathrm{d}N_{\pi^\pm}}{\mathrm{d}E_{\pi^\pm}}\, F_{\pi^\pm\to\overset{(-)}{\nu}_\mu}(E_\pi;E_\nu) \ , \qquad \text{(A-5)}$$

where

$$F_{\pi^\pm\to\overset{(-)}{\nu}_\mu}(x) = \frac{1}{1-r_\pi}[1-\theta(x-1+r_\pi)] \ , \qquad \text{(A-6)}$$

obeys the scaling (A-2) and $r_\pi = (m_\mu/m_\pi)^2$, and (ii) the neutrinos emitted in the subsequent muon decay. The latter can be obtained by convoluting

$$\frac{\mathrm{d}N_{\mu^\pm}}{\mathrm{d}E_{\mu^\pm}}(E_\mu) = \int_{E_{\pi,\min}}^{E_{\pi,\max}} \mathrm{d}E_\pi\, \frac{\mathrm{d}N_{\pi^\pm}}{\mathrm{d}E_{\pi^\pm}}\, F_{\pi^\pm\to\mu^\pm}(E_\pi;E_\mu) \ , \qquad \text{(A-7)}$$

in Eq. (A-1), where

$$F_{\pi^\pm\to\mu^\pm}(x) = \frac{1}{1-r_\pi}\theta(x-r_\pi) \ . \qquad \text{(A-8)}$$

B
Energy Conservation on a Grid

Evaluating EPP and ICS spectra for initial and final energies constrained to the `energies` grid in γ-Cascade can lead to a few issues. More precisely, after calculating the spectra given in Eqs. (2-30) and (2-42) at discrete energy values, one must be careful to guarantee that Eqs. (2-31), (2-32), (2-43) and (2-44) are respected. If not, energy may leak away from or into the cascade, leading to unphysical results. There are several features of these spectra that cause such problems. In general, these numerical problems are solved by numerical integrators by employing adaptive sampling techniques. However, since we know the behavior of these functions a priori, we can perform numerical post processing in order to avoid using time-consuming adaptive algorithms. To illustrate these numerical pitfalls, we consider some concrete examples below and discuss how to fix them without compromising the physics.

First, let us examine the issues arising in EPP spectra. Consider a monoenergetic flux of γ rays with energy $E_\gamma = 1$ EeV at redshift $z = 0$, all of which interact with the CMB/EBL to generate an electron spectrum given by Eq. (2-30). The left panel of Figure B.1 shows the exact spectrum in red, overlapped by black points along the `energies` grid at which the spectrum was evaluated. Notice how the spectrum is highly peaked at nearly 1 EeV (i.e. the width of the peak is smaller than the width of the energy grid spacing ΔE_e), which is expected from the low inelasticity of EPP at such a high CM energy. This region is where most of the outgoing energy is concentrated. Meanwhile, at precisely 1 EeV it evaluates exactly to zero, which is why there is no grid point at the vertical gray dashed line marked by E_γ, even though 1 EeV is a value in the `energies` grid. As a result, the trapezoidal integration over the grid points given in Eq. (2-58) will indicate missing energy/particle number in the outgoing spectrum,

$$\int dE_e' \frac{dN_{\gamma\to e}}{dE_e'}(E_e', E_\gamma, z) \approx \sum_{k=1}^{299} \left[\left(\frac{dN_{\gamma\to e}}{dE_e'}\right)_{i,j,k+1} + \left(\frac{dN_{\gamma\to e}}{dE_e'}\right)_{i,j,k} \right] \frac{E_{k+1} - E_k}{2} < 2\ . \quad \text{(B-1)}$$

To fix this, we introduce a non-zero value for the spectrum at the 1 EeV grid point, representing the energy in electrons of peak energy $E_\gamma - \delta E_e$ for $\delta E_e \ll \Delta E_e$, in order to enforce Eqs. (2-31), and consequently (2-32), under trapezoidal integration. The result of this procedure is shown in the right

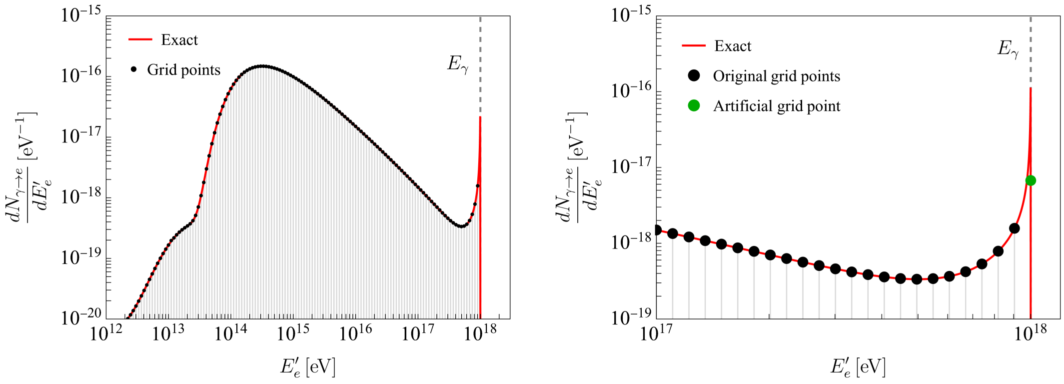

Figure B.1: *Left*: Electron spectrum from a monoenergetic flux of $E_\gamma = 1$ EeV γ rays at $z = 0$. The exact spectrum is given by the red curve, while the black points mark its values at the energies in the `energies` grid. *Right*: Zoom into the region around 1 EeV, showing the adjusted grid point (in green) added to enforce energy/particle number conservation.

panel of Figure B.1, zooming in to the region around 1 EeV, where the green point was introduced to compensate the particle number deficit. Although this solution leads to the unphysical creation of electron at E_γ, it is justified by the the peaked nature of the spectrum, and reproduces all the important features required for a reliable electromagnetic cascade simulation.

In some cases, where the spectra drops rapidly within a grid width, the particle number deficit is too large, causing the previous fix to introduce a point that is unreasonably high when compared to the spectrum. The left panel of Figure B.2 displays this situation for a EPP spectrum from γ rays at ≈ 25 GeV, where the green adjusted point is clearly too high. When this happens, instead of employing the previous solution (which is only appropriate for peaked spectra), we compensate the missing particles/energy by multiplying the entire grid by a constant factor (which is only slightly greater 1), as shown by the blue points in the left panel of Figure B.2.

A third an final problem that arises in EPP spectra occurs when a steeply falling spectrum causes the trapezoidal sum in Eq. (B-1) to be slightly > 2. Employing the fix from the first scenario would generate an adjusted point with a negative value. In this case, we enforce Eq. (2-31) by once again artificially multiplying the entire grid by a constant factor (this time, slightly smaller than 1).

In the case of ICS, grid-related problems can arise in both the outgoing γ-ray and/or electron spectra. Luckily, their spectral shapes exhibit similar features to the EPP spectra when evaluated on a grid, meaning we can fix both the γ-ray and electron ICS grids independently by employing the same three kinds of modifications described above. However, the behavior of ICS at

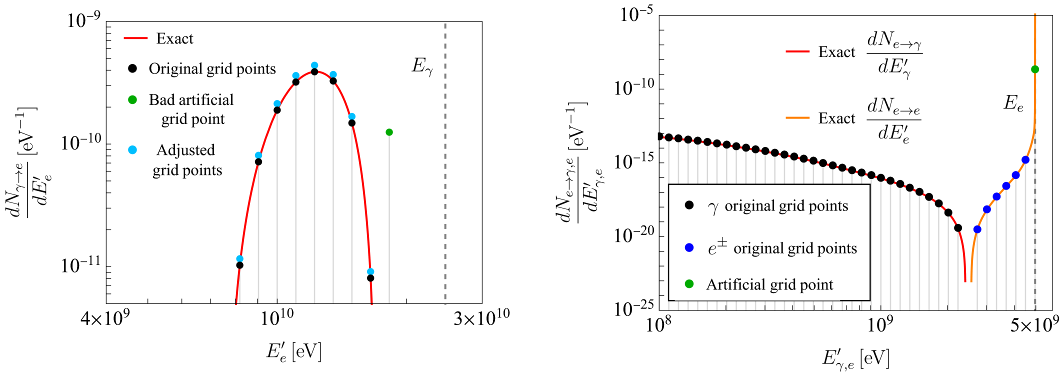

Figure B.2: *Left*: Same as Figure B.1, but for $E_\gamma \approx 25$ GeV. Although adding the green point fixes energy conservation, it does not reflect the behavior of the spectrum. Instead, the black grid points are all raised by a small constant value, becoming the blue points. *Right*: γ-ray and electron spectra from a monoenergetic flux of $E_e \approx 5$ GeV electrons at $z = 0$. Black and blue grid points mark the values of the γ-ray and $e^\pm$ spectra, respectively, at the `energies` grid values. To fix the electron grid, we artificially add the green point such that particle number/energy conservation is preserved. Note that a significant portion of the γ-ray spectrum lies below 10^8 eV. We discuss the enforcement of conservation beyond the limits of the `energies` grid in Appendix C.

low energies leads to an additional issue: the γ-ray spectrum extends itself well below 10^8 eV, where the `energies` array ends. This is depicted in the right panel of Figure B.2, which shows the outgoing photon and electron spectra from the ICS of $E_e =$ `energies[40]` ≈ 5 GeV electrons. The black and blue points mark their values from their corresponding $dN_{e\to\gamma}/dE'_\gamma$ and $dN_{e\to e}/dE'_e$ grids, respectively, while the green point was adjusted in the electron grid to conserve energy and mimic the exact spectrum's behavior. Clearly, trying to enforce particle number conservation on the γ-ray spectrum by trapezoidal integration along the `energies` grid is not appropriate. It is also not necessary, as γ-Cascade should really lose part of its initial particle number/energy to the $< 10^8$ eV region. Since these are well-normalized by design, we leave that grid untouched for now.

C
On-The-Spot Approximation on a Grid

Our on-the-spot approximation requires the evaluation of several generations of subsequent ICSs, as depicted in Figure 2.9. A severe issue arises when attempting to do this calculation on a discrete energy grid. As E_e decreases, the outgoing electron spectra from ICS become extremely peaked and constrained to a narrow energy region at just below E_e, causing energy loss to slow down significantly. At some point, it eventually stalls completely, leading to an unphysical accumulation of γ rays at low energies. For our on-the-spot approximation to work on a grid, we must modify the outgoing ICS spectra $dN_{e\to\gamma,e}/dE_{\gamma,e}$ from Eq. (2-42) beyond the changes already applied to them for energy conservation (see Appendix B). This is made through the following step-by-step procedure:

1. First, apply all modifications described in Appendix B to the ICS spectra.

2. Check if energy loss is getting stalled. This occurs when the condition

$$\int dE'_\gamma \, E'_\gamma \, \frac{dN_{e\to\gamma}}{dE'_\gamma}(E'_\gamma, E_e, z) < \int dE'_e \, E'_e \, \frac{dN_{e\to e}}{dE'_e}(E'_e, E_e, z) - \int dE'_e \, E'_e \, \frac{dN_{e\to e}}{dE'_e}(E'_e, E_e - \Delta E, z) \approx \Delta E \quad \text{(C-1)}$$

   is satisfied, in its discrete (trapezoidal integration) version, where $E_e - \Delta E$ is the energy directly below E_e in the `energies` array. In other words, this occurs when the energy channeled into photons from the ICS of electrons at E_e is less than the difference between the energy going to electrons from ICSs starting at E_e and $E_e - \Delta E$. This energy difference is approximately ΔE because the electron carries away most of the energy from ICS at low energies.

3. If stalled, then we modify the grid of outgoing electrons from an initial energy E_i, such that the new grid is just as if the initial electron's energy had been E_{i-1},

$$\frac{dN_{e\to e}}{dE'_e}(E'_e, E_e, z) \to \frac{dN_{e\to e}}{dE'_e}(E'_e, E_e - \Delta E, z) \ . \quad \text{(C-2)}$$

   This forces ICS to progress from E_i to E_{i-1} in a single generation, instead of over many (potentially never-ending) generations.

4. The energy difference is channeled into the γ-ray sector. These γ rays are produced following approximately the ICS spectrum from an electron at E_e. Thus, we simply renormalize the outgoing γ-ray grid from initial energy E_i such that (2-44) is satisfied[1],

$$\frac{dN_{e\to\gamma}}{dE'_\gamma}(E'_\gamma, E_e, z) \to \frac{dN_{e\to\gamma}}{dE'_\gamma}(E'_\gamma, E_e, z) \times \frac{\Delta E}{\int dE'_\gamma\, E'_\gamma\, \frac{dN_{e\to\gamma}}{dE'_\gamma}(E'_\gamma, E_e, z)} \,. \tag{C-3}$$

This last step comes at the cost of abandoning particle number conservation for γ rays, but this is justified. Electrons at E_i slowly lose their energy through many ICS interactions and eventually reach E_{i-1} within a Hubble timescale. Condensing many interactions into a single one, like what we are doing, is bound to increase the outgoing particle number. The drifting of the γ-ray spectra to < 0.1 GeV energies also breaks particle number conservation.

The result of this procedure is shown in left panel of Figure C.1, where we display the outgoing spectra, along with the grid points associated to them, from the ICS of a monoenergetic flux of electrons with $E_e = 10$ TeV at $z = 0$. Black grid points are obtained evaluating the exact spectra $dN_{e\to\gamma,e}/dE'_{\gamma,e}$ over the `energies` array. The green point in the electron grid was added to enforce energy conservation, as described in Appendix B. This point is actually the cause of the stalling in future ICS generations: the green point causes electrons to get stuck at E_e. To force ICS to move along, allowing for our on-the-spot approximation, we modify both grids such that they become the blue points. The new γ-ray grid is just a rescaling of its black grid points given by Eq. (C-3). The new electrons grid matches the grid obtained from initial electrons at the next lower energy in the `energies` array (corrected for energy conservation), as represented in Eq. (C-2). This makes ICS progress to lower energies with each generation.

With our new grids, we can obtain the grid for $dN_{e\to\gamma,\mathrm{OTS}}/dE'_\gamma$ iteratively through the process described in Eqs. (2-69)–(2-72). The right panel of Figure C.1 shows the resulting on-the-spot spectrum, in red, for initial monoenergetic electrons at $E_e = 10$ PeV and $z = 0$, interpolated over the grid. For comparison, we show in blue the same grid used in γ-Cascade V3. The corrections at high energies are due to the energy conservation fixes described in Appendix B. Note that the spectrum correctly follows the $dN/dE'_\gamma \propto dE'^{-1.5}_\gamma$ analytical prediction from (8) for cascades in the low energy regime (where only ICS occurs).

---

[1] This requires extending the `energies` array to lower energies to get its correct energy, since a considerable fraction of it is below 0.1 GeV.

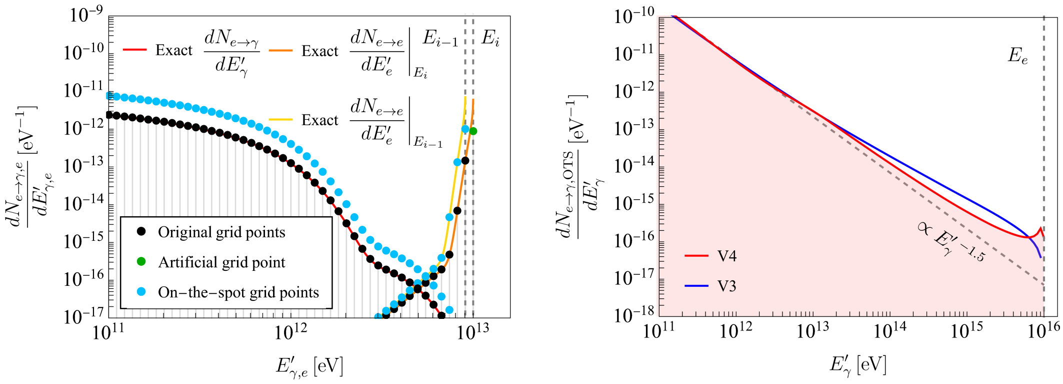

Figure C.1: *Left*: Grid points for monoenergetic ICS spectra before any fixes (black points), after ensuring energy conservation (added green point; see Appendix B), and after the modifications required for our on-the-spot approximation (blue points). See text for the description and justification behind these modifications. The exact spectra were obtained for initial electron energies of E_i = `energies[116]` = 10 TeV and E_{i-1} = `energies[115]`. Note that the modified electron grid for E_i follows the E_{i-1} spectrum, avoiding any stalling of electrons at E_i. *Right*: On-the-spot spectrum from electrons initially at E_e = 10 PeV. The red and blue curves are the current (V4) and previous (V3) version's interpolated grids, respectively. Both converge to the $dN/dE'_\gamma \propto E'^{-1.5}_\gamma$ analytical prediction by Berezinsky at low energies (8).

D
γ-Cascade Functions

γ-Cascade provides four γ-ray propagation functions: `GCascadeAttenuate`, `GCascadePoint`, `GCascadeDiffuseConstant` and `GCascadeDiffuse`, along with two additional functions which allow the user to change the intergalactic magnetic field strength[1] and the EBL model used in the code: `changeMagneticField` and `changeEBLModel`, respectively. By default, γ-Cascade considers a magnetic field of 10^{-12} G and the EBL model by Saldana-Lopez et al. (2021) (289). The functions are as follows:

- `GCascadeAttenuate[injected spectrum, source redshift]` produces an attenuated flux at $z = 0$ without including cascade evolution (*i.e.* accounting for PP attenuation and cosmological energy redshifting, without the regeneration of γ rays via ICS).
- `GCascadePoint[injected spectrum, source redshift]` produces the observed flux at $z = 0$ from full-on electromagnetic cascades, taking into account PP, ICS, synchrotron losses and cosmological redshifting.
- `GCascadeDiffuseConstant[injected spectrum , maximum source redshift, comoving density distribution of sources]` produces the observed diffuse flux at $z = 0$ from a population of identical sources (*i.e.* with the same injection spectra) following a given comoving density distribution in redshift, taking into account cosmological expansion and electromagnetic cascade evolution.
- `GCascadeDiffuse[injected spectrum, maximum source redshift, comoving density distribution of sources` produces the observed flux at $z = 0$ from a population of evolving sources (*i.e.* with redshift-dependent spectra) following a given comoving density distribution in redshift, taking into account cosmological expansion and electromagnetic cascade evolution.
- `changeMagneticField[new magnetic field, name]` changes the intergalactic magnetic field strength and produces new libraries corresponding to the chosen value, with the standard library names prepended with `name`.
- `changeEBLModel[new EBL model index]` changes the EBL model used in γ-Cascade. Each model is associated to an integer index, from `0` to `6`,

---

[1] γ-Cascade is not sensitive to its coherence length; only synchrotron losses are taken into account, not to magnetic deflection.

which are:

`0` - no EBL, cascades develop under the CMB only;
`1` - default value, best-fit Saldana-Lopez et al. (2021) model (289);
`2` - 1σ upper limit of the Saldana-Lopez et al. (2021) model (289);
`3` - 1σ lower limit of the Saldana-Lopez et al. (2021) model (289);
`4` - Finke et al. (2022) model (341);
`5` - Franceschini and Rodighiero (2017) model (342);
`6` - Domínguez et al. (2011) model (288), used in γ-Cascade V3.

For details on the format and units of the inputs/outputs of these functions, the useful `Tutorial.nb` notebook is provided along with the γ-Cascade package.

E
Neutrinos from Evaporating Primordial Black Holes

This appendix is a summary of a side project during my PhD research that culminated in the publication of a paper (1). The main idea was to study the neutrino and γ-ray emission from evaporating primordial black holes (PBHs) in our local neighborhood (within a parsec), assessing their detection prospects by using multimessenger correlations.

PBHs are objects formed by the gravitational collapse of overdense regions in the early Universe (488) and whose existence is still purely hypothetical. Depending on their exact time of formation, PBHs can have initial masses ranging from Planck mass up to thousands of solar masses. This is a crucial characteristic that distinguishes PBHs from "conventional" black holes whose formation mechanisms (*e.g.* stellar collapse) severely restrict their possible masses to $\gtrsim$ a few solar masses. We are interested in PBHs with initial mass $M^* \sim 10^{15}$ g which have (supposedly) existed since $\sim 10^{-23}$ s after the Big Bang and are expected to be currently on their final moments of existence due to the inevitable process of black hole evaporation.

Black hole evaporation is a consequence of Hawking radiation (489, 490), a phenomenon which converts the black hole's mass into energy in the form of radiated particles. The emitted quasi-blackbody spectrum has peak temperature (in natural units) $T = (8\pi M)^{-1}$, where M is the mass of the black hole which decreases at a rate $\dot{M} \sim M^{-2}$ (491). This means that black hole evaporation is a runaway process: a large mass black hole slowly radiates low-energy particles until its temperature is high enough for heavier particles to be emitted, accelerating the evaporation. This process culminates in an intense emission of all particles in the Standard Model with up to Planck scale energies, stopping as soon as the black hole dies. This event is fittingly known as a black hole explosion. Witnessing such an explosion is our best shot at directly observing Hawking radiation taking place. However, we do not expect conventional black holes to explode anytime soon due to their large mass. This is why PBHs formed with mass M^* are of particular interest; if they exist and are sufficiently abundant in our local Universe, we can hope to see evaporation byproducts from their explosions in our high-energy particle detectors at the Earth.

In particular, we study the potential of neutrinos as PBH explosion signals. Although detecting them is certainly a lot more challenging than γ rays which are usually the focus of PBH searches, we find that neutrinos bring

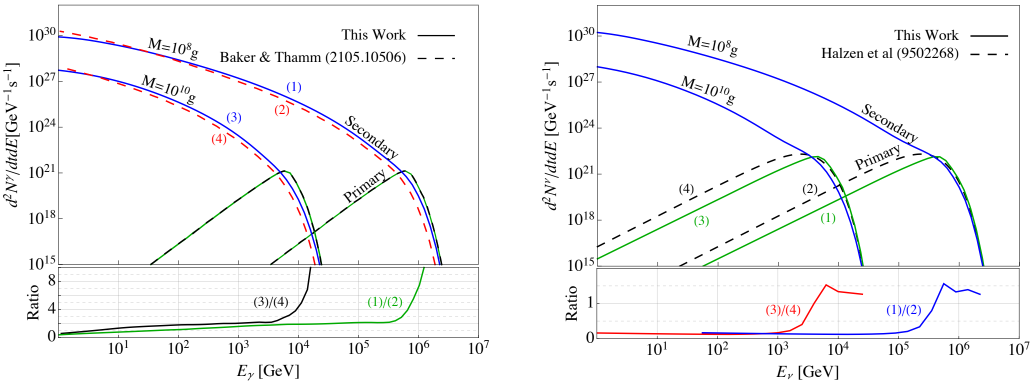

(a) (b)

Figure E.1: *Left*: The instantaneous primary and secondary γ-ray spectra from an evaporating PBH. The solid curves show our results and the dashed curves are taken from (496). The lower part shows the ratio of solid to dashed secondary emissions curves. *Right*: same as left plot, but for neutrinos. The dashed curves are taken from (497). Figure from (1).

a three-fold advantage to the table: (i) neutrino detectors have a 4π sr field-of-view, a big advantage over the $\sim 1-2$ sr of extensive air shower experiments like HAWC and LHAASO which look for γ rays, (ii) neutrinos would be able to easily escape the PBH environment if it is embedded in a high density and/or magnetic field region, or if it is surrounded by a speculated thick photosphere (492, 493, 494) that absorbs γ rays, and perhaps most importantly (iii) it can be hard to distinguish a γ-ray signal coming from a PBH explosion from a signal coming from other (conventional) sources. In the event of a coincident neutrino/γ-ray detection, time and spectral correlations between them can help in correctly attributing their origin to PBHs.

The first step of this work was to study in detail the particle emission by black holes, which turns out to be a relatively complicated process. The emission spectrum of particle species i (leptons, quarks and bosons) arising directly from Hawking radiation (also called "primary" emission) is a graybody spectrum

$$\frac{\mathrm{d}^2 N_{\mathrm{p}}^i}{\mathrm{d}t\mathrm{d}E}(E, M) = \frac{n_{\mathrm{dof}}^i\,\Gamma^i(M, E)}{2\pi(e^{E/T} \pm 1)} \;, \tag{E-1}$$

where n_{dof}^i is the number of quantum degrees of freedom of a particle of type i, Γ^i the greybody factor and the $+(-)$ sign corresponds to fermions (bosons). Note that the time dependence is implicit since $M = M(t)$. The only non-trivial term is Γ^i, which depends on the mass, spin and internal degrees of freedom of particle species i. Evaluating these greybody factors precisely requires the aid of numerical calculations. Therefore, we use the state-of-the-art `BlackHawk` code (495) for primary spectra calculations.

However, there are also secondary emission spectra arising from hadronization, fragmentation and electroweak corrections, which become increasingly important as the energy increases. These can be obtained by convolution of the primary spectra, $\frac{\mathrm{d}^2 N_{\mathrm{p}}^i}{\mathrm{d}t\mathrm{d}E_{\mathrm{p}}}$, with the spectrum of the secondary particle j generated by the primary particle i, $\mathrm{d}N^{i\to j}/\mathrm{d}E$,

$$\frac{\mathrm{d}^2 N_{\mathrm{s}}^j}{\mathrm{d}t\mathrm{d}E}(E, M) = \sum_i \int_0^{\infty} \mathrm{d}E_{\mathrm{p}} \, \frac{\mathrm{d}^2 N_{\mathrm{p}}^i}{\mathrm{d}t\mathrm{d}E_{\mathrm{p}}}(E_{\mathrm{p}}, M) \frac{\mathrm{d}N^{i\to j}}{\mathrm{d}E}(E, E_{\mathrm{p}}) \; . \tag{E-2}$$

In order to compute $\mathrm{d}N^{i\to j}/dE$, we use the `HDMSpectra` code which accurately accounts for hadronization/fragmentation and electroweak corrections up to Planck scale energies. This is in contrast with `PYTHIA` which has been used in past works and is unsuitable for calculations above a few tens of TeVs. `HDMSpectra` also gives us the probabilities that the primary particles survive without becoming secondaries, which is necessary to obtain the final emission spectra, $\mathrm{d}^2 N_{\mathrm{tot}}^i/\mathrm{d}t\mathrm{d}E$. For more details of these calculations, I kindly ask you to refer to our paper. Figure E.1 shows the primary and secondary emission spectra for γ rays (E.1a) and neutrinos (E.1b) from black holes with masses 10^8 g and 10^{10} g. We compare our results with some results from the literature, including the ratios between our secondary γ-ray spectra and that from (496) (which uses `PYTHIA` for the secondaries computation) and between our primary spectra and the ones used in (497) (which uses analytical approximations for the graybody factors) and more recently by the IceCube Collaboration in (498). There are noticeable differences in both cases which reflect the improvement in our evaluation of these spectra by using `BlackHawk` for the primaries and `HDMSpectra` for the secondaries, especially at higher energies.

The flux of particles arriving at the Earth is obtained by dividing the emission spectrum by $4\pi d^2$, where d is our distance to the PBH (cosmological redshift effects are negligible since we are considering PBHs closer than a parsec to us). We can further estimate the expected number of events at a detector with effective area $A_{\mathrm{eff}}(E, \theta_z)$, where E is the energy of the incoming particle and θ_z is it's zenith angle, by integrating the flux times A_{eff} over a given time interval and over a given energy range. For particle species i, this translates mathematically to

$$N_i(\theta_z, t_i \to t_f) = \frac{1}{4\pi d^2} \int_{E_{\mathrm{min}}}^{E_{\mathrm{max}}} \mathrm{d}E \int_{t_i}^{t_f} \mathrm{d}t \, \frac{\mathrm{d}^2 N_{\mathrm{tot}}^i}{\mathrm{d}t\mathrm{d}E} \, A_{\mathrm{eff}}(E, \theta_z) \; . \tag{E-3}$$

In our paper, we calculate the expected number of muon neutrino events from a PBH explosion at IceCube for different zenith angles and time windows. Figure E-3 shows our expectations for the last 1000, 100 and 10 seconds before the death of a PBH located 10^{-3} pc away from us. Note that we consider the effect of decoherent neutrino oscillations during propagation, which is non-

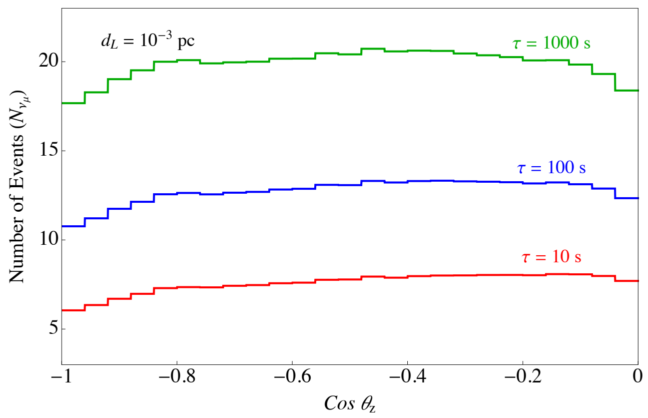

Figure E.2: Expected number of μ-track events at IceCube from an evaporating PBH, located $d = 10^{-3}$ pc from us and at different zenith angles, in the last τ seconds before its death. Figure from (1).

negligible at these distance scales, unlike the effect of the Earth's rotation and the PBH's proper movement across the sky, which we estimate to be both very small. Also, because this is a relatively short-lived transient event, the observation turns out to be essentially background free.

The lack of PBH signals at our detectors allows us to set upper limits on the local PBH explosion rate density,

$$\dot{\rho}_{\max}(\tau) = \frac{N_{\max}}{V_{\max}(\tau) T} , \tag{E-4}$$

where $N_{\max}$ is the maximum number of events expected from PBHs given that there have been no candidate events observed experimentally, $V_{\max}$ is the maximum volume that can be probed by the detector (beyond which PBH events would be compatible with background) and T is the total operating lifetime of the detector. For brevity, we avoid the details of how to calculate $N_{\max}$ and $V_{\max}$, which can be found in our paper. It suffices to show our constraints on the local PBH burst rate in Table E.1, from muon neutrino observations are IceCube over 10 years, for different time windows before a PBH's death. These upper limits are weak when compared to those coming from γ-ray experiments, the strongest of them coming from the HAWC Collaboration at 3400 pc^{-3} yr^{-1} at 99% confidence level (499), mostly due to the small neutrino cross sections lowering IceCube's effective area. In fact, we estimate that the HAWC result can be improved by a factor of ~ 3 with our new evaluation of the primary and secondary emissions. Nevertheless, the results in Table E.1 still serve as a point of reference to show the capability of neutrino detectors in PBH searches. As a side note, although surviving low-mass PBHs are expected to have lost all their initial spin by now (500), we also show in our paper that the constraints for maximally spinning PBHs are

Table E.1: Upper limits on $\dot{\rho}$, at 90% confidence level, from the ten-years IceCube μ-track data set, for three different time intervals τ before the PBH's death.

τ [s]	$\dot{\rho}_{\max}$ [pc^{-3} yr^{-1}]
10	1.7×10^7
10^2	8.2×10^6
10^3	4.1×10^6

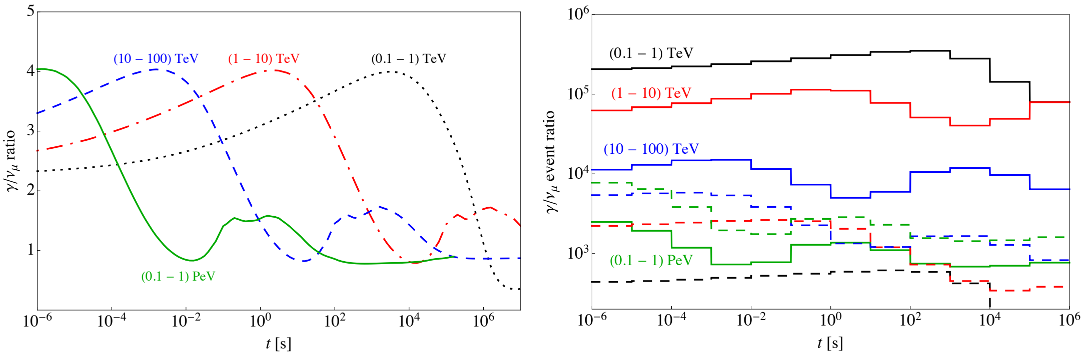

(a) (b)

Figure E.3: *Left*: Ratio of the energy-integrated spectra of γ rays to neutrinos in the stated bins of energy. *Right*: Ratio of the number of γ-ray to neutrino events, respectively at HAWC and IceCube experiments, for a PBH located at declination $\delta = 20°(70°)$ in solid(dashed) curves. Figure from (1).

only marginally stronger that the spinless case.

Lastly, we consider the advantages of a simultaneous multimessenger observation of a PBH explosion in both γ rays and neutrinos. The PBH emission has a characteristic energy and time dependence that we can use to distinguish it from a conventional high-energy multimessenger transient. In particular, the ratio between the the γ-ray and neutrino spectra provides a unique signature of PBHs, while their individual spectra might be replicated by a conventional source with enough parameter tweaking. Figure E.3a shows the time evolution of the γ-ray to neutrino ratio of their spectra integrated over different energy intervals,

$$\int_{E_{\min}}^{E_{\max}} \mathrm{d}E \, \frac{\mathrm{d}^2 N_{\mathrm{tot}}^{\gamma}}{\mathrm{d}t \mathrm{d}E} \Bigg/ \int_{E_{\min}}^{E_{\max}} \mathrm{d}E \, \frac{\mathrm{d}^2 N_{\mathrm{tot}}^{\nu_\mu}}{\mathrm{d}t \mathrm{d}E} \, . \tag{E-5}$$

In that plot, t is the time remaining until the PBH fully evaporates. We see that the peak of the ratio moves towards later times (smaller t values) for higher energies, a special characteristic of PBHs which would be visible at our current detectors with $\sim$ nanosecond time resolution. Also shown is the time evolution of the ratio between the number of events expected at HAWC and IceCube in Figure E.3b, integrated over the same energy intervals, for an explosion coming from two different declinations in the sky ($\delta = 20°$ and $70°$). Of course, the individual numbers of events will depend on our distance to the PBH; the closer the better in terms of statistics, leading to a better determination of the source's nature.